

Some pages of this thesis may have been removed for copyright restrictions.

If you have discovered material in AURA which is unlawful e.g. breaches copyright, (either yours or that of a third party) or any other law, including but not limited to those relating to patent, trademark, confidentiality, data protection, obscenity, defamation, libel, then please read our [Takedown Policy](#) and [contact the service](#) immediately

ION PLATING

By Babak Mahmoudian

Submitted for the degree of Ph.D.

at The University of Aston in Birmingham

July 1983

Dedicated to my aunt MS M.Mahmoudian

Summary

ION PLATING

By Babak Mahmoudian

submitted for the degree of Ph.D.

at the University of Aston in Birmingham, 1983.

Summary

Under ideal conditions ion plating produces finely grained dense coatings with excellent adhesion. The ion bombardment induced damage initiates a large number of small nuclei. Simultaneous coating and sputtering stimulates high rates of diffusion and forms an interfacial region of graded composition responsible for good adhesion. To obtain such coatings on components for industrial applications, the design and construction of an ion plater with a 24" (0.6m) diameter chamber were investigated and modifications of the electron beam gun were proposed. A 12" (0.3m) diameter ion plater was designed and constructed.

The equipment was used to develop surfaces for solar energy applications. The conditions to give extended surfaces by sputter etching were studied. Austenitic stainless steel was sputter etched at 20 and 30 mTorr working pressure and at 3, 4 and 5 kV. Uniform etching was achieved by redesigning the specimen holder to give a uniform electrostatic field over the surfaces of the specimens.

Surface protrusions were observed after sputter etching. They were caused by the sputter process and were independent of grain boundaries, surface contaminants and inclusions.

The sputtering rate of stainless steel was highly dependent on the background pressure which should be kept below 10^{-5} Torr.

Sputter etching improved the performance of stainless steel used as a solar selective surface. A twofold improvement was achieved on sputter etching bright annealed stainless steel. However, there was only slight improvement after sputter etching stainless steel which had been mechanically polished to a mirror finish.

Cooling curves were used to measure the thermal emittance of specimens.

The deposition rate of copper was measured at different levels of power input and was found to be a maximum at 9.5 kW. The diameter of the copper feed rod was found to be critical for the maintenance of a uniform evaporation rate.

Key words: ion plating, sputter etching, stainless steel.

LIST OF CONTENTS

	Page
List of Tables	IX
List of Figures	XI
Acknowledgements	XXII
<u>CHAPTER ONE:</u>	
Introduction to Ion Plating	1
1.1: Ion Plating Processes	3
1.2: Development and improvements in ion plating	4
1.2.1: Modifications related to sputtering of the specimen	4
1.2.1.1: R.F. sputtering	4
1.2.1.2: Triode assisted ion plating	6
1.2.1.3: Reactive discharge	6
1.2.1.4: Use of a magnetic field	6
1.2.2: Vapour sources	7
1.2.2.1: Thermal evaporation	7
1.2.2.1.1: Resistive heating	7
1.2.2.1.2: R.F. heating	8
1.2.2.1.3: Arc evaporation	9
1.2.2.1.4: Plasma evaporation	9
1.2.2.1.5: Electron beam heating	9
1.2.2.2 : Sputtering	10
1.2.2.3: Chemical ion plating	11
1.3: Process Modifications	11
1.3.1: Bias sputtering	11

	Page
1.3.2: Reactive ion plating	12
1.4: Mechanisms involved in ion plating	12
1.5: Ion plating processes in detail	15
1.5.1: Precautions to avoid contamination and excessive back sputtering	16
1.5.2: Ion bombardment effects prior to coating	18
1.5.2.1: Sputtering	18
1.5.2.2: Defect production	22
1.5.2.3: Crystallographic disruption	24
1.5.2.4: Surface morphology changes	25
1.5.2.5: Gas incorporation	25
1.5.2.6: Temperature rise	26
1.5.2.7: Surface contamination	27
1.5.2.8: Physical mixing	27
1.5.3: Ion bombardment effects during the coating	28
1.5.3.1: Physical mixing	28
1.5.3.2: Enhanced diffusion	29
1.5.3.3: Nucleation modes	29
1.5.3.4: Preferential removal	31
1.5.3.5: Surface coverage	31
1.5.3.6: Morphology	32
1.5.3.7: Crystallography	34
1.5.3.8: Composition	34
1.5.3.9: Physical properties	35
1.6: Ion plated films	37
1.6.1: Properties and applications	37
1.6.2: Effects of operational parameters on properties	40

	Page
<u>CHAPTER TWO:</u>	
Glow Discharge	42
<u>CHAPTER THREE:</u>	
Sputtering	54
3.1: Sputtering from linear collision cascades	55
3.2: Non-linear effects	58
3.3: Multiple component target	59
3.3.1: Primary sputtering effects	59
3.3.2: Secondary effects	61
3.4: Dependence of sputtering yield on angle of incidence	62
<u>CHAPTER FOUR:</u>	
Surface Roughness Caused by Ion Bombardment	66
4.1: Cone formation by use of seed atoms	66
4.2: Seedless cone formation	71
4.3: Effect of specimen temperature	88
4.4: Texturing of stainless steel	88
<u>CHAPTER FIVE:</u>	
Solar Energy	91
5.1: Light	91
5.2: A perfect blackbody	95
5.2.1: Definition of a blackbody	95
5.2.2: Planck's law	95
5.2.3: Wien's displacement law	96
5.2.4: Total emitted power	98
5.3: Radiation terminology	98
5.3.1: Suffixes	98

	Page
5.3.2: Prefixes	98
5.4: Radiation properties of non-black surfaces	99
5.4.1: Absorptivity	101
5.4.2: Emissivity	102
5.4.3: Kirchhoff's law	103
5.4.4: Reflectivity	105
5.4.4.1: Reflection function	105
5.4.4.2: Hemispherical reflectance	106
5.4.5: Relationship between absorptance, emittance and reflectance	110
5.5: Selective surfaces	111
 <u>CHAPTER SIX:</u>	
Production of Solar Selective Surfaces	115
6.1: Previous work	115
6.2: The proposed experimental work	121
6.3: Experimental procedure	124
6.3.1: Materials	124
6.3.1.1: Specimens	124
6.3.1.2: Coating material	124
6.3.2: Specimen preparation	124
6.3.3: Jigging	125
6.3.4: Measurements	126
6.3.4.1: Pressure	126
6.3.4.2: Current	126
6.3.4.3: Voltage	126

	Page
6.3.4.4: Total energy input	127
6.3.4.5: Temperature	127
6.3.4.6: Roughness	128
6.3.4.7: Weight	128
6.3.4.8: Average thickness of removed material	128
6.3.4.9: Coating thickness measurement	129
6.3.4.10: Solar absorptivity measurement	129
6.3.4.11: Infrared emissivity measurement	133
6.3.4.12: Thermal emittance measurement using cooling curves	134
6.3.5: Effect of background pressure	136
6.3.6: Deposition of copper	136
 <u>CHAPTER SEVEN:</u>	
The Equipment	139
7.1: The vacuum systems	139
7.1.1: The top vacuum chamber	139
7.1.2: The bottom chamber	141
7.1.3: Control panels	141
7.1.4: Operation	142
7.2: The glow discharge unit	144
7.2.1: The control panel	144
7.2.2: Operation	144
7.3: The rod fed crucible	146
7.4: The electron beam gun	146
7.4.1: Operation	147
7.5: Modifications to the ion plating equipment	149
7.5.1: Repositioning the ion gauge in the top chamber	149

	Page
7.5.2: Modifications to the Auto Glow Discharge Unit	150
7.5.3: Modifications to the bottom chamber	152
7.6: Addition of an air compressor	156
7.7: Problems encountered with commissioning	157
7.8: Design of electron beam guns	164
7.8.1: General design of transverse electron beam guns	167
7.8.2: Discussion of the characteristics of a power supply for transverse electron beam guns	170
7.8.3: Design of the electron beam gun and the power supply supplied by the Electrotech Equipments Limited	174
7.8.4: Protection system of the power supply and the electron beam gun	176
7.8.5: Discussion and proposed modifications of the electron beam gun	180
7.9: Design and construction of a 12" chamber diameter ion plater	182
7.9.1: General specification of the "Speedivac" coating unit	182
7.9.2: Design alterations	183
7.9.3: Construction details	188
7.9.4: Further requirements of the ion plater	198
 <u>CHAPTER EIGHT:</u>	
Results and Discussion	199

	Page
8.1: Sputtering results obtained using jig number one	199
8.2: The edge effects	212
8.3: Effect of background pressure	215
8.4: Results obtained using jig number 2	217
8.5: Solar absorptivity and thermal emissivity measurements	233
8.6: Cooling curve thermal emittance measurements	241
8.7: Deposition of copper	252
 <u>CHAPTER NINE:</u>	
Conclusions	262
 <u>CHAPTER TEN:</u>	
Further Work	264
 <u>APPENDIX A</u>	
1: Design and construction of jig number one	266
2: Design and construction of jig number two	274
3: Design and construction of the thermocouple holder	277
 <u>APPENDIX B</u>	
Operational Procedure for the small Ion Plater	281
1: Original switch on	282
2: To open the chamber	282
3: Pump down procedures	283
4: Glow discharge operation	284
5: Evaporation procedure	284

	Page
6: Complete shut off procedure	285
7: Emergency shut off procedure	285
8: Proposed guide lines	285
<u>REFERENCES</u>	287

List of Tables

Table number		Page
1.1	Sputtering yields of various materials bombarded by Ar ⁺	20
1.2	Sputtering yield of Cu target, bombarded by 1 KV ions of different masses	21
6.1	Percentage reflectance at normal incidence of freshly evaporated mirror coatings of Au, Ag, Al and Cu	122
8.1	Results obtained from 24 specimens, using jig number 1	203
8.2	Statistical analysis of the vigour of the sputtering	204
8.3	Effect of background pressure	216
8.4	Statistical analysis of the results presented in Table 8.3	216
8.5	Results obtained using jig number 2	218
8.6	Statistical analysis of results presented in Table 8.5	220
8.7	ρ_{λ} measurements of the Bright Annealed & the "Mirror Polished" specimens before and after sputter etching: based on Weighted Ordinates method	235

Table number		Page
8.8	ρ_{λ} measurements of the Bright Annealed and the "Mirror Polished" specimens before and after sputter etching based on Selected Ordinates method	236
8.9	Infrared specular spectral reflectivity measurements of the Bright Annealed and the "Mirror Polished" specimens before and after sputter etching	238
8.10	Measured absorptivities and emissivities of the Bright Annealed and the "Mirror Polished" specimens	239
8.11	Performance of the Bright Annealed and the "Mirror Polished" surfaces before and after sputter etching; as selective surfaces	239
8.12	Measured temperatures for calculation of emittance	242,243
8.13	Calculated thermal emittances based on cooling curves	244
8.14	Deposition rates of copper (melt at level A)	254
8.15	Deposition rates of copper (melt at level B)	256
8.16	Statistical analysis of results presented in Table 8.15	257

List of Figures

Figure number		Page
1.1	A simple system for bias ion plating	5
1.2	Sputtering yield of Cu, Ni and Mo as a function of the energy of bombarding ions and the angle of incidence	21
2.1	Voltage/current behaviour of an electric discharge	43
2.2	Spatial distribution of dark space and luminous zones, electric field, space charge densities, and current densities in a glow discharge	44
2.3	Product of dark space thickness and pressure as a function of cathode fall for an Fe cathode in various gases	51
2.4	Dependence of abnormal cathode fall on the reduced current density for an Fe cathode in various gases	52
3.1	Series of collision processes leading to sputtering of atoms	55
3.2	Comparison between Sigmund's theoretical curve and $\alpha(M_2/M_1)$ values obtained by Andersen and Bay	57
4.1	The motion of the intersection between two plane surfaces during erosion	71

Figure number		Page
4.2	The erosion of a surface step	74
4.3	Contour plot of deposited energy	76
4.4	Formation of grooves around the bottom of cones based on Sigmond's theory	77
4.5	Variation of sputtering yield with angle of incidence for Ar^+ on silica glass	81
4.6	Polar diagram of the reciprocal sputtering ratio for silica glass	81
4.7a	Erosion slowness curve, trajectories, and profiles of a deep trough on a silica glass surface due to sputtering	84
4.7b	Erosion slowness curve, trajectories, and evolved profiles of a shallow hemispherical trough on a silica glass surface due to sputtering	84
4.8	The evolution of sputtered shapes from an initial sinusoidal glass surface during ion bombardment	85
4.9	Formation & stability of hillocks on slow and fast etching crystal surfaces	85
4.10	Equilibrium topography of a hillock where the trajectories of intersections are normal to the flat surface	87

Figure number		Page
4.11	Influence of ion bombardment duration on density of cones, observed on stainless steel	90
5.1	A standard spectral irradiance curve compiled by NASA	92
5.2	Spectrum of electromagnetic radiation	93
5.3	Spectral distribution of blackbody radiation	97
5.4	Spatial distribution of incident and reflected radiation on a mirror like surface	106
5.5	The spectral reflectance of an ideal selective surface	112
5.6	Spectral reflectances of several selective surfaces	112
6.1	Thornton's diagram	119
6.2	Modified Thornton's diagram	119
6.3	Reflectance of freshly evaporated mirror coatings of Al, Cu, Ag and Au	123
6.4	Solar irradiance at sea level with surface perpendicular to the sun's ray and air mass of 2	131

Figure number		Page
6.5	Absolute reflectance values of BaSO ₄ paint	132
6.6	Position of the melt level relative to the electron beam gun assembly and the crucible	138
7.1	Block diagram of the 24" chamber diameter ion plater	140
7.2	Vacuum systems and glow discharge control panels of the 24" chamber diameter ion plater	143
7.3	Electron beam gun and rod feed control panels, and the ANAVAC-2 massspectrometer	145
7.4	Position of the needle and shut off valves	151
7.5	Lower chamber's high vacuum valve	154
7.6	Pneumatic valve controls	155
7.7	Assembly of the electron beam gun and the water cooled rod fed crucible	158
7.8	Juxtaposition of the electron beam gun and the crucible	159
7.9	Signs of arcing on the crucible assembly	159
7.10	The electron beam gun assembly	162

Figure number		Page
7.11	Signs of arcing underneath the anode bowl. Operating voltage 10 KV	162
7.12	Damaged anode bowl of the electron beam gun assembly	163
7.13	Inside of the anode bowl	163
7.14	Influence of applied voltage and temperature on emission current density	165
7.15	Juxtaposition of the filament, beam former and the anode plate	168
7.16	Cross section of a 270° beam bend transverse electron beam gun	168
7.17	General design of a 270° beam bend transverse electron beam gun	169
7.18	Characteristics of a constant current triode power supply	173
7.19	Characteristics of a current limited (switches) triode power supply	173
7.20	Characteristics of a constant voltage/current triode power supply	173
7.21	Signs of arcing on the outside of the anode bowl. Operation voltage 7.5 KV	175
7.22	A hole burnt in the anode bowl	175

Figure number		Page
7.23	Flow chart of the power supply of the ion plater	177
7.24	A part of the arc trip module indicating the probable fault region within the hatched area	179
7.25a	Original design of the electron beam gun assembly	181
7.25b	The proposed design of the electron beam gun assembly	181
7.26a	Block diagram of the vacuum line of the "Speedivac" coating unit	185
7.26b	Block diagram of the vacuum line of the 12" chamber diameter ion plater	186
7.27	Wiring diagram of the ion plater	187
7.28	Stainless steel chamber of the ion plater	190
7.29	The assembly of the high tension lead-through	192
7.30	The low tension leadthrough assembly	195
7.31	The winch system and front view of the ion plater	197
7.32	Side view of the ion plater	197

Figure number		Page
8.1	Influence of applied voltage and pressure on sputtering rate	200
8.2	Sputter etched specimens at 20 mTorr pressure and 5 KV applied voltage	201
8.3	30 minutes sputter etched specimens at 20 mTorr pressure	202
8.4	30 minutes sputter etched specimens at 30 mTorr pressure	202
8.5	Sputter etched surface of specimen A16	205
8.6	Pillar type segregates on sputter etched surface of specimen A16	205
8.7	Sputter etched surface of specimen A22	207
8.8	Magnesium silicate inclusions on sputter etched surface of specimen A22	207
8.9	Sputter etched surface of specimen A21	209
8.10	Sputter etched surface of specimen A17	209
8.11	Sputter etched surface of specimen A26	210
8.12	Sputter etched surface of specimen A03	211
8.13	Sputter etched surface of specimen A03	211
8.14	Microstructure of the edge of specimen A19	214

Figure number		Page
8.15	Variation of sputtering rate by sputtering time	219
8.16	Changes in brightness of specimens sputter etched at 30 mTorr & 4 KV using jig number 2	221
8.17	Brightness uniformity of specimens sputter etched at 30 mTorr, 4 KV, & 60 min., held in jig number 2	221
8.18	Comparison of field force lines of specimens fixed in jigs number 1 & 2	222
8.19	Sputter etched surface of specimen A67	225
8.20	Large ripples on specimen A67	225
8.21	Three differently etched grains on specimen A67	226
8.22	Sputter etched surface of specimen A55	228
8.23	Orientation dependence of sputtering and the depth of etching on specimen A55	228
8.24	Specimen A50, sputter etched at 30 mTorr, 4 KV, & 60 mins.	230
8.25	Sputter etched surface of specimen A50	230
8.26	Magnitude of surface roughness and growth of etch pits on sides of unetched grains of specimen A50	231

Figure number		Page
8.27	Visible range reflectivity of the "Mirror Polished" specimen prior to and after ion bombardment	234
8.28	Visible range reflectivity of the Bright Annealed specimen prior to and after ion bombardment	234
8.29	Infrared specular spectral reflectiv- ities of the Bright Annealed and the "Mirror Polished" specimens before and after sputter etching	237
8.30a	Measured temperatures and calculated cooling curve of specimen D03	245
8.30b	Measured temperatures and calculated cooling curve of specimen D02	245
8.30c	Measured temperature and calculated cooling curve of specimen D04	246
8.30d	Measured temperatures and calculated cooling curve of specimen D01	246
8.31a	Measured temperatures and calculated cooling curve of specimen D08	247
8.31b	Measured temperatures and calculated cooling curve of specimen D07	247

Figure number		Page
8.31c	Measured temperatures and calculated cooling curve of specimen D06	248
8.31d	Measured temperatures and calculated cooling curve of specimen D05	248
8.32a	Measured temperatures and calculated cooling curve of specimen D12	249
8.32b	Measured temperatures and calculated cooling curve of specimen D10	149
8.32c	Measured temperatures and calculated cooling curve of specimen D11	250
8.32d	Measured temperatures and calculated cooling curve of specimen D09	250
8.33	Positions of the melt level in the water cooled crucible	253
8.34	Plot of deposition rate of copper versus power input (melt at level B)	258
A1	Parts of jig number 1	268-271
A2	Assembly of jig number 1	272
A3	Three main parts of jig number 1	273
A4	A specimen held in jig number 1	273
A5	Jig number 2	275
A6	A specimen held in jig number 2	276

Figure number		Page
A7	The thermocouple holder	279
A8	The operational position of the thermocouple holder	279
A9	Principal mechanism of relative movements of the thermocouple and the thermocouple holder	280

Acknowledgements

I wish to express my sincerest gratitude to Dr.D.J.Arrowsmith for his support and excellent supervision throughout the course of this work.

I would like to thank Professor T.Mulvey for his most valuable discussions.

My thanks also go to all the technicians in the Department of Metallurgy and Materials Engineering for their valuable assistance, in particular Mr.E.Watson for his technical advice and encouragement during hard times.

I would also like to thank the University of Aston in Birmingham for providing me with the studentship.

My thanks also extend to Mrs.A.Howell for typing this thesis.

I am most grateful to my parents and sister for their encouragement, patience and financial support.

CHAPTER ONE:

INTRODUCTION.

In 1938 a patent was issued to B.Berghaus⁽¹⁾. In that patent it states "This invention relates to a method of coating articles of any kind by means of thermally vaporised material, and it consists in that the vaporisation of the material is effected in a reduced pressure of 40 to 0.001 mm Hg, preferably at 5 to 0.01 mm Hg, at which a glow discharge takes place, with the article connected up permanently or temporarily as the cathode of the glow discharge, and the voltage being so chosen that the article is completely covered by the glow of the discharge."

In that patent Berghaus suggests a voltage of 400 to 20,000 volts and an argon atmosphere for the discharge. To remove surface oxides or grease, he recommends a glow discharge in a reducing atmosphere for a certain period before vaporisation. He also mentioned the use of organics (such as organo-metallic gases) and inorganic compounds as sources of coating materials.

The term "Ion plating" is first reported in a technical report in 1964 by D.M.Mattox⁽²⁾, referring to the same general approach. There he has described Ion Plating as: "A generetic term applied to atomistic film deposition processes in which the substrate surface is subjected to a flux of high energy ions sufficient to cause appreciable sputtering before and during film formation."

Because of its unique and promising features, the technique has been subjected to intensive research, and is now commercially available. Much is still needed for a full understanding of the technique and of the mechanisms involved, but in reviewing work done, Mattox⁽³⁾ broadened his previous⁽²⁾ definition of ion plating to: "A generetic term applied to film deposition processes in which the substrate surface and/or the depositing film is subjected to a flux of high energy particles, sufficient to cause changes in the interfacial region or film properties compared to a non-bombarded deposition. Such changes may be reflected in the adhesion, film morphology, film stress, film density, or the coverage of the surface by the depositing film material."

The fundamentals and application of ion plating processes have been discussed by Mattox^(4,5,6,7) who has also published an extensive bibliography on ion plating and related subjects⁽⁸⁾.

In general, ion plating techniques are capable of producing relatively dense coatings, and (depending on the evaporation source) at fast deposition rates, difficult to match using any other technique (20 $\mu\text{m}/\text{minute}$ is common⁽⁹⁾). The most important advantage of ion plating is having very good adhesion between coating and substrate, even in the case of incompatible materials⁽¹⁰⁾. Also it is possible to apply coatings of refractory materials, carbides and nitrides^(11,12), by using reactive gases. Another big advantage is the absence of effluent treatment and its

associated problems. But the big disadvantage is that ion plating is a wasteful process, and because of the complexity of the mechanisms involved and the interaction of the many variables, reproduceability is not very good.

ION PLATING PROCESSES:

1.1: The basic ion plating process (bias ion plating).

In the simplest process of ion plating which is called "Bias ion plating", the chamber is subjected to a vacuum of about 10^{-6} Torr to remove a substantial amount of undesirable air, as well as substantial amounts of gases and water vapour adsorbed on the specimen and chamber walls. Then an inert gas (usually argon) is introduced into the chamber, and while maintaining the flow of the gas, the pressure is set between 5 to 50 mTorr. A high negative voltage of 2 to 5 KV is applied to the specimen. This will produce a glow around the specimen and an electric discharge between the specimen (cathode) and body of the chamber (anode) which is electrically earthed. This glow discharge causes ion bombardment of the specimen and by a sputtering action removes contaminants and oxide off the specimen surface. When the required clean surface is obtained, the coating material is evaporated. Atoms and clusters of vaporised material enter the glow discharge, some of them become charged, and proceed to the specimen covering it, under ion bombardment.

Care must be taken that rate of deposition is kept higher than the rate of removal by sputtering, otherwise there

would be no coating of the specimen. When the required thickness of coating is obtained, evaporation is stopped and the glow discharge switched off.

Figure 1.1 shows the apparatus used for bias ion plating.

1.2: Development and improvements in ion plating.

The above mentioned basic ion plating process has limitations, and therefore for specific purposes modifications are necessary. In general these modifications fall into two categories; (1) modifications related to the specimen and its sputter cleaning, and (2) modifications related to the source of coating material.

1.2.1: Modifications related to sputtering of the specimen.

1.2.1.1: If electrically insulating specimens are attached to the cathode of a d.c. discharge, they will not be cleaned in the same way as metals⁽¹³⁾. They rapidly build up a surface charge which repels further bombardment by positive ions. To overcome this problem, radio frequency power can be introduced to the cathode. This will maintain the surface of insulators at a negative potential. This phenomenon of self biasing is a result of the much greater mobility of the electrons in a discharge compared with that of the ions.

Walley⁽¹⁴⁾ showed the use of RF excitation when ion cleaning makes the process more effective by allowing lower working

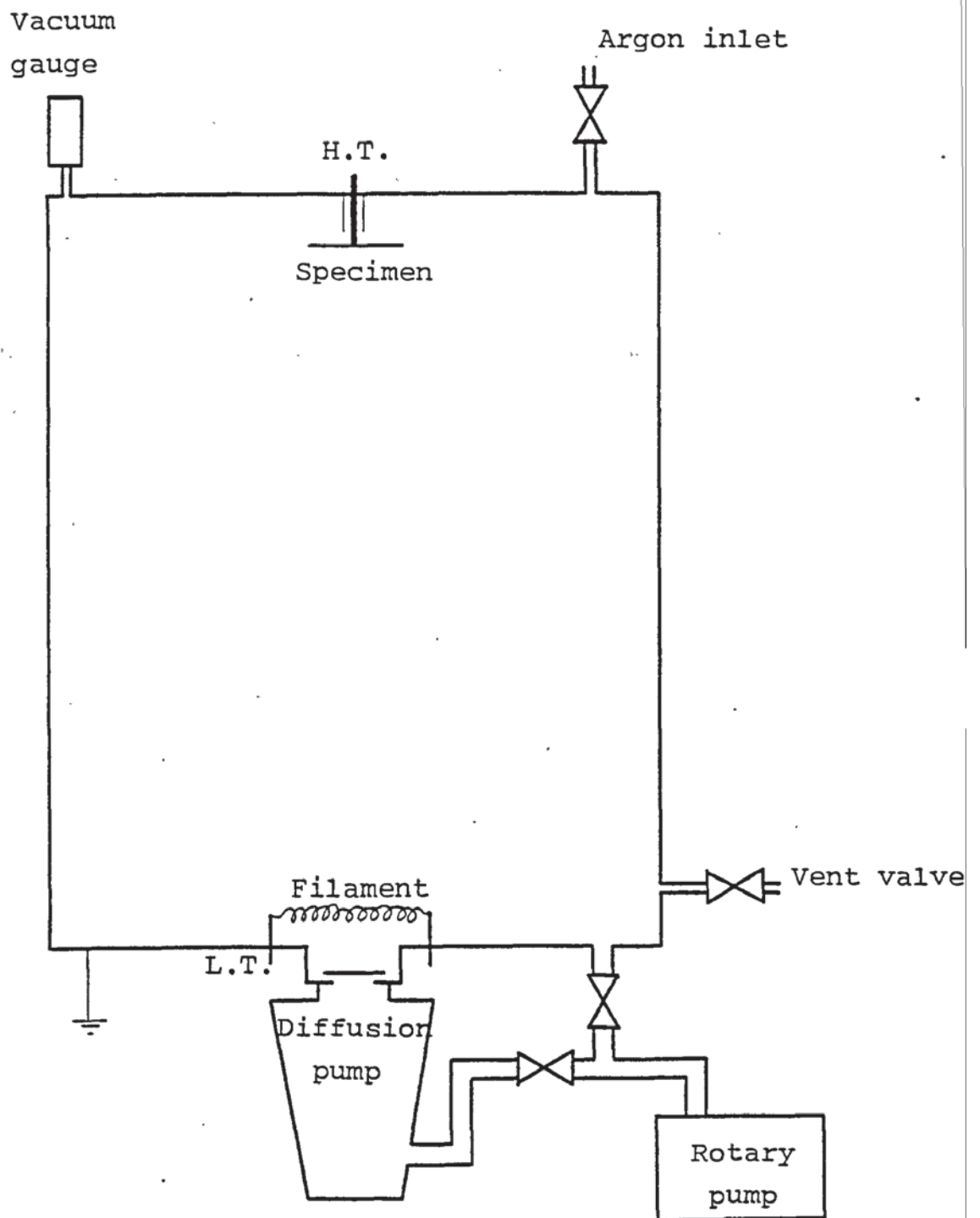


Fig.1.1: A simple system for bias ion plating.

pressures. If ion clean-up is operated at relatively high pressures (say 100 mTorr) approximately 80% of all material removed is reflected back to the cathode due to the short mean free path (mfp) at this pressure. At 10 mTorr most of the sputter etched material escapes from the cathode region. The operating region for ion clean-up is a compromise between the maximum current density obtainable (which increases with pressure), and the maximum escape efficiency (which decreases with pressure), and this operating region can be optimised by the use of RF excitation.

1.2.1.2: Triode assisted ion plating.

The second development allowing work at lower pressures is the use of an auxiliary cathode which thermionically supplies auxiliary electrons from a filament^(15,16). This increases the total ionisation and the ionisation efficiency and therefore the glow discharge can be established at lower pressures.

1.2.1.3: Reactive discharge.

For oxide ceramics, an oxygen discharge may be used to advantage, since it will tend to volatilize hydrocarbon contaminants by forming CO⁽⁶⁾.

1.2.1.4: Use of a magnetic field.

The ionisation efficiency can be increased by increasing the path length of the ionising electrons, by a transverse magnetic field normal to the electric field. Such a field will concentrate the discharge at one side of a planar

cathode and thus will reduce the uniformity of the deposit. This disadvantage may be overcome by the use of a cylindrical cathode and a magnetic field parallel to its axis⁽¹⁷⁾. Much more uniform deposits particularly on three-dimensional specimens can be obtained by depositing on a substrate placed inside a hollow cathode. The 'hollow cathode effect' allows the anode to be placed outside without interfering with the discharge.⁽¹⁸⁾ Gill & Kay⁽¹⁹⁾ used a hollow cathode discharge supported by an external magnetic field with an internal coaxial anode at 10^{-5} Torr.

Enhanced sputtering rates up to 30 times are obtained by using both transverse and longitudinal magnetic fields⁽²⁰⁾.

1.2.2: Vapour sources.

To transfer the coating material onto the specimen, the coating material must be in the form of vapour. There are three methods of producing the coating material in vapour form :- thermal evaporation, sputtering, and by chemical reaction.

1.2.2.1: Thermal evaporation.

In this method the coating material is evaporated by means of a heat source. There are quite a few ways of evaporating the coating materials⁽²¹⁻²³⁾. The following are examples of those methods.

1.2.2.1.1: Resistive heating.

This method consists of heating the material with a

resistively heated filament or boat, generally made of refractory metals such as W, Mo, Ta and Nb, with or without ceramic coatings. The main factor in choosing the container is the chemical reactivity of the evaporant material at temperatures near to its boiling point.

Multiple-component alloys or compounds can be evaporated by this method, providing that the required temperature can be obtained. But the problems are that the components may evaporate at different rates because of their different vapour pressures, their different tendencies to react with support material, and possible thermal decomposition of the parent material. These factors will obviously produce nonstoichiometric films; but on the other hand, the higher the evaporation temperature of an alloy of widely different vapour-pressure component is, the closer is the composition of the film to the bulk alloy⁽²⁴⁾. Therefore the remedy is a rapid, high temperature evaporation. This can be obtained by continuously dropping fine particles of the material onto a hot source so that numerous discrete evaporations occur^(25,26). This method is called 'flash evaporation'. But it must be mentioned that flash-evaporated films in some cases have shown considerable deviation from the original composition⁽²⁷⁾.

1.2.2.1.2: RF heating.

The RF or induction heating may be applied to the evaporant directly or indirectly from the crucible⁽²⁸⁻³⁰⁾. It is accompanied by an associated magnetic field. Care must be

taken about the effect of this magnetic field on the glow discharge⁽³¹⁾.

1.2.2.1.3: Arc evaporation.

By striking an arc between two electrodes of a conducting material, sufficiently high temperatures can be generated to evaporate refractory materials such as Nb and Ta.

1.2.2.1.4: Plasma evaporation.

A plasma source can be used to vaporise and partially ionize the coating material⁽³²⁾.

1.2.2.1.5: Electron beam heating.

The simple resistive heating of an evaporation source has the disadvantages of possible contamination from the support material and the limitation of input power, which make it difficult to evaporate high-melting-point materials.

A basic form of electron-beam evaporation source for conducting materials consists of a thermionic emitter filament at a high negative potential placed near to the evaporant. If the evaporant is held at earth potential, electrons emitted from the filament accelerate and then lose their energy in the form of heat dissipated in the evaporant⁽³³⁾. This type of electron beam gun is not suitable for evaporating insulating materials. There are designs of electron beam guns having built-in anode and focusing magnets to direct a high energy focussed beam of electrons into any material. In this way, very high power inputs can

be applied in very small areas and any desired material can be easily vaporised. The very high power densities available also make it possible to evaporate very pure materials by heating the central part of the evaporant to its boiling point while keeping the outer parts cold in contact with a water cooled crucible; in this way the material effectively forms its own crucible.

To produce thick films, large crucibles and also rod-fed sources can be used⁽³⁴⁻³⁶⁾.

In using electron beam guns it must be noticed that the electron beam ionizes some of the evaporant vapour, and this causes extra sputtering on the specimen; therefore it may be necessary to decrease the applied potential to the specimen, to avoid excessive sputtering and therefore achieve the required thickness of coating.

1.2.2.2: Sputtering.

Sputtering is another way of producing the required vapour. Sputtering has advantages over evaporation when dealing with alloy deposition and when a precise rate of evaporation is required. In this technique the sputtering action produces the ejected atoms which make the cloud of coating material.

A relatively new development in sputtering techniques is the use of an intense magnetic field to confine the electrons produced in the plasma⁽³⁷⁾ which enables operation

at very high current densities. An additional advantage of this technique is that secondary electron heating of the substrate is avoided and substrate temperature can be independently controlled.

All previously mentioned methods of improving sputter cleaning of the specimen, such as triode sputtering, are applicable to this technique as well. These techniques are now widely used to deposit metals, alloys, and semi-conductors under controlled conditions.

1.2.2.3: Chemical ion plating⁽³⁸⁾.

Another way of obtaining the vaporised material is a chemical reaction in vapour phase. In this technique, chemical vapour deposition is used to produce the coating material. This is the major technique for depositing certain coatings such as amorphous-silicon⁽³⁹⁾, TiC, TiN, and $\text{TiC}_x\text{N}_{1-x}$ ⁽⁴⁰⁾

1.3: Process modifications.

Bias ion plating is the simplest ion plating technique. By combining the above mentioned modifications on specimen sputtering and evaporation sources, much improved coatings can be obtained. Each of the major techniques explained in this section has its unique advantages.

1.3.1: Bias sputtering⁽⁴¹⁾.

In this technique the RF power is shared between the cathode and anode. This results in sputtering of weakly bonded atoms from the substrate and also much reducing gas

content in the sputtered films.

1.3.2: Reactive ion plating.

It is very difficult to obtain certain coating materials in vapour phase, e.g. nitrides and carbides. A way of doing this is to evaporate or sputter the metal and use nitrogen or a suitable hydrocarbon in the glow discharge gas. The metal vapour reacts with the reactive gas and produces the compound which is deposited on the specimen^(42,43). By this method hard coatings such as TiC, TiN and WC can be deposited.

1.4: Mechanisms involved in ion plating.

The mechanisms involved in ion plating have been discussed by many investigators⁽⁴⁴⁾. The view implicit in most of the early papers was that a substantial proportion of the evaporated atoms were ionized in the glow discharge and arrived at the substrate with the maximum energy, i.e. 5 KeV for a 5 KV bias.

Deposition on the back surface of the specimen was attributed to the ions following field lines which ended on the back surface. The graded interface was thought to be caused by ion implantation aided by diffusion where possible. The diffusion would be accelerated both by high surface temperatures caused by the ion-bombardment and by a high concentration of vacancies in the surface layer (also produced by the ion bombardment).

Leder⁽⁴⁵⁾ attributes the improved adhesion of coatings produced by ion plating to the effect of deposited ions, and states that the preferential removal of un-ionized and therefore loosely bonded deposit by sputtering results in a net deposit with a much larger percentage of ionized material than existed in the vapour phase. Teer⁽⁴⁴⁾ dismisses this idea on the grounds that the sputtering rate, in a filament evaporation source, is less than 30% of the deposition rate⁽⁴⁶⁾ and it does not show any improved adhesion compared with electron beam gun evaporation sources, which have much higher deposition rates.

A number of estimates of the efficiency of ionization in the ion plating process have been made. In a discussion session following a conference on ion plating⁽⁴⁷⁾, estimates varying from 1% to about 30% were made. The figure of 30% was based on the fact that the thickness of coating on the back surface of an ion-plated flat plate was 30% of the thickness on the front surface, and the assumption was made that back surface coating was due only to ions (following the field lines) whereas that on the front surface was due to both ions and neutrals. This assumption can be shown to be incorrect and therefore this high estimate of ionization efficiency can be discounted. In a paper presented to the same conference, Aisenberg⁽⁴⁸⁾ states that the ionization efficiency will usually be less than 1%⁽⁴⁹⁾ and therefore the large majority of deposited material is brought to the substrate in the form of unionized atoms rather than in the form of ions. This view

is further substantiated⁽⁴⁸⁾ by lists of ionization efficiencies previously reported for various plasma conditions. These efficiencies range from 0.035% to 1.98% with an average figure of 0.52%.

The comparison between the cathode current (consisting of ions arriving at, and electrons leaving, the cathode) with the number of atoms striking the cathode per second at the usual gas pressures used gives ionization figures of about 0.1%⁽⁴⁴⁾. Another approach can be achieved by assuming that all the ions arriving at the cathode are vapour atoms; the ionization efficiency can be calculated from the comparison of the ions reaching the cathode, with the number of deposited atoms (calculated from the thickness of the deposit). This gives a maximum ionization value of 1%⁽⁴⁴⁾, but it must be noted that the approach is only partially correct because many of the ions arriving at the cathode are inert gas ions and many of the deposited atoms are sputtered off; therefore the calculated value is an over estimate.

Davis and Vanderslice⁽⁵⁰⁾ have presented a theory for the ion-energy distribution in a glow discharge. It is calculated⁽⁴⁴⁾ that under ion plating conditions the average energy of ions is 10% of the maximum possible energy and that the total energy carried by the ions to the cathode is also 10% of the energy dissipated in the system. According to Davis and Vanderslice's⁽⁵⁰⁾ theory, the energy lost by ions is transferred to the neutrals. Teer⁽⁵¹⁾

has proposed an approximate theory for the energy distribution of the neutrals. This indicates that as a result of charge transfer collisions within the cathode dark space, energetic neutrals are formed, and their maximum possible energy is equal to the maximum possible energy of an ion.

Measurements indicate that about 70% of the energy transferred to the neutrals reaches the cathode⁽⁵²⁾. Therefore ion plating appears to be the deposition of a small number of energetic ions and a much larger number of energetic neutrals⁽⁴⁴⁾. The average energies involved are an order of magnitude less than the maximum possible energies, but are still much higher than in other deposition processes. These ideas are shown to be generally correct⁽⁵²⁾.

1.5: Ion plating processes in detail.

In ion plating, the sample is subjected to a negative potential and therefore is the cathode relative to the body of the chamber which is earthed. The chamber is pumped down to a vacuum of about 10^{-6} Torr. Then an inert gas is introduced into the chamber and pressure is set at about 20 mTorr, and the potential is applied to the cathode to establish the glow discharge.

The glow discharge causes sputtering of the cathode and after a while the sample (cathode) is clean and most of the oxide and other contaminants are removed. Then the coating material is evaporated and injected into the glow

discharge. In this stage, while sputtering of the cathode continues the coating material deposits all over the chamber as well as onto the cathode.

This is an oversimplified description of ion plating. For a better understanding, each part of the process will be described in detail.

1.5.1: Precautions to avoid contamination and excessive back sputtering.

In ion plating it is usual to pump down the vacuum system to around 10^{-6} Torr, and then back-fill with Argon gas to the required pressure. In this way the level of gaseous impurities and water vapour, which will interfere with the process, is kept to a minimum. The ultimate vacuum before introducing the argon gas is often referred to as background pressure and gives a measure of the oxygen, water vapour, and nitrogen present during the process. But this background pressure is not the only source of contamination. Possible back-streaming of oil from the diffusion pump is another source of very serious contamination. To avoid this problem, an optically dense baffle plate and a liquid nitrogen trap must be used. The latter helps to increase the speed of pumping.

Another source of contamination is the argon gas itself. It is worth noting that 99.95% pure argon gas is a severe source of contamination, because at 25 mTorr pressure it will give a 1.25×10^{-5} Torr background impurity level,

which is an order of magnitude higher than the original background pressure of the vacuum chamber.

In the presence of contaminants such as oxygen, nitrogen or hydrocarbons, the coating material in the vapour phase reacts with them in the glow discharge environment and produces oxide, nitride or carbide contaminated coatings. Depending on the amount of these contaminants, the entire coating can contain compounds, or there can be a compound gradient in the coating; either case may be undesirable, and if so then the contaminants must be minimised by a better vacuum, higher purity argon gas, and sputtering the first layer of coating from the substrate before further deposition. This can be done by adjustment of sputtering rate and evaporation rate.

The glow discharge produces ions and energetic neutrals which bombard the cathode; therefore the intensity of the discharge is important. The intensity of the glow discharge is dependent on the gas pressure, applied potential, and the nature of gas, as well as geometry of the specimen. By increasing the pressure there are more gas atoms to undergo charge and energy transfer collisions, and therefore ionization increases. The higher the applied potential, the more electrons are emitted from the cathode; this in turn increases the ionization. The geometry of the specimen and jigging greatly affect the production of low field regions in which secondary electrons are essentially trapped⁽⁶⁾, giving localised regions of high plasma density and causing local heating and back sputtering of sputtered material.

1.5.2: Ion bombardment effects prior to coating.

Ion bombardment of a surface results in a number of phenomena including:- sputtering, defect production, crystallographic disruption, surface morphology changes, gas incorporation, temperature rise, change in surface composition, and physical mixing of near-surface materials.

1.5.2.1: Sputtering.

Physical sputtering which is usually referred to as sputtering⁽⁵³⁾ is a momentum transfer process in which an incoming particle creates a collision cascade which intersects the surface with the ejection of a surface atom. The sputtering yield is defined as the number of atoms ejected per incident particle, and is a function of the relative masses of the impinging ions and surface atoms, incident particle energy, angle of incidence of impinging particle, surface morphology, and the bombardment history of the surface. High mass and high energy impinging particles will give increasing sputtering yields up to the point where most of the energy is dissipated so deeply in the surface region that the major portion of the collision cascade produced does not intersect the surface. The sputtering yield will increase with off-normal angle of incidence up to $60-70^\circ$ and then decrease as the incident ions are reflected from the surface. Typically, angular dependence can account for a factor of two variation in the sputtering yield. Fig.1.2 shows the sputtering yield of Cu, Ni and Mo as a function of the energy of bombarding ions and the angle of incidence, and Table 1.1 shows the sputtering yield of

various materials bombarded by Ar^+ (55), while Table 2 shows the sputtering yield of a Cu target bombarded by 1 KV ions of different masses (55).

Sputtering yield is also bombardment dose dependent (3), increasing with bombardment dose to some nearly equilibrium value (56). The increasing sputtering yield with dose is attributed to the introduction of defects and foreign atoms into the near-surface region which produces the local atom bonding. The variation of sputtering yield is also a function of the bombarding environment. For instance if there is a high residual gas pressure, the sputtered atoms will be backscattered to the surface.

If materials having a low sputtering yield are mobile on the target surface, then the low yield material may agglomerate into an island structure giving cone formation on the surface (57). The surface mobility may allow appreciable amounts of bulk material to be removed without removing the initial surface material. This has led to problems with composition profile measurements by sputter profiling and analysis by Auger electron spectroscopy and secondary ion mass spectrometry in some systems.

Chemical sputtering of a surface results when the energetic and activated bombarded species form a chemical bond with the surface species giving a volatile or more easily sputtered material. This effect enhances the apparent sputtering yield. It is difficult to separate the physical

Target	Bombarding energy, KV					
	0.2	0.6	1	2	5	10
Ag	1.6	3.4				8.8
Al	0.35	1.2				
Au	1.1	2.8				
Co	0.6	1.4				
	0.7	1.3				
Cu	1.1	2.3	3.2	4.3	5.5	6.6
Fe	0.5	1.3	1.4	2.0 [@]	2.5 [@]	
Ge	0.5	1.2	1.5	2.0	3.0	
Mo	0.4	0.9	1.1			2.2
Nb	0.25	0.65				
Ni	0.7	1.5	2.1			
Os	0.4	0.95				
Pd	1.0	2.4				
Pt	0.6	1.6				
Re	0.4	0.9				
Rh	0.55	1.5				
Si	0.2	0.5	0.6	0.9	1.4	
Ta	1.3	0.6				
Th	0.3	0.7				
Ti	0.2	0.6				
U	0.33	1.0				
W	0.3	0.6				
Zr	0.3	0.75				
GaSb (111)	0.4	0.9	1.2			
SiC		1.8				

@: Type 304 stainless steel.

Table 1.1: Sputtering yields of various materials
bombarded by Ar⁺ (55).

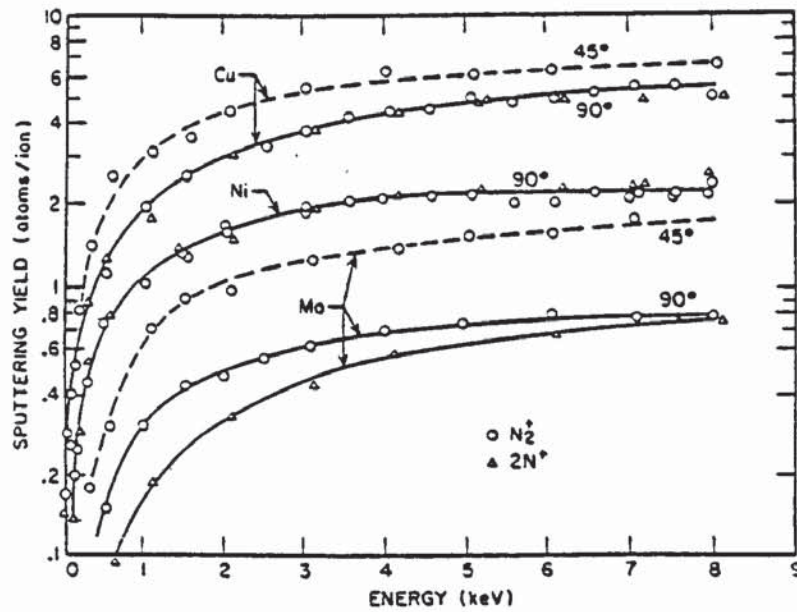


Fig.1.2: Sputtering yield of Cu, Ni, and Mo as a function of the energy of bombarding ions and the angle of incidence⁽⁵⁴⁾.

Positive ion	Approximate mass	Yield
He	4	0.08 (at 600 V)
N	14	1.5
Ne	20.2	1.8
N_2	28	2.0
Ar	39.9	3.2
Kr	83.8	3.4
Xe	131.8	3.6
Hg	200.6	1.3 (at 400 V)

Table 1.2: Sputtering yield of Cu target, bombarded by 1 KV ions of different masses⁽⁵⁵⁾.

and chemical sputtering components of the sputtering of materials by reactive gases.

Sputtering of a surface results in the removal of surface material, and hence may be called sputter-cleaning. The use of a reactive gas gives reactive-plasma-etching⁽⁵⁸⁾ or reactive-plasma-cleaning⁽⁵⁹⁾ of the surface.

1.5.2.2: Defect production.

The amount of energy transferred to the lattice atom (E_t) by the bombarding particle depends on the relative masses of the particle and is given by:

$$E_t = \frac{4M_i M_t}{(M_i + M_t)^2} \times E \quad (\text{Eq.1})$$

where E is the energy of the incident particle of mass M_i , and M_t is the mass of the target atom. If the transferred energy exceeds about 25 eV, the lattice atoms may be displaced to an interstitial site and a point defect is formed (damage threshold). If less than 25 eV, the energy will all appear as heat.

During heavy ion bombardment of metals at temperatures where both vacancies and interstitials are mobile, radiation damage is manifest in the formation of defect clusters to a depth equal to the range of the incident ions. Such clusters grow rapidly into a complex dislocation network which intersects the bombarded surface. This latter point infers that the surface receives a substantial flux of

both defects and essentially acts as an infinite sink. Furthermore, as a consequence of processes such as dislocation slip and climb the dislocation network is in continuous motion during irradiation. This behaviour is readily seen during observations of damage production in sophisticated experiments performed in combined ion accelerator-electron microscopy facilities⁽⁶⁰⁾.

Dislocations are associated with comparatively long range elastic strain fields which interact in a complex way with each other and with the free surface. The dislocation networks formed during ion bombardment will therefore be associated with excess elastic strain energy, and in a dynamic system, such as during irradiation, the network will move in such a way as to minimize the total free energy. This is manifest by the loss of dislocations to the surface due to strong image forces which are set up, and by the tendency for dislocations to align themselves in specific crystallographic directions.

During irradiation, atoms are continually removed from the surface by sputtering, so leaving surface vacancies. However, for every surface vacancy so created, at least an order of magnitude more vacancies and interstitials migrate to the surface from the bulk. Surface vacancies and interstitials are thought to be highly mobile and a substantial fraction recombine. A consequence of this is that as well as the loss of atoms by sputtering, the bombarded surface is in a highly mobile state. Under such circumstances any gradients in chemical potential will

influence the flow of matter, both towards and over the surface. For instance, a surface pit will tend to fill in so as to lower the total surface free energy.

The above discussion is clearly very generalized and the detailed behaviour of a particular metal will depend on a variety of parameters, such as: crystal structure, surface cleanliness, activation energies for defect migration, temperature, sputtering yield, etc. For instance in the case of copper at room temperature, the vacancy is just mobile. This means that recombination within the metal will significantly restrict the flux of defects to the surface. On the other hand, the dislocation density will build up to a relatively high value so causing significant elastic strain in the surface region.

Even with agglomeration of defects, there remains an extremely high residual concentration of point defects in the surface region of an ion bombarded surface. These defects have been studied by the trapping and desorption of low energy helium ions and show that the trapping sites are vacancies with varying binding energies⁽⁶¹⁾.

1.5.2.3: Crystallographic disruption.

If the defects produced by ion bombardment are sufficiently immobile, the surface crystallography will be disrupted into an amorphous structure^(62,63). Also gas incorporation will tend to disrupt the surface crystallography. These effects have been shown by investigators concerned with

Low Energy Electron Diffraction (LEED) studies of surface crystallography. These studies normally require that ion bombarded surfaces be extensively annealed in order to restore the surface crystallography⁽⁶⁴⁾.

1.5.2.4: Surface morphology changes.

Ion bombardment of a surface results in a wide variety of topographic changes⁽⁵⁷⁾ on both crystalline and amorphous surfaces giving increased surface roughness and changes in sputtering yield. Generally, there is a strong dependence of surface morphology on ion bombardment dose, particle energy, species and angle of incidence, as well as surface conditions such as crystallography and impurity concentration. This is further discussed in Chapter Four.

1.5.2.5: Gas incorporation.

During the ion bombardment of a surface, an appreciable quantity of the bombarding ions and atoms become trapped within the target. The saturation concentration of injected atoms depends on chemical and physical parameters such as solubility, mobility, trapping sites, temperature, and energy of depositing species. Generally amorphous materials trap more gas than do crystalline materials⁽⁶⁵⁾. In bias sputter deposition, done with Ar, the gas concentration may be as high as several percent and may cause blistering on subsequent annealing. Gas incorporation increases with particle energy until heating by bombardment causes the release of the entrapped gas. Inert gases have been deliberately incorporated into surfaces and films by low

energy ion bombardment for a variety of reasons including surface thermometry (Kr^{85}) (66), and diffusion studies (H,He) (67). An atom ratio of helium in a gold matrix as high as 40 atomic % has been reported even though the solubility of helium in gold is zero (67).

From the phase diagram of simple binary alloy systems, it is understood that once the solubility limit has been exceeded, precipitation occurs. In the case of inert gases which are essentially insoluble in the target, precipitation leads to isolated second phases of the injected atoms. At temperatures where thermal or irradiational enhanced diffusion occurs, such gas atoms will rapidly agglomerate. Such agglomeration forms small pockets of gas within the solid which behave very similarly to gas bubbles in a liquid, eg. they grow to a size defined by the surface energy of the solid, they can migrate through the solid by diffusion processes, they may grow by coalescence, and will burst when they intersect a free surface. Such agglomerates therefore are called gas bubbles, and their behaviour is readily studied by techniques using equipment such as a combined ion accelerator and electron microscope.

1.5.2.6: Temperature rise.

Most of the energy of bombarding particles appears as surface heating. The surface to mass ratio, thermal properties of the system, and the energy input of the system determines the resulting bulk temperature of the bombarded

material. However, the atoms in an ion bombarded surface are being displaced from their equilibrium positions with energies up to, or greater than, 25 eV (damage threshold) and the meaning of a surface temperature with such great agitation is uncertain.

1.5.2.7: Surface composition.

Without diffusion, atoms will be removed from a surface by sputtering in a stoichiometric ratio after an initial conditioning period. Because of differential sputtering yields of the components of a system, the surface composition may differ from that of the bulk⁽⁶⁸⁾. Ion bombardment itself may result in surface composition changes due to preferential 'knock-on' or recoil effects, sometimes called 'recoil implantation',⁽⁶⁹⁾.

Diffusion in the surface region can have a pronounced effect on composition. The presence of a high defect concentration and a high temperature will enhance diffusion such as is found with radiation enhanced diffusion⁽⁷⁰⁾. Since the surface acts as a sink for point defects, the defect flow will allow solute segregation with small ions segregating to the surface⁽⁷¹⁾.

1.5.2.8: Physical mixing.

Physical mixing of near-surface material results in what may be termed a 'pseudodiffusion',⁽⁷²⁾ layer where the mixing occurs without the need for solubility or diffusion.

Recoil implantation results in surface materials such as oxygen or carbon to be embedded into the surface region⁽⁶⁹⁾. If the sputtered atoms are returned to the surface by back-scattering⁽⁷³⁾, there will be an intermixing. If the sputtered atoms are ionized and accelerated back to the surface⁽⁶⁾, they will become embedded into surface region.

1.5.3: Ion-bombardment effects during the coating.

After sputter cleaning, the coating material can be evaporated onto the substrate. To form a coating it is necessary to have higher rate of coating than the rate of sputtering removal.

Because the ion bombardment of specimen continues during the coating stage, it is necessary to discuss the effect of ion bombardment during the coating, the interface formation and film growth.

Ion bombardment of a surface, while adding coating atoms, results in: physical mixing, enhanced diffusion, modified nucleation modes, preferential removal of loosely bonded atoms, and improved surface coverage.

1.5.3.1: Physical mixing.

Mixing of the near surface region by non-diffusion type mechanisms will occur due to implantation of high energy particles⁽⁷⁴⁾, backscattering of sputtered atoms⁽⁷³⁾, and recoil implantation of surface atoms⁽⁷⁵⁾. The high energy particles may arise from a variety of sources. The coating

atoms may be ionized and accelerated while traversing the plasma in the glow discharge⁽⁷⁶⁾, or may be ionized in an ion source, then extracted and accelerated through a vacuum (ion-beam plating). High energy particles may also be formed by being sputtered from the surface, ionized in the plasma, and then accelerated back to the surface. The net effect of this intermixing will be to form the aforementioned 'Pseudodiffusion' type interface.

1.5.3.2: Enhanced diffusion.

The high defect concentration and temperature of the near-surface region will enhance the diffusion rates⁽⁷⁷⁾.

Diffusion into the bulk, or surface segregation may be enhanced by solute segregation effects where small ions will tend to segregate to the surface which acts as a sink for point defects⁽⁷¹⁾.

1.5.3.3: Nucleation modes.

The behaviour of an atom condensing on the substrate is determined by its interaction with the surface. If there is no strong bonding between the condensing atom and the surface, the atom will diffuse over the surface until it nucleates at a high energy site or by collision with other diffusing atoms. This may be termed as a non-reaction nucleation mode, and will lead to widely spaced nuclei.

The growth of the nuclei will possibly lead to a 'dewetting' type growth⁽⁷⁸⁾ with interfacial porosity⁽⁷⁹⁾ as the nuclei grow together. The nuclei will not grow together until they have reached an appreciable thickness.

This type of nucleation and growth leads to the island-channel-continuous growth pattern often studied with electron microscopy⁽⁸⁰⁾.

If the condensing atom acts strongly with the surface, the surface mobility will be limited and the nucleation density will increase and in the limit, the depositing atoms will form a continuous monolayer on the substrate surface⁽⁸¹⁾. If there is chemical reaction or diffusion, the condensing atoms will react with the surface to form compound or alloy layers which extend both normally and laterally to the surface. This mode of growth will tend to decrease interfacial porosity and 'grade' the properties of the interfacial region⁽⁷²⁾. Extensive interfacial reaction may degrade the interface by the formation of porosity due to differential diffusion rates or by high intrinsic stresses generated by thick interfacial compound layers⁽⁸²⁾. Very thin contamination layers on the surface can convert the diffusion/reaction nucleation mode to the nonreaction mode with an attendant undesirable interfacial region⁽⁷⁸⁾.

An ion bombarded surface, with its surface morphology and disruption probably provides more nucleation sites than an undisrupted surface giving a higher nucleation density even for nonreactive systems. Ion bombardment of the surface will tend to remove and disrupt contamination and barrier layers which prevent the diffusion/reaction mode⁽⁸³⁾.

Implanted atoms may also act as nucleation sites.

1.5.3.4: Preferential removal.

Since sputtering of surface atoms is dependent on the local bonding, it is not unexpected that ion bombardment of a surface will tend to sputter the more loosely bonded atoms. This is particularly evident when the reaction/diffusion type of interface is being formed and has been used to deposit Pt-Si layers by sputter depositing Pt on Si and back-sputtering the excess platinum⁽⁸⁴⁾. It has also been noted the 'high quality' SiO₂ films can be formed by bias sputtering and this is attributed to backspattering of loosely bonded atoms⁽⁸⁵⁾, though other effects may be important.

1.5.3.5: Surface coverage.

The increased 'throwing power' of the ion plating process over large areas and out of line-of-sight of the vapour source, when used in a gas discharge, is most probably due to gas scattering. The effect has been seen at high gas pressures without the discharge present⁽⁸⁶⁾, but ion bombardment is probably important in obtaining an adherent coating since evaporation into a high gas pressure will lead to vapour phase nucleation and the deposition of a fine powder as is done in 'gas' evaporation⁽⁸⁷⁾. Vapour phase nucleated particles in a gas discharge will assume a negative potential and be repulsed by the cathodically charged ion plating substrate⁽⁶⁾ or may be used for 'Ionized Cluster Beam' deposition⁽⁸⁸⁾.

On a microscopic scale, the enhanced surface coverage is probably due to sputtering of the deposited atoms into regions out of line-of-sight of the surface⁽⁸⁹⁾. Back-sputtering has been used to preferentially deposit materials on vertical side walls even to the extent that all deposited material on the surfaces normal to the impinging ion beam is completely removed⁽⁹⁰⁾.

Deposited materials often have properties which are appreciably different from that found in bulk material. These include small grain size, high defect content, low recrystallization temperatures (metals), low strain point (glasses), high intrinsic stresses, metastable crystallography and phase composition, among others.

Ion bombardment of a film during deposition may affect film morphology, crystallographic composition, physical properties, and other properties.

1.5.3.6: Morphology.

The morphology of a depositing film depends on how the depositing atoms are incorporated into the existing structure. On a smooth surface, preferential growth of one area over another may result from varying surface mobilities of the depositing atoms, usually as a result of grain orientation. Preferential growth leads to a dominant grain orientation and a surface roughening with thickness. As the surface gets rough, the geometrical shadowing will lead to preferential growth of the elevated regions giving a

columnar morphology to the deposit⁽⁸⁹⁾. A pre-existing surface roughness or preferential nucleation will also lead to shadowing and columnar morphology. An elevated substrate temperature will affect the morphology by increasing surface mobility, enhancing bulk diffusion, and allowing recrystallization to occur. These effects have led to the structure zone model of deposited materials of Movchan and Demchiskan⁽⁹¹⁾. The model consists of the formation of three zones which depend on the ratio of the surface temperature (T) to the melting point of the deposited material (T_m).

Zone one results when adatom diffusion is insufficient to overcome the effects of shadowing, giving a columnar structure with low density boundaries between the columns⁽⁹²⁾. The individual columns are polycrystalline, are usually highly defective and of small grain size. The surface morphology is generally rounded. This zone is defined by $T/T_m < 0.3$.

Zone two is defined as the range of $0.3 < T/T_m < 0.5$, where adatom diffusion dominates and the columnar structure consists of less defected and larger grains with higher density boundaries between columns. The surface morphology of the zone two material is generally more angular than that of the zone one material.

Zone three is the $0.5 < T/T_m < 1$ region where bulk diffusion and crystallization dominates⁽⁹²⁾. The material is more

equiaxed with high density grain boundaries and large grains.

Rough surfaces⁽⁸⁹⁾, high gas pressure⁽⁹²⁾, oblique adatom flux⁽⁹³⁾, and reactive contaminant gases will tend to lower T/T_m values for the zone boundaries. Ion bombardment, during deposition, may tend to raise the T/T_m values for the zone boundaries⁽⁹⁴⁾ though this effect may be offset by gas incorporation and smaller initial grain size.

1.5.3.7: Crystallography.

Structural order is generally controlled by the surface mobility of the adatom. Low mobility will lead to amorphous or small grained material. High mobility will lead to large grained material and more structural perfection. Bulk diffusion will determine the crystallography of materials deposited at elevated temperatures (zone three). Preferential crystallographic orientations will result from the differential surface mobilities at low temperatures or the recrystallization kinetics at high temperatures.

Ion bombardment of the depositing material may influence crystallography by enhancing diffusion and recrystallization, or by altering the nucleation stage of the film growth.

1.5.3.8: Composition.

As previously discussed, ion bombardment can alter the composition of the depositing material by preferentially

sputtering loosely bound atoms or implanting atoms into the growing surface region to form metastable phases. In the extreme case, as much as 40 atomic percent of insoluble gases can be incorporated into a depositing film by ion bombardment⁽⁶⁷⁾.

1.5.3.9: Physical properties.

Intrinsic stress is probably one of the most obvious properties which is affected by ion bombardment. Intrinsic stress is generated by atoms which are not in their lowest energy configuration. Generally, evaporative-deposited films have a tensile stress while sputter-deposited films have a compressive stress. The magnitude of the stresses often approaches the yield point of the bulk materials, and, in some cases, may exceed the yield point of pure bulk materials because of incorporated impurity atoms. Compressive stresses develop when the atoms are in closer proximity to one another than they would be under more equilibrium circumstances. Tensile stresses develop when atoms are further apart than they would be under equilibrium circumstances, possibly due to large numbers of interstitial atoms. Some care must be taken within these interpretations since stress is often measured by X-ray analysis of lattice parameters which tell nothing about intergranular forces. Beam deformation measurements give an integrated stress value which may be more meaningful⁽⁹⁵⁾.

For sputter-deposited films, an elevated gas pressure, an oblique adatom flux, or an elevated temperature will reduce

the compressive film stress⁽⁹⁶⁾. In some cases, stress may be reduced by a relief mechanism such as diffusion or recrystallization. Recrystallization temperature and rate are dependent on the intrinsic strain energy and defect concentration. In other cases, the structure may be unable to support the stress such as the low density structure of zone one material where the weak columnar boundaries will not be able to transmit a stress. In such a case the X-ray analysis may show high stress but a bending beam test will show little integrated stress.

Ion bombardment during deposition may increase the stress by forcing atoms into non-equilibrium positions and suppressing zone one formation, or may decrease stress by enhancing stress relief mechanisms such as diffusion and recrystallization. Generally the more refractory the material, the more likely ion bombardment is to increase stress. A low intrinsic stress is usually desirable for good adhesion⁽⁷²⁾ though, in some cases, a compressive stress may be beneficial since materials under compression are generally stronger than unstressed materials, because fractures will tend not to propagate.

Studies on deposition from cylindrical-postmagnetron (CPM) sputtering⁽⁹⁶⁻¹⁰⁰⁾, using argon gas have revealed that for each different material there is a transition working pressure, below which the sputtered coatings are in compression and above which they are unstressed or in tension. The phenomenon has been found in such a wide



variety of pure metals and alloys that it seems to be a characteristic of the process itself rather than a particular material being sputtered. The transition working pressure is markedly dependent on the atomic mass of the coating material, increasing from 2.25 mTorr for Cr to about 15 mTorr for Ta^(98,99).

In the experiments done by J.A.Thornton et al⁽¹⁰⁰⁾, large compressive stresses are found only where geometric factors indicated enhanced bombardment by argon reflected at the cathode. Therefore it is surmised that it is not the presence of the entrapped argon, but the atomic peening action of the reflected argon on the growing coating which causes the stress.

C.P.M. sputtering of Mo in a variety of gases (Ne, Ar, Kr, Xe)⁽¹⁰¹⁾ has shown that the transition pressure varies inversely with the mass of the sputtering gas from less than 2.25 mTorr for Xe to over 6.75 mTorr for Ne.

The concentration of the inert gas in the films also varies inversely with the mass of the gas.

1.6: Ion plated films.

1.6.1: Properties and applications.

The most important property of ion plated films is good adhesion to the substrate. Adhesion between film and substrate depends on interface formation and its depth which

are affected by the sputter cleaning prior to coating and the degree of solid solubility which the film/substrate combination possesses. A number of various film/substrate combinations are reported where the depth of the interfacial region is estimated. In all the following combinations, Au/Al⁽¹⁰²⁾, Al/Ti⁽¹⁰³⁾, In/Cu⁽¹⁰⁴⁾, Au/Cr⁽¹⁰⁵⁾, Cr/Ni⁽¹⁰⁶⁾, Cu/steel⁽¹⁰⁷⁾, the depth of the graded interface ranged from a few micrometers to about 15 μm . In the case of Cu/Ni which has complete solid solubility, the interface depth is in the range of a micrometer while insoluble film/substrate combinations such as Ag/Ni⁽¹⁰⁸⁾ have a narrow interfacial region in the order of 0.05 μm .

The coating defect growth is mainly dependent on the substrate finish and topography⁽¹⁰⁹⁾, whereas the coating-matrix morphology is controlled by the process parameters, mainly the substrate temperature. To improve the homogeneous growth morphology by reducing the film defect concentration, a highly polished and smooth surface is needed⁽¹¹⁰⁾.

When 200 nm thick gold films were ion plated on tool steel and on Ni-Cr alloy surfaces and tested under vacuum, the following improvements were observed compared with vapour deposited films⁽¹¹¹⁾: increase in endurance life, lower coefficient of friction, and avoidance of catastrophic failure.

The friction and wear characteristics of ion plated and

electro-plated films were compared in liquid hydrogen by Wisander⁽¹¹²⁾, and it was shown that ion-plated films were superior.

Co and Pb ion-plated films on steel⁽¹¹³⁾ had low coefficients of friction and exceptionally low wear rates.

The diffusion zone of Al ion-plated Ti⁽¹¹⁴⁾ has a hardness greater than 1000 VHN and shows low friction and good wear resistance. A tenfold increase in the operating life of rotary engine parts due to use of ion plating is reported by White⁽¹¹⁵⁾.

Ion-plating of Ni and Inconel tensile specimens with 150 nm thick Cu has increased the tensile and yield strength of the specimens by 5-8%⁽¹¹⁶⁾. Similar results are reported⁽¹¹⁷⁾ on ion-plating of 316 stainless steel and W wires with Cu and Ti. 150 nm thick gold and Cu ion-plated films have increased the fatigue life of Ni and Inconel fatigue specimens⁽¹¹⁷⁾. The creep resistance has been also improved when a Ti-6242 alloy was ion-plated with Pt and tested at room and elevated temperatures up to 455°C⁽¹¹⁸⁾.

Ion plated films of Fe-Ni-Cr and Fe-Cr alloys have been shown to have very high pitting potentials⁽¹¹⁹⁻¹²¹⁾, especially those containing more than 8% Cr. Ion plated films of iron-based chromium alloys onto stainless steel substrates have shown higher resistance to pitting corrosion in 1 M NaCl aqueous solutions than the substrate⁽¹²²⁾

Al ion plated coatings are used on uranium fuel elements for corrosion protection⁽¹²³⁾ which provides much better protection than the electroplated Ni films which tend to spall under thermal cycling.

Cd ion plated coatings are used on steel fasteners for corrosion protection^(124,125). Ti alloy fasteners used in aircraft can be Al ion plated for corrosion protection⁽¹²⁶⁾. Also ion plating is used to improve coating on blades used in hot section of gas turbines^(127,128).

Ion plated gold films are used to coat reed blade contacts⁽¹²⁹⁾

A further important and promising application of ion plating is in joining incompatible metals and metals to alloys⁽¹³⁰⁾.

Zinc sulphide is ion plated⁽¹³¹⁾ on germanium as an antireflection coating for infrared components.

1.6.2: Effect of operational parameters on properties.

The influence of residual gases on the properties of Al-1.5% Si ion plated films were investigated by Nowicki⁽¹³²⁾. He has shown that a 1% concentration of oxygen and nitrogen in an argon sputtering atmosphere has a great effect on the structure of the coating, while the same amount of hydrogen has a negligible effect on the reflectivity, grain size, and resistivity.

Magnetron sputter deposition of Al-Si alloys has been studied by Hartsough and Denison⁽¹³³⁾ with regard to deposition parameters.

McLeod and Hartsough⁽¹³⁴⁾ have studied planar magnetron-sputtered Al coatings. It was found that the substrate temperature is the limiting factor in obtaining highly reflective Al and Al-Si films. However, reducing the residual gas content had further enhanced the reflectance.

CHAPTER TWO:

GLOW DISCHARGE.

When a large cylindrical glass tube with two plane electrodes at its ends is filled with a gas at a pressure of the order of 1mm Hg and the potential difference V between the electrodes is slowly raised, then a small current of order of 10^{-12} A or so can be observed to flow through the gas⁽¹³⁵⁾. This is due to ionization in the gas and at the electrodes or walls by cosmic particles. As V is increased the ionization by collision in the gas begins and thus the current will rise. At the same time, some of the electrons will become attached to the inner glass walls, while an equal amount of positive charge will stay in the gas. In the neighbourhood of the anode the conditions are reversed, but not symmetrically. The majority of positive and negative charges, however, will flow to their respective electrodes. As a result of these wall charges, a radial electric field develops which restricts the flow of electrons to the walls. By increasing V still more, space charges appear which will distort the axial component of the field. At still higher V , space charges collect in front of the electrodes, and finally the current becomes large enough to bring about a transition from the dark discharge into the more complex form known as a glow discharge.

Fig.2.1 shows the lowest maintenance potentials of self sustained discharges. The fall in V suggests that processes

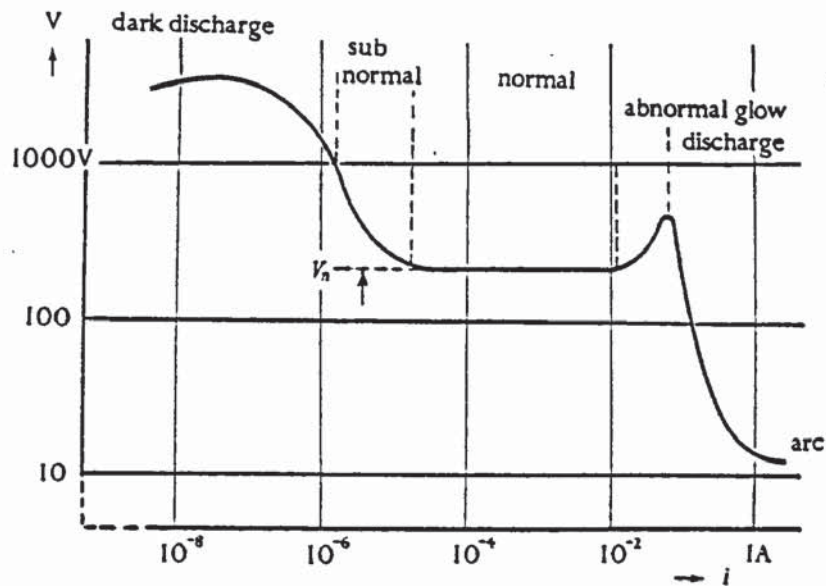


Fig.2.1: Voltage/current behaviour of an electric-discharge⁽¹³⁵⁾. V_n is the normal cathode fall in potential.

have become operative which either facilitate ionization, reduce the losses, or both. The current 'i' is determined by the property of the discharge as well as by the applied voltage and circuit constants.

When the glow discharge is established, the visible light emitted from the discharge is distributed over the length of the tube as shown in Fig.2.2.

Starting at the cathode, there exists sometimes a very narrow dark space (Aston's) close to it followed by a

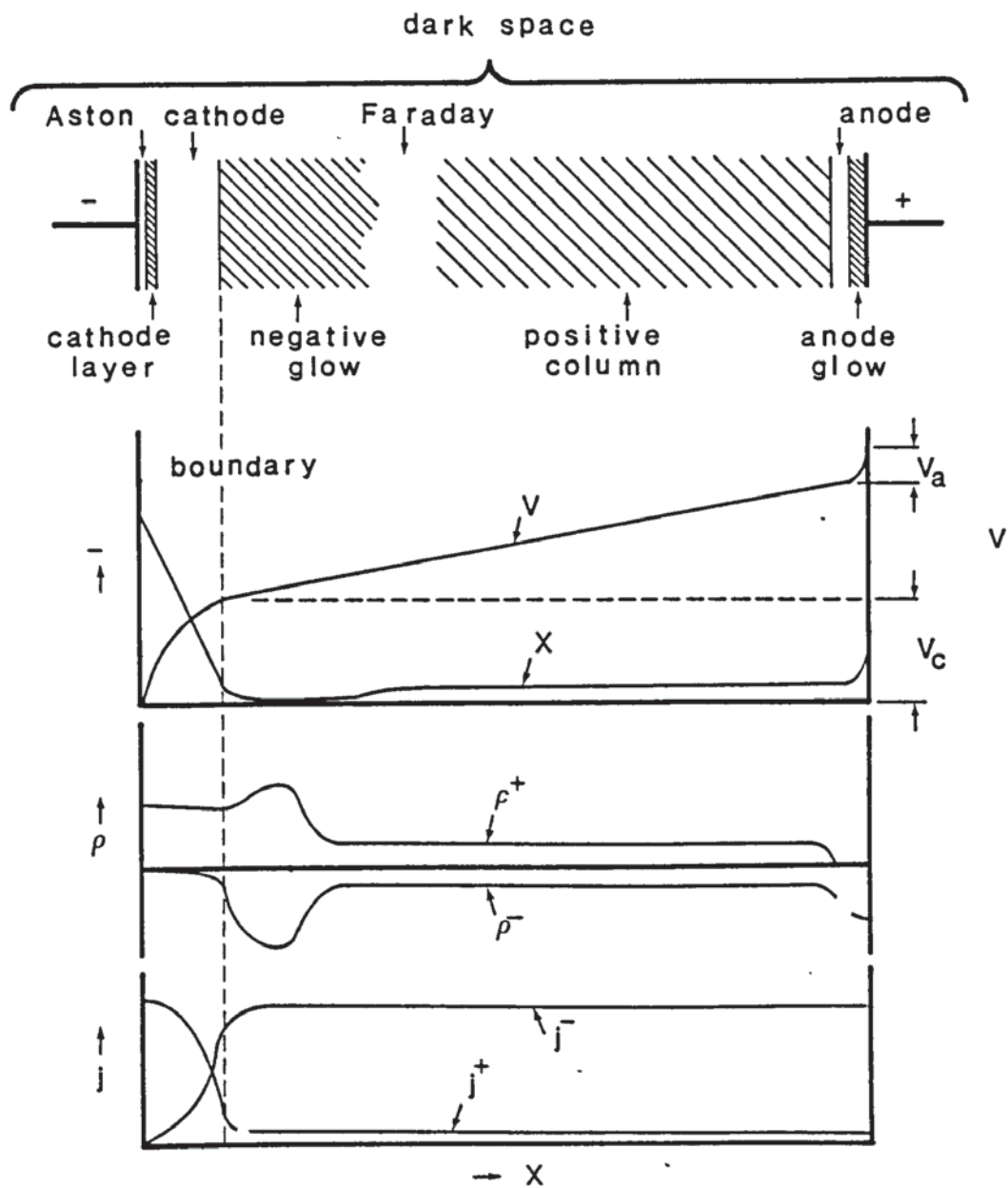


Fig.2.2: Spatial distribution of dark space and luminous zones, electric field X , space charge-densities ρ^+ and ρ^- , and current densities j^+ and j^- in a glow discharge⁽¹³⁵⁾.

thin relatively feeble sheath luminous layer, the cathode glow, which in turn is followed by the cathode dark space. Thereafter is a negative glow which is separated from the dark space by a sharp boundary. The negative glow becomes progressively dimmer towards the Faraday dark space. At the positive end of this is the positive column. It is either a region of uniform luminosity or regularly striated. At the positive end of the positive column there is sometimes visible an anode dark space followed by the anode glow close to the anode itself.

The transport of current through a glow discharge occurs by the axial motion of electrons and positive ions. The flow of current through the cathode zones can be understood by referring to the distribution of an electric field and its axial component as shown in Fig.2.2. The field has been found to be large at the cathode, decreasing in intensity towards the negative glow, and after passing a minimum in the Faraday dark space, it stays constant throughout the positive column and only rises again at the anode.

Consider an electron emitted from the cathode, for example by a positive ion which impinges on it. This electron is first accelerated in a strong field, but initially it executes few ionizing collisions because its energy is not sufficiently far above ionization potential. However, further from the cathode, though the field has become weaker, the electron ionizes more efficiently and strong electron

multiplication will take place. Near the boundary between the cathode dark space and the negative glow the field has become very weak, and thus only the fast electrons which have not lost energy by inelastic collision will be able to ionize in that region. However, a large number of electrons will cross the boundary and enter the negative glow.

Due to multiplication the number of electrons able to ionize has increased between the cathode and the glow boundary, and a large number of positive ions has been formed representing a strong positive space charge. These positive ions will move through the cathode dark space and impinge on the cathode. Also metastable atoms, fast unexcited atoms, and radiation will fall on the cathode with the result that secondary electrons are emitted from it. In order to have a steady state, each electron which is emitted by the cathode must produce sufficient ionization and excitation to effect the release of one further electron from the cathode.

This picture also explains the distribution of the emitted light⁽¹³⁶⁾. An electron usually starts at the cathode with a very small initial speed of the order of 1eV. It is not able to excite gas molecules unless its energy has reached at least excitation potential, which will not occur within the first few V (5-10 eV) from the cathode, corresponding to Aston's dark space. The cathode layer is the region within which the electron acquires an energy corresponding

to the maxima of the excitation functions.

At a higher cathode potential fall Aston's dark space and cathode layer are replaced by the cathode glow. At larger distances from the cathode most (but not all) electrons have speeds which lie far beyond the maximum of the excitation functions and thus little visible light is emitted from the cathode dark space. At the negative glow boundary the number of slow electrons has become very large and their speed decreases with increasing distance from the cathode.

The electrons entering the glow consist of at least two groups: firstly those which have been produced at or near the cathode, are fast and have not suffered losses by collisions in the dark space, and secondly a larger group of electrons which have made many inelastic collisions, have been created in the dark space and are therefore slow. Since the slow electrons have energies below the ionization maximum but above or at excitation maximum, they experience many exciting collisions and produce the negative glow. Afterwards their energy becomes so small that recombination with positive ions can take place. This process is likely to occur in and beyond the negative glow since the concentration of ions and electrons in that region is large and the field low. The emission of light due to recombination is in general small. With increasing distance from the boundary fewer fast electrons are found and less visible light is emitted. The field rises slowly, the

probability of recombination decreases, and the Faraday dark space ensues. This is the anteroom to the positive column, and its properties are probably intermediate between those of the positive column and those of the negative zones.

In the uniform positive column the axial component of the electric field is found to be constant at any point. It follows that the net space charge is zero or that the concentration of electrons at any point is equal to that of the positive ions. Because of the small mobility of positive ions the electrons carry practically the whole discharge current while the positive ions compensate the electron space charge. The field in the positive column is several orders of magnitude smaller than that found in the dark space. This fact as well as the uniform appearance of the positive column indicates that ionization is not obtained from the drift velocity of electrons in the field direction but rather from their large random velocity acquired by numerous elastic collisions in the elastic field.

At the anode side of the positive column, the electrons are attracted by the anode and the positive ions repelled. Consequently a negative space charge is set up in front of the anode. As shown in Fig.2.2, this gives rise to an increase of the electric field as well as a rise in potential⁽¹³⁷⁾. An electron emerging from the positive column enters the anode fall region with a small initial

energy. It is now accelerated towards the anode and after having crossed the anode dark space it has acquired a speed which is sufficient to excite and ionize the gas in front of the anode, and cause the anode glow.

When a glow discharge is maintained between two plane electrodes at a pressure of 1 mm Hg, the potential drop across the discharge (without a positive column) as a function of current is as shown in Fig.2.2. There is a constant voltage drop over a current range of 2-3 orders of magnitude (approximately 10^{-5} - 10^{-2} A). It is found that the current density at the cathode remains hereby sensibly constant, that is, the 'covered area' expands proportionally with the current. This is the region of 'normal' cathode fall in potential. At the larger currents, when the whole cathode surface appears to be covered by the glow, an increase in current can only be obtained by an increase in current density. A larger cathode emission is necessary, and this again increases the cathode fall and at the same time the dark space shrinks. This region is called 'abnormal glow discharge'.

If the anode moves towards the cathode, the positive regions narrow down and then disappear in turn. In the same way the Faraday dark space narrows as the anode is moved still further. The anode can be moved right up to the edge of the cathode dark space before the glow is extinguished.

Ion plating is carried out in the abnormal region and

therefore the characteristics of the abnormal region are important.

When the negative glow covers the cathode, an increase in current produces an increase in cathode fall and in current density and a decrease in the thickness of the dark space. This is the region of the abnormal cathode fall.

Fig.2.3 shows the product of thickness of dark space and pressure (d.p) as a function of the cathode fall (V_c) on an iron cathode in various gases⁽¹³⁸⁾. The differences come from the differences in ionization coefficients of the different gases.

Attention must be drawn to the fact that the observed values of d.p at large V_c are not very reliable because the heat produced in the gas reduces its density; thus the pressure reading gives values that are too high. A more accurate method would consist in measuring the gas-density distribution in the dark space and to derive from it the average density.

The dependence of the cathode fall on the current density for an iron cathode in various gases is shown graphically on Fig.2.4 where the relation between current density (j), cathode fall (V_c) and the reduced dark space (d.p) is given by⁽¹³⁵⁾:

$$j/p^2 = \left(\frac{e}{M} p \lambda_{+0} \right)^{1/2} \frac{1}{\pi} \frac{V_c^{3/2}}{(d.p)^{5/2}} \frac{(1 + \gamma_i)}{(1 - G)}$$

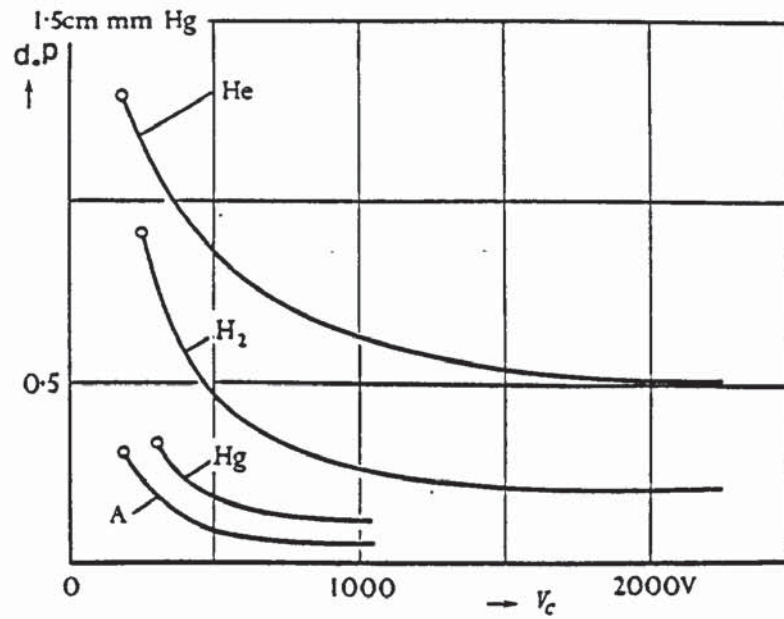


Fig.2.3: Product of dark space thickness and pressure ($d.p$) as a function of the cathode fall (V_c) for an Fe cathode in various gases⁽¹³⁸⁾.

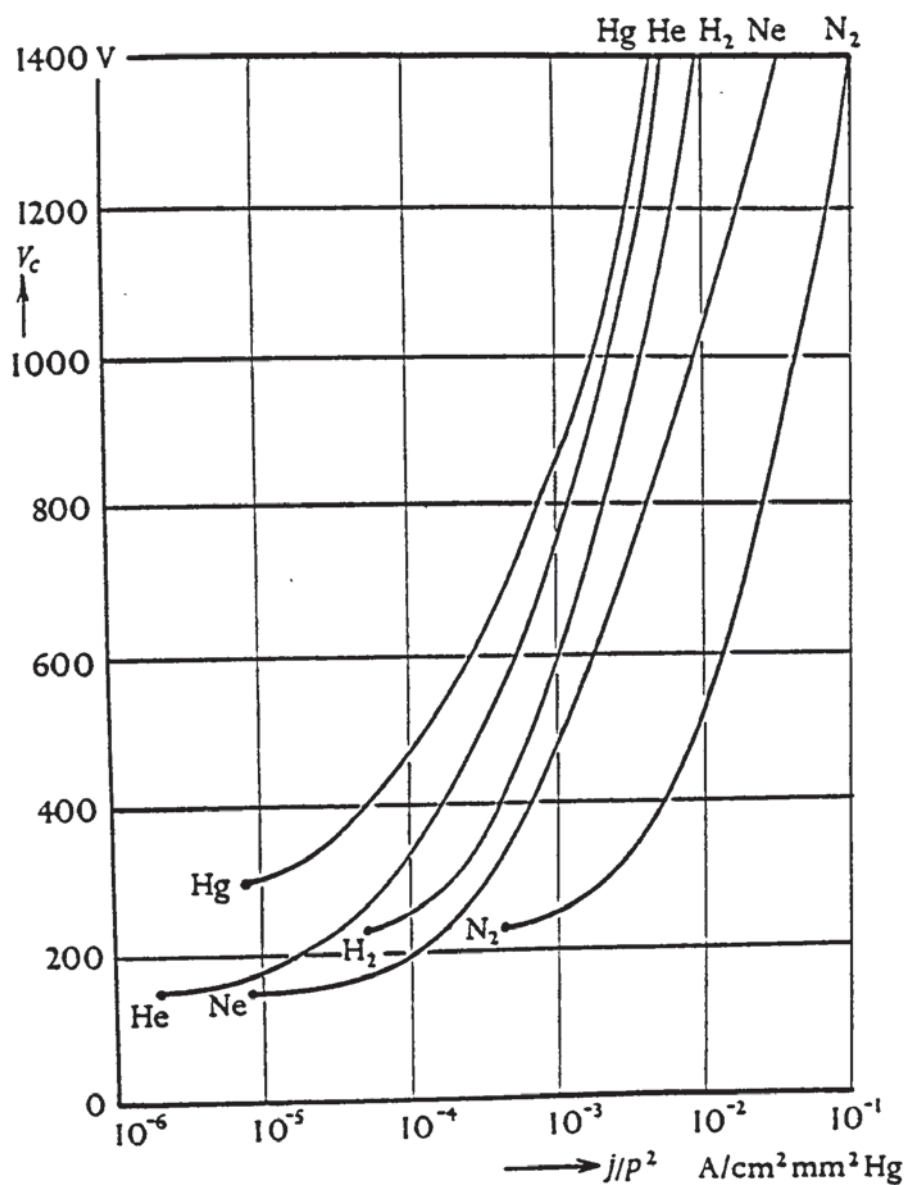


Fig.2.4: Abnormal cathode fall V_c dependent on the reduced current density j/p^2 for an Fe cathode in various gases⁽¹³⁸⁾.

where λ_{+0} is the mean free path for charge transfer,
M is the mass of the ions,
G is the secondary emission coefficient due
to radiation from the glow,
 γ_i is the ion production yield in the dark space.

So far the cathode has been assumed to be a simple conducting surface. If the cathode consists of a thin insulating or semi-conducting substrate like C or Al with a layer of Al_2O_3 or glass powder, a discharge develops without a dark space; only the negative glow, the Faraday dark space, and the positive column exists. The potential of this 'spray discharge', which is shown to occur in rare and molecular gases, is about ten times smaller than that of a conventional glow discharge, namely of the order 40 V, and the current densities j/p^2 about 10^3 times larger than j_n/p^2 at gas pressures of 10^{-2} to 10^{-1} Torr. Ageing of the cathode is very pronounced and this prevents any application of this phenomenon. The absence of the cathode fall has been explained by field emission: Positive ions are adsorbed at the surface of the insulating particles and the ensuing field in the crystallites is sufficiently high to extract electrons. At the cathode side of the particles a similar process or a transfer of ions occurs. The light emitted originates mainly in the gas⁽¹³⁹⁾.

CHAPTER THREE:

SPUTTERING.

The basic issue in sputtering theory is the physics of the individual sputtering event. That event may be caused by the elastic interaction of the ion with individual target atoms (collision cascade, or knock-on sputtering) or by ionization action of the bombarding ions (electronic sputtering). When present at all, the latter process may actually dominate. There is general consensus that knock-on sputtering dominates for metallic elements and compounds, and there is little doubt that knock-on collisions are the major effect in the sputtering of semiconducting targets under such bombardment conditions that prevail in sputter profiling and deposition.

Theoretical efforts have been increasingly successful in understanding the main features of sputtering in terms of a series of quasielastic collision processes induced by the bombarding ions. Usually the first collision does not lead to backward sputtering directly; at least for perpendicular incidence a hit target atom always has a velocity component in the direction away from the target surface (Fig.3.1). Thus sputtering is a typical multiple collision process involving a cascade of moving target atoms. This cascade may extend over a considerable region inside the target, but for sputtering only the intersection with one or more of the target surfaces is of interest.

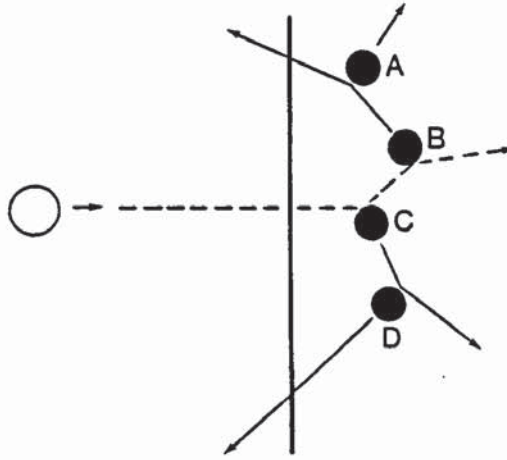


Fig.3.1: Series of collision processes
leading to sputtering of atoms
B and D.

3.1 : Sputtering from linear collision cascades.

According to Sigmund's theory⁽¹⁴⁰⁾, the following expression can be derived for the sputtering yield Y :

$$Y(E, \theta) = \Lambda F_D(E, \theta, 0) \quad \text{Eq. 2.}$$

where E and θ are the energy and angle of incidence of the ion, Λ a material constant characterizing the target, and $F_D(E, \theta, 0)$ the density of energy deposited⁽¹⁴¹⁾ per bombarding ion, as a function of penetration depth x .

The latter can be written in the form:

$$F_D(E, \theta, 0) = \alpha(\epsilon, \theta, M_2/M_1) (dE/dx)_n \quad \text{Eq. 3.}$$

where M_1 and M_2 are the atomic masses of ion and target, ϵ a scaled energy parameter⁽¹⁴¹⁾, $(dE/dx)_n$ the nuclear

stopping power of the ion^(41,142), and α is a function that has first been evaluated in Ref.143, where the dependence on ϵ was ignored.

The material constant Λ can be written in the general form as:

$$\Lambda = \frac{\Gamma_m}{4} \int \frac{dE_o}{E_o \frac{dE_o}{dx}} \int d \cos^2 \theta_o P(E_o, \theta) \quad \text{Eq. 4.}$$

where dE_o/dx is the stopping power of target atom at energy E_o , Γ_m a constant $\approx 6/\pi^2$, and $P(E_o, \theta_o)$ the ejection probability for an atom at the surface as a function of the angle θ against the surface normal.

With specific assumptions concerning dE_o/dx (Born-Mayer scattering) and $P(E_o, \theta_o)$ (planar surface potential U_o which is usually set to the sublimation energy of the target material), the following expression is found⁽¹⁴³⁾ for Λ :

$$\Lambda = (3/4 \pi^2) (1/N C_o U_o) \quad \text{Eq. 5.}$$

with

$$C_o \approx (\pi/2) \lambda_o a^2 \quad \text{Eq. 6.}$$

and $\lambda_o \approx 24$, $a \approx 0.219 \text{ \AA}$, and N the atomic density of the target material.

Originally, Eq.3 has been evaluated on the basis of the stopping power for Thomas-Fermi interaction⁽¹⁴⁴⁾. Actual stopping power lies closer to Lenz-Jensen interaction^(144,145).

The function α given in Ref.140 as well as later versions containing an energy dependence⁽¹⁴⁶⁾ was evaluated for slowing down in an infinite medium. Therefore it gives rise to too high values of F_D for light⁽¹⁴⁷⁾ and/or obliquely incident ions.

The proportionality of sputtering yield on stopping power is argued by H.H.Andersen and H.L.Bay⁽¹⁴⁷⁾; and based on measurements with 15 different ions on Si, 21 on Cu, and 15 on Ag, they have calculated that the discrepancy at high M_2/M_1 is possibly caused by a lack of surface correction in the theory.

The proportionality is found experimentally⁽¹⁴⁷⁾ for relatively light ions (mainly Ne and Ar) on all targets and also for intermediate ions(eg. Kr) on light targets.

Fig.3.2 shows the Sigmund's theoretical curve and results obtained by Andersen and Bay. Deviation from theory is seen to occur for very heavy ions (\geq krypton).

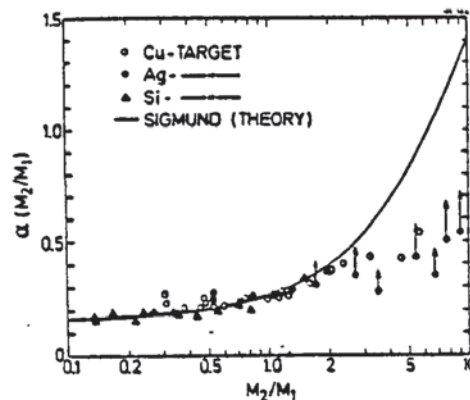


Fig.3.2 : $\alpha(M_2/M_1)$ extracted from measurements with 15 different ions on Si, 21 on Cu, and 15 on Ag⁽¹⁴⁷⁾.

3.2 : Nonlinear effects.

The sputtering theory underlying the above mentioned equations is linear in the sense that the stopping powers entering into Equations 2 & 4 depend on the composition of the target but not on its state of motion⁽¹⁴⁰⁾, ie. that target atoms and ions move independently. For a high density of deposited energy, the density of moving particles in a cascade becomes substantial; this results primarily in a decrease of the stopping power (dE_o/dx) in Equation 4 and therefore in an increased sputtering yield. Drastically increased sputtering yields (well above a factor of 2) can be observed, and the energy dependence of the yield is modified in comparison with the prediction of Equation 3. A qualitative picture of an elastic-collision spike explains the observed phenomena⁽¹⁴⁸⁾, but considerable uncertainty remains with regard to the origin of the increased sputtering effect. It is not known whether it is an increased ejection probability (smaller surface potential), an increased mobility of target atoms or, as implied so far⁽¹⁴⁸⁾, a transport of excess energy from the centre of the spike to the surface which causes enhanced sputtering yields under spike conditions.

Under spike conditions, the U_o^{-1} dependence of the sputtering yield (eq.8) on the surface potential goes over into an exponential one⁽¹⁴⁸⁾. Therefore, the variation of the sputtering yield with ion type, energy, and angle of incidence depends on the magnitude of the surface potential and not only on the mass of the target, unlike linear

cascades, Equation 2.

3.3 : Multiple component target.

An understanding of the sputtering behaviour of multiple component targets is of primary importance for several reasons⁽¹⁴⁹⁾;

I) prolonged bombardment of an elemental target normally leads to an alloy incorporating the bombarding species.

II) applications of sputtering in the production and analysis of thin films almost invariably deal with multiple component targets.

III) varying composition of the target provides an extra dimension to fundamental sputtering studies that may yield a clue to the understanding of the material dependence of the sputtering yield, Equation 4.

3.3.1: Primary sputtering effects.

Primary effects comprise the physics of an individual sputtering event on a target with a given composition. Experimental studies of primary sputtering effects on multiple component targets require low-fluence bombardment ($\ll 10^{15}$ ions/cm²).

With regard to primary processes, the two components of a binary target do not in general sputter stoichiometrically. For roughly equal masses of the constituent atoms, Equation 2 modifies into:

$$Y = C_1 Y_1 + C_2 Y_2 \quad \text{Eq. 7.}$$

with

$$Y_i = \Lambda_i F_D (E, \theta, 0), \quad i = 1, 2 \quad \text{Eq. 8.}$$

where C_1 and C_2 are the respective atomic fractions ($C_1 + C_2 = 1$)

and Λ_1 and Λ_2 are given by Eq.5 with $U_0 = U_1$ & U_2 respectively.

If the two surface potentials differ from one another, the more loosely bound species sputter preferentially, and the target is enriched in the more tightly bound species (150).

When the two constituents have very different atomic masses, the collision dynamics also influence the partial sputtering yields.

Within the same approximation that leads to Eq.2, one finds (151),

$$\Lambda_1 = \Gamma_{m_1} \int \frac{dE_0}{E_0 N S_{12}(E_0)} h\left(\frac{C_1}{C_2}, \frac{M_1}{M_2}\right) \int d(\cos^2 \theta_0) P_1(E_0, \theta_0) \quad \text{Eq. 9.}$$

and

$$\Lambda_2 = \Gamma_{m_2} \int \frac{dE_0}{E_0 N S_{21}(E_0)} h\left(\frac{C_1}{C_2}, \frac{M_1}{M_2}\right) \int d(\cos^2 \theta_0) P_2(E_0, \theta_0) \quad \text{Eq. 10.}$$

where S_{ij} is the mutual stopping cross section for an i atom hitting a j atom, $P_i(E_0, \theta_0)$ the ejection probability for an i atom, $\Gamma_{m_i} \approx 6/\pi^2$, and h a function of the mass ratio of the constituents and the concentration, which approaches 1 for $M_1 \approx M_2$.

Within the range of validity of Equations 7 & 8, the composition of the sputtered flux is independent of the type, energy, and angle of incidence of the bombarding ion. More pronounced effects can be expected under spike conditions, both with regard to the influence of differences in the surface potential and in mass.

3.3.2: Secondary effects.

As a consequence of preferential sputtering, the composition profile changes near the target surface. Therefore, the contribution of the enriched species to the sputtering yield is expected to increase at prolonged bombardment until the composition of the sputtered flux reflects that of the bulk target, ie. until the target is sputtered stoichiometrically.

Complications arise due to the fact that ion bombardment causes bulk processes in addition to sputtering, and that in fact a much larger fraction of the energy goes into bulk processes than into sputtered atoms. It is therefore by no means obvious whether the sputtering process itself is the dominating factor in determining observable composition changes of multiple-component targets at moderate and high fluences.

Matter may be rearranged within the damaged layer by collisional mixing as well as diffusion and segregation. Some bulk processes tend to generate spatial variations in composition under ion bombardment, others tend to randomize the target. To the first category belongs recoil

implantation^(152,153), which tends to transport the lighter species deeper into the target, and segregation, which may produce different phases both at the target surface and in deeper layers⁽¹⁵⁴⁾. Cascade mixing^(155,158) and diffusion both randomize existing composition variations; the relative importance of these effects depends on current and/or temperature.

The effect of recoil implantation and preferential sputtering are separable by way of their dependence on ion fluence⁽¹⁵²⁾. Preferential sputtering gives rise to a shallow surface layer enriched in the low-sputtering-yield species at all fluences. Recoil implantation causes near-surface enrichment of the heavier species at low fluence, but near-surface enrichment of the lighter species at high fluence. Either effect may be smeared by cascade mixing and diffusion.

Composition changes may extend over the entire penetration depth of the ion beam⁽¹⁵⁹⁾. This can hardly be caused by cascade mixing.

3.4 : Dependence of sputtering yield on angle of incidence.

Sputtering yield $S(\theta)$ is defined⁽¹⁶⁰⁾ as the number of atoms ejected by each ion incident at an angle θ to the surface normal. This may safely be assumed to be proportional to the energy deposited in the surface layer of depth R . If dE_1/dx is the rate at which the ion loses its energy E_1 in collision with the atoms of the crystal, the

energy lost in the surface layer, in which the path length is $R \sec \theta$, is

$$\int_0^{R \sec \theta} \frac{dE_1}{dx} dx \quad \text{Eq. 11.}$$

Provided that E_1 is less than about M_1 KeV, where M_1 is the atomic mass number of the ion, energy loss to electron excitation may be neglected⁽¹⁶¹⁾. dE_1/dx can be approximately written as

$$dE_1/dx = (\pi^2/4) a^2 n E_a \quad \text{Eq. 12.}$$

valid for $E_1 \lesssim E_a$. Here n is the density of atoms per unit volume, and E_a is the value of E_1 that allows the ion and atom to approach to a distance $a = a_0/(Z_1 Z_2)^{1/6}$ in a head-on collision, ie. :

$$E_a = 2E_r (Z_1 Z_2)^{7/6} (M_1 + M_2) / M_2 e \quad \text{Eq. 13.}$$

Here E_r is the Rydberg energy 13.6 eV, e is 2.718, Z_1 and Z_2 are the atomic numbers of ion and atom, M_1 and M_2 are corresponding mass numbers.

Expression 12 shows that dE_1/dx is independent of energy; thus the integral in Equation 11 is trivial and we can write for sputtering yield:

$$S(\theta) = (\pi^2/4) S a^2 n E_a R \sec \theta \quad \text{Eq. 14}$$

valid for $E_1 \lesssim E_a$, where S is a crystal constant giving the number of atoms ejected per unit energy deposited in

the surface layer. For polycrystalline solids, where one averages over many orientations, such a dependence on $\sec \theta$ is roughly true for angles of θ up to about 60° at energies of the order of E_a (1 to 100 KeV, depending on Z_1 and Z_2). With single crystals, anisotropies occur owing to effects such as channelling⁽¹⁶²⁻¹⁶⁵⁾ but these may be neglected in the first approximation.

At large angles θ , the sputtering yield increases less slowly than $\sec \theta$, passes through a maximum between 70° and 80° and falls towards zero at $\theta = 90^\circ$, as shown in Fig.3.3^(163,164).

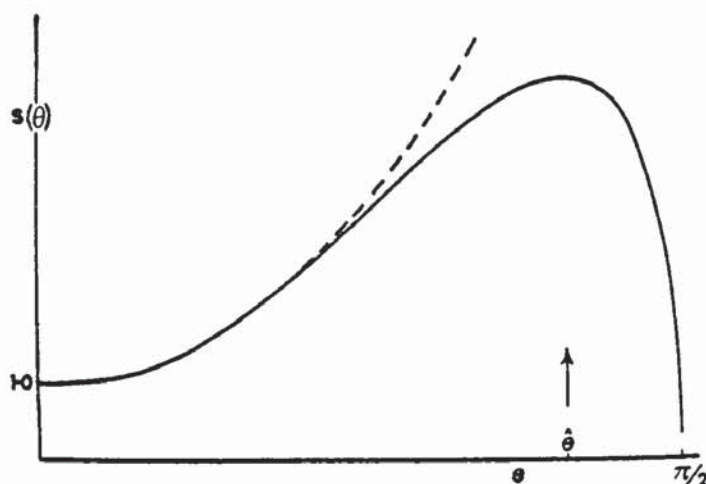


Fig.3.3: Schematic graph of sputtering yield versus angle of ion incidence.

It is suggested that this occurs because, as θ increases, the incident ion has an increasing probability of being reflected without traversing the effective surface layer. Hence the energy deposited eventually falls with increasing θ .

A simple physical criterion may be applied to determine $\hat{\theta}$, the angle at which $S(\theta)$ reaches its maximum value: when $\theta = \hat{\theta}$, reflection of the ion from the potential barrier associated with the surface plane of atoms prevents penetration⁽¹⁶⁶⁾. Lindhard⁽¹⁶⁷⁾ has shown that the critical angle for such reflection is given by :

$$\pi/2 - \theta = \left[\frac{5 \pi a_o^2 n^{2/3} Z_1 Z_2 E_r}{(Z_1^{2/3} + Z_2^{2/3}) E_1} \right]^{1/2} \quad \text{Eq. 15.}$$

Thus when $\theta > \hat{\theta}$, penetration is not possible.

CHAPTER FOUR:

SURFACE ROUGHNESS CAUSED BY ION BOMBARDMENT.

Erosion of the surface is a consequence of ion bombardment. Interesting changes in surface topography are observed, such as appearance of cones and spikes, although the mechanisms involved are not fully understood.

4.1: Cone formation by use of seed atoms.

In 1942 Guenther Schulze and Tollmein⁽¹⁶⁸⁾ observed angular variations in the surface reflectivity of glow discharge cathodes; this has been suggested to be the result of submicroscopic surface texture.

Stewart and Thompson⁽¹⁶⁰⁾ observed conical protrusions on surfaces that have been eroded by sputtering under 5 to 8 KeV argon ion bombardment. There appeared to be a correlation between the number of cones and the presence of inclusions in the specimen. It can be concluded that the cones form where low sputtering yield particles protect the underlying material from sputtering. Wehner and Hajicek⁽¹⁶⁹⁾ have shown that surface texture can be created by supplying surfaces with lower sputtering yield atoms (seed material) during sputter etching.

It is thought that the low sputtering yield atoms agglomerate into microscopic regions which protect the higher sputtering yield atoms beneath. Hudson⁽¹⁷⁰⁾ has shown that this is not a general rule and the actual case

is much more complex. In his work 30 different elements were tried to see what texture developed using tantalum as the seed material. Those elements (four) that were not successfully textured were Nb, Mo, Ta and W. These are all relatively low sputter yield materials. However, several elements having lower sputtering yields than Ta were textured (C, Si, Ti and Zr), while W which has higher sputtering yield than Ta did not texture. The all-unt textured elements belong to columns V B and VI B of the periodic chart. Wehner⁽¹⁷¹⁾, Wehner and Rosenberg⁽¹⁷²⁾ have shown that there is a periodicity effect of the low energy sputter yield of elements, which can be compared with the results obtained by Hudson.

Where possible, Hudson has differentiated and categorized morphological changes of the 26 elements that were textured. A large number of elements had textures that are classified as either a ridge structure or a cone structure. Many of the low sputtering yield materials (Ni, Ti, Fe, Co, Zr, Hf and Gd) have shown ridge morphologies, whereas many of the higher sputtering yield materials (Cu, Mg, Cr, Ag, Au, Al, C, Si, Se, Pd and Bi) have had morphologies that look like densely packed cones or needles. The other textured materials (Cd, Be, Zn, In, Sn, and Sb) have had unique textures which were neither ridge structures nor cone structures.

Supposing there is a foreign particle, or a particle with lower sputtering yield than the surrounding material, on

the surface subjected to ion bombardment, it will produce a step under its edge. As the particle itself shrinks, the step will be inclined at an angle $\hat{\theta}$ according to the mechanism explained in the next section, and eventually when the particle is removed, the step contracts inwards until it becomes a cone of angle $(\pi - 2\theta)$ with its axis along the direction of ion incidence.

Lower sputtering yield materials such as copper oxide and carbon are used as seed material on OFHC copper⁽¹⁷³⁾. This has caused the texturing of the OFHC copper in a form of close packed arrays of cones, which otherwise do not exist. A carbon surface layer generally gives a much more uniform texturing than the oxide itself. Berg and Kominiak⁽¹⁷³⁾ used continuous seeding by sputtering their samples on a carbon table during the ion bombardment. In their experiments, the time required for the development of the cone texture was found to be proportional to the total amount of oxide and carbon. Due to low mobility of carbon on metal surfaces, they suggested that the texture was the result of a very high density of small carbon agglomerates on the metal surface. This suggests that there must be clustering of seed atoms at the apexes of cones. But clustering can occur by diffusion of seed atoms. Therefore surface diffusion and seed clustering must be considered. Diffusion is a temperature controlled process and therefore substrate temperature comes into account and also the bonding between seed atom and the substrate which must be overcome for agglomeration. Kaufman and Robinson⁽¹⁷⁴⁾

have calculated the relation between cone spacing and temperature and have found that there is a critical temperature below which cones do not form. Assuming the probability that an adsorbed seed atom will be sputtered as a result of collision is unity, the critical temperature can be written as:

$$T = E_d/k \ln (E_d^{1/2} F_s N_o^{1/3} / 2^{1/2} m_s^{1/2} R_i r_c^2) \quad \text{Eq.16}$$

where E_d is the activation energy for diffusion (the energy barrier between adsorption sites), k the Boltzmann's constant ($1.3805 \times 10^{-23} \text{ J K}^{-1}$), F_s the seeding fraction, N_o the atomic density, m_s the mass of the seed atom, R_i the rate at which incident beam ions strike a unit surface area, and r_c the critical cluster radius (the radius below which the cluster is not stable).

By assuming $F_s = 0.01$ as the correct order of magnitude, a typical value of 10^{29} m^{-3} for N_o , $R_i = 6 \times 10^{19} \text{ m}^{-2} \text{ s}^{-1}$ at 10 A m^{-2} ion current, $r_c = 10 \text{ \AA}$ (175). With these values, the critical substrate temperature can be approximated as:

$$T = 587 E_d \quad \text{Eq. 17.}$$

and here the activation energy (E_d) is in eV. For details refer to reference number 174.

The formula to calculate cone spacing is:

$$r_d = (E_d^{1/2} N_o^{1/3} / 2^{1/2} m_s^{1/2} R_i 1/a)^{1/2} \exp(-E_d/2kT) = R_o \exp(-E_d/2kT) \quad \text{Eq. 18.}$$

Here r_d is the random-walk distance which is half the cone spacing in \AA , and $1/a$ is the probability that the adsorbed seed atom will be sputtered as a result of the collision.

The above formula can be written as:

$$\ln r_d = (-E_d / 2k) 1/T + \ln R_0 \quad \text{Eq. 19.}$$

The plot of $\ln r_d$ as a function of $1/T$ is a straight line; the slope of this line is $-E_d / 2k$ while the ordinate intersect is R_0 . Also from the slope of this line, the surface diffusion activation energy can be calculated.

Kaufman and Robinson⁽¹⁷⁴⁾ used Al substrates with Mo and Au as seed materials. The significance of their work is that Mo has a lower sputtering yield than Al, while Au has a higher sputtering yield. The calculated values for cone spacing and R_0 for both seed materials were 3.5 times less than measured values, while the calculated critical temperatures were in close agreement with experimental values. This close agreement is said to be due to the presence of most of the variables in a logarithmic form.

These results show that the clustering of seed atoms is responsible for cone formation, and seed material with higher sputtering yield than the substrate can be used if it is sufficiently mobile to replenish the sputtering loss from a seed cluster.

4.2: Seedless cone formation.

It very rarely happens that a surface is atomically clean; and even if so, very seldom is it atomically smooth.

When by any reason there is a step on the surface, during ion bombardment, that step moves as explained by Stewart and Thompson⁽¹⁶⁰⁾, who considered a surface (Fig.4.1) consisting of two inclined planes A and B on which bombarding ions are incident at angles α and β respectively.

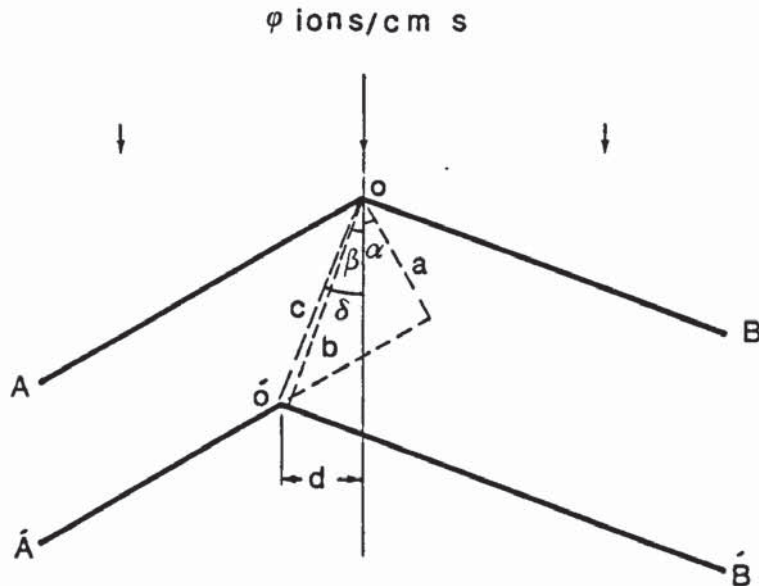


Fig.4.1: The motion of the intersection between two plane surfaces during erosion.

During erosion planes move to position A' and B', and their line of intersection moves from O to O'. The angle δ is made between the direction of ion incidence and the path OO' followed by the intersection. The distances advanced by the planes are a and b, that advanced by the intersection is c and the sideways movement of the inter-

section, transverse to the direction of incidence, is d . The flux of ions crossing unit area of surface normal to their direction is φ in the course of the erosion. On unit area of the two planes the respective fluxes are $\varphi \cos \alpha$ and $\varphi \cos \beta$, and the distances advanced are:

$$a = 1/n \quad \varphi \cos \alpha \quad S(\alpha)$$

$$b = 1/n \quad \varphi \cos \beta \quad S(\beta).$$

From the geometry of the system:

$$a = c \cos(\alpha + \delta)$$

$$b = c \cos(\beta - \delta)$$

These equations can be used to calculate the ratio d/a which relates the sideways movement of the intersection to the distance by which plane A advances:

$$\frac{d}{a} = \frac{S(\beta) - S(\alpha)}{S(\alpha) \cos \alpha (\tan \alpha + \tan \beta)} \quad \text{Eq. 20.}$$

This equation provides the means of deciding whether the intersection point o moves towards A or towards B during erosion (ie. whether d is positive or negative).

- I) If $S(\alpha) = S(\beta)$, $d = 0$ and o does not move laterally;
- II) If $S(\alpha) > S(\beta)$, $d < 0$ and o moves into B;
- III) If $S(\alpha) < S(\beta)$, $d > 0$ and o moves into A.

If the angle between the planes had been acute, viewed from above, rather than obtuse, the direction of motion would have been reversed. Thus the crest of a ridge will move towards the side for which $S(\theta)$ is least. The foot

of a valley will move towards the side for which $S(\theta)$ is greatest. In the special case where $\alpha = 0$ and ions are incident normally on plane A, equation 20 becomes:

$$\frac{d}{a} = \frac{S(\beta) - S(0)}{S(0) \tan \beta} \quad \text{Eq. 21}$$

and if $\beta \sim \hat{\theta}$, consideration of Fig.4.1 shows that this is of order of unity; consequently such a ridge should move sideways at about the same rate as it moves downwards.

Consider a step on a surface undergoing erosion by ion bombardment, as shown in profile 1 of Fig.4.2. This can be treated as though it were an assembly of planer facets, such as $0_1 0_2$ on the convex part of the step and $0_3 0_4$ on the concave part of the surface. Suppose the function $S(\theta)$ has the form shown in Fig.3.3, then by applying the above criterion to the corners at 0_1 , 0_2 , 0_3 and 0_4 it deduces:

- I) if $\theta < \hat{\theta}$

$$\left[\begin{array}{l} 0_1 \text{ and } 0_2 \text{ move to the right,} \\ 0_3 \text{ and } 0_4 \text{ move to the right.} \end{array} \right.$$
- II) if $\theta > \hat{\theta}$

$$\left[\begin{array}{l} 0_1 \text{ and } 0_2 \text{ move to the left,} \\ 0_3 \text{ and } 0_4 \text{ move to the left.} \end{array} \right.$$
- III) if $\theta = \hat{\theta}$

$$\left\{ \begin{array}{l} 0_1 \text{ moves to the left,} \\ 0_2 \text{ moves to the right, and facet grows,} \\ 0_3 \text{ moves to the right,} \\ 0_4 \text{ moves to the left, and the facet} \\ \text{shrinks.} \end{array} \right.$$

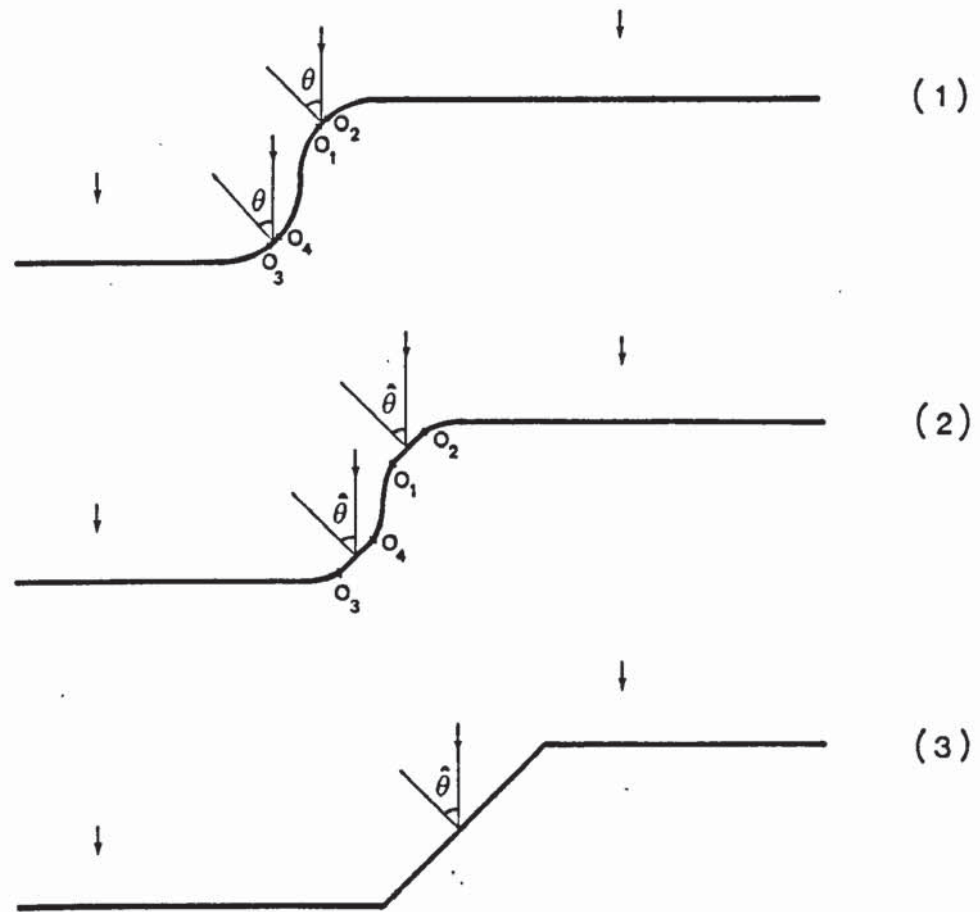


Fig.4.2: The erosion of a surface step.

The effect on the convex part of the step is to form a facet with the angle of incidence $\hat{\theta}$, whilst the concave part develops a smaller radius of curvature as the corners for which $\theta < \hat{\theta}$ run towards those for which $\theta > \hat{\theta}$, eventually making a single concave corner. Finally one obtains the profile 3 in which a single facet making an angle of incidence $\hat{\theta}$ moves across the surface. Note that if $S(\theta)$ has more than one peak, owing to crystallographic effects, facets will grow at first corresponding to each peak. But when these meet, the one for which $S(\theta)$ is greatest will always win; and this is generally expected to be at $\theta = \hat{\theta}$.

It must be pointed out that the effect of surface diffusion processes, enhanced by ion bombardment, have been entirely neglected. Cases undoubtedly occur when this would not be justified, and if diffusion were the dominant mechanism, surface-faceting of crystal planes with low free energy might then result. In such cases one should expect dependence on ion current density, which is absent here.

Another mechanism for roughening the surface by means of ion bombardment is given by Sigmund⁽¹⁷⁶⁾. This is purely a theoretical approach, but can explain some of the observations.

If a collimated monochromatic ion beam bombards a solid target with a plane surface, the average number of sputtered atoms per bombarding ion is given as⁽¹⁴⁰⁾:

$$S(x) = \Lambda F_D(x) \quad \text{Eq. 22.}$$

where x is the depth at which sputtering is observed, Λ is a constant characterizing the target material, and $F_D(x)$ is the average energy deposited per unit depth at depth x . The last two functions have been discussed in detail in previous sections.

Straightforward extension of Equation 22 to an arbitrary (non-planar) geometry yields:

$$S(r) \, da = \Lambda F_D(r) \, da \quad \text{Eq. 23.}$$

where $S(r) da$ is the average number of target atoms sputtered from a surface element da at a vector distance r from the point of impact of the bombarding ion, and $F_D(r)$ is the energy deposited per unit volume at r . Note that the orientation of the surface element da has not entered into the calculation of Equation 23. Therefore $S(r)$ is called local or differential sputtering yield.

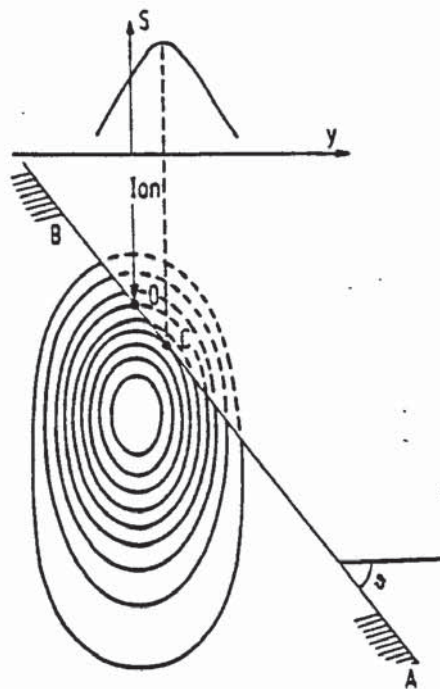


Fig.4.3 : Contour plot of deposited energy⁽¹⁷⁷⁾. Target surface AB, angle of incidence θ , point of ion impact O, and point of maximum sputtering yield C.

Upper graph: distribution of sputtering yield along surface for ion incidence at 0° .

A contour plot of deposited energy (F_D), calculated for equal masses of bombarding ion and target is shown in

Fig.4.3⁽¹⁷⁷⁾.

It is seen that the maximum of the deposited energy function along the surface plane is not the point of impact, but is in point C further downstream. This means that the maximum of local sputtering yield is at C and not at the point of impact. This is a special case of a more general result: because of the initial momentum of the ion, the centre of deposited energy distribution is located at a finite distance from the point of impact as seen in the direction of the bombarding ion. Hence there will usually be parts of the sputtered surface that are sufficiently close to the centre to be on a higher contour than the point of impact.

Now let us bombard a surface with a structure of the type sketched in Fig.4.4. Assume that the distance between the points A & B, B & C, etc. correspond to the distance OC in Fig.4.3. Then, sputtering around the point B is dominated by those ions hitting near A, sputtering around

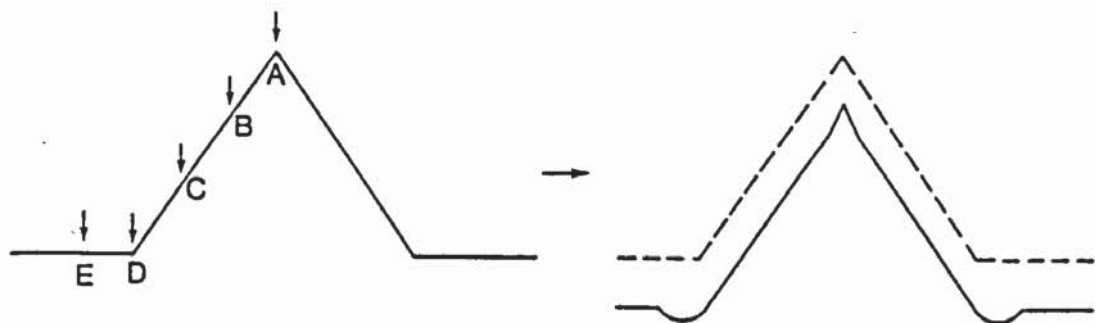


Fig. 4.4 : See the text.

the point C by ions hitting near B, etc. There is little sputtering near A, but more than average at D, since also ions hitting at E contribute a little.

This is a general feature, which could have been sketched qualitatively by using a very differently shaped structure. The main point is that the surface is not planar, so there is a tendency towards less sputtering near a peak and more sputtering near a valley. Obviously, there is an instability. It means that a microscopically flat surface is unstable under high dose ion bombardment, unless atom migration acts as a dominating smoothing effect.

For developing this model, several assumptions have been made which include random slowing down of bombarding ions by target atoms, the use of statistical average for $F_D(r)$ instead of an average distribution for an individual cascade, and the ignoring of possible interruption of a collision cascade by the target surface.

While the theory put forward by Stewart and Thompson⁽¹⁶⁰⁾ does not explain the grooves seen around the bottom of cones, Sigmund's theory predicts the formation of such grooves at points such as D in Fig. 4.4. Formation of such grooves is explained by alternative theories involving scattered ions or high energy sputtered atoms⁽¹⁷⁸⁻¹⁸¹⁾. For details refer to reference number 181.

In 1955 Lighthill and Whitham^(182,183) derived the

kinematic wave equation relating flux and concentration of a quantity when a functional relation exists between these parameters.

Frank^(184,185) has applied the kinematic wave equation to dissolution of crystals to explain chemical etching. From this work, Frank has concluded with two theorems. The first of the dissolution theorems states that if the rate of dissolution of a crystal surface at any given time is a function only of orientation, then during dissolution the locus of an elemental area of crystal surface with a particular orientation is a straight line. Any such locus is called a dissolution trajectory. The second theorem states that if the dissolution rate is defined as measured normal to the actual crystal surface, and the polar diagram of the reciprocal of this dissolution rate as a function of orientation is constructed, then the trajectory of an elemental area of crystal surface of given orientation is parallel to the normal to the polar diagram at the point of corresponding orientation.

From these two theorems it can be calculated that when there is a discrete change of orientation between adjacent elements of area, such as crystal edge, its dissolution trajectory is given by the normal to a chord of the polar diagram joining the points corresponding to the orientations of these two adjacent elements.

Frank's theorems are successfully applied to interpret

experimental results on the dissolution of crystals.^(186,187)

Comparing Frank's theorems with orientation dependence of sputtering yield, one can see the existing similarity. It has been demonstrated that Frank's theorems are equally applicable to the erosion of surfaces by ion bombardment.⁽¹⁸⁸⁾

If the θ is the angle which the ion beam makes with the normal to the target surface, the corresponding sputtering yield is $S(\theta)$, and the depth sputtered from a plane surface is given by:

$$d = \phi t/n S(\theta) \cos \theta \quad \text{Eq. 24.}$$

where ϕ is the flux of ions striking unit area of surface normal to their direction, while n is the number of atoms per unit volume of target material, and t is the time of bombardment. The thickness of material removed by sputtering at any given time can be shown by a plot of $S(\theta) \cos \theta / S(0)$ against θ . Fig. 4.5 shows the plot of $S(\theta) \cos \theta / S(0)$ against angle of incidence for Ar^+ ions on silica glass.⁽¹⁸⁹⁾

From the data in Fig.4.5, the reciprocals of the sputtering ratio $S(\theta) \cos \theta / S(0)$ can be plotted on polar graph paper in accordance with the second theorem of Frank. This is called the erosion slowness polar diagram (Fig.4.6). Given a particular starting surface shape, the successive sputtered topographies for silical glass can be deduced.

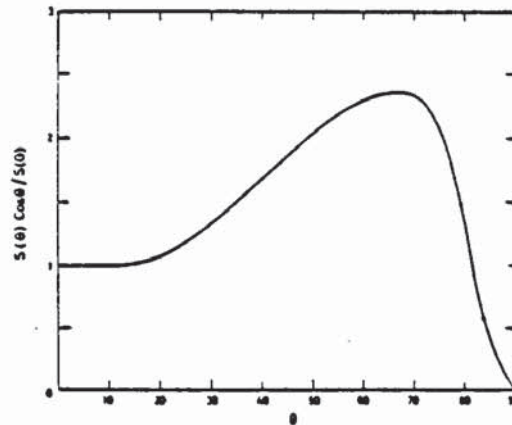


Fig.4.5 : Variation of sputtering yield with angle of incidence for Ar^+ ions on silica glass.

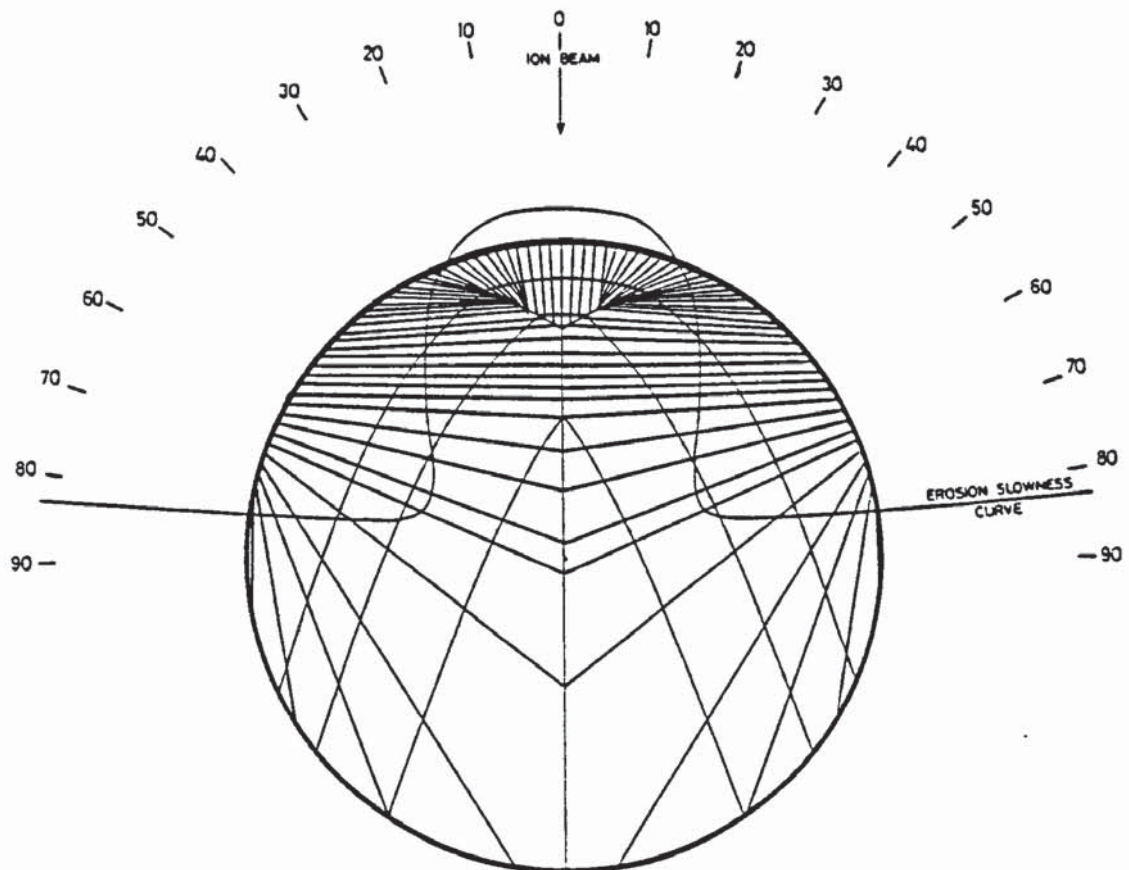


Fig.4.6: Polar diagram of the reciprocal sputtering ratio for silica glass.

First consider the case of a glass sphere which is represented in two dimensions by a circle on polar graph paper. The starting circular shape shown in Fig.4.6 is conveniently superimposed on the erosion slowness curve. The next step is to draw the orientation trajectories which obey the dissolution theorems. These trajectories are parallel to the direction of the normals to the slowness curve at corresponding orientation. They are drawn inwards towards the inside of the circle because of the erosion caused by ion bombardment. According to Frank^(184,186) the interpretation in terms of crystal surface, when two trajectories representing different orientations meet in space, must be that a discontinuity, ie. an edge, is produced. These edge trajectories are not necessarily straight. Hence, in Fig.4.6 where two trajectories meet, their lines are erased beyond the meeting point and the direction of the resulting trajectory is drawn normal to the chord joining points of corresponding orientations on the erosion slowness curve.

The final step is to derive resultant topographies at any given time during bombardment from the trajectory array constructed. First with the 0° orientation on the initial circular profile of the sphere, ie. normal incidence, the distance corresponding to the depth eroded appropriate to a given bombardment time should be marked off on the trajectory. For other orientations one edge of a pair of parallel rules must be placed at a tangent to the initial profile; this selects a point on the profile corresponding to a particular surface orientation. Then side-step the

parallel rules along the trajectory from that orientation for a distance appropriate to the same bombardment time as that for normal incidence. This distance is some multiple of the distance for 0° orientation as determined from the sputtering curve (Fig.4.5). Then according to Frank's first theorem⁽¹⁸⁴⁾ the rule is still at a tangent to the evolving surface and this new position of the surface element can be marked off on the trajectory. Three resultant shapes of the bombarded surface are shown in Fig.4.6; the first corresponds to the shape after a short time of bombardment and the second and third correspond to longer periods. These shapes agree quite well with the experimental observations on ion bombarded metal spheres by Wehner⁽¹⁶³⁾.

Figs.4.7 & 4.8 show similar treatment applied to a hemispherical trough and a sinusoidal surface respectively. Sputtering of a deep trough (Fig.4.7a) will turn it into a shaft-like depression with vertical walls and a flat bottom, whereas sputtering of a shallower trough (Fig.4.7b) will result in the widening of the trough and decrease of the slope. These profiles agree reasonably well with the observations by Bayly⁽¹⁸¹⁾ even though the secondary effects such as ion reflection and redeposition are not taken into account. In Fig.4.8 the evolution of the sputtered shapes from the initial sinusoidal surface indicates a polishing process, with the peaky topography progressing towards flatness. This is considered the more accurate description of what actually goes on during the

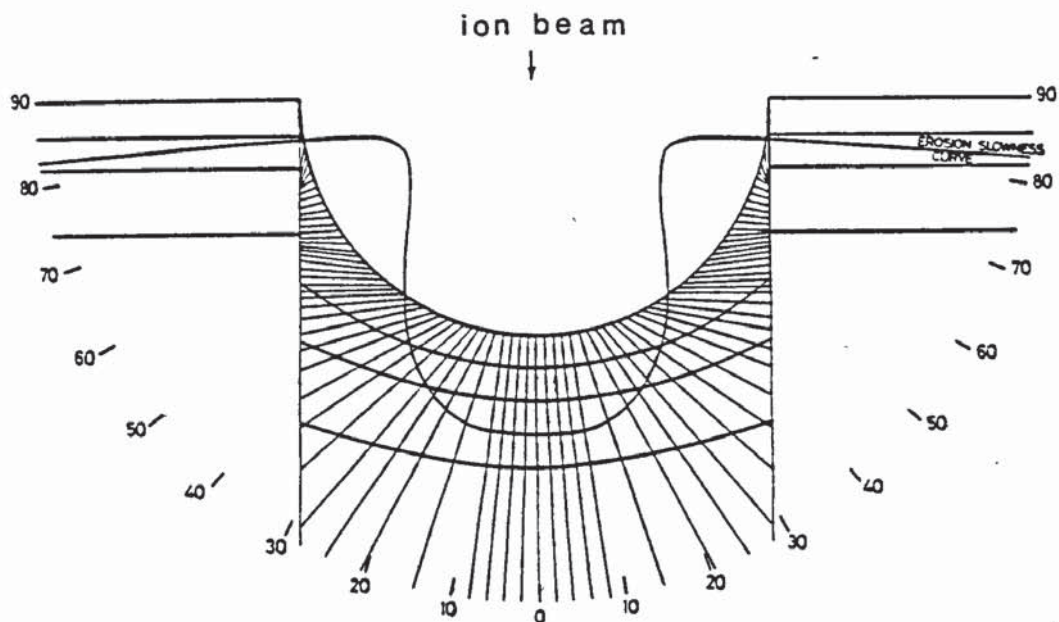


Fig.4.7a : Erosion slowness curve, trajectories, and profiles of a deep trough on a silica glass surface due to sputtering.

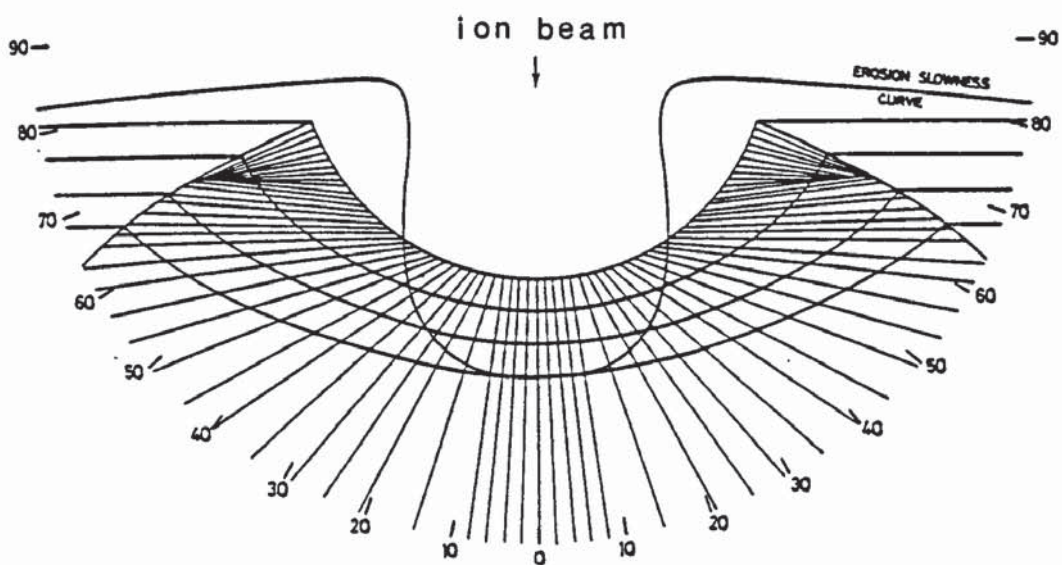


Fig.4.7b : Erosion slowness curve, trajectories, and evolved profiles of a shallow hemispherical trough on a silica glass surface due to sputtering.

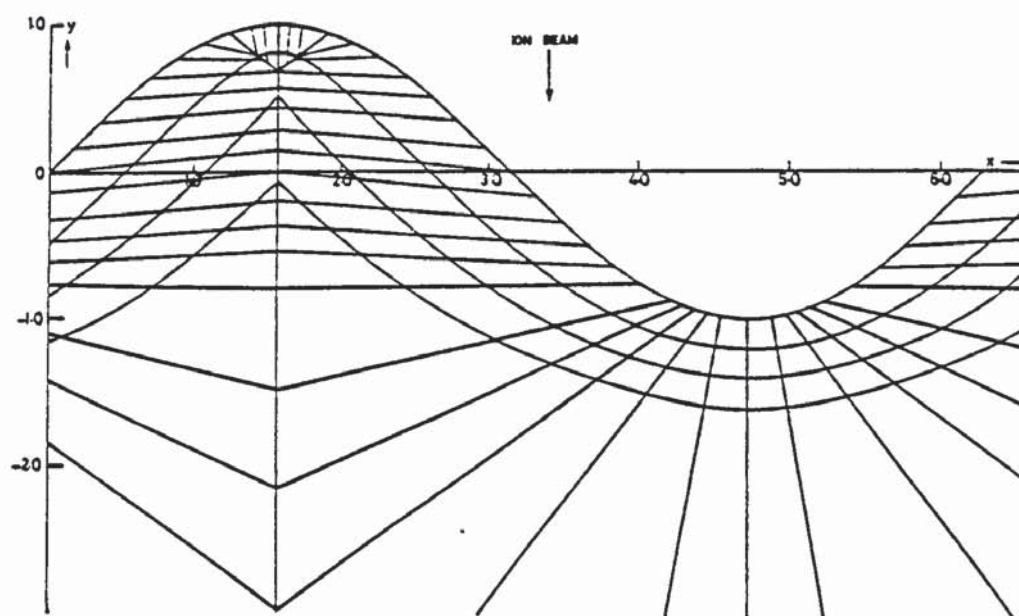


Fig. 4.8 : The evolution of sputtered shapes from an initial sinusoidal glass surface during ion bombardment.

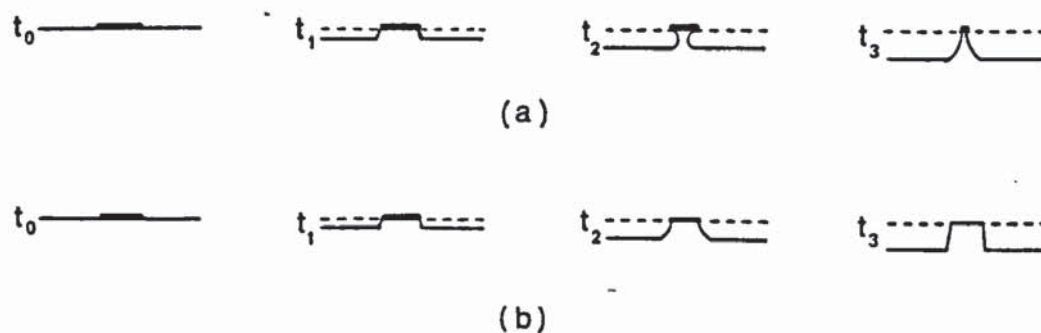


Fig. 4.9 : a) Instability of a hillock due to adhering contamination on a slow-etching crystal surface. b) Stability of a hillock on a fast etching crystal surface⁽¹⁹¹⁾.

bombardment of a sinusoidal surface than that reported by Catana et al⁽¹⁹⁰⁾ whose computer simulation predicts an equilibrium topography of a sharp peak and a plateau. The difference is certainly not a consequence of the exact form of sputtering curve, but rather a spurious result arising in the computational procedure.

Fig. 4.9 shows the effect of chemical etching of a crystal surface with adhering contaminants⁽¹⁹¹⁾. The situation (a) corresponds to near-normal incidence, ie. $\theta \approx 0^\circ$, and to grazing incidence, ie. $\theta \geq 75^\circ$, where the erosion rate decreases rapidly with increase of incidence angle. At normal incidence, no undercutting will occur as depicted. Similar profiles will result only if the contaminant disintegrates under bombardment. Situation (b) corresponds to sputtering at or near the incidence angle where the erosion is greatest, ie. $\theta \approx 70^\circ$. Construction of sputtering trajectories for cases shown in Fig. 4.9 is no longer directly applicable since the erosion rate depends on both position and orientation owing to the shadowing effect by the contaminant. Nevertheless, Fig. 4.9 leads to the conclusion that hillocks formed at normal incidence or extreme grazing incidence are only transient and will eventually disappear while such irregularities are more persistent at angles of incidence where sputtering is near maximum. Permanent hillocks will persist at normal incidence only if they obey the conditions depicted in Fig. 4.10 where the eroded depth of the flat and inclined surfaces are given by the

equation:

$$d_1 \cos \theta = d_2 \quad \text{Eq. 25}$$

From Eq.24, this means:

$$S(\theta) = S(0) \quad \text{Eq. 26.}$$

Hence permanent hillocks will form if the half-angle of the apex, α , is equal to $\pi/2 - \theta$, where θ is the angle at which the sputtering yield is again equal to that at normal incidence. This is the same conclusion reached by Catana et al⁽¹⁹⁰⁾ in their analysis of the computer-simulated topographies.

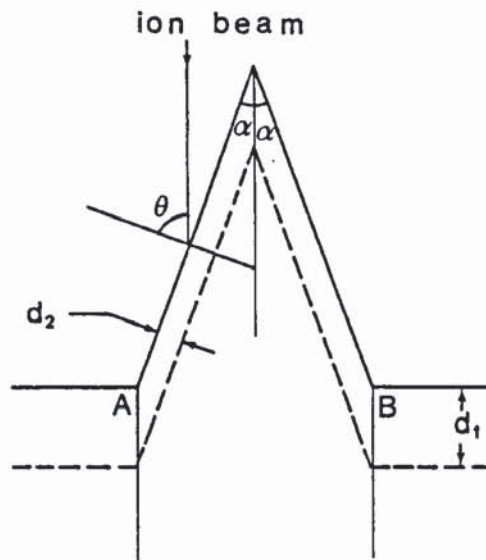


Fig.4.10: Equilibrium topography of a hillock
where the trajectories of the intersections
A & B are normal to the flat surface.

4.3 : Effect of specimen temperature.

The effect of sample temperature on surface topographies produced by ion bombardment is an important factor. By increasing the temperature, diffusion becomes an important factor in trying to flatten the surface. On the other hand the sputtering yield may change.

The effect of specimen temperature on ion erosion of iron has been investigated⁽¹⁹²⁻¹⁹⁵⁾. Vasiliu⁽¹⁹²⁾ et al have shown that below the self diffusion temperature (T_d), ion erosion is the most influential effect; whereas above T_d , the surface topography is a result of ion erosion and thermal etching, and a flattening process caused by diffusion occurs. They also found selective ion etching features (etch lines, scale-shaped microrelief) formed on top of the thermal etching microstructures on polycrystalline iron samples.

The effect of specimen temperature on sputtering yield has been investigated⁽¹⁹⁶⁻²⁰¹⁾. In some cases sputtering yield is found to increase with increase in temperature^(196,197), in some cases remain constant to a certain temperature^(198,200,201), and in some cases even reduces with increase in temperature⁽¹⁹⁷⁻¹⁹⁹⁾.

4.4 : Texturing of stainless steel.

Ion bombardment of stainless steel⁽²⁰²⁾ results in the formation of conical protrusions and pillar type structures. The conical protrusions are found to arise from slag silicate particles while the pillar type structures result

from fibrous manganese sulphide inclusions.

It has been shown⁽²⁰³⁾ that the sputtering yield of steel may be obtained solely by taking the average of the sum of the yields of the constituent elements. It has also been shown⁽²⁰⁴⁾ that sputter yields increase fairly steadily within each group of elements reaching a maximum for the inert gas species of the group. Since the yield falls almost to zero thereafter⁽²⁰⁵⁾, the sputtering yield of sulphur is very low. While the presence of MnS fibres is not unexpected in stainless steel, it is not unexpected to see longer pillars of MnS than cones formed by the shadowing effect of silicate inclusions, since sulphur has a lower sputtering yield than silicon, and the pillars are wholly MnS.

Fig.4.11 shows that by increasing the bombardment time, the number of cones increases. It also shows that after ion bombardment for a long time an equilibrium condition arises under which cones disappear at the rate at which fresh precipitates are uncovered.

Witcomb⁽²⁰²⁾ observed a faceting effect on cones; the faceted cones have diameters smaller than the matrix grain size and are therefore a single crystal effect.

The faceting effect has been observed on argon etched gold⁽²⁰⁶⁾, and there is enough evidence to conclude its occurrence to be the result of the high sputtering yield

of low index crystal planes, such as $\{100\}$, $\{110\}$, $\{111\}$, $\{114\}$, and $\{116\}$ in fcc metals⁽²⁰⁷⁾

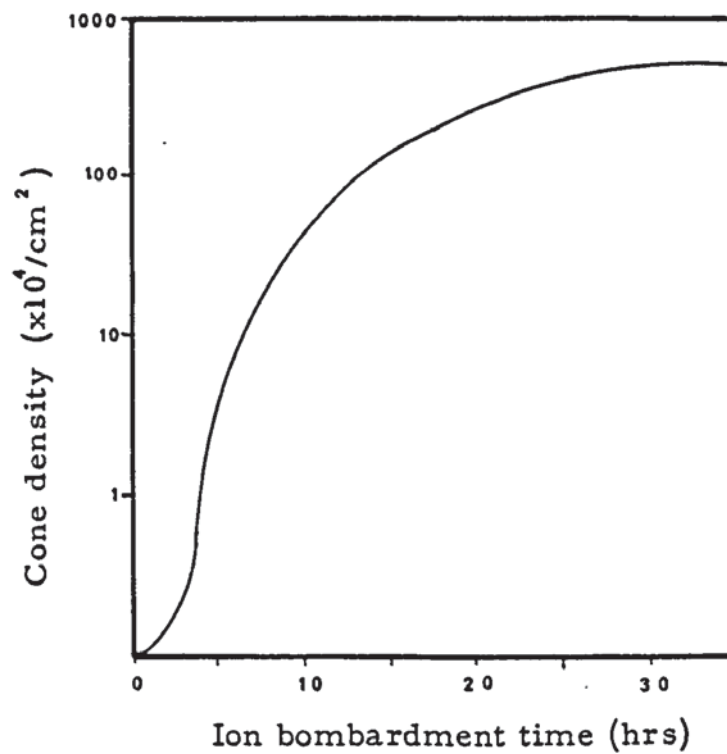


Fig.4.11: Cone density v ion bombardment time⁽²⁰²⁾.

CHAPTER FIVE.

SOLAR ENERGY.

This chapter is dedicated to solar energy and its utilization.

The sun is a sphere of intensely hot gaseous matter with a diameter of 1.39×10^6 Km, and is, on the average 1.5×10^8 Km from the earth. The surface of the sun is at an effective temperature of about $5762^{\circ}\text{K}^{(208)}$, and the density about 80 to 100 times that of water.

The characteristics of the sun and its spatial relationship to the earth results in a nearly fixed intensity of solar radiation outside of the earth's atmosphere. The "solar constant" (I_0) is the total energy from the sun, per unit time, received on a unit area of surface perpendicular to the radiation, in space, at the earth's mean distance from the sun. Based on recent measurements, Thekaekara and Drummond⁽²⁰⁹⁾ have proposed a standard value of 1353 Wm^{-2} for the solar constant.

A standard spectral irradiance curve has been compiled by NASA, based on high altitude and space measurements⁽²¹⁰⁾, and is shown in Fig.5.1.

5.1: Light.

Light is defined as the product of the visibility and the radiant power, the latter being the rate of propagation

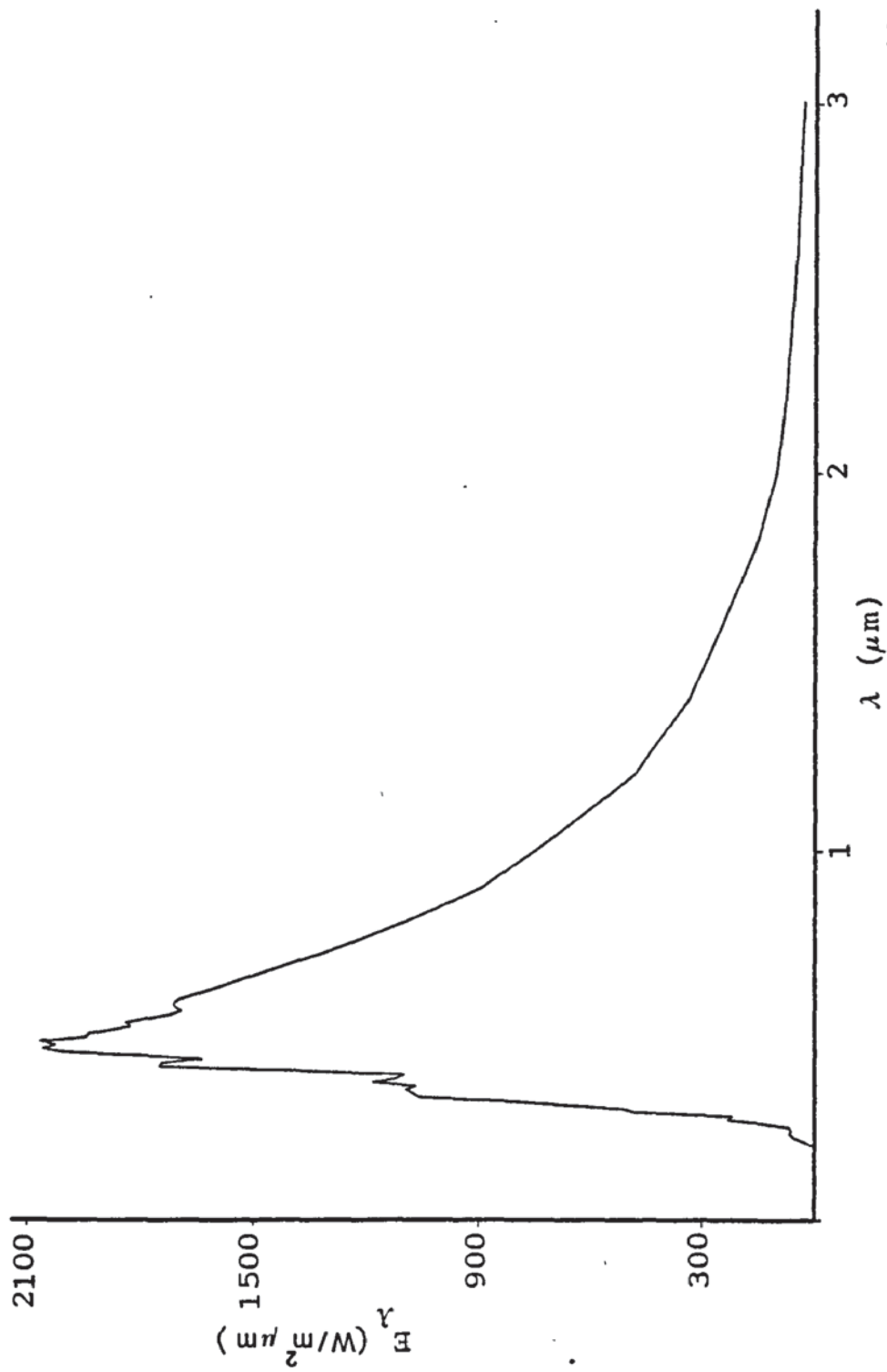


Fig.5.1.1: Standard spectral irradiance curve compiled by NASA (210).

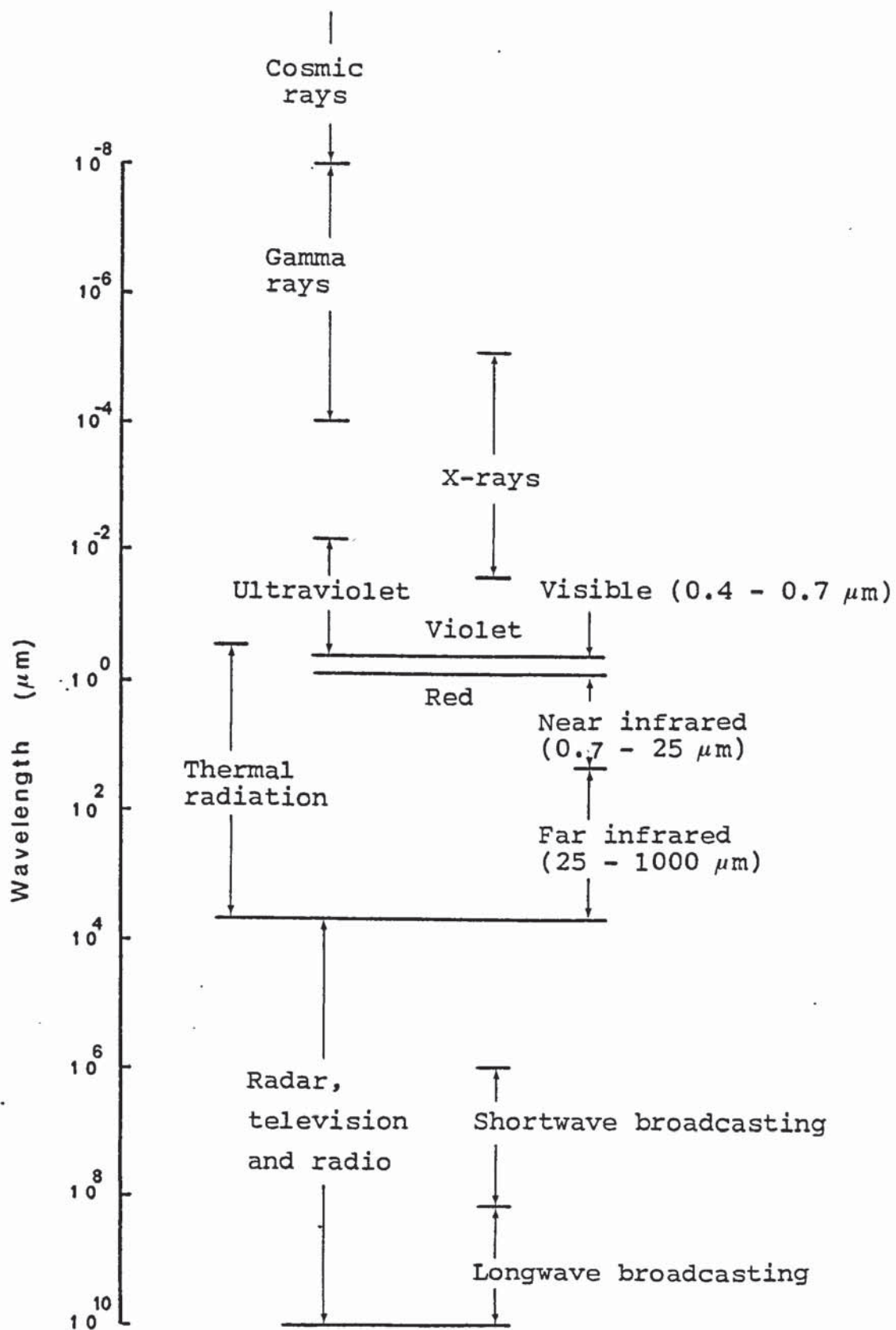


Fig.5.2: Spectrum of electromagnetic radiation

of radiant energy.

Within the framework of wave theory, electromagnetic radiation follows the laws governing transverse waves that oscillate in a direction perpendicular to the direction of travel. The speed of propagation of electromagnetic radiation is the same as for light. In a vacuum the speed of propagation is $C_0 = 2.998 \times 10^8 \text{ ms}^{-1}$.

The speed of light (C) in a medium is less than the speed of light (C_0) in a vacuum and is commonly given in terms of the refraction index of the medium $n = C_0/C$.

For some purposes the classical electromagnetic wave view of radiation does not explain the observed phenomena. To overcome this problem it is necessary to consider the energy of a particle called a photon which can be thought of as an energy unit with zero mass and zero charge. The energy of photon is given as:

$$E = h \nu \quad (\text{Eq. 27})$$

where h is Planck's constant ($6.6256 \times 10^{-34} \text{ JS}$), and ν is the frequency. As is clear, the energy of a photon increases as the frequency increases (i.e. when the wavelength decreases). This is an important fact to notice, particularly where a minimum photon energy is needed to cause a required change (e.g. in photovoltaic cell, where a hole-electron pair should be created by photons).

The type of electromagnetic radiation can be classified by wavelength λ in vacuum (or frequency). Fig.5.2 shows the spectrum of electromagnetic radiation, and it can be seen that light covers just a small portion of the spectrum.

5.2: A perfect blackbody.

5.2.1: Definition of a blackbody.

A blackbody is defined as an ideal body that allows all the incident radiation to pass into it (no reflected energy) and absorbs internally all the incident radiation (no transmitted energy). This is true for all wavelengths of radiation and all angles of incidence. Hence the blackbody is a perfect absorber of incident radiation. All other quantitative aspects of blackbody behaviour can be derived from this definition.

Although a true blackbody does not exist in nature, some materials approach a blackbody. For example, a sufficiently thick quantity of carbon black can absorb about 99% of all incident thermal radiation:

A blackbody is also a perfect emitter of thermal radiation, in all wavelengths and in every direction.

5.2.2: Planck's Law.

Electromagnetic radiations in the wavelength range of about 0.2 to about 100 μm are called thermal radiation

and are emitted by all substances according to their temperature. The wavelength distribution of this radiation for a blackbody is given by Planck's law⁽²¹¹⁾ as:

$$e_{b\lambda} = \frac{2\pi hc_0^2}{\lambda^5 (e^{hc_0/\lambda kT} - 1)} \quad \text{Eq. 28.}$$

where h is Planck's constant, k is Boltzmann's constant, and $e_{b\lambda}$ represents energy per unit area per unit time per unit wavelength interval at wavelength λ for a blackbody. The terms $2\pi hc_0^2$ and hc_0/k are often called the first and second radiation constants, and are represented as $C_1 = 3.7405 \times 10^{-16} \text{ Wm}^2$ and $C_2 = 0.0143879 \text{ m}^0\text{K}$, respectively⁽²⁰⁸⁾.

Planck's spectral distribution gives the maximum intensity of radiation at a given wavelength for a given temperature.

5.2.3: Wien's displacement law.

Another quantity of interest with regard to the blackbody emissive spectrum is the wavelength λ_{\max} at which the emissive power $e_{b\lambda}(\lambda)$ is maximum for a given temperature. This maximum shifts towards shorter wavelengths as the temperature is increased; this is shown in Fig.5.3. This maximum can be found by differentiating Planck's distribution (Equation 28) and setting the left hand side of the equation to zero. This leads to:

$$\lambda_{\max} T = \frac{C_2}{5} \times \frac{1}{1 - e^{-C_2/\lambda_{\max} T}} \quad \text{Eq. 29.}$$

The solution of this equation is of the form:

$$\lambda_{\max} T = C_3$$

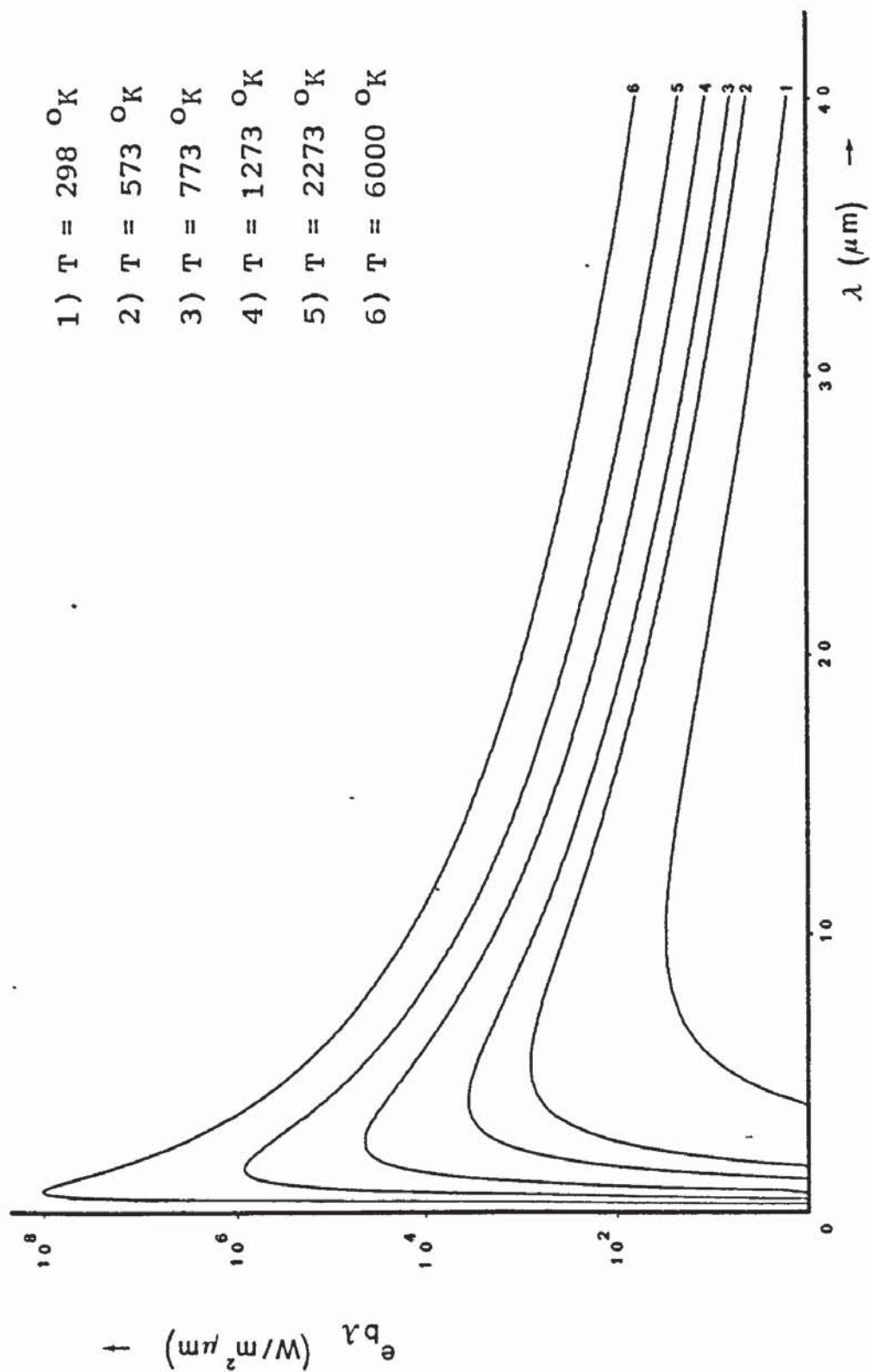


Fig.5.3: Spectral distribution of blackbody radiation

This is called Wien's displacement law, and

$$c_3 = 2897.8 \mu K^{\circ}(208).$$

5.2.4: Total emitted power.

Planck's law gives spectral distribution of radiation from a blackbody. By integration of Equation 28 over all wavelengths, the total emitted energy at a particular temperature can be calculated.

$$e_b = \int_0^{\infty} e_{b\lambda} d\lambda = \sigma T^4 \quad \text{Eq. 30.}$$

where σ is the Stefan-Boltzmann constant and has the value $5.6697 \times 10^{-8} \text{ W}_m^2 \text{ K}^{-2}$.

5.3: Radiation Terminology.

5.3.1: Suffixes.

According to widely accepted nomenclature, the following suffixes are used :

- ance : is used to specify quantitative measures at or near the condition of use; eg. emittance.
- ivity: is used to specify a physical property of a material; eg. absorptivity.
- ion : is used to specify a general effect of the action of a material upon a beam of radiation; eg. reflection.

5.3.2: Prefixes.

The following prefixes are used to specify particular conditions of irradiation :

- monochromatic - : specifies radiation at a single wavelength λ ;
- directional - : specifies radiation to or from a direction (β, φ) , where β is the cone angle measured from the direction normal to the surface, and φ is the circumferential angle;
- hemispherical - : specifies the average of radiation to or from all directions, and can be calculated by integrating the directional quantity over the entire hemisphere
- (ie. $\int_{\beta=0}^{\pi/2} \int_{\varphi=0}^{2\pi} \dots d\beta d\varphi$);
- spectral - : specifies the dependence of the measured quantity on the wavelength of radiation;
- total - : specifies the average of the radiation over all wavelengths, and can be calculated by integrating the spectral quantity over all wavelengths

(ie. $\int_{\lambda=0}^{\infty} \dots d\lambda$).

5.4: Radiation properties of non-black surfaces.

When radiation is incident on a homogeneous body, some of the radiation is reflected, and the remainder penetrates into the body. The radiation may then be absorbed as it travels through the medium. If the material thickness required to substantially absorb the radiation is large compared with the thickness dimension of the body, or if the material is transparent, then most of the radiation

will be transmitted entirely through the body and will emerge with its nature unchanged. On the other hand if the material is a strong internal absorber, the radiation that is not reflected from the body will be converted into internal energy within a very thin layer adjacent to the surface. It should be carefully noted that there is a distinction between the ability of a material to let radiation pass through its surface, and its ability to internally absorb the radiation after it has passed into the body. For example a highly polished metal will generally reflect almost all the incident radiation, but the radiation passing into the body will be strongly absorbed and converted to internal energy within a very short distance within the material. Thus a highly polished metal has strong internal absorption ability, but is a poor absorber of incident radiation since most of the incident radiation is reflected. Non-metals may exhibit the opposite tendency, ie. they may allow a substantial portion of the incident radiation to pass into the material, but a comparatively large thickness may be required to internally absorb the radiation and convert it into internal energy. When all the radiation that passes into the body is absorbed internally, the body is called opaque. The following discussion in this chapter will be restricted to opaque materials.

The radiation behaviour of a real body depends on many factors such as composition, angle at which radiation is either being emitted or intercepted by the surface and

the spectral distribution of the radiation incident on the surface.

5.4.1: Absorptivity.

Absorptivity is defined as the fraction of the energy incident on a body that is absorbed by the body.

The monochromatic directional absorptivity is a property of a surface, and is defined as the fraction of the incident radiation of wavelength λ from the direction (β, φ) that is absorbed by the surface and can be expressed as :

$$\alpha_{\lambda}(\beta, \varphi) = \frac{I_{\lambda, a}(\beta, \varphi)}{I_{\lambda, i}(\beta, \varphi)} \quad \text{Eq. 31}$$

where subscripts a and i represent absorbed and incident respectively.

Directional absorptivity is defined as the fraction of all the radiation from the direction (β, φ) that is absorbed by the surface, and can be expressed as :

$$\begin{aligned} \alpha(\beta, \varphi) &= \frac{\int_0^{\infty} \alpha_{\lambda}(\beta, \varphi) I_{\lambda, i}(\beta, \varphi) d\lambda}{\int_0^{\infty} I_{\lambda, i}(\beta, \varphi) d\lambda} \\ &= \frac{1}{I_i(\beta, \varphi)} \int_0^{\infty} \alpha_{\lambda}(\beta, \varphi) I_{\lambda, i}(\beta, \varphi) d\lambda \quad \text{Eq. 32.} \end{aligned}$$

Unlike monochromatic directional absorptivity, directional absorptivity is not a property, but a function of the wavelength distribution of the incident radiation.

The monochromatic hemispherical absorptivity and

hemispherical absorptivity can be written as:

$$\alpha_{\lambda} = \frac{\int_{\beta=0}^{\pi/2} \int_{\varphi=0}^{2\pi} \alpha_{\lambda}(\beta, \varphi) I_{\lambda, i}(\beta, \varphi) \sin \beta \cos \beta d\beta d\varphi}{\int_{\beta=0}^{\pi/2} \int_{\varphi=0}^{2\pi} I_{\lambda, i} \sin \beta \cos \beta d\beta d\varphi} \quad \text{Eq. 33.}$$

and

$$\alpha = \frac{\int_{\beta=0}^{\pi/2} \int_{\varphi=0}^{2\pi} \int_{\lambda=0}^{\infty} \alpha_{\lambda}(\beta, \varphi) I_{\lambda, i}(\beta, \varphi) \sin \beta \cos \beta d\beta d\varphi d\lambda}{\int_{\beta=0}^{\pi/2} \int_{\varphi=0}^{2\pi} \int_{\lambda=0}^{\infty} I_{\lambda, i}(\beta, \varphi) \sin \beta \cos \beta d\beta d\varphi d\lambda} \quad \text{Eq. 34.}$$

respectively.

5.4.2: Emissivity.

The emissivity is a measure of how well a body can radiate energy compared with a blackbody. The emissivity is dependent on factors such as body temperature, the particular wavelength being considered for the emitted energy, and the angle at which the radiation is taking place. The monochromatic directional emissivity is defined as the ratio of the monochromatic intensity emitted by a surface in a particular direction, to the monochromatic intensity that would be emitted by a blackbody at the same temperature, and is expressed as :

$$\epsilon_{\lambda}(\beta, \varphi) = \frac{I_{\lambda}(\beta, \varphi)}{I_{b, \lambda}} \quad \text{Eq. 35.}$$

The directional emissivity is a property of a surface, as is the monochromatic directional emissivity; and is defined as the ratio of the emitted total intensity in the direction (β, φ) to the blackbody intensity.

$$\epsilon(\beta, \varphi) = \frac{\int_0^{\infty} \epsilon_{\lambda}(\beta, \varphi) I_{b, \lambda} d\lambda}{\int_0^{\infty} I_{b, \lambda} d\lambda} = \frac{1}{I_b} \int_0^{\infty} \epsilon_{\lambda}(\beta, \varphi) I_{b, \lambda} d\lambda \quad \text{Eq. 36.}$$

Integration of Equations 35 and 36 over the enclosing hemisphere gives the monochromatic hemispherical emissivity and hemispherical emissivity, respectively, as:

$$\begin{aligned} \epsilon_{\lambda} &= \frac{\int_{\beta=0}^{\pi/2} \int_{\varphi=0}^{2\pi} \epsilon_{\lambda}(\beta, \varphi) I_{b, \lambda} \sin\beta \cos\beta d\beta d\varphi}{\int_{\beta=0}^{\pi/2} \int_{\varphi=0}^{2\pi} I_{b, \lambda} \sin\beta \cos\beta d\beta d\varphi} \\ &= \frac{1}{\pi} \int_{\beta=0}^{\pi/2} \int_{\varphi=0}^{2\pi} \epsilon_{\lambda}(\beta, \varphi) \sin\beta \cos\beta d\beta d\varphi \quad \text{Eq. 37.} \end{aligned}$$

and

$$\begin{aligned} \epsilon &= \frac{\int_{\beta=0}^{\pi/2} \int_{\varphi=0}^{2\pi} \int_{\lambda=0}^{\infty} \epsilon_{\lambda}(\beta, \varphi) I_{b, \lambda} \sin\beta \cos\beta d\beta d\varphi d\lambda}{\int_{\beta=0}^{\pi/2} \int_{\varphi=0}^{2\pi} \int_{\lambda=0}^{\infty} I_{b, \lambda} \sin\beta \cos\beta d\beta d\varphi d\lambda} \\ &= \frac{1}{e_b} \int_{\lambda=0}^{\infty} \epsilon_{\lambda} e_{b, \lambda} d\lambda \quad \text{Eq. 38.} \end{aligned}$$

where e represents the emissive power.

5.4.3: Kirchhoff's law.

Considering an evacuated isothermal enclosure at temperature T , which is isolated from surroundings, it can be said that the enclosure and any substance within

it are in thermodynamic equilibrium. This means that an arbitrary body within the enclosure absorbs the same amount of energy as it emits. An energy balance on an element of the surface of the arbitrary body yields :

$$\alpha q = \epsilon e_b \quad \text{Eq. 39.}$$

If a second body with different surface properties is placed in the enclosure, the same energy balance must apply and the ratio q/e_b must be a constant, ie.

$$\frac{q}{e_b} = \frac{\epsilon_1}{\alpha_1} = \frac{\epsilon_2}{\alpha_2}$$

Since this must also apply to a blackbody, which has $\epsilon = \alpha = 1$, the ratio of ϵ/α for any body in thermal equilibrium must be equal to unity, ie. for conditions of thermal equilibrium:

$$\epsilon = \alpha \quad \text{Eq. 40.}$$

It must be noted that α is not a property, and since this equation was developed for conditions of thermal equilibrium, it may not be valid if the incident radiation comes from a source at a different temperature.

Equation 40 may be extended for all conditions including conditions other than thermal equilibrium as follows:

$$\alpha_\lambda (\beta, \varphi) = \epsilon_\lambda (\beta, \varphi) \quad \text{Eq. 41.}$$

this is the most general form of Kirchhoff's law⁽²¹²⁾.

5.4.4: Reflectivity.

When radiant energy intercepts a surface, some of the radiation reflects back and the rest passes through the surface.

When considering reflection of a beam of radiation from a surface, two limiting spatial distributions exist. The first is specular reflection which is identical to reflection from a mirror, and the second is diffuse reflection which distributes the radiation uniformly in all directions. In actual practice reflection from a surface is neither specular nor diffuse, but is far more complex. In general, the magnitude of the reflected intensity in a particular direction for a given surface is a function of the wavelength, and the spatial distribution of the incident radiation.

5.4.4.1: Reflection function.

When a convergent energy flux of amount $I_{\lambda,i} \cos \beta_i \Delta \omega_i$ is incident on a surface with cone angle of $\Delta \omega_i$, from the direction of β_i, φ_i (Fig. 5.4) the intensity of the reflected energy in the direction β_r, φ_r is $I_{\lambda,r}(\beta_r, \varphi_r)$. The reflection function is used to express the intensity of reflected radiation in a particular direction as:

$$\rho_{\lambda}(\beta_r, \varphi_r, \beta_i, \varphi_i) = \frac{\pi I_{\lambda,r}(\beta_r, \varphi_r)}{I_{\lambda,i} \cos \beta_i \Delta \omega_i} \quad \text{Eq. 42.}$$

π is used so that the numerator looks like an energy flux. In the special case of a diffuse surface, the reflection function is a constant.

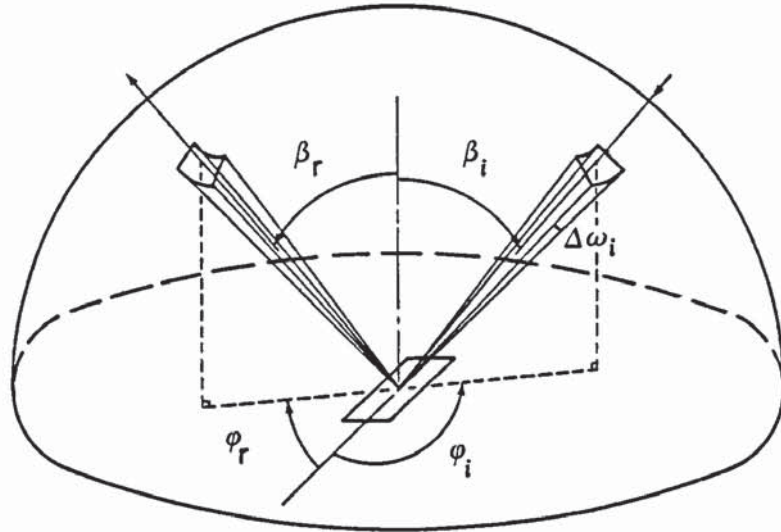


Fig. 5.4 : Spatial distribution of incident and reflected radiation on a mirror like surface.

5.4.4.2: Hemispherical reflectance.

Two types of hemispherical reflectances exist. The angular-hemispherical reflectance is found when a narrow convergent radiation beam is incident on a surface, and all the reflected radiation is collected; it is designated by $\rho(\beta_i, \phi_i)$. The hemispherical-angular reflectance results from collecting reflected radiation in a particular direction when the surface is irradiated from all directions, and is designated $\rho(\beta_r, \phi_r)$.

The monochromatic angular-hemispherical reflectance is

defined as the ratio of the monochromatic radiant energy reflected in all directions to the incident radiation flux within a small solid angle $\Delta \omega_i$. The hemispherically reflected incident energy can be found to be:

$$q_{\lambda,r} = \frac{1}{\pi} \int_{\beta=0}^{\pi/2} \int_{\varphi=0}^{2\pi} \rho_{\lambda}(\beta_r, \varphi_r, \beta_i, \varphi_i) I_{\lambda,i} \cos \beta_i \Delta \omega_i \cos \beta_r d\beta_r d\varphi_r$$

Eq. 43.

and therefore the monochromatic angular-hemispherical reflectance can be expressed as :

$$\begin{aligned} \rho_{\lambda}(\beta_i, \varphi_i) &= \frac{q_{\lambda,r}}{I_{\lambda,i} \cos \beta_i \Delta \omega_i} \\ &= \frac{1}{\pi} \int_{\beta=0}^{\pi/2} \int_{\varphi=0}^{2\pi} \rho_{\lambda}(\beta_r, \varphi_r, \beta_i, \varphi_i) \cos \beta_r d\beta_r d\varphi_r \end{aligned}$$

Eq. 44.

This equation also shows that $\rho_{\lambda}(\beta_i, \varphi_i)$ is a property of the surface.

The monochromatic hemispherical-angular reflectance is defined as the ratio of the reflected monochromatic intensity in the direction β_r, φ_r to the monochromatic energy from all directions divided by π (which then looks like an intensity). The incident energy can be written in terms of the incident intensity integrated

over a hemisphere:

$$q_{\lambda,i} = \int_{\beta=0}^{\pi/2} \int_{\varphi=0}^{2\pi} I_{\lambda,i} \cos \beta_i d\beta_i d\varphi_i$$

Eq. 45.

and the monochromatic hemispherical-angular reflectance is then :

$$\rho_{\lambda}(\beta_r, \varphi_r) = \frac{I_{\lambda,r}(\beta_r, \varphi_r)}{q_{\lambda,i}/\pi}$$

Eq. 46.

In terms of the reflectance function, this equation can be written as :

$$\rho_{\lambda}(\beta_r, \varphi_r) = \frac{\int_{\beta=0}^{\pi/2} \int_{\varphi=0}^{2\pi} \rho_{\lambda}(\beta_r, \varphi_r, \beta_i, \varphi_i) I_{\lambda,i} \cos \beta_i d\beta_i d\varphi_i}{\int_{\beta=0}^{\pi/2} \int_{\varphi=0}^{2\pi} I_{\lambda,i} \cos \beta_i d\beta_i d\varphi_i}$$

Eq. 47.

Since $\rho_{\lambda}(\beta_r, \varphi_r)$ is dependent upon the angular distribution of the incident intensity, it is not a surface property.

In the special case of diffuse incident radiation, the monochromatic hemispherical-angular reflectance is identical to the monochromatic angular-hemispherical reflectance. The equality of $\rho_{\lambda}(\beta_i, \varphi_i)$ and $\rho_{\lambda}(\beta_r, \varphi_r)$ when $I_{\lambda,i}$ is uniform is of great importance since the

measurement of $\rho_{\lambda}(\beta_r, \varphi_r)$ is much easier than $\rho_{\lambda}(\beta_i, \varphi_i)$.

Both $\rho_{\lambda}(\beta_i, \varphi_i)$ and $\rho_{\lambda}(\beta_r, \varphi_r)$ can be considered on a total basis by integration over all wavelengths. In the case of angular-hemispherical reflectance, it will be:

$$\begin{aligned} \rho(\beta_i, \varphi_i) &= \frac{\int_{\lambda=0}^{\infty} q_{\lambda,r} d\lambda}{\int_{\lambda=0}^{\infty} I_{\lambda,i} \cos \beta_i \Delta \omega_i d\lambda} \\ &= \frac{1}{\pi I_i} \int_{\beta=0}^{\pi/2} \int_{\varphi=0}^{2\pi} \int_{\lambda=0}^{\infty} \rho_{\lambda}(\beta_i, \varphi_i, \beta_r, \varphi_r) I_{\lambda,i} \cos \beta_r d\beta_r d\varphi_r d\lambda \end{aligned}$$

Eq. 48.

which unlike the monochromatic angular-hemispherical reflectance is not a property of the surface.

Monochromatic hemispherical reflectance is defined as:

$$\rho_{\lambda} = \frac{q_{\lambda,r}}{q_{\lambda,i}} \quad \text{Eq. 49.}$$

which is the characteristic of a case, when a surface element is irradiated from all directions and all the reflected radiation is collected. The reflected monochromatic energy ($q_{\lambda,r}$) can then be expressed in terms of the reflection function and the incident intensity as:

$$q_{\lambda,r} = \int_{\beta=0}^{\pi/2} \int_{\varphi=0}^{2\pi} \left[\int_{\beta=0}^{\pi/2} \int_{\varphi=0}^{2\pi} \frac{\rho_{\lambda}(\beta_r, \varphi_r, \beta_i, \varphi_i)}{\pi} I_{\lambda,i} \cos \beta_i d\beta_i d\varphi_i \right] \cos \beta_r d\beta_r d\varphi_r$$

Eq. 50.

The incident energy expressed in terms of the incident intensity is:

$$q_{\lambda,i} = \int_{\beta=0}^{\pi/2} \int_{\varphi=0}^{2\pi} I_{\lambda,i} \cos \beta_i d\beta_i d\varphi_i \quad \text{Eq. 51.}$$

By substituting the above quantities into equation 49 and integrating the resultant over all wavelengths the hemispherical reflectance can be calculated.

For simple engineering calculations, a special form of hemispherical reflectance can be used, subject to the assumption that the reflection function is independent of both direction (diffuse approximation) and wavelength (gray approximation).

Hereafter, for simplicity, the prefix hemispherical will be omitted, and whenever reflectance, emittance and absorptance are used, the presence of prefix hemispherical can be assumed, except where otherwise stated.

5.4.5: Relationship between absorptance, emittance and reflectance.

Consider a surface located in an isothermal enclosure maintained at temperature T . The monochromatic intensity in direction β, φ from an infinite small area of the surface consists of emitted and reflected radiation, and must be equal to $I_{b,\lambda}(T)$.

$$\begin{aligned} I_{b,\lambda} &= I_{\lambda}(\beta, \varphi) \Big|_{\text{emitted}} + I_{\lambda}(\beta, \varphi) \Big|_{\text{reflected}} \\ &= \epsilon_{\lambda}(\beta, \varphi) I_{b,\lambda} + \rho_{\lambda}(\beta, \varphi) I_{b,\lambda} \end{aligned}$$

Dividing both sides by $I_{b,\lambda}$ and rearranging gives:

$$\epsilon_{\lambda}(\beta, \varphi) = 1 - \rho_{\lambda}(\beta, \varphi)$$

and according to the Kirchhoff's law

$$\epsilon_{\lambda}(\beta, \varphi) = \alpha_{\lambda}(\beta, \varphi) = 1 - \rho_{\lambda}(\beta, \varphi)$$

Therefore if the monochromatic angular-hemispherical reflectance is known, all the emittance properties can be calculated, and also if the incident intensity is specified all the non-property absorptances can be calculated.

5.5: Selective surfaces.

An examination of solar collector energy balances shows the desirability of obtaining surfaces with the combination of high absorptance for solar radiation and low emittance for long-wave radiation. Such surfaces are called selective surfaces. The concept of a selective surface can be shown by consideration of a monochromatic reflectance as shown in Fig.5.5. This idealized surface is called a semi-gray surface since it can be considered gray in the wavelength range of up to $3\mu\text{m}$, and also gray but with different properties at wavelengths greater than $3\mu\text{m}$ in the solar spectrum (referring to Fig. 5.3 , it can be seen that the blackbody radiation at $T = 400^{\circ}\text{K}$ is very small at wavelengths smaller than $3\mu\text{m}$). For this ideal surface, the monochromatic reflectance is very low below a critical, or cut off wavelength (λ_c), and very high at wavelengths greater than λ_c . Consequently the

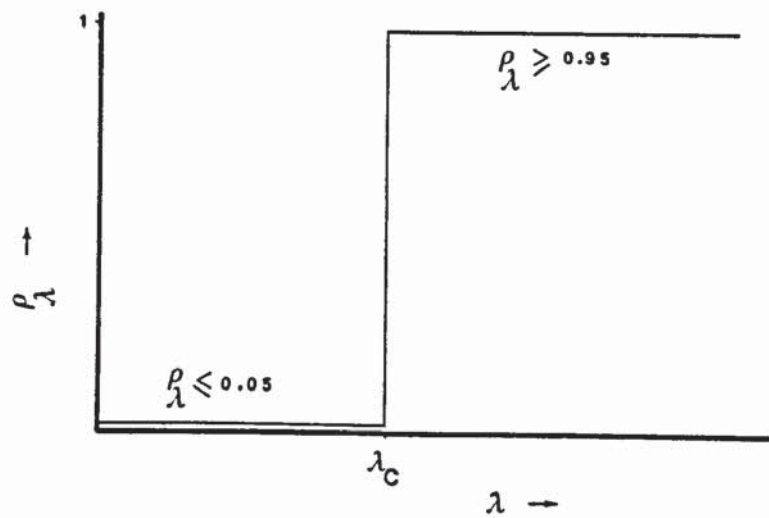


Fig.5.5 : The spectral reflectance of an ideal selective surface.

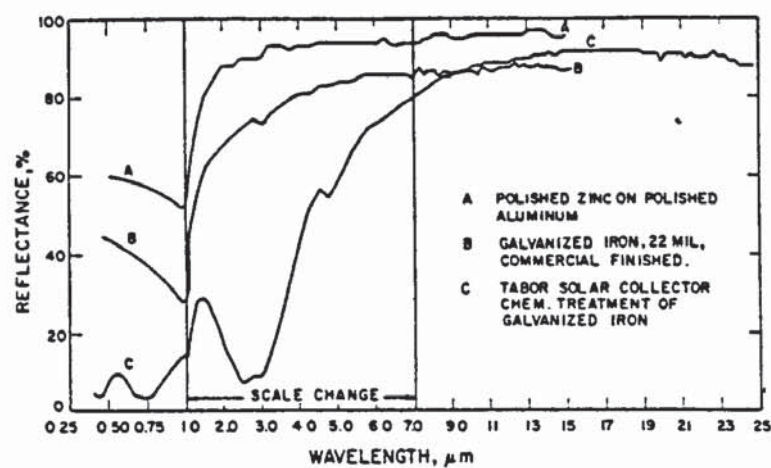


Fig. 5.6 : Spectral reflectances for several surfaces (213).

absorptance for solar energy will be very nearly $(1 - \rho_\lambda)$ for $\lambda < 3 \mu\text{m}$. In practice, the wavelength dependence of ρ_λ differs from the ideal curve of Fig. 5.5. Examples of ρ_λ versus λ for several real surfaces are shown in Fig. 5.6 (213).

As real selective surfaces do not have a well defined cut-off wavelength, nor uniform properties in the short and long wavelength ranges, values of emittance will be more sensitive to surface temperature than those of an ideal semi-gray surface. Therefore integration over the emitted spectrum is necessary to estimate the emittance, and over the solar spectrum to estimate solar absorptance.

The potential utility of selective surfaces in solar collectors has been discussed by Hottel and Woertz⁽²¹⁴⁾, Gier and Dunkle⁽²¹⁵⁾, and Tabor⁽²¹⁶⁻²¹⁸⁾. Metal oxide coatings on metal substrates which show desirable properties have been developed by Tabor⁽²¹⁸⁾, Hottel and Unger⁽²¹⁹⁾, and Kokropoulos et al⁽²²⁰⁾. Finely divided lead sulphide coatings were studied by Williams et al⁽²²¹⁾; the structure of these coatings significantly affected the selectivity.

Interference filters can be applied to low emittance substrates. The filters are formed by depositing alternate layers of metal and dielectric in quarter wavelength films for visible and near-infrared wavelengths. Martin and Bell⁽²²²⁾ have shown that a three layer coating of

$\text{SiO}_2\text{-Al-SiO}_2$ on Al can have a reflectance less than 0.10 for short-wavelengths and greater than 0.90 for long-wave radiation.

It has been suggested that the surface structure of metal, normally of high reflectance, can be designed to make the surface a good absorber of short-wave radiation. This is done by grooving or pitting the surface to create cavities of dimensions near the cut-off wavelength. The surface acts as an assembly of cavity absorbers for short wavelengths, but for long wave radiation, radiates as a flat surface. The degree of selectivity obtained by this technique has been limited⁽²⁰⁸⁾.

Surfaces of deep V-grooves, large compared with all wavelengths of radiation concerned, can be arranged so that radiation from near normal directions to the overall surface, will be reflected several times in the grooves, each time absorbing a fraction of the beam. This multiple absorption gives an increase in the solar absorptance, but also increases the long-wavelength emittance. However, Hollands⁽²²³⁾ has shown that a surface having nominal properties of $\alpha = 0.60$ and $\epsilon = 0.05$ used in a fixed optimally oriented flat-plate collector over a year, with 55° grooves, will have an average effective absorptance of 0.90 and emittance of 0.10.

PRODUCTION OF SOLAR SELECTIVE SURFACES.

6.1: Previous Work.

In solar collectors for thermal energy conversion, it is desirable to maximize the absorbed energy, while minimizing the energy lost by emission. An ordinary black surface will maximize the absorption of incident solar energy, but at the same time, it also maximizes the emissive losses. Surfaces can be manufactured having large absorptivity in the spectral region of short wavelengths around the peak in the spectrum of solar energy, yet small in the spectral region of longer wavelengths where peak emission occurs. Such surfaces are called "spectrally selective".

Metals have high infrared reflectivity; therefore one way of manufacturing a selective surface is coating a metallic substrate with a thin non-metallic layer. The essence of this method is that at long wavelengths the thin coating is essentially transparent and therefore the surface behaves as the un-coated metal. At short wavelengths, however, the radiation characteristics of the non-metallic layer will be dominant, yielding to overall high absorptivity at short wavelengths and low emissivity at long wavelengths. This method can be optimized by use of multiple layers, each having a maximum absorption peak complementary to the maximum

peak of the other layers. This method requires close control of the thickness produced and the right choice of coating materials. Different processes are used for the formation of non-metallic layers including electrochemical treatments⁽²²⁴⁾ and other oxide film formation processes^(215,219,220,225). A coating consisting of a transparent matrix with small metallic particles dispersed in it may also be used to provide spectral selectivity⁽²²⁶⁾. When the wavelength is smaller than the particle size absorption occurs, while at longer wavelengths the layer is transparent.

Another method is to use multiple reflection on an extended surface. Multiple reflection of incident radiation increases the absorption of energy such that the fraction of incident energy being absorbed after n reflection can be calculated as:

$$1-(1-\alpha)^n$$

where α is the absorptance. The type and extent of surface roughness determines the wavelengths absorbed. A metallic surface covered with spikes or needles about $1\text{ }\mu\text{m}$ apart can absorb a very large proportion of wavelengths up to $1\text{ }\mu\text{m}$, while the surface appears flat for longer wavelengths. Employment of a metal with high reflectivity for infrared wavelengths such as aluminium or copper can produce high short-wavelength absorptance and low long-wavelength emittance. In using this technique, great care should be taken to produce the optimum size, shape and distribution of spikes.

Chemical Vapour Deposition (C.V.D.) has been employed to produce such selective surfaces by depositing tungsten⁽²²⁷⁾ on a variety of substrates. Cuomo et al⁽²²⁷⁾ produced tungsten dendrites with spacings of around a micron. Their results proved the feasibility of this technique and later persuaded Grimmer et al⁽²²⁸⁾ to use $\text{Ni}(\text{CO})_4$ to form Ni dendrites on aluminium substrates. According to their results⁽²²⁸⁾, the absorptivity increased with increase in size of dendrites, until dendrite curving produced surface bridging. In fact these surface deformities first led to increased reflectivity in the visible region and eventually affected the emissivity in infrared region.

To produce a selective surface for solar energy applications, plasma assisted techniques have also been used. Uniformly etched copper sheets have been produced with planar⁽²²⁹⁾ and cylindrical⁽²³⁰⁾ magnetrons using sputtered titanium as seed material. These copper sheets exhibited solar absorptances as high as 0.94 and emittances as low as 0.13 at 300°K. Sputtering techniques have also been used to produce absorber coatings consisting of layers of stainless steel, copper and a composite metal-carbon layer^(231,232) deposited on glass tubes. These coatings were found to have a solar absorptance of 0.88 and emittance of 0.035 at 300°K.

Stainless steel coatings containing carbon are known to have selective spectral properties⁽²³³⁻²³⁵⁾ and have been reactively sputtered on the inside of glass tubes⁽²³⁶⁾.

Physical Vapour Deposition (P.V.D.) techniques could be used to produce extended surfaces giving multiple reflection and solar selectivity. The morphology of P.V.D. coatings has already been discussed in some detail above (Chapter 1, Section 5.3.6., page 32). The structures obtained depend on the deposition conditions, the technique, pressure, and the working gas used. The three types of structure produced in different working conditions were zoned by Movchan and Demchishin⁽⁹¹⁾ whose work was extended by Thornton^(237,238) by adding an extra axis on the zone diagram to account for the effect of the working gas (argon), with a transition zone T between zones 1 and 2. Thornton's diagram (Fig. 6.1) is based on examination of 25 to 250 μm thick coatings of Ti, Cr, Fe, Cu, Mo, and aluminium alloys deposited on metal and glass substrates at rates in the range of 50 to 20,000 $\text{\AA} \text{ min}^{-1}$ using cylindrical-post and hollow-cathode magnetron sputtering sources.

This classification was further studied by Craig and Harding⁽²³⁹⁾. Their investigations were carried out at temperatures ranging from 30-450°C, at pressures ranging from 0.5 to 100 Pa (4 to 750 mTorr), and with deposition rates of 0.5 $\mu\text{m} \text{ min}^{-1}$ using planar magnetron sputtered copper films. The 48 experimentally obtained results led to a modified version of Thornton's diagram (Fig. 6.2).

Although zone I crystals tend to align in the direction of the coating flux vector^(91, 240-243), oblique

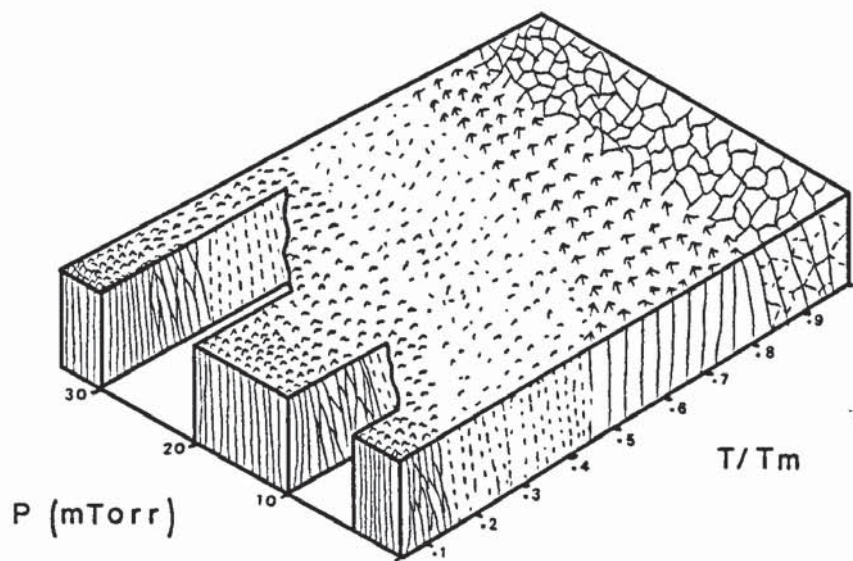


Fig. 6.1 : Thornton's diagram (237,238) showing zones of pressure and temperatures producing different types of structures.

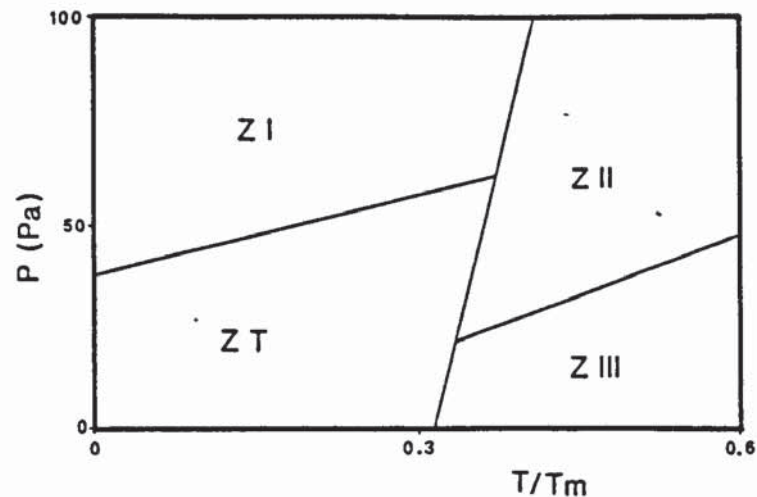


Fig. 6.2: Thornton's diagram modified by Craig and Harding⁽²³⁹⁾ showing zones of pressure and temperature producing different types of structures. (Re-drawn with axes reversed).

deposition and substrate surface roughness are complementary in producing shadow induced zone I⁽²⁴⁴⁾ structures. Also at low T/T_m as the working gas pressure increases, intergrain boundaries become more open^(237,245) which bring the structure formed in zone T, into zone I.

Work done by Bland, Kominiak and Mattox⁽⁸⁹⁾ suggest that ion bombardment during deposition may suppress zone I structure by creating more nucleation sites or by eroding surface roughness peaks. Thornton investigated bias-sputter-deposited copper at low T/T_m ⁽⁹⁴⁾ and found that suppression of open boundaries required an ion bombardment flux adequate to back-sputter about 30-60% of the incident coating flux. This fraction increased with the magnitude of the substrate surface roughness. Therefore it is believed that the mechanism is basically a sputter-induced re-distribution of coating material.

Although Thornton's diagram predicts denser coatings with columnar growth in zone II, under high surface diffusion conditions it is also possible to have platelets and needles grown from the substrate. These platelets and needles tend to stand upright and form a porous layer⁽²⁴⁶⁾. Faceted and platelet structures of evaporated Zn are produced at T/T_m of 0.5 and 0.6 respectively⁽²⁴⁷⁾. Needle growth is observed in evaporated Ti and T/T_m of about 0.6, and Be at T/T_m of about 0.7⁽²⁴⁸⁾.

Summarising the above section, it has been shown how a

rough surface can be produced and how it can be used for selective absorption in the thermal conversion of solar energy.

The aim of present work has been to study selective surfaces produced by ion plating.

Stainless steel was chosen for the substrate because of its good corrosion resistance and good reflectivity. Copper, aluminium, and nickel were chosen as coating materials. The reason for this choice was that these metals have reasonably high reflectivity, especially at infrared wavelengths. Table 6.1 gives a comparison of the percentage reflectance of freshly evaporated mirror coating of aluminium, copper, with that of silver and gold. The same information is presented graphically in Fig.6.3.

6.2: The proposed experimental work.

As discussed in the previous section, ion plating a rough substrate at a high gas pressure results in type zone I to zone II coating structures, depending upon T/T_m values. As a first step it was decided to investigate the effect of ion bombardment on surface roughness. This investigation was designed to provide information about the ion bombardment duration, pressure, and voltage bias required to produce a minimum desirable roughness. It would also provide information about the surface temperature of the specimen.

λ (μm)	Au	Ag	Al	Cu
.220	27.5	28.0	91.5	40.4
.240	31.6	29.5	91.9	39.0
.260	35.6	29.2	92.2	35.6
.280	37.8	25.2	92.3	33.0
.300	37.7	17.6	92.3	33.6
.315	37.3	5.5	92.4	35.5
.320	37.1	8.9	92.4	36.3
.340	36.1	72.9	92.5	38.5
.360	36.3	88.2	92.5	41.5
.380	37.8	92.8	92.5	44.5
.400	38.7	94.8	92.4	47.5
.450	38.7	96.6	92.2	55.2
.500	47.7	97.7	91.8	60.0
.550	81.7	97.9	91.5	66.9
.600	91.9	98.1	91.1	93.3
.650	95.5	98.3	90.3	96.6
.700	97.0	98.5	89.9	97.5
.750	97.4	98.6	88.0	97.9
.800	97.7	98.6	86.3	98.1
.850	97.8	98.7	86.0	98.3
.900	98.0	98.7	89.0	98.4
.950	98.1	98.8	91.8	98.4
1.0	98.2	98.9	94.0	98.5
1.5	98.2	98.9	96.8	98.5
2.0	98.3	98.9	97.2	98.6
3.0	98.4	98.9	98.0	98.6
4.0	98.5	98.9	98.2	98.7
5.0	98.6	98.9	98.4	98.7
6.0	98.6	98.9	98.5	98.7
7.0	98.7	98.9	98.6	98.7
8.0	98.8	98.9	98.7	98.8
9.0	98.9	98.9	98.7	98.8
10.0	98.9	98.9	98.7	98.9
15.0	99.0	99.0	98.9	99.0
20.0	99.0	99.2	99.0	99.2
30.0	99.0		99.2	
40.0	99.1			

Table 6.1: Percent reflectance at normal incidence of freshly evaporated mirror coatings. (227)

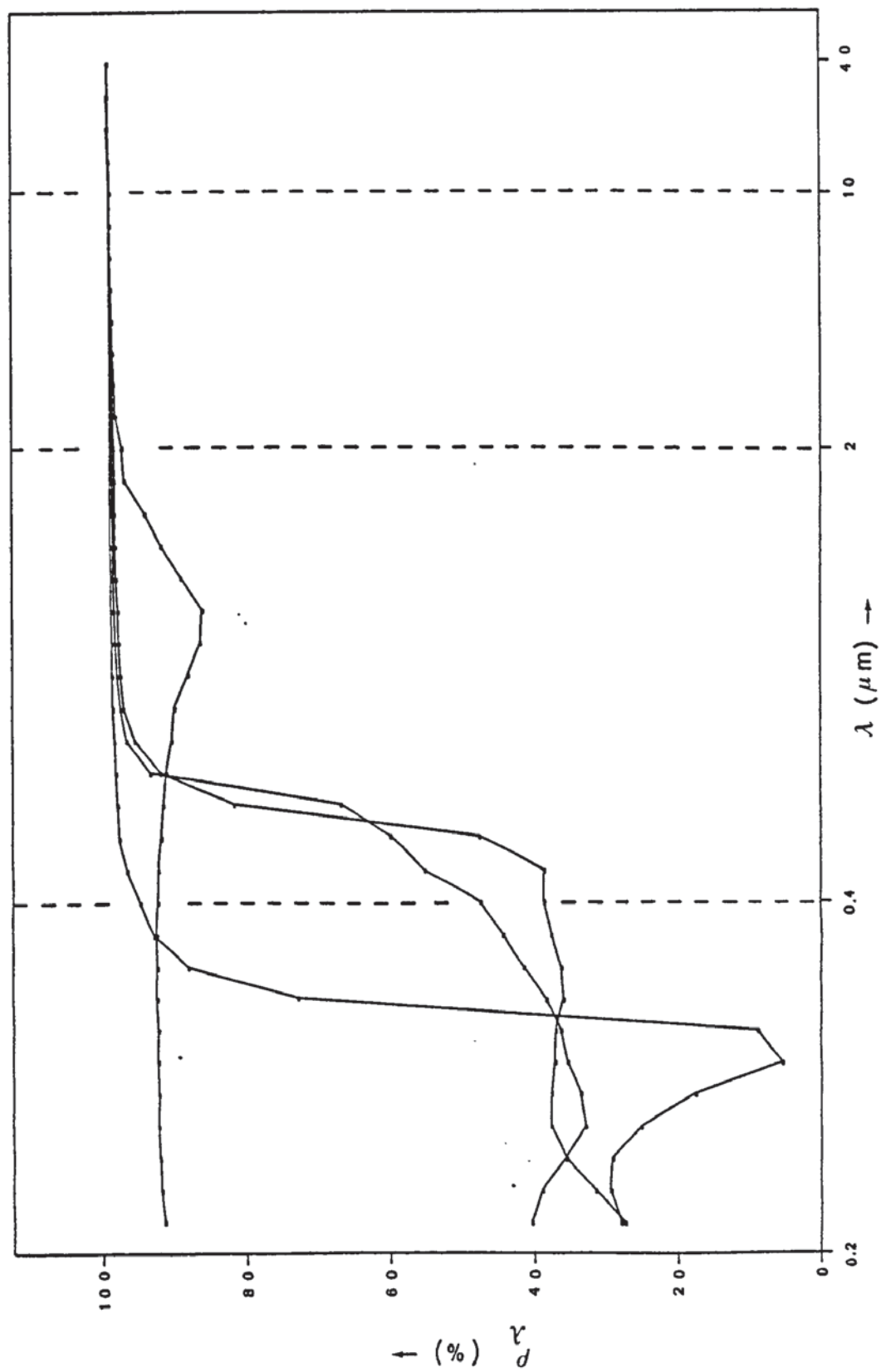


Fig.6.3: Reflectance of freshly evaporated mirror coatings of Al, Cu, Ag and Au.

A second step would be coating of this surface and the finding of those conditions which optimized the desired optical properties of specimens. The applicability to this work of theories based on results from other techniques of evaporation could then be tested. The validity of temperature measurements in the previous step (sputter etching) could also be assessed in the light of the structures obtained.

6.3: Experimental procedure

6.3.1: Materials.

6.3.1.1: Specimens.

Unless otherwise stated, specimens were made of 1 mm thick bright annealed type 302 stainless steel which was supplied by the BSC. The steel, according to the supplier, had the following nominal composition:

18.33% Cr, 8.65% Ni, 0.35% Si, 1.47% Mn, 0.011% S, 0.023% P, and 0.05% C.

6.3.1.2: Coating material.

Vacuum casted oxygen free high conductivity copper with a purity better than 99.99% was supplied by IMI. A rod of 37 mm in diameter and 22 cm long was made from the copper and was used to feed the water cooled crucible of the ion plater.

6.3.2: Specimen preparation

5 x 10 cm specimens were cut from the 1 mm thick bright

annealed stainless steel sheet. All specimens were washed with detergent to remove oil and grease, dried and then stored in a box in a dry room until used. Specimens were washed with warm water and then isopropyl alcohol, and hot air dried just before use.

6.3.3: Jigging:

Two jigs were used for holding specimens during ion bombardment in the vacuum chamber. The first jig had an earthed shield designed to minimize the current carried by the jig, so that the ion bombardment current of the specimen could be measured. This jig proved to be unsuccessful because it did not prevent the undesirable edge effects.

The second jig was designed to overcome the edge effects, and also to minimize heat loss from the specimen through conduction. This jig was constructed of stainless steel tube formed into a closed loop around the specimen and coming into contact with it at the four corners. Specimens were mounted on the jig by means of four small locating sites machined into the wall thickness of the tube at the inner corners of the loop so that the specimen could rest on them.

Details of both jigs are presented in Appendix A.

6.3.4: Measurements.

6.3.4.1: Pressure.

Pressure was measured by gauges mounted on the 24" chamber diameter ion plating rig. These were ion gauges calibrated against a standard gauge to provide correct readings within the required ranges, i.e. 10^{-2} Torr for the top, and 10^{-5} Torr for the bottom chamber. The pressure of the working gas was set by means of an Edwards LB 2B needle valve, and assumed to be constant if no detectable change was observed on the meter for five minutes prior to the start of any experiment. While experiments proceeded changes in pressure were ignored as these were mainly caused by thermal expansion of the gas, due to the glow discharge.

6.3.4.2: Current.

Current was indicated by a meter with a full scale deflection equivalent to 500 mA. A three position range switch was used to expand the full scale reading to 250 and 100 mA. A chart recorder was used to record the changes in current.

6.3.4.3: Voltage:

Applied bias voltages were set by means of a Variac sliding contact resistor on the primary side of the power supply. The change in voltage during an experiment was negligible, and therefore the voltage was assumed to be constant during each test.

6.3.4.4: Total energy input.

The energy input was calculated by taking the average cathode current at 30 second intervals and multiplying it by the applied voltage. The sum of these values for the total duration of the glow discharge gives the total energy input to the cathode in joules.

6.3.4.5: Temperature.

Temperature was measured by a shielded Ni/Cr v Ni/Al thermocouple, mounted in a specially designed holder. To reduce the response time of the thermocouple, the tip of the earthed shield was removed so that about 0.5 cm of the thermocouple wires were exposed. These wires were spot welded together. The thermocouple was placed in a stainless steel tube which could be lowered by tilting one end through a gear mechanism and a rotary feed-through, from outside the chamber. As the tube moved down from its original horizontal position, the thermocouple moved out of it. They were arranged in such a way that when the thermocouple was lowered, it would touch the middle of the specimen.

While the tube was horizontal the thermocouple was well inside and thus protected from sputtered and evaporated material. Details and diagrams of the thermocouple holder are given in Appendix A.

The above mentioned thermocouple was used for all specimen temperature measurements. A 10 channel Eurotherm digital

indicator was used for temperature readings.

6.3.4.6: Roughness.

No measurement of the surface roughness was made using stylus type instruments such as the Talysurf. For a realistic indication of surface roughness, Scanning Electron Micrographs were obtained at magnification up to 10,000 X. These S.E.M. photomicrographs showed the extent of surface roughness and also the shapes and distribution of protruberances.

6.3.4.7: Weight.

Specimens were weighed in a Releas-O-Matic Oertling balance having an accuracy of 0.2 mg per smallest division.

6.3.4.8: Average thickness of removed material.

The average thickness of removed material from the surface of specimens was calculated as follows:

$$\text{specimen area} = A = \frac{W_o}{\rho \times 0.1} \times 2 = 20 \frac{W_o}{\rho} \text{ cm}^2$$

$$\text{removed volume} = v = \frac{W_L}{\rho} = A \times \text{removed thickness (d)} \text{ cm}^3$$

$$\text{and therefore: } d = v/A = \frac{W_L}{20W_o} \text{ cm}$$

$$\text{or: } d = 500 \times \frac{W_L}{W_o} \text{ } \mu\text{m}$$

where W_o is the original weight in g,

W_L is the weight loss in g,

ρ is density in g/cm³.

Assuming that the measured time was accurate up to 1 second, an approximation of the vigour of sputtering was obtained by dividing the removed thickness by the sputtering duration (t), i.e:

$$\text{material removed per second} = 5 \times 10^6 \times \frac{W_L}{W_o \times t} \quad \text{\AA/s}$$

These two values are reasonable approximations, since even if the time measurement accuracy were ± 60 seconds, the maximum errors introduced into the calculations would be +7% and -6%. There is another error which arises from the area under the jaws of the jig (if jig number 1 is used) and also the surface area on the thickness of specimens. This leads to an error of less than 1% in the calculation of the total area of specimen, subjected to the ion bombardment.

6.3.4.9: Coating thickness measurement.

The average thickness of the coating was measured by dividing the weight change of a specimen by the surface area and the bulk density of the coating materials.

Results obtained by this method were assessed by examining the cross sections of the same specimens, and found to be in close agreement.

6.3.4.10: Solar absorptivity measurements.

A 100x50x1 mm bright annealed 304 stainless steel specimen "mirror polished" on one side, was held in the jig number 1 and subjected to glow discharge at 30 mTorr pressure and

4KV voltage, for 45 minutes. The steel was supplied by the BSC and according to the supplier had the following nominal composition:

18.4% Cr, 8.5% Ni, 1.5% Mn, 0.32% Si, 0.025% S, and 0.042% C.

Spectral reflectance of these surfaces before and after ion bombardment were measured in the range of 300 to 1850 nm, corresponding to the visible region of the solar spectrum, using a Perkin-Elmer spectrophotometer at the Solar Energy Unit, University College, Cardiff. The optical sphere of the spectrophotometer was painted white with a BaSO₄ paint, to which all the measurements were therefore relative. The absolute reflectance values of the BaSO₄ paint are given by Grum and Luckey⁽²⁵¹⁾ and are presented in Fig. 6.5. To calculate the absolute reflectivity of the surfaces, the measured values must be multiplied by the absolute reflectance of the BaSO₄ paint at each wavelength, and divided by the value of the base line.

The solar absorptivity of the surfaces was calculated as:

$$\alpha_s = \frac{\int_{\lambda_1}^{\lambda_2} \alpha_{\lambda} G_{\lambda} d\lambda}{\int_{\lambda_1}^{\lambda_2} G_{\lambda} d\lambda}$$

or:

$$\alpha_s = \frac{\sum_{i=1}^n \alpha_{\lambda_i} G_{\lambda_i} d\lambda_i}{\sum_{i=1}^n G_{\lambda_i} d\lambda_i}$$

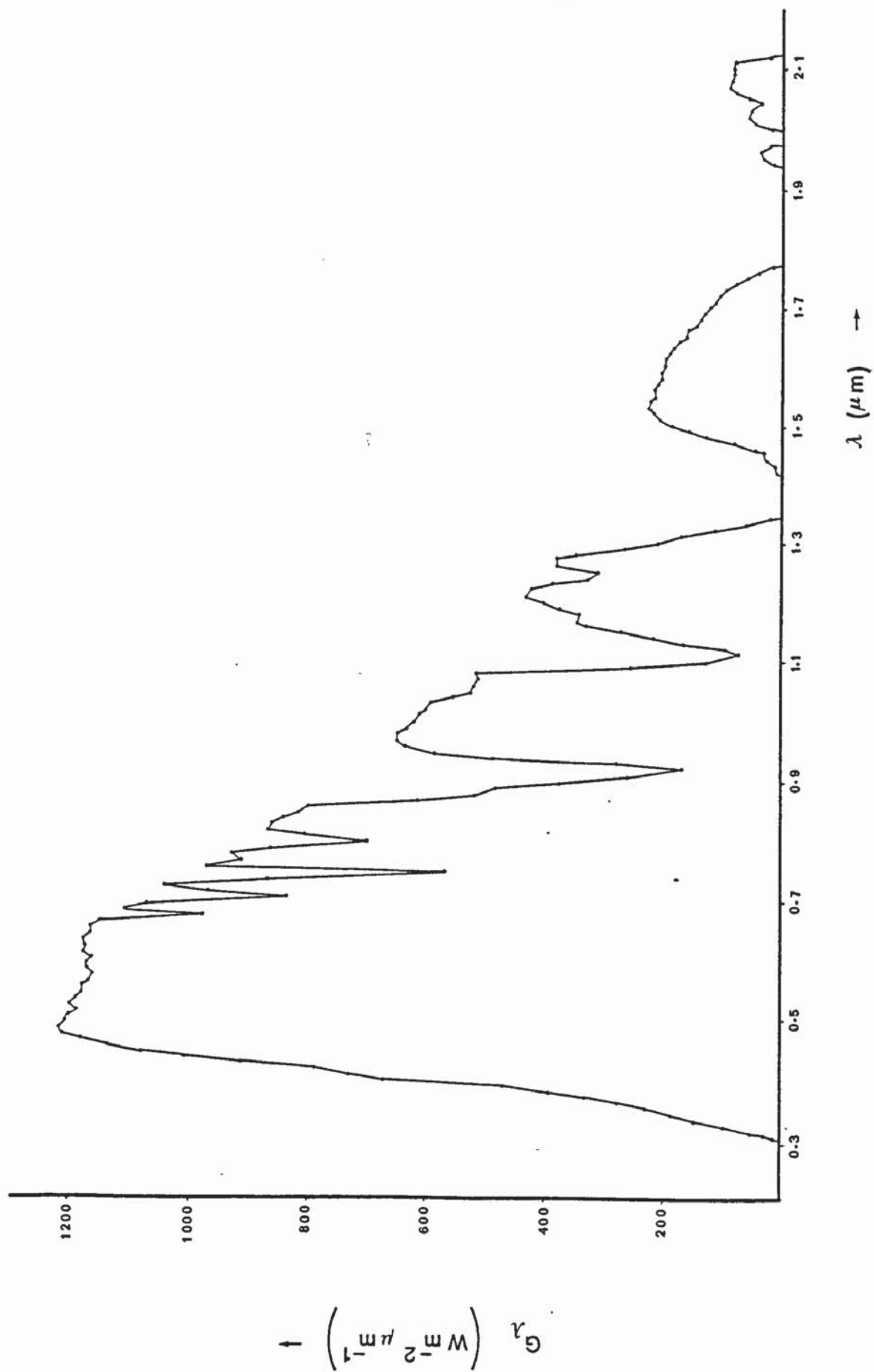


Fig.6.4: Solar irradiation at sea level with surface perpendicular to sun's ray,
air mass = 2

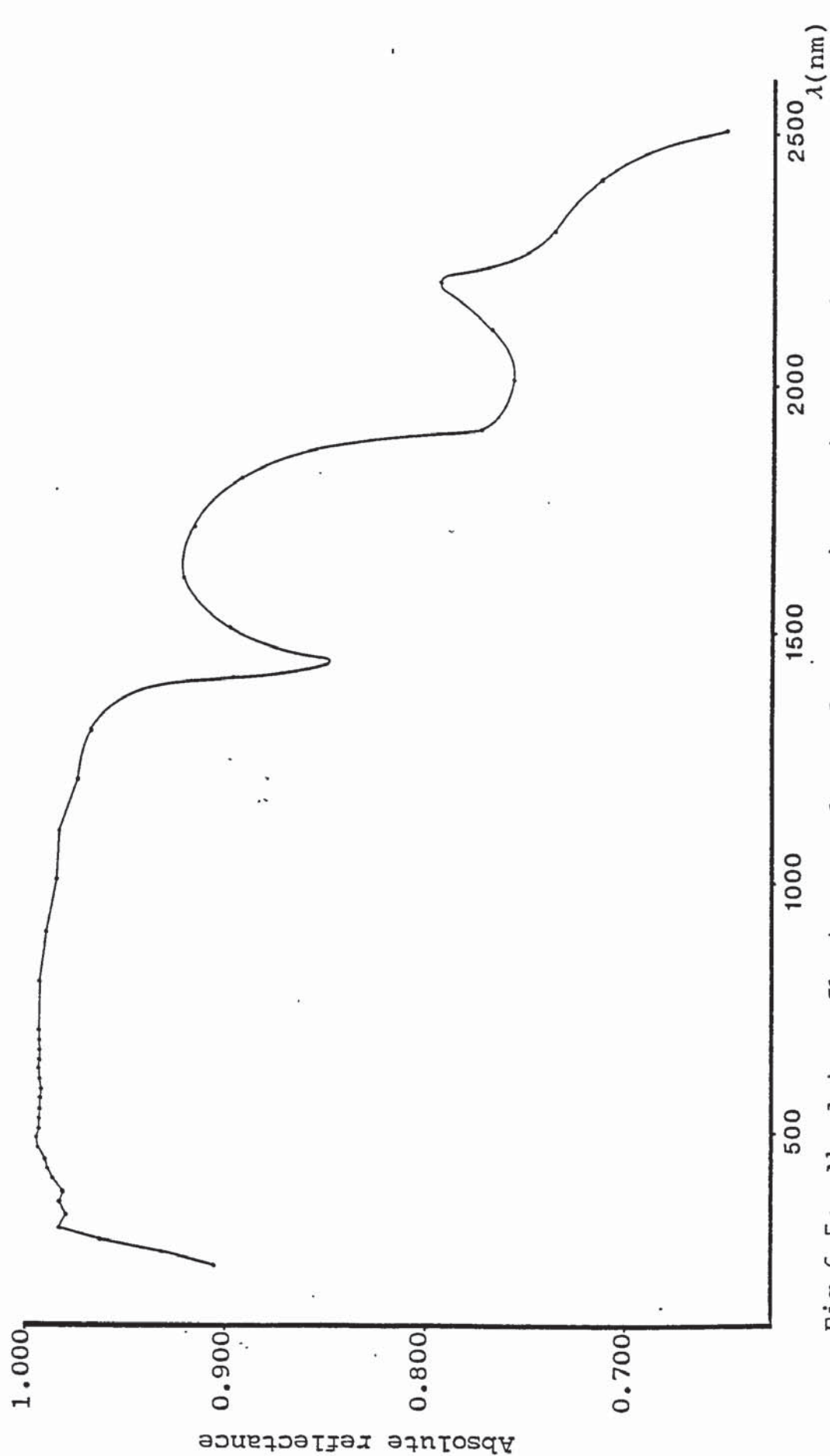


Fig.6.5: Absolute reflectance values of BaSO_4 paint. Points obtained from numerical data obtained by Grum & Luckey (251). Points joined graphically.

where G_λ is the solar irradiance at wavelength λ .

For opaque materials, $\tau = 0$, and therefore:

$$\alpha_\lambda = 1 - \rho_\lambda$$

Data for G_λ are published by various authors, and the values published by Moon⁽²⁴⁹⁾ are commonly used as standard. Fig.6.4 represents Moon's data for solar irradiation at sea level with surface perpendicular to the sun's rays, and air mass of 2. There are two methods of simplifying the calculations: Selected Ordinates and Weighted Ordinates. In the Selected Ordinates method, the desired waveband is divided into smaller bands so that each contains the same amount of solar irradiance and presented by its mid-band wavelength. In visible region of the solar spectrum 20 wavebands with corresponding mid-wavelengths are recommended⁽²⁵⁰⁾ as follows:

390, 444, 481, 510, 543, 574, 606, 639, 669, 705, 745, 786, 831, 877, 959, 1026, 1105, 1228, 1497 and 1722 nm.

In the Weighted Ordinates method, the desired waveband is divided into equally sized smaller wavebands. The amount of energy in each band is represented as a percentage of the total energy in the desired waveband. In this work, wavebands and the relative energies were obtained from ASTM E424-71.

6.3.4.11: Infrared Emissivity measurement.

The infrared specular reflectivity was measured in the range of 2.5 to 50 μm wavelengths by a double beam Perkin-Elmer I.R. Spectrophotometer against a standard mirror polished aluminium piece. The base line of the infrared

chart was obtained by using two standard mirrors on both beams, and therefore one expected the line to be straight. Thus any deviation from a straight line was an instrumental effect, and had to be taken into consideration when calculating reflectivity. In order to calculate the infrared reflectivity, the measured values were divided by the percentage reflectivity of the base line at each wavelength. Then, by Kirchhoff's law, the emissivity was calculated as:

$$\epsilon_{\lambda} = \alpha_{\lambda} = 1 - \rho_{\lambda}$$

6.3.4.12: Thermal emittance measurement using cooling curves.

Twelve specimens were fixed on jig number 2, and were sputter etched at 20 and 30 mTorr pressures, and 3 and 4 KV applied voltages. After the glow discharge was extinguished by dropping the applied voltage to zero, the temperature of the specimens was measured with the mobile thermocouple and readings were taken at 15 second intervals. Originally, the temperature rose to a maximum, and then started dropping. This drop in temperature was monitored up to approximately 17 minutes after the extinction of the glow discharge. The data of the last 10 minutes of each cooling curve was used to calculate the emittance within each interval, and then averaged to find the mean emittance in that temperature range.

As a heated specimen cools down in a vacuum, its heat losses are mainly by conduction and radiation. Due to the fact that the contact area between a specimen and the jig were very small, the heat losses due to conduction were

considered negligible. Therefore, the cooling of the specimen could be represented as:

$$-\frac{dT_s}{dt} (m C_p) = A_s \sigma \epsilon (T_s^4 - T_c^4)$$

where m is the mass of the specimen, and C_p is its specific heat.

Assuming T_c is constant, the equation can be solved for t as (252);

$$t = \frac{m C_p}{2A_s \sigma \epsilon T_c^3} \left[\frac{1}{2} \ln \left(\frac{T_s/T_c + 1}{T_s/T_c - 1} \right) + \tan^{-1} (T_s/T_c) \right] + C$$

Cooling curves can be used to obtain the emittance of specimens at a certain temperature in the vacuum⁽²⁵³⁾.

Taking the specimen temperature as T_1 and T_2 at the beginning and the end of a short period of time respectively, the average emittance of the specimen between the two temperatures was calculated as follows:

$$t_1 = \frac{m C_p}{2A_s \sigma \epsilon_1 T_c^3} \left[\frac{1}{2} \ln \left(\frac{T_1/T_c + 1}{T_1/T_c - 1} \right) + \tan^{-1} (T_1/T_c) \right] + C$$

$$t_2 = \frac{m C_p}{2A_s \sigma \epsilon_2 T_c^3} \left[\frac{1}{2} \ln \left(\frac{T_2/T_c + 1}{T_2/T_c - 1} \right) + \tan^{-1} (T_2/T_c) \right] + C$$

$$t_2 - t_1 = \frac{m C_p}{2A_s \sigma \bar{\epsilon} T_c^3} \left\{ \frac{1}{2} \left[\ln \left(\frac{T_2/T_c + 1}{T_2/T_c - 1} \right) - \ln \left(\frac{T_1/T_c + 1}{T_1/T_c - 1} \right) \right] + \tan^{-1} (T_2/T_c) - \tan^{-1} (T_1/T_c) \right\}$$

$$\bar{\epsilon} = \frac{m C_p}{2A_s \sigma (t_2 - t_1) T_c^3} \left\{ \frac{1}{2} \left[\ln \left(\frac{T_2/T_c + 1}{T_2/T_c - 1} \right) - \ln \left(\frac{T_1/T_c + 1}{T_1/T_c - 1} \right) \right] + \tan^{-1}(T_2/T_c) - \tan^{-1}(T_1/T_c) \right\}$$

The calculation of emittance has been based on the assumption that the temperature measurements have been accurate; in addition, the temperature range has been small enough to justify the assumption that the emittance has remained constant. To satisfy the latter condition, temperature ranges of less than 100°C were chosen, and the maximum starting temperature was 218°C which coincides with the upper boundary of the temperature range over which a selective surface might be used.

6.3.5: Effect of background pressure.

In order to investigate the effect of background pressure, nine specimens were ion bombarded at 30 mTorr argon pressure and 5KV applied voltage for 30 minutes. A background pressure of approximately 10^{-5} Torr was observed for four specimens; for the other five, a value of much less than 10^{-5} was maintained. It must be emphasized that no figure can be given for pressures below 10^{-5} Torr, as it was the lowest pressure which could be directly read on the meter.

6.3.6: Deposition of copper.

Two sets of experiments were carried out to find the right conditions for reproducible deposition rates.

Specimens were mounted on jig number 2 at a fixed position above the crucible which was fed by a 37 mm diameter copper rod.

In the first set of experiments, 10KV was chosen as the acceleration voltage with 0.7 A as the beam current. The melt level was kept at position A as shown in Fig.6.6, which gave a 33.5 cm source to specimen distance.

The second set of experiments were carried out with the melt level at position B of Fig.6.6, which gave a source to specimen distance of 35.6 cm. In this set of experiments, four levels of beam currents were tried, viz 0.6, 0.7, 0.8 and 0.9 A at 10KV acceleration voltage.

In both sets of experiments, the LATERAL SWEEP AMPLITUDE knob was set at zero, which corresponded to a beam width of about 1.5 cm on the source; the LONGITUDINAL SWEEP AMPLITUDE knob was set at 2, which corresponded to a scan range of about 2 cm. In order to maintain constant conditions, SWEEP FREQUENCY was kept at 5.

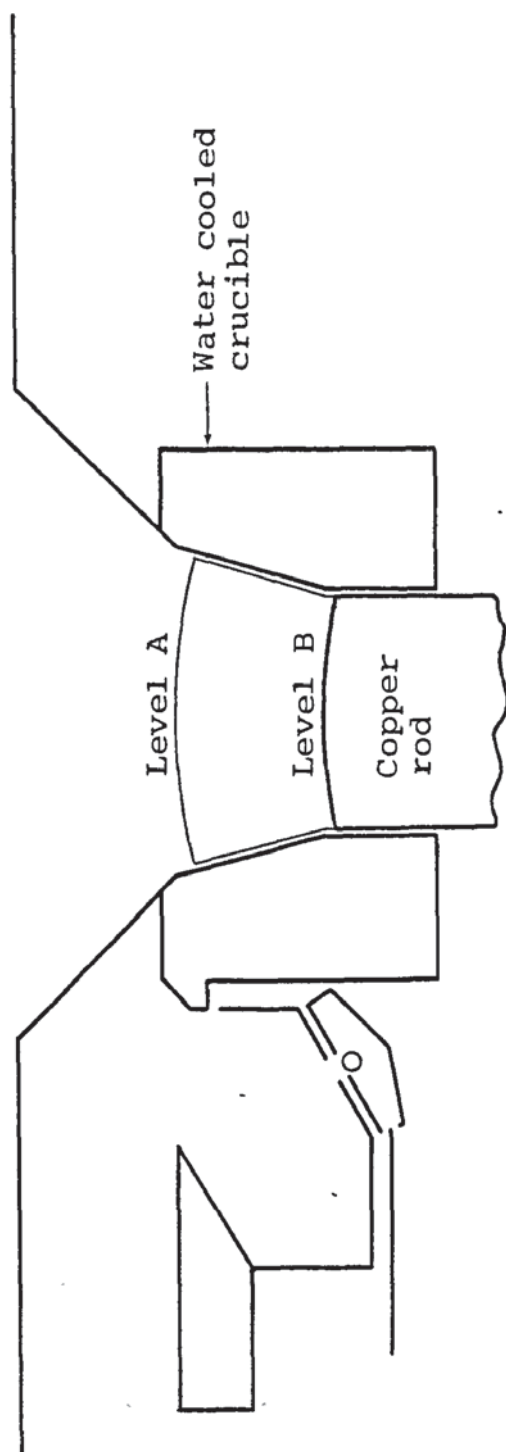


Fig.6.6.6: Positions of the melt level, relative to the electron beam gun assembly and the crucible

Details of the ion plating equipment.

The ion plating equipment was supplied by Electrotech Equipments Limited. It consists of two vacuum systems, a glow discharge unit, an electron beam gun, and a rod fed crucible.

7.1: The vacuum systems.

There are two vacuum chambers; each has its own pumping system which can be operated from the control panel either manually or automatically. If the system is being operated in the automatic mode, there are interconnections between the two control units as explained later in this chapter. A block diagram of the vacuum systems is illustrated in Fig.7.1.

7.1.1: The top vacuum chamber.

The top chamber houses the specimen and consists of a cylinder with internal dimensions 24" in diameter and 24" high. It is pumped by an Alcatel rotary pump and a 16" diffusion pump. The oil backstreaming from this pump is minimized by use of a water cooled copper chevron baffle, a liquid nitrogen cooled cold plate and a water cooled high vacuum valve. The pumping speed of this pump is rated at 5500 l s^{-1} ; the pumping speed of the rotary pump is $50 \text{ m}^3 \text{ h}^{-1}$. Access to the top chamber is via a semi-cylindrical door which acts as half of the chamber. The body of this chamber is water cooled (door, wall,

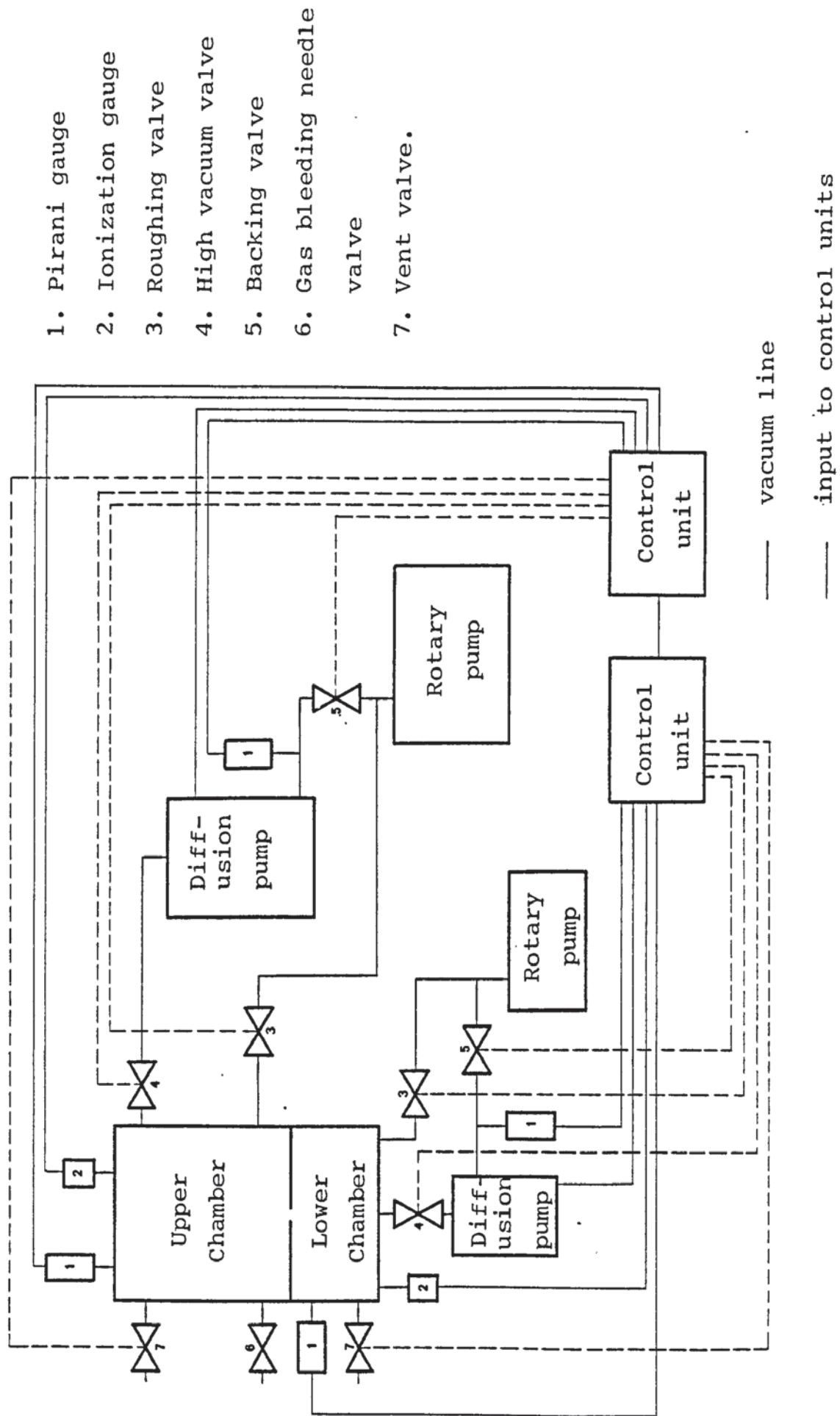


Fig.7.1: Block diagram of the ion plater.

and flanges). Its inner walls are shielded by stainless steel foil to help cleaning.

7.1.2: The bottom chamber.

The bottom chamber is located immediately beneath the top chamber and houses the electron beam gun, crucible, and the rod feed system. This cylindrical chamber is 24" in diameter and 12" high. It is pumped by an Alcotel rotary pump, and a 10.5" diffusion pump. The oil back-streaming from this pump is minimized by use of a liquid nitrogen trap. The pumping speed of the diffusion pump is rated at 3000 l s^{-1} , and of the rotary pump $32 \text{ m}^3 \text{ h}^{-1}$. Access to this chamber is via a 24" diameter $\frac{1}{4}$ " thick stainless steel plate which acts as partition between the two chambers.

All the valves are pneumatic except the vent valves which are solenoid operated.

In both systems, foreline and chamber pressures are measured by Edwards Pirani and ionization gauges.

7.1.3: Control panels.

Each chamber has its own control panel. These panels are identical, except for the high vacuum range on the ion gauges. On each panel, there are two ON/OFF push buttons for the rotary and diffusion pumps, a diagram to illustrate the vacuum system having ON/OFF push buttons at the position of valves, a meter for pressure readings,

and a knob to select one or the other foreline pressure gauge, or the chamber Pirani gauge, or the range for the ion gauge. Also there is a knob to choose the mode of operation (i.e. manual or automatic), and another knob to be used in the automatic mode for pumping, venting, or standby. All the push buttons are illuminated in the ON position. These control panels are shown in Fig.7.2.

7.1.4: Operation.

When the automatic mode of operation is used, by turning the operation knob from STANDBY to PUMP position, roughing of the corresponding chamber starts, providing the other chamber is not in the VENT position. At this stage the foreline valve closes and the roughing valve opens. When the chamber pressure drops to about 3×10^{-2} Torr, the roughing valve closes, the foreline valve opens, and then the high vacuum valve opens. If both chambers are on AUTOMATIC operation and one of them is venting then the other chamber's high vacuum valve will not open, and vice-versa. This dependency does not apply to MANUAL operation.

On MANUAL operation, push buttons operate the valves. In this mode there is no interlock between valves and it is possible to operate them independently.

The ion gauge meter covers a range from 10^{-2} to 10^{-5} Torr for the top chamber, and 10^{-4} to 10^{-7} Torr for the bottom chamber.

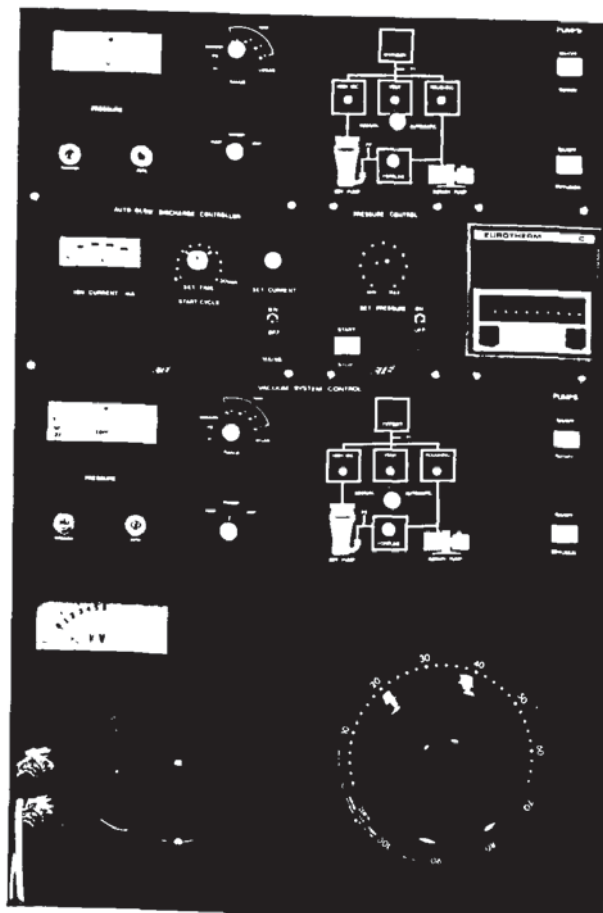


Fig.7.2: Vacuum systems and glow discharge control panels.

On the range knob there are two extra positions which are marked EMISSION and DEGASSING. The Emission position is to set the voltage of the filament of the ion gauge at the appropriate reading for the required pressure by means of a variable potentiometer on the panel. The DEGASSING position is to degas the grid of the ion gauge by increasing its temperature to about 900°C.

7.2: The glow discharge unit.

The glow discharge unit consists of a power supply capable of providing 500 mA at 3 KV, a solenoid gas bleeding valve, and a control unit.

7.2.1: The control panel.

Incorporated in the control panel is an ON/OFF switch (illuminated when in the ON position), an ammeter, a timer switch (permitting a maximum of 30 minutes) with a start push button which flashes repeatedly when the timer is ON, and a control knob to set the current. This control panel is shown in Fig.7.2.

7.2.2: Operation.

After switching the unit on with the timer set for the required duration, the process can be started by pressing the push button. This closes the high vacuum valve of the top chamber, switches on the power supply, and introduces the working gas into the chamber via the gas bleeding valve. At this stage the high vacuum valve will partially open to continue the pumping. Then by turning



Fig.7.3: Electron beam gun and rod feed control panels, and the ANAVAC-2 massspectrometer.

the SET CURRENT knob the current can be adjusted to give the required reading on the meter. This controls the gas pressure, in order to maintain the set current. When the timer trips off, it will disconnect the power supply and fully open the high vacuum valve.

7.3: The rod fed crucible.

The water cooled crucible is located at the top of the bottom chamber just under the partition plate. There is a hole at the bottom of the crucible for access of the rod of coating material. An electric motor feeds the rod into the crucible and maintains the level of the melt during evaporation. A second electric motor rotates the rod to improve the uniformity of the melt. Both electric motors have identical controls consisting of illuminated ON/OFF switches, three position movement switches (forward / standby / reverse), and variable potentiometers to control the speed. Control units of the rod fed crucible are shown in Fig.7.3.

7.4: The Electron Beam Gun (E.B.G.).

The E.B.G. unit contains the E.B.G. assembly, power supply, and controls. The power supply is capable of providing up to 1 A at 10 KV, and is water cooled. There are two control panels. The upper control panel controls the high voltage control. The panel contains a master key for the entire system, a START/STOP push button, eight interlock indicators, ON and OFF push buttons, a voltage range knob, and a meter to read the output voltage of the power supply.

The lower control panel controls the magnitude and deflection of the electron beam. The panel contains a FILAMENT / BEAM CURRENT meter, BEAM push button to connect / disconnect the filament to the power supply, a FILAMENT CURRENT check push button, a variable potentiometer to set the beam current, and five knobs to control the beam and its scan over the crucible. These control panels are shown in Fig.7.3.

7.4.1: Operation.

By turning the master key on the high voltage control panel to the ON position, the control panels are powered. Then by depressing the START button, it illuminates and the positions of the interlocks are displayed. These indicators and their functions are as follows:

The CABINET indicator is connected to four micro-switches in the E.B.G. power supply cabinet to make sure that all the panels of the cabinet are closed, and safeguard the operator from electrocution in the high voltage unit.

The CHAMBER indicator is connected to a micro-switch at the top hinge of the chamber door, to make sure that when the door is open, there is no high voltage power supply on.

The VACUUM indicator is connected to the ion gauge of the top chamber, and it assumes the right vacuum, when the ion gauge is on.

The CONTINUITY device sends a small current to the filament to check that the filament is not broken, the

high voltage leads are connected, and there are no blown fuses.

The ISOLATION device makes sure that there is no short circuit in the high voltage leads or in the high voltage parts of the gun assembly.

The WATER FLOW device ensures the flow of water to the power supply.

The DEFLECTION device checks the connection of the deflection coils.

The ACCESSORY interlock is used when an accessory unit such as a thickness monitoring device is in operation.

When all the interlocks are in the operational safe position (and all the indicators are illuminated) the red HV ON push button starts flashing repeatedly. There is then a three minutes delay, before the power supply can be switched on. The delay is to make sure that the Triode tube is cooled down by water flow before it can be switched on. When the power supply is switched on, the indicator remains on and the meter displays the output voltage. The voltage can be set to any value between 5.5 and 10 KV in 0.5 KV increments. When at the desired voltage, depressing the BEAM ON/OFF push button connects the E.B.G. to the power supply and illuminates the button. By keeping the FILAMENT CURRENT button depressed and turning the BEAM CURRENT potentiometer clockwise, when a current passes through the filament, its value can be checked on the meter. On observing a small current, the FILAMENT CURRENT button should be released; the meter then

indicates the beam current. The beam current should then be increased gradually to obtain the required power input for melting the coating material.

The deflection coil control knobs function as follows:

The LONGITUDINAL SWEEP AMPLITUDE control sets the range of longitudinal scan of the beam over the source, while the LONGITUDINAL SWEEP FREQUENCY control sets its frequency. The LATERAL SWEEP AMPLITUDE control sets how much the beam is to spread laterally, while the LATERAL DEFLECTION control sets how much off centre the beam should be.

7.5: Modifications to the ion plating equipment.

As received, the ion plating equipment was not suitable for research. There were also unforeseen operational difficulties and design faults.

The following necessary modifications were carried out:

7.5.1: Repositioning the ion gauge in the top chamber.

The ion gauge for measuring the vacuum in the top chamber was originally located just in front of the high vacuum valve. It was connected to the chamber by means of a short stainless steel tube. Whenever the pressure was about 20 mTorr (or more) with a glow discharge in the chamber, the short length of the tube caused a glow discharge at the tube. This in turn caused the gauge to indicate an unduly high pressure with little relationship to the pressure of the top chamber.

To avoid this problem the short horizontal stainless steel tube was replaced with an "L" shaped tube which was considerably longer. This eliminated the glow discharge at the inlet of the ion gauge into the chamber, but it also increased the response time of the gauge.

7.5.2: Modifications to the Auto Glow Discharge Unit.

As described in the previous section, the glow discharge parameters are controlled by the Auto Glow Discharge Unit. The use of this unit, as received, was found to suffer from some lack of control and other limitations. The lack of control on the discharge parameters was due to the fact that control of the unit was based on a set current. This resulted in changes in the applied voltage during the process with a corresponding uncertainty of the voltage and hence the power applied. There were also variations in pressure in order to maintain the set current. To avoid this lack of control, the automatic gas bleeding valve was disconnected and a manually operated needle valve used to introduce the working gas into the chamber. This enabled the operator to set the pressure, independent of a set current, at any desired value. This needle valve and the corresponding shut-off valve are shown in Fig.7.4.

A Variac (variable resistance controller) was added to the primary side of the power supply. This enabled the operator to set the applied voltage independent of the set current. These modifications allowed the glow discharge to be established at a pre-set pressure and voltage,



Fig.7.4: Positions of the needle and shut off valves on the side of the ion plater's main frame.

both of which affect the magnitude of the glow discharge current. To complete these modifications, the SET CURRENT unit was disconnected and a TIMER OVERRIDE switch added to the timer circuit. This switch enabled the operator to extend the duration of the glow discharge to any desired length of time, without interruption of the glow. The Variac and timer override switch are shown in Fig.7.2.

7.5.3: Modifications to the bottom chamber.

(1) The roughing port, high vacuum valve, and ion gauge for the bottom chamber are located at the base plate of the chamber. Debris from the ion plating such as small pieces of metal and oxides coming from the coating material could drop on the high vacuum valve. On opening and closing of the valve debris could become inbedded into the "O"ring valve seal and, in subsequent closings, prevent the valve being properly sealed. This could damage the valve seating and, in subsequent ventings, let air into the diffusion pump and oxidise the oil. The debris could also enter the roughing valve and cause similar damage to its "O"ring and seating. Debris falling into the ion gauge could cause an electrical short circuit. To avoid such problems, all those ports were covered with fine stainless steel mesh. This reduced pumping speeds and increased the response time of the ion gauge, which in effect meant slightly longer pump-down periods. The benefits were less maintenance and more reliable operation.

(2) Even with stainless steel mesh over the high vacuum

valve, it was occasionally necessary to clean the "O"ring . To do this safely, the ion plater had to be switched off and the compressed air cut off. On opening the high vacuum valve, it goes down for about 1" and then moves away; therefore to clean the "O"ring it should be kept in a position which is low enough but not away from the port. It was very difficult to keep the valve in that position, because there was always enough pressure on one side of the air cylinder to make it impossible to adjust it properly by hand. To solve this problem, a pneumatic switch valve was added to the line in front of the pneumatic control switch for the high vacuum valve. This enabled the operator to exhaust both sides of the air cylinder without any need to turn off the compressed air to other parts of the equipment, saving the need to switch off the whole apparatus. The use of this switch enabled the position of the valve to be altered by hand as both sides of the air cylinder were exhausted. The lower chamber's high vacuum valve is illustrated in Fig. 7.5 . Pneumatic valve controls are shown in Fig.7.6.

(3) Oil backstreaming from the diffusion pump into the bottom chamber occurred when the liquid nitrogen trap was not in use. To avoid this problem, a water cooled aluminium chevron baffle was positioned between the chamber and the diffusion pump. This also minimized the amount of oil coming into contact with liquid nitrogen trap.

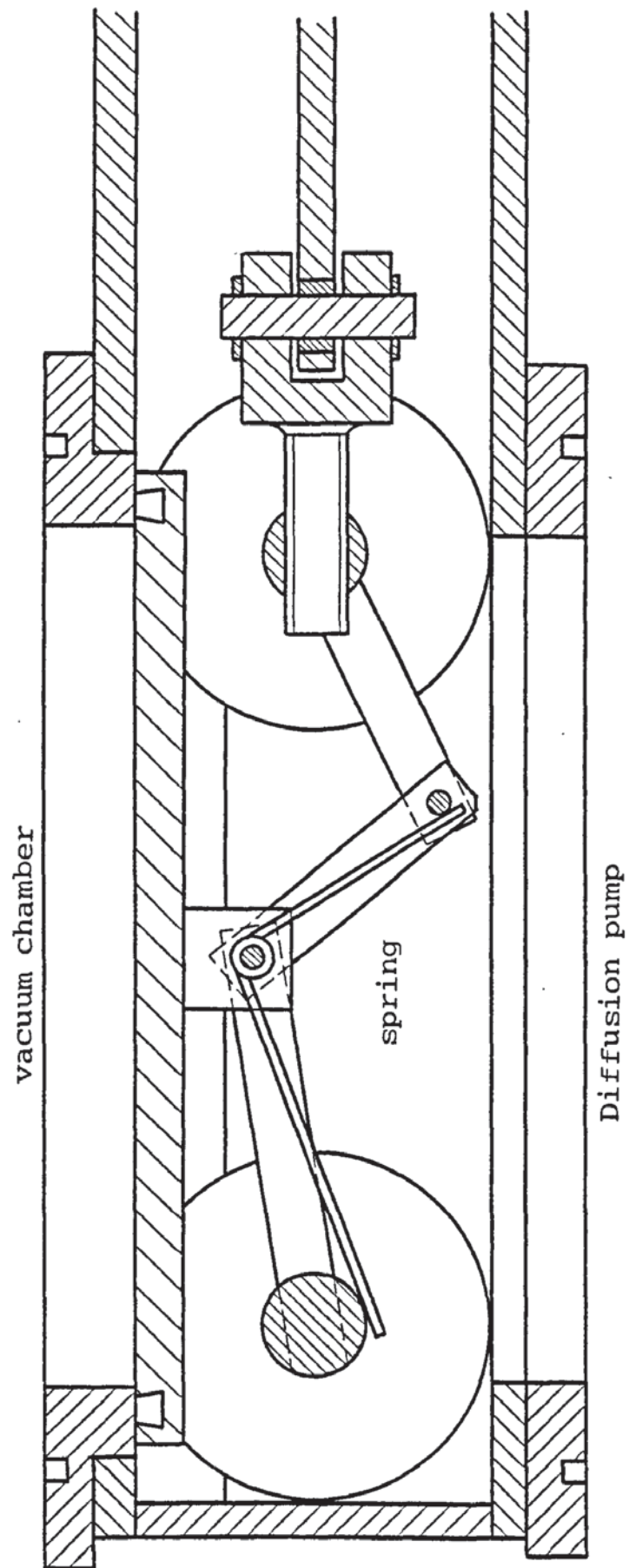


Fig.7.5: High vacuum valve of the lower chamber

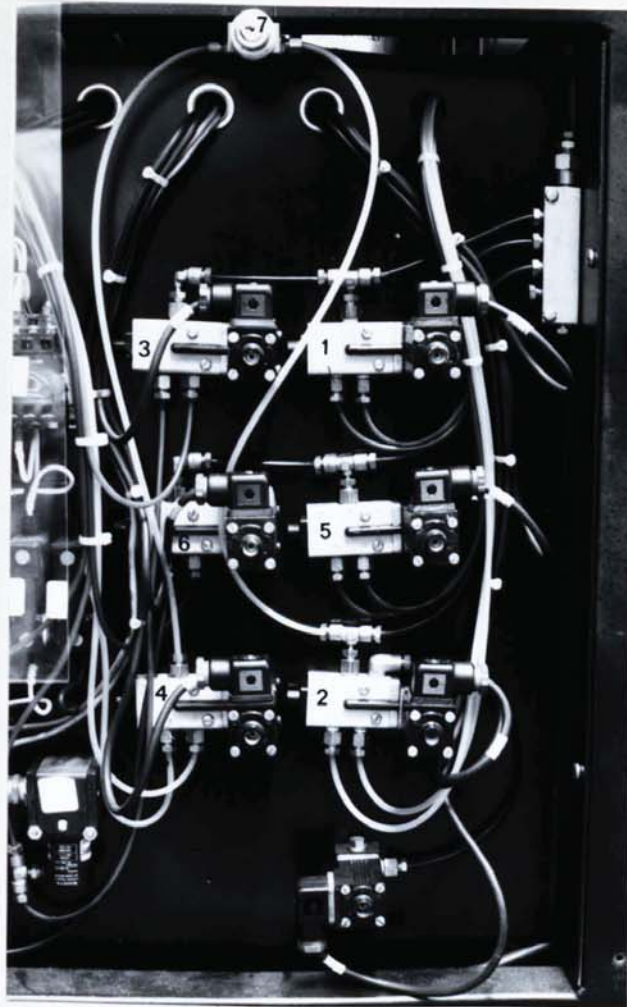


Fig.7.6: Pneumatic valve controls of the ion plater.

1. top chamber's roughing valve control,
2. top chamber's high vacuum valve control,
3. bottom chamber's roughing valve control,
4. bottom chamber's high vacuum valve control,
5. top chamber's backing valve control,
6. bottom chamber's backing valve control,
7. bottom chamber high vacuum valve's safety switch valve.

7.6: Addition of an air compressor.

The university air compressor is switched off at 5.00pm each day; consequently the compressed air pressure drops. This caused a change in position of some of the pneumatic valves on the ion plating equipment; eg. if the high vacuum valve for the bottom chamber is closed and the chamber is not at high vacuum, the valve will partially open. The same happens to the roughing valve of the bottom chamber. Obviously if that happens, there will be a high pressure in the backing line which will lead to oil backstreaming into the chamber. Also if for any reason the door of the upper chamber is left open, the rotary pump would be pumping at atmospheric pressure, and because it is not rated to work at such pressures for long periods of time, it will over-heat and burn out. This is in addition to the certain loss of the diffusion pump oil through oxidation and backstreaming. To avoid these problems, a portable air compressor was added to the compressed air line to maintain the required pressure at all times of the day and night. A control system was designed so that the portable compressor operated when the University compressed air supply was switched off. As an additional safety feature to prevent the rotary pumps burning out and backstreaming problems, a gas bottle of nitrogen was incorporated in the control system to supply compressed nitrogen should the portable compressor fail.

7.7: Problems encountered with commissioning.

The ion plater was delivered in April 1980, and commissioning was to have been completed by the end of that month. It has not yet been accomplished (August 1982). The main problem has always been with the electron beam gun, and was encountered the very first time the equipment was used.

The difficulty is aggravated by the fact that the electron beam gun does not malfunction on every occasion. This makes it more time consuming to try to find the cause, and also makes it that much more unreliable. There could be more than one fault, one or more of which could be intermittent. The fault(s) could be in the E.B.G. or in the electronic control units.

There have been four problems with the electron beam gun assembly; Fig. 7.7 shows a cross-section of the crucible and the gun assembly, and indicates the four problem regions. The juxtaposition of the gun assembly and the crucible can be seen in Fig. 7.8 ; Fig. 7.9 shows the crucible without the gun assembly, and Fig. 7.10 shows the electron beam gun assembly.

(1) The gap between the filament shield and the base plate was too small and led to arcing. To prevent this, a piece of the base plate, just under the gun assembly, was cut off by the manufacturers which led to the next problem.

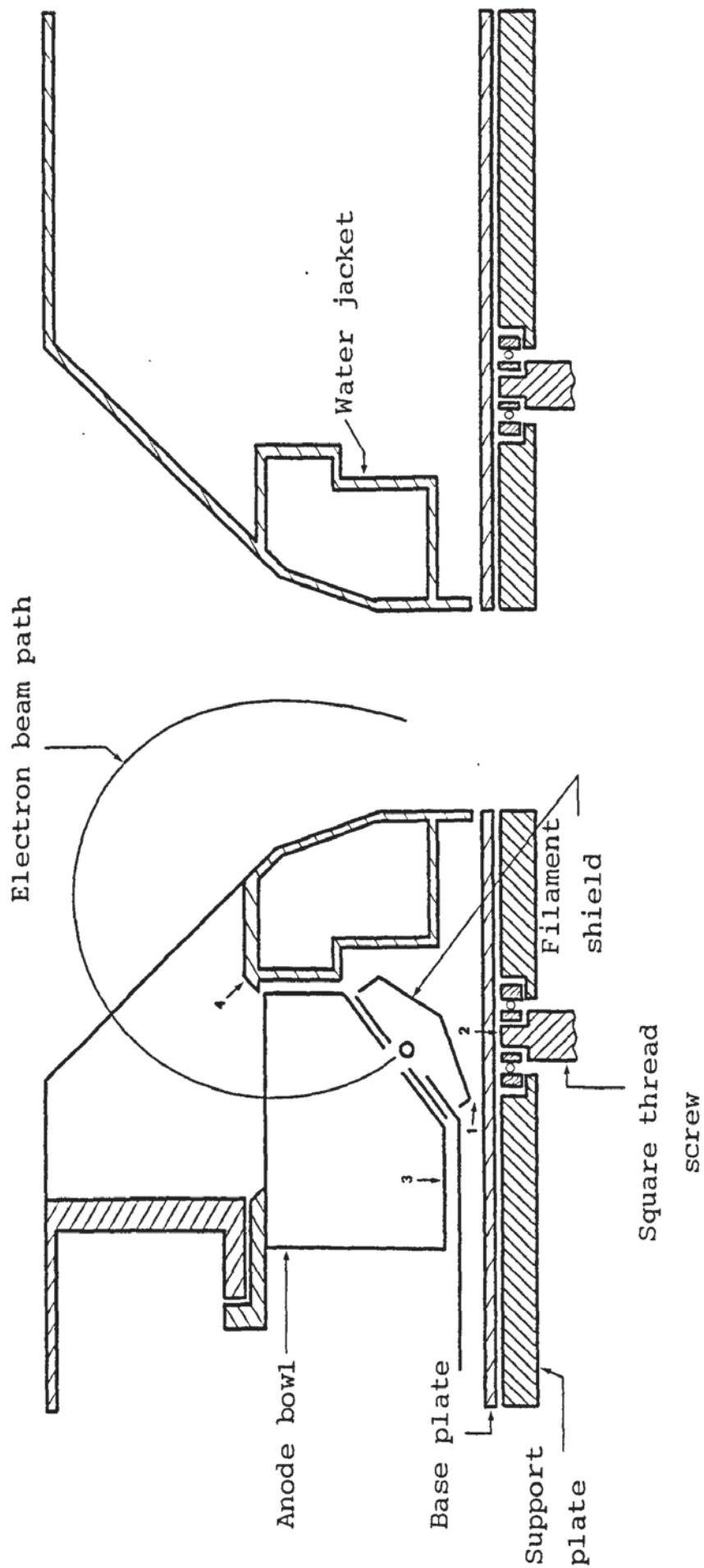


Fig.7.7: Assembly of the electron beam gun and the water cooled rod fed crucible.

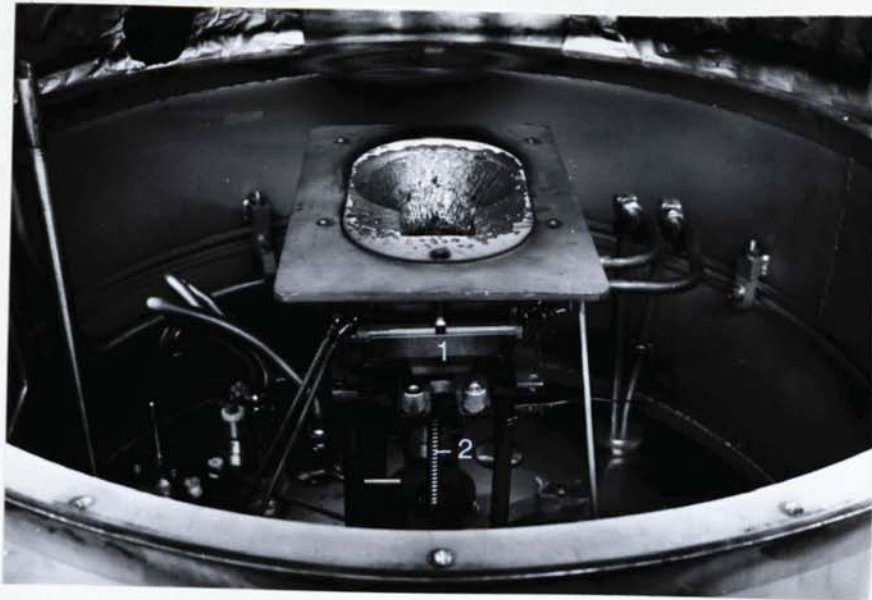


Fig.7.8: Juxtaposition of the electron beam gun
and the rod fed water cooled crucible
1: Electron beam gun assembly
2: Square thread screw.

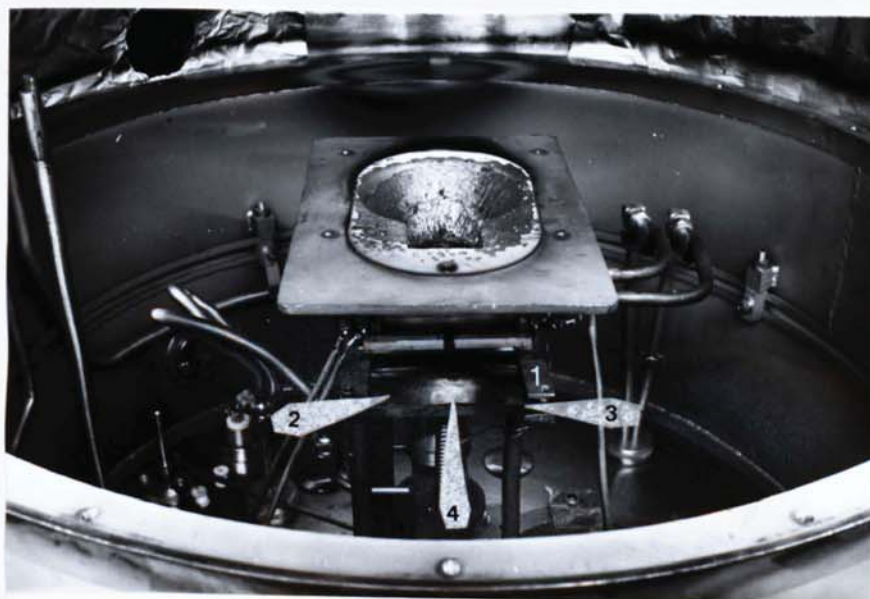


Fig.7.9: The rod fed water cooled crucible
1: Base plate
2: The thin stainless steel plate
3: Support plate
4: Signs of arcing.

(2) Two square thread screws are used to feed the coating material rod into the crucible. They are held in a ball bearing race at each end. The top bearings are housed in the support plate, and were originally held in place by the base plate. By cutting off part of the base plate to prevent the above arcing, one of the bearings became unsupported so that when the rod was lowered, the bearing became displaced. In turn, this resulted in reducing the distance between the filament shield and the bearing and led back to arcing again. To overcome this problem, a thin stainless steel plate was inserted between the base plate and the support plate. Over a period of time, this plate distorted and bulged up due to thermal stresses induced by the gun assembly, again leading to arcing.

The thin stainless steel plate, the base plate, the support plate and signs of arcing are seen in Fig.7.9.

(3) Operating the electron beam gun at high power led to the burning of a hole in the bottom of the anode bowl. The position of this burn is shown in Fig.7.7.

Regardless of some evidence suggesting that this burn was due to arcing between the anode bowl and the high tension parts of the filament assembly, it was thought that an ion beam could have been responsible for this burn, and therefore efforts were made to reduce the pressure in the anode bowl region. To achieve this aim, a thin molybdenum sheet was put on the anode bowl and an attempt

was made to burn an orifice in it with the help of the electron beam gun. This did not produce the required result, particularly because the molybdenum sheet cracked from thermal shock. When the molybdenum sheet was removed, it was found that thermal diffusion had bonded part of it to the electron beam gun assembly, as seen in Figs. 7.10 and 7.13. This residual molybdenum sheet produced a gap between the crucible and the gun assembly which resulted in higher pressures in the bottom chamber. As the pressure in the bottom chamber should not exceed 4×10^{-4} Torr, such a gap or any hole in the anode bowl (except the electron beam slot) is undesirable. The same experience was achieved by using a thin tungsten sheet which had a small orifice.

After the lack of success in reducing the pressure in the anode bowl, an attempt was made to prevent the burning of a hole. A thick piece of tungsten was welded onto the bottom of the anode bowl as seen in Fig. 7.13. In practice the tungsten prevented the burning of a hole, but it did not remedy the original cause of the problem. As Fig. 7.11 shows, some arcing still occurred on the outside of the anode bowl.

(4) As shown in Fig. 7.7, the electron beam accelerates through the anode slot and bends about 210° in a magnetic field to be focused on the source. This beam should have a clear path and must not be obstructed, but in practice it hits the front side of the anode bowl and the edge of the crucible. To prevent it happening, a tungsten block



Fig.7.10: The electron beam gun assembly
 1. The tungsten block,
 2. place of impingement of the electron beam,
 3. Remaining of the molybdenum sheet.



Fig.7.11: Signs of arcing underneath the anode bowl. Operation voltage 10 KV.



Fig.7.12: The electron beam gun assembly.

1. The tungsten block,
2. damaged area of the anode bowl due to the heating of the tungsten block.

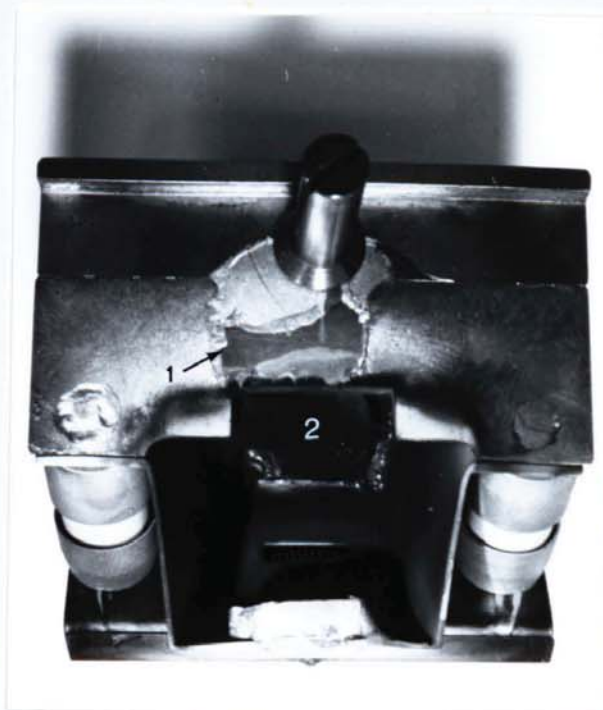


Fig.7.13: The electron beam gun assembly.

1. Remaining of the molybdenum sheet,
2. the tungsten block at the bottom of the anode bowl.

was welded onto the front side of the anode bowl as shown in Fig.7.10. However, the beam hits the tungsten block, heats it up, and distorts the stainless steel bowl. Fig.7.12 shows the damaged area. The heating of the tungsten block eventually caused the stainless steel to burn through. This damage is shown in Fig.7.13.

7.8: Design of Electron Beam Guns.

There are two types of electron beam guns, Cold Cathode and Hot Cathode. The cold cathode electron beam guns are largely used for electron beam welding, while hot cathode guns are mainly used in electron microscopes and metal deposition processes. In a cold cathode gun the electron emission is due to a large potential difference between cathode and anode, while a hot cathode gun emits electrons thermionically. Here hot cathode guns will be discussed with special reference to the metal deposition processes.

In a thermionic emission, current density can be calculated by Richardson-Dushman equation as:

$$j = A T^2 \exp(-Q / K T)$$

where j is the current density (A/cm^2), A is a material constant, T is the cathode temperature (K), Q is the cathode work function (joules), and K is the Boltzmann's constant (1.3805×10^{-23}). This equation indicates that the controlling factor is the cathode temperature. However, at high current densities, cathode-anode spacing and voltage become the controlling factors, due to the effect of the generated electrostatic field. The Langmuir-Child equation describes the emission current density in this region as:

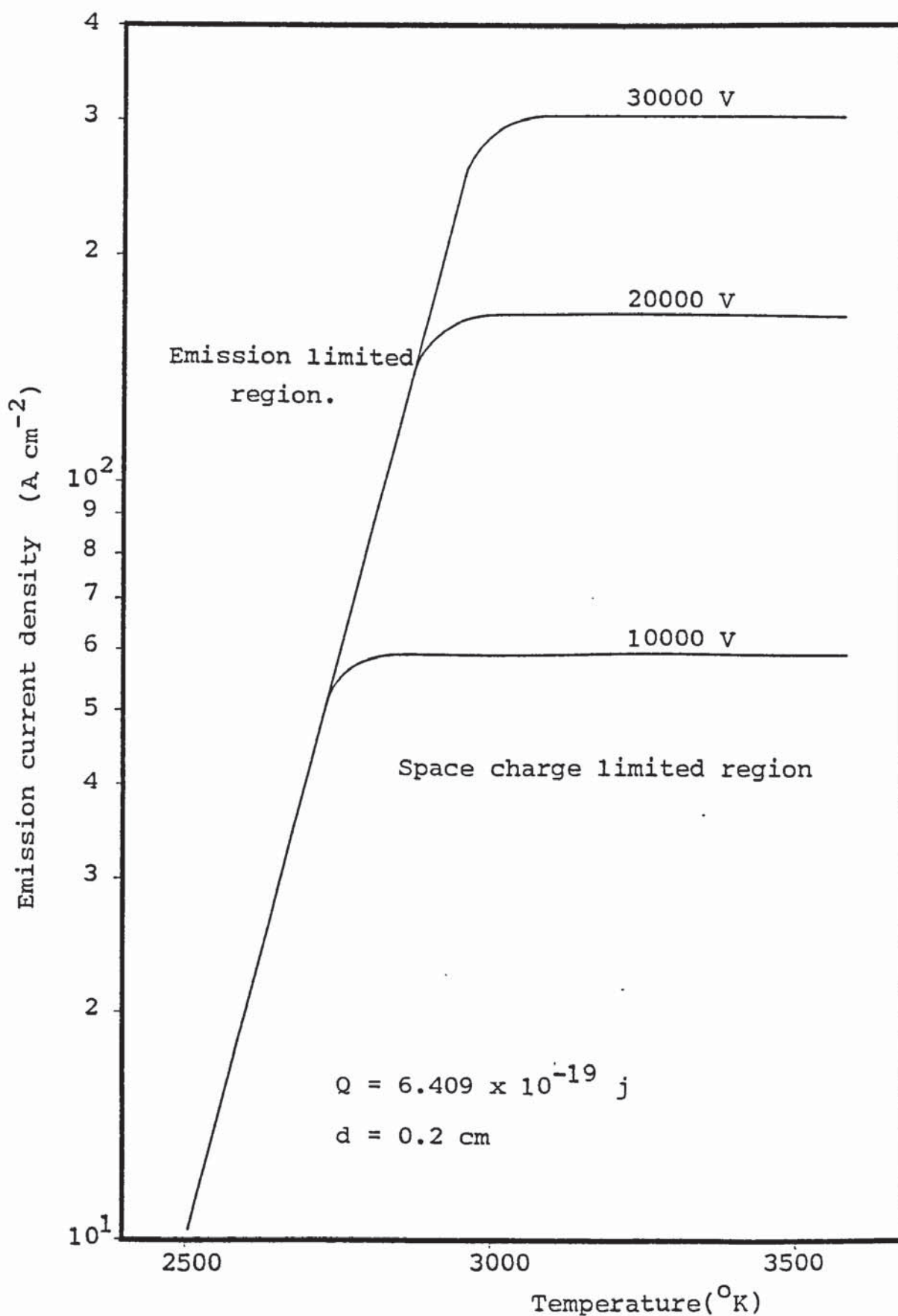


Fig.7.14: Influence of applied voltage and temperature on the emission current density.

$$j = B V^{3/2} / d^2$$

where V is the potential difference (volts), d is anode-cathode spacing (cm), and B is a constant ($2.335 \times 10^{-6} \text{A/cm}^2$). This space charge effect indicates that to increase the current density, increasing the cathode temperature is no longer effective, but instead the voltage must be increased. Fig.7.14 shows this effect for a specific gun configuration.

The early electron beam guns used in metal deposition processes were work-accelerated. This means that the electrons had to accelerate through the potential difference between the filament and the crucible; therefore, the gun assembly had to be in line of sight of the crucible. The main problem with such guns was their tendency to become coated by the evaporant and short out. The development of self-accelerating electron beam guns (anode included within the gun assembly) with a 270° beam deflection has overcome that problem. Nowadays, there are two main types of hot cathode electron beam guns used in metal deposition processes, Pierce-type and Transverse-type. Pierce-type guns work in the space charge limited mode, whereas transverse guns work in the emission limited mode.

The Pierce-type electron beam gun produces a straight, coaxially focused beam; hence it must be positioned in line of sight of the crucible^(254,255). This type of gun is self accelerated and usually recommended for very high power requirements, and for very large evaporation applications where a straight or a 90° bent beam can be used. The main advantage of this type of gun is their very high power (1.2MW guns are currently available⁽²⁵⁶⁾). The

disadvantages are that special power supplies are required and a separate vacuum system is needed to protect the emitter section on long operation times.

The Transverse design is used for power requirements up to 200KW⁽²⁵⁶⁾. In this design the electron beam gun is located outside the line of sight of the crucible and the electron beam is bent and focused into the crucible by means of a magnetic field. This field may either be generated by a permanent magnet or by an electromagnet. In simple, small, commercially available electron beam guns, usually a permanent magnet is used to produce the main magnetic field, while electromagnets are used to control the sweep of the beam on the evaporation source.

7.8.1: General design of Transverse electron beam guns.

A tungsten filament is heated by applying a small voltage; this causes thermionic emission of electrons in all directions. In order to produce an electron beam the filament is located in the groove of a beam former. The beam former is a strip of refractory metal bent to a V shape, and is at a high negative potential. Electrons emitted towards the beam former will be reflected back by the electrostatic field. In order to complete the formation of a well defined beam, an orifice is provided in the assembly plate in front of the filament. This orifice is the exit port of the electron beam. An anode plate having an identical orifice is used in front of the filament assembly plate to accelerate the electrons. The potential difference between the filament and this anode plate provides the acceleration voltage. Fig.7.15 shows this configuration. To protect the

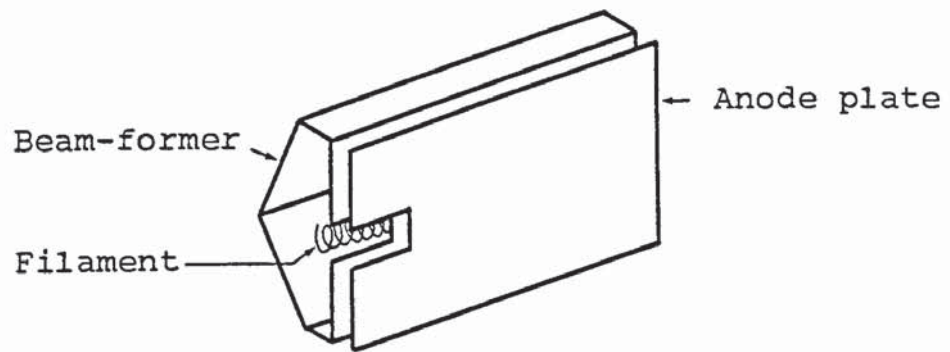


Fig.7.15: Juxtaposition of the filament,
beam-former and the anode plate.

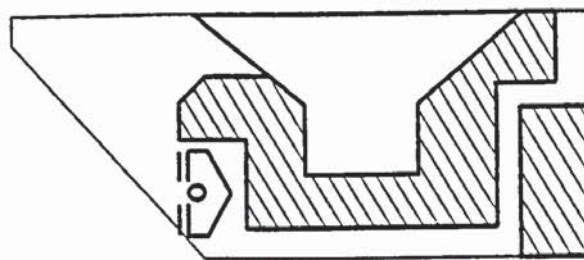


Fig.7.16: Cross section of a 270° beam
bend transverse electron beam gun.

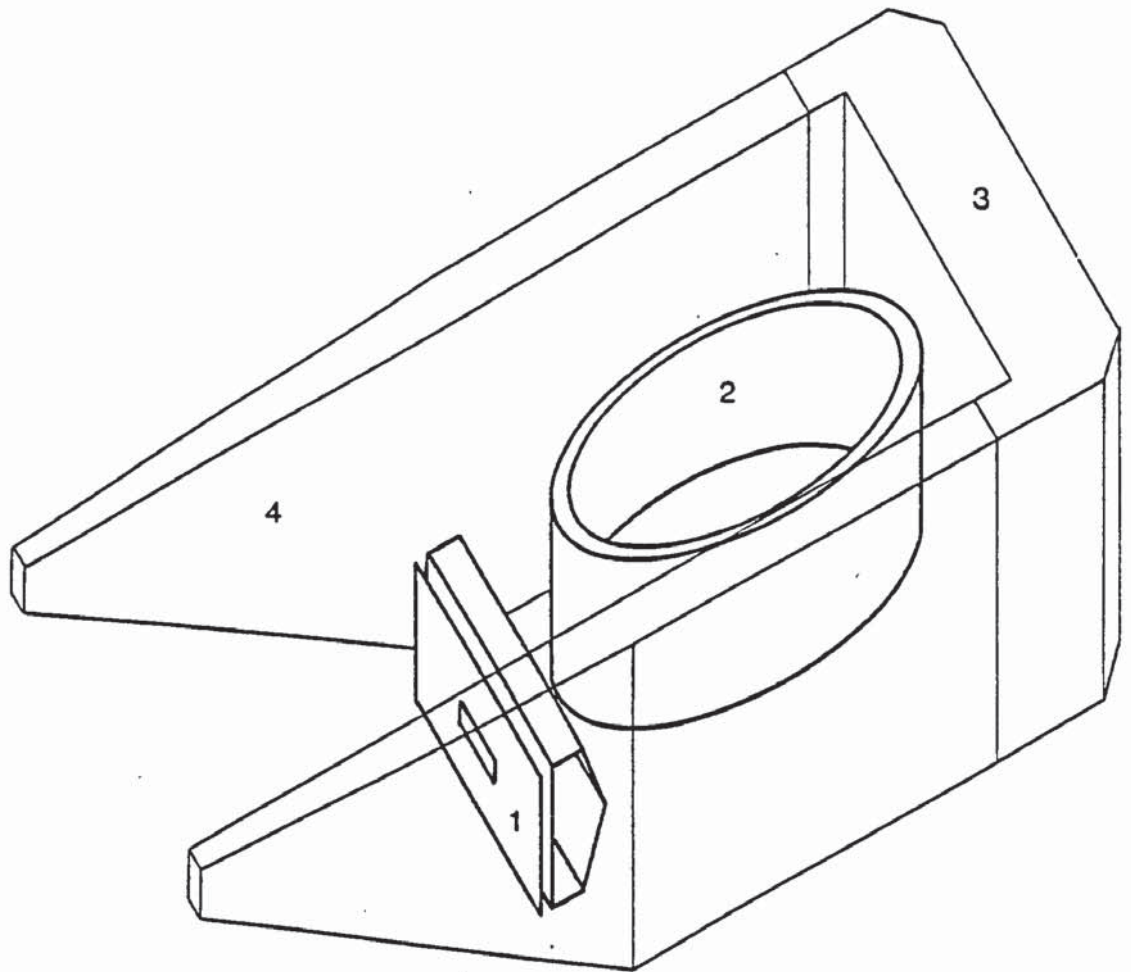


Fig.7.17: General design of a 270° beam bend transverse electron beam gun.

- 1: filament assembly,
- 2: water cooled crucible,
- 3: Permanent magnet,
- 4: extended pole arm.

electron beam gun from the evaporant, the assembly is located out of line of sight of the crucible, usually in such a way that the ejection direction of the beam makes an angle larger than 180° with the surface of the melt. A horse-shoe permanent magnet is located behind the crucible with its arms extending to the electron beam gun assembly. This general design, for a 270° bend beam, is shown in Figs. 7.16 and 7.17.

7.8.2: Discussion of the characteristics of a power supply for Transverse electron beam guns.

Every power supply used for transverse electron beam guns must satisfy the following two conditions:

- a) - the beam position must remain constant in a fixed deflection magnetic field,
- b) - the gun must be protected in event of arcing.

As the low power transverse electron beam guns use a permanent magnet to produce the magnetic field, to have a fixed curvature of the beam bend the acceleration voltage must remain stable for long periods of operation and for different beam currents. This means the gun must operate in the temperature controlled emission mode. A low impedance power supply satisfies this condition.

Beam forming parts of the gun are at a high negative potential and therefore there is a strong electric field around the high tension parts of the assembly. Even at high vacuum, there is a small ionization current between anode and cathode. When gas atoms and molecules enter this region, they become ionized. If there are enough ions in relation

to electrons, the space charge created by electrons will be neutralised which eases passage of current. As the pressure rises, perhaps due to heating and further outgasing, the ionization current increases rapidly, and eventually an arc discharge will occur, providing that the power supply is capable of supplying the necessary current. A low impedance power supply would maintain such a discharge. This stable arc will eventually cause destruction of the respective electrodes and possible damage to the power supply. If a high impedance power supply is used, not only will the first condition (beam stability) not be satisfied, but arcing cannot be eliminated either, as an arc may be maintained at low voltages (e.g. 10 v). To minimize arcing and avoid a stable arc, a device must be used to cut off the power supplied to the electron beam gun as soon as a pre-set current is reached. This pre-set limit is the maximum current whcih can be supplied to and consumed by, the electron beam gun without any damage to the equipment. A low impedance power supply will deliver this current without any appreciable drop in voltage. When the pre-set current is reached, the protection device will drop the voltage to zero very rapidly. Given enough time, the arc will extinguish, and ions and electrons recombine. The time constant of this device is critical and must be as short as possible.

A triode valve may be used to regulate the power supply; this is done by controlling the grid of the triode. One method is to put the triode in series with the electron beam gun and simply sense the current. If the load

resistance drops below the pre-set value due to an arc, the triode dissipates the power and therefore the voltage supplied to the electron beam gun will rapidly approach zero. As the arc extinguishes, the voltage will then rapidly rise to the initial value. This system is shown in Fig.7.18. In this system a triode valve with higher anode dissipation than the capacity of the electron beam gun is required. It has the advantage of being automatic, but has the disadvantage of needing a high capacity triode valve which can be very expensive or even unavailable at high powers. Another method is to employ a small triode in conjunction with a logic circuit on the grid control, as shown in Fig.7.19. In this system a large amount of energy dissipates in the valve only when the grid is biased, with a large current through the valve and a high voltage across it. Therefore, if the grid is switched strongly negative at the time of an arc, the power dissipation through the triode can be greatly reduced. This system is known as "switching supply". There are two problems encountered with this system. First, the control signal to the grid is initiated by the arc, but there is no mechanism to turn on the valve again once it is shut off, thus a timer circuit is required to turn the voltage on again. The second problem is that although there is little power dissipated in the anode during on and off conditions, there is a substantial amount during any transition between the two. To prevent overheating of the anode, the off time of the valve may be lengthened. This in effect reduces the amount of power to the electron beam gun under arcing

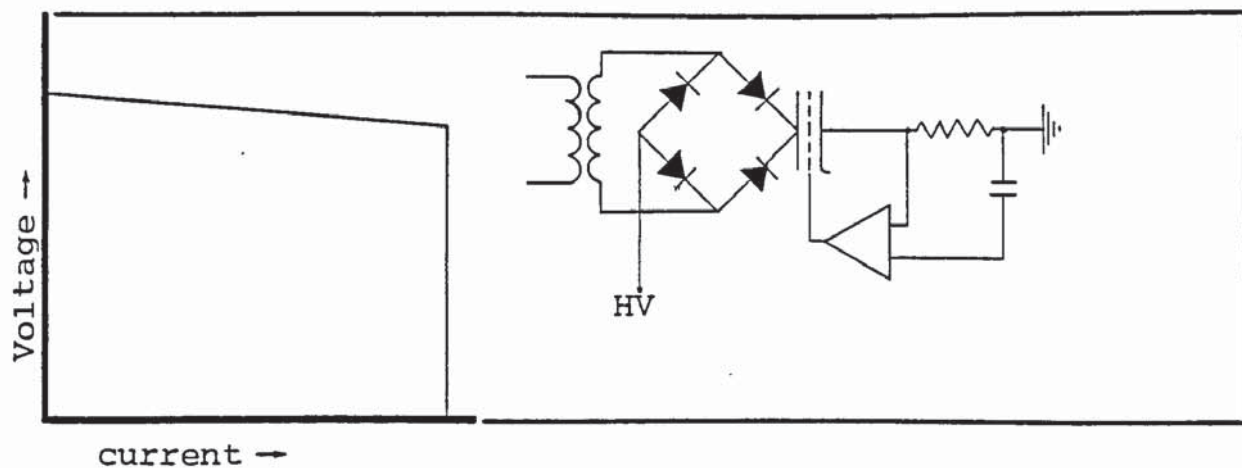


Fig.7.18: Characteristics of a constant current triode power supply.

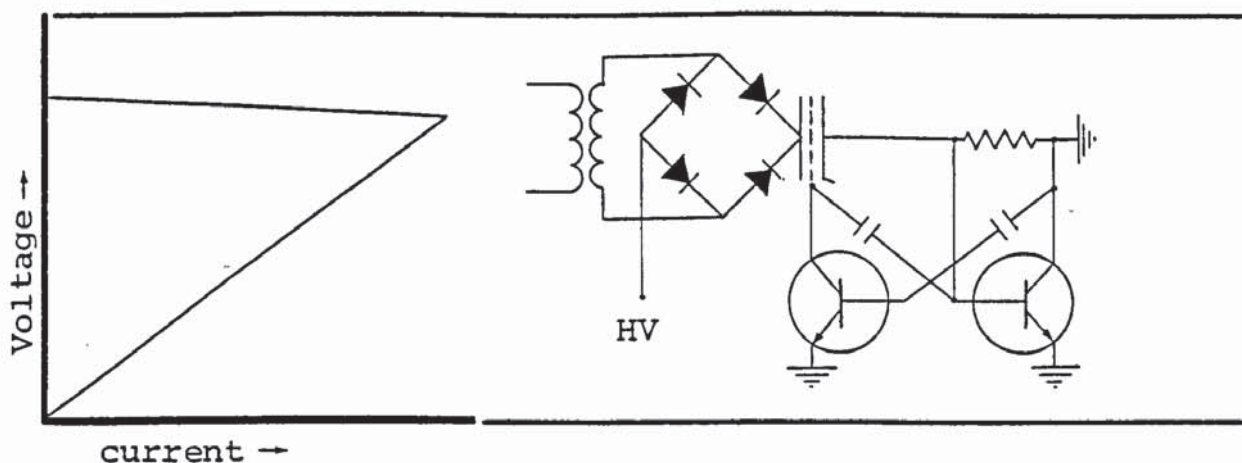


Fig.7.19: Characteristics of a current limited (switcher) triode power supply.

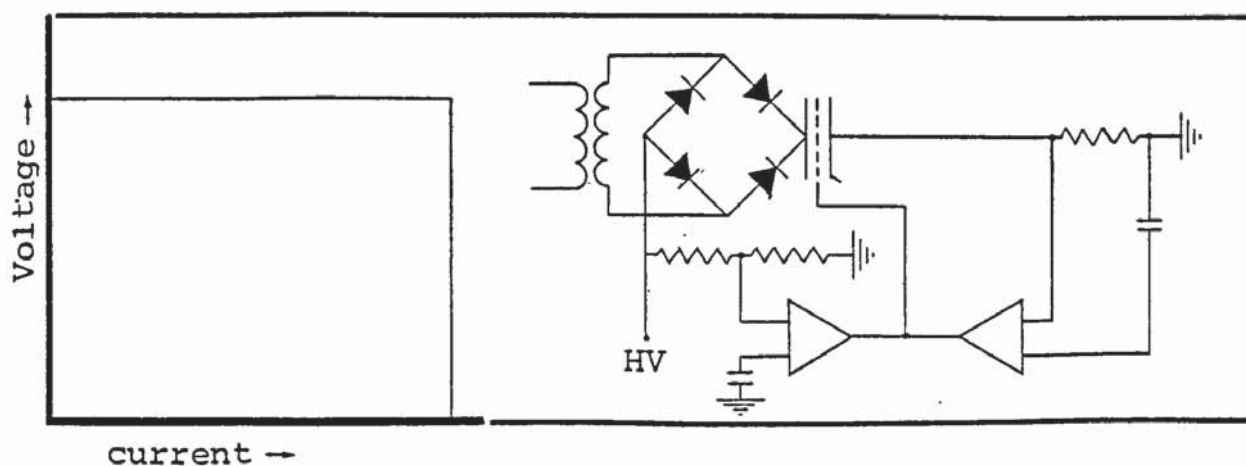


Fig.7.20: Characteristics of a constant voltage/current triode power supply.

conditions. A detailed review of the subject is given by R.J.Hill⁽²⁵⁶⁾.

Characteristics of an ideal constant voltage / current triode power supply are shown in Fig.7.20.

7.8.3: Design of the electron beam gun and the power supply supplied by the Electrotech Equipments Ltd. The electron beam gun supplied by the Electrotech has the same general design as described in section 8.1 above, with the difference that it is a modified version having a 210° beam bend angle. The power supply has a voltage regulating magnetic beam triode. Problem areas of the gun assembly and crucible configuration are shown in Fig.7.7, section 7 of this chapter. As mentioned in section seven, the main problem has always been the arcing between high tension leads and the anode bowl. As explained in the previous section, an ionization avalanche causes the arcing. This avalanche may at least be retarded by design modifications in the electron beam gun, but the true answer may lie in the power supply.

Experience on the present status of the equipment, (October 1982) has shown that in the event of a stable arc none of the protective systems is effective. On occasions, the power supply remained overloaded until it was switched off by the operator. For every such instance, regardless of how quickly the power supply was switched off, or how low the high tension was, the minimum damage was a sign

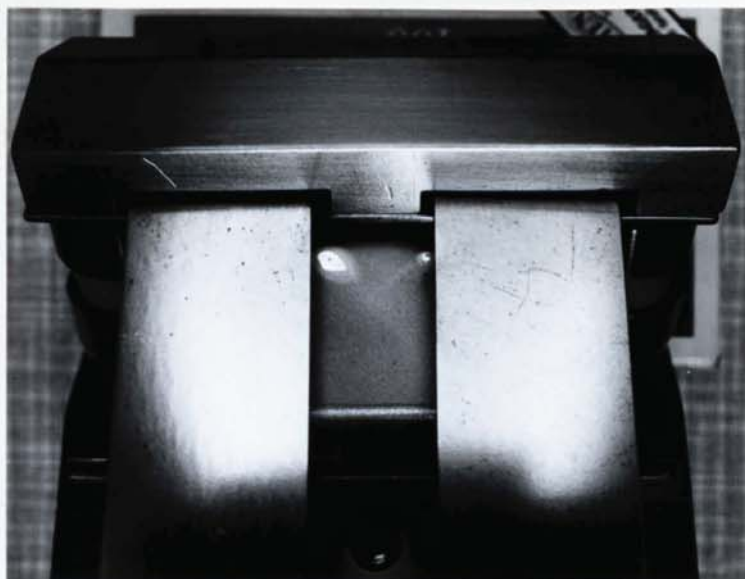


Fig.7.21: Signs of arcing on the outside of the anode bowl. Operation voltage 7.5 KV

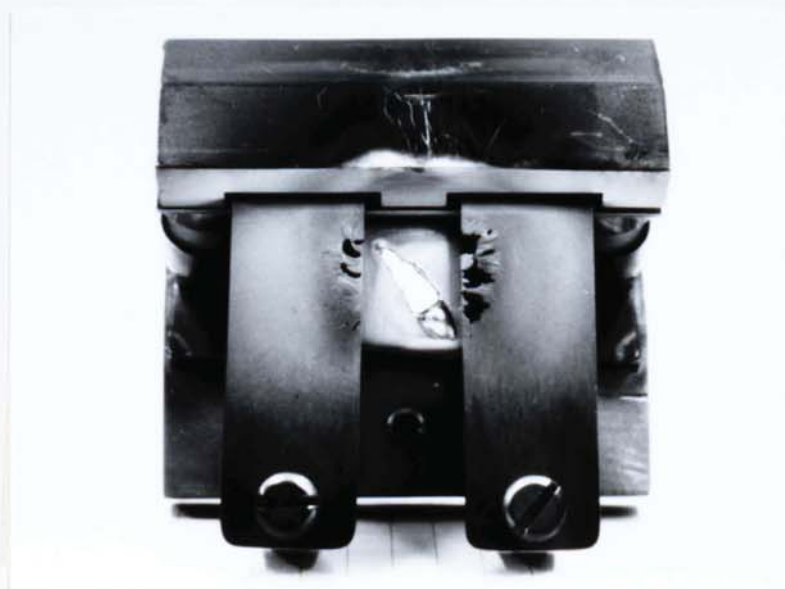


Fig.7.22: A hole burnt in the anode bowl, caused by arcing.

of arcing the same as shown in Fig.7.21 for operating at 7.5KV, or as shown in Fig.7.11 for operation at 10KV. Although the arcing marks of Fig.7.21 might seem negligible if arcing had continued, it would have caused a burn through such as the one shown in Fig.7.22.

7.8.4: Protection system of the power supply and the electron beam gun.

Fig.7.23 is a flow chart of the power supply and the protection system based on circuit diagrams provided by the manufacturer. To operate the equipment, turning the key switch on supplies the safety unit with three phase electricity. Then, by pressing the START push button a set of interlocks will be checked. As they are satisfied, the first set of contactors of the safety contactor unit closes. The HV ON push button energises the second set of contactors of the unit and the valve stack contactors. It also results in activation of the filament drive unit. Energising the contactors supplies the high tension transformer, whereas the filament transformer is activated by pressing the BEAM ON push button, and the filament emission is controlled by the BEAM CURRENT variable resistor.

The current between filament assembly and earth, including the crucible, is checked by the sense resistor. In the event of arcing, this current rises, and therefore the voltage across the sense resistor increases. At this point the triode valve drops the applied high voltage to the

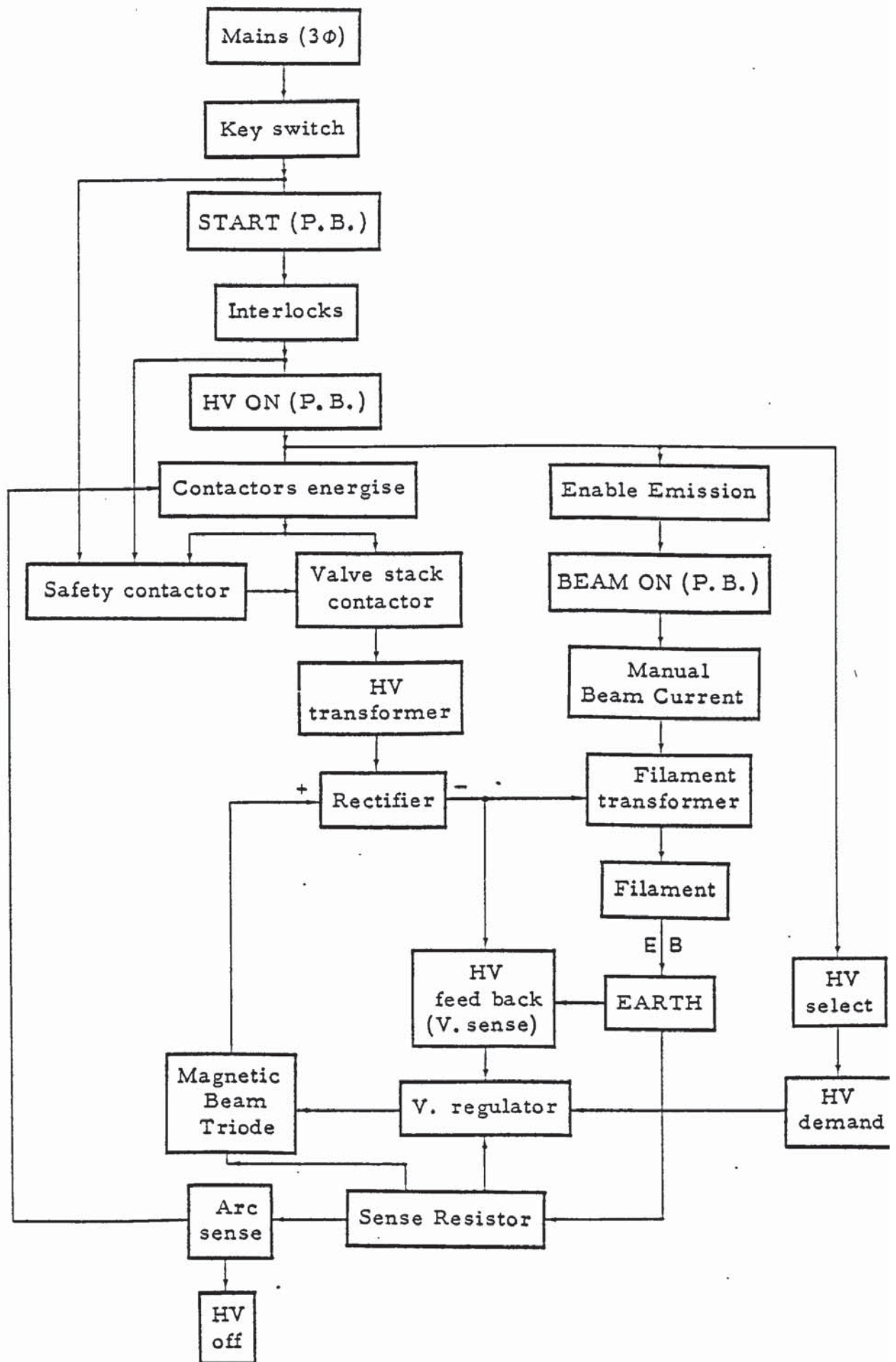


Fig.7.23: Block diagram of the ion plater power supply.

electron beam gun to zero.

The arc trip part of the circuit is shown in Fig.7.24. At the indication of a current higher than the value pre-set by the sense resistor, the arc trip relay closes. This activates transistor number 1 after a short delay, which sends a signal to de-energise the second set of contactors of the safety contactor unit and the valve stack contactors. This delay provides sufficient time for flashovers to extinguish due to the drop in applied potential by the triode. If this happens, the voltage across the sense resistor drops, the relay opens and operation of the first transistor aborts. This transistor also turns on the second transistor, which in turn activates transistor number 3, after a short delay. An unstable arc does not extinguish during the first delay, but the second delay can provide the necessary time. If so, the arc trip relay will open and further action stops and the contactors re-energise. When the arc does not extinguish during the second delay, the third transistor activates and sends a signal, which in effect is the same as pressing the HV OFF push button. At this stage it is necessary to re-start the operation of the electron beam gun by re-pressing the HV ON push button.

Up to October 1982 the protection system has failed to advance the trip sequence to the point of complete switch off of the power supply. This indicates a fault in the hatched area of Fig.7.24. The fault might be a break in

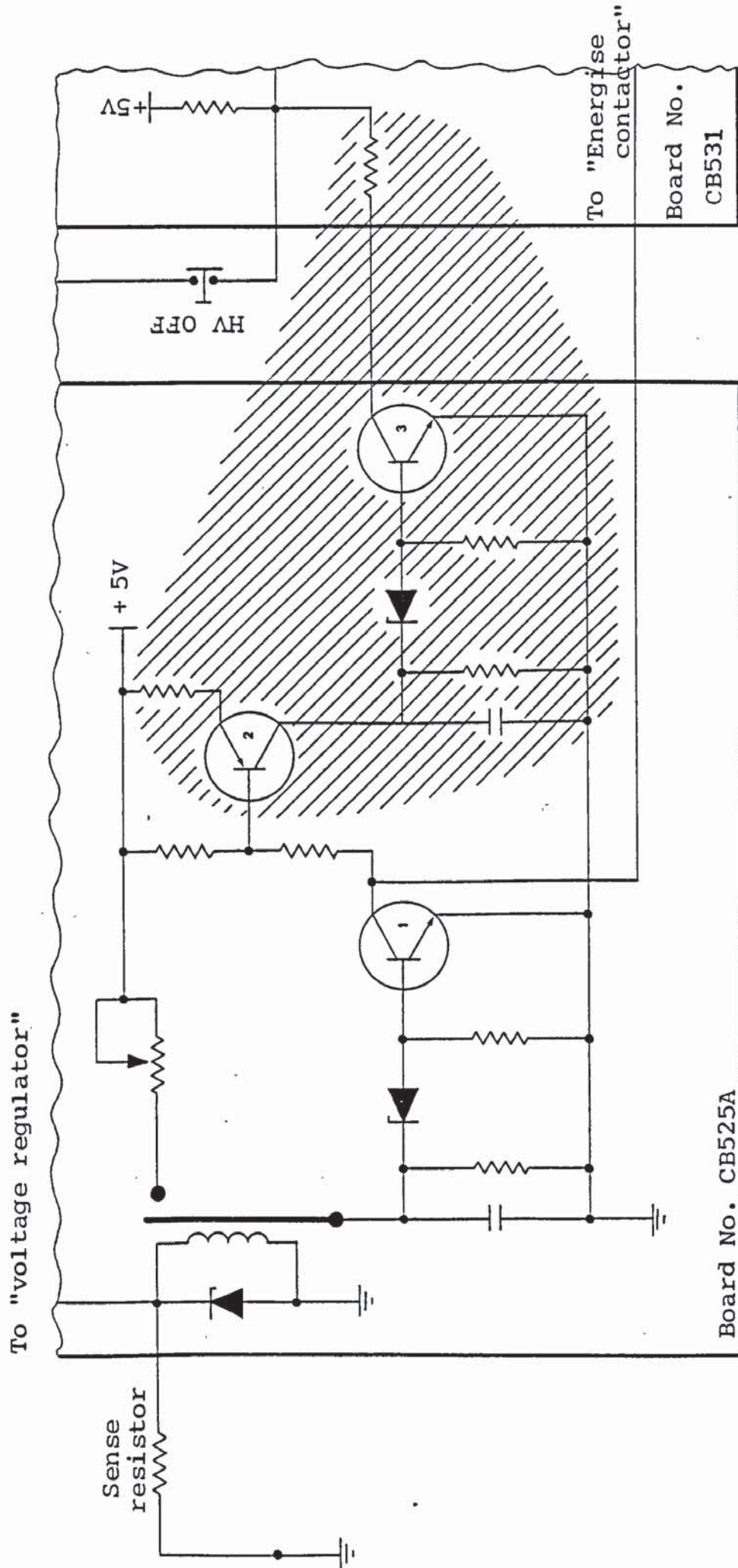


Fig.7.24: Part of the arc trip module, indicating the probable fault region within the hatched area.

the circuit, a faulty transistor, or a short circuit.

7.8.5: Discussion and proposed modifications of the electron beam gun.

As is clear in Figs. 7.11 and 7.21, signs of arcing appear quite close to the cross over points of the high tension leads and the filament assembly plate. These signs start just in front of the gap between the high tension leads and the beam former shield and the filament assembly plate. From these photographs it is also clear that the bigger the gap, the bigger the sign of arcing. This pattern indicates the importance of those gaps. The gaps are also points of high electrostatic field. The fact is that not all of the electrons emitted by the filament emerge from the slot in the filament assembly plate; a large number of them are trapped between the beam former and the assembly plate. Some of these electrons will eventually escape from the open ends of the assembly, while the rest may come out of the assembly through the aforementioned gaps. Exit of electrons through these gaps and their strength may be effected by the high tension, the emission current and instabilities of the system. These small streams of electrons try to escape from the corners in order to get away from the high negative field region. They are also affected by the proximity of the anode bowl, and by the magnetic field. These result in the X shape sign left on the anode bowl, which can be distinguished in Figs. 7.11 and 7.21.

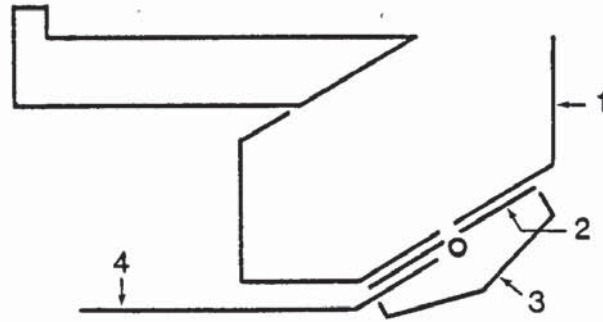


Fig.7.25(a): Original design of the electron beam gun assembly, supplied by the Electrotech.

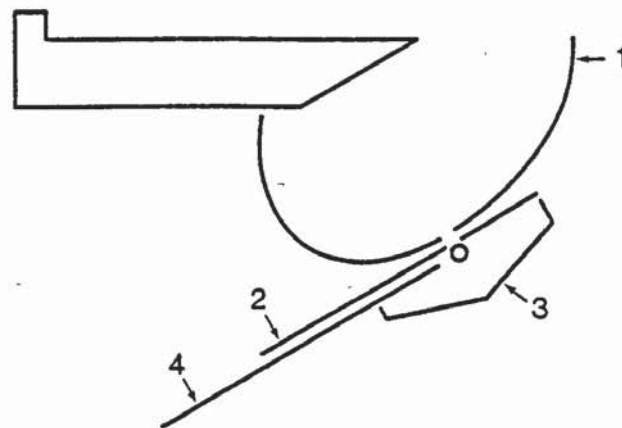


Fig.7.25(b): The proposed design of the electron beam gun assembly.

- 1: anode bowl,
- 2: filament assembly plate,
- 3: beam former,
- 4: high tension lead.

To avoid this problem, it may be recommended that the filament assembly plate be extended so that it shields the anode bowl from the high tension leads, and covers it from the two gaps. Even with this configuration, however, there is a possibility of flashovers and arcing. To avoid a stable arc and to help extinguish unstable arcs, it is desirable that the anode-cathode distance gradually increases. Therefore, if any arc is initiated at the small distances, it can move out towards larger distances until it blows up. In order to achieve this goal, the anode bowl should have a curved cross section, as is illustrated in Fig.7.25, which shows the proposed electron beam gun assembly design.

7.9: Design and construction of a 12" chamber diameter ion plater.

An old "Speedivac" coating unit was used as the basis for construction of a 12" diameter chamber ion plater.

7.9.1: General specification of the "Speedivac" coating unit.

Rotary pump: "Speedivac model 1SC150B single stage gas ballasted. Oil capacity, 1.56 l.

Diffusion pump: "Speedivac" model 403 A (4" intake diameter). Oil capacity, 100 ml.

Backing line capacity tank: containing P_2O_5 , capable of backing the diffusion pump for 30 minutes, without the rotary pump.

High vacuum valve: 4".

Backing valve: 1/2".

Roughing valve: 1/2".

Capacity tank isolation valve: 1/2".

Chamber air admittance valve: Edwards model RS1A.

Rotary pump air admittance valve: Edwards model RS1A.

Gas inlet valve: Edwards model OS1.
Pressure switch: "Speedivac" model VSK1.
Pirani-Penning gauge: "Speedivac" model 2A.
Pirani gauge head: model M6A, range: 1 to 10^{-2} Torr.
Penning gauge head: model 5MF, range: 10^{-2} to 10^{-5} Torr.
Low tension power supply: 60 A at 10 V.
Low tension protection system: magnetic circuit breaker.
High tension power supply: 50 mA at 3000 V AC (open circuit 5000 V). Capable of withstanding intermittent short circuits on secondary winding.
Electricity supply: 200 to 250 V, single phase 50 c/s.
Water supply: 0.7 l/min at supply temperature of 15°C.

7.9.2: Design alterations.

In order to obtain a low degassing rate, the glass dome had to be replaced by a metal chamber. This chamber would have also helped uniformity of the discharge during the process. The most suitable metal was stainless steel, which has a degassing rate in the range of 10^{-9} Torr-l/s. Therefore, type 304 stainless steel was used to construct the chamber. A water jacket was added around the chamber to help degassing of the chamber when hot water passes through it, and keep the chamber cool with cold water during the ion plating process.

In order to increase the pumping speed and to eliminate oil backstreaming from the diffusion pump, a liquid nitrogen trap was used. This trap was located between the high vacuum valve and the diffusion pump.

The backing line capacity tank was removed and the

diffusion pump was directly connected to the rotary pump via the backing valve.

The "Speedivac" unit had just one Pirani gauge which was located on the inlet side of the rotary pump, so it could be used to monitor either the backing line or the roughing line pressures. Disadvantages of this system were not only that the chamber pressure could not be measured, but also the gauge head could become contaminated if there were oil backstreaming from the rotary pump. To avoid these problems, the Pirani gauge head was relocated on the backing line between the diffusion pump and the backing valve. In this location, the gauge could continuously monitor the backing line pressure. To measure the chamber pressure, an Edwards Pirani 12 gauge was used, with a Pirani head type PRCT 10-K mounted on the lid of the vacuum chamber.

Fig.7.26a shows a block diagram of the vacuum line of the "Speedivac" coating unit, while Fig.7.26b shows a block diagram of the vacuum line of the ion plater.

The "Speedivac" coating unit was rewired and sections such as Carbon Sputtering which were not needed were removed.

The new wiring diagram is shown in Fig.7.27. In this rewiring, 3 ampere switches were used for the diffusion and rotary pumps, low and high tension power supplies.

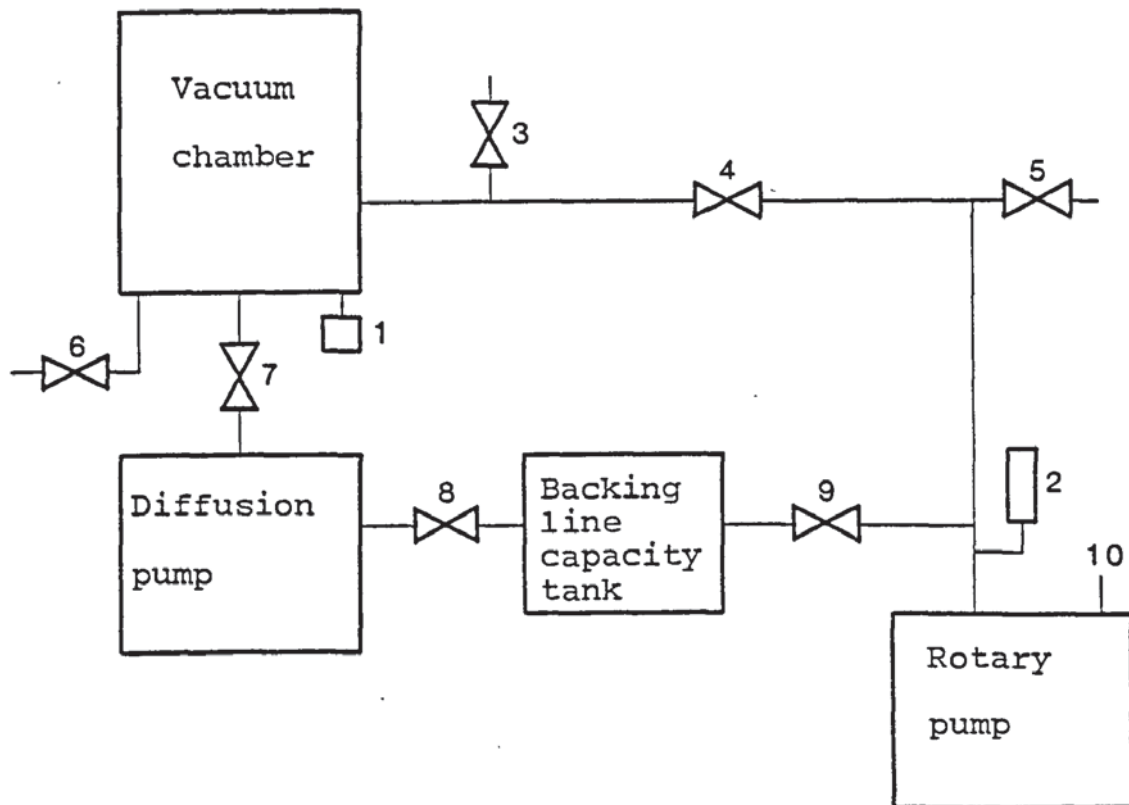


Fig.7.26(a): The vacuum line of the "speedivac" coating unit.

- 1: Penning gauge head,
- 2: Pirani gauge head,
- 3: vent valve,
- 4: roughing valve,
- 5: rotary pump air admittance valve,
- 6: gas inlet valve,
- 7: high vacuum valve,
- 8: tank isolation valve,
- 9: backing valve,
- 10: exhaust pipe.

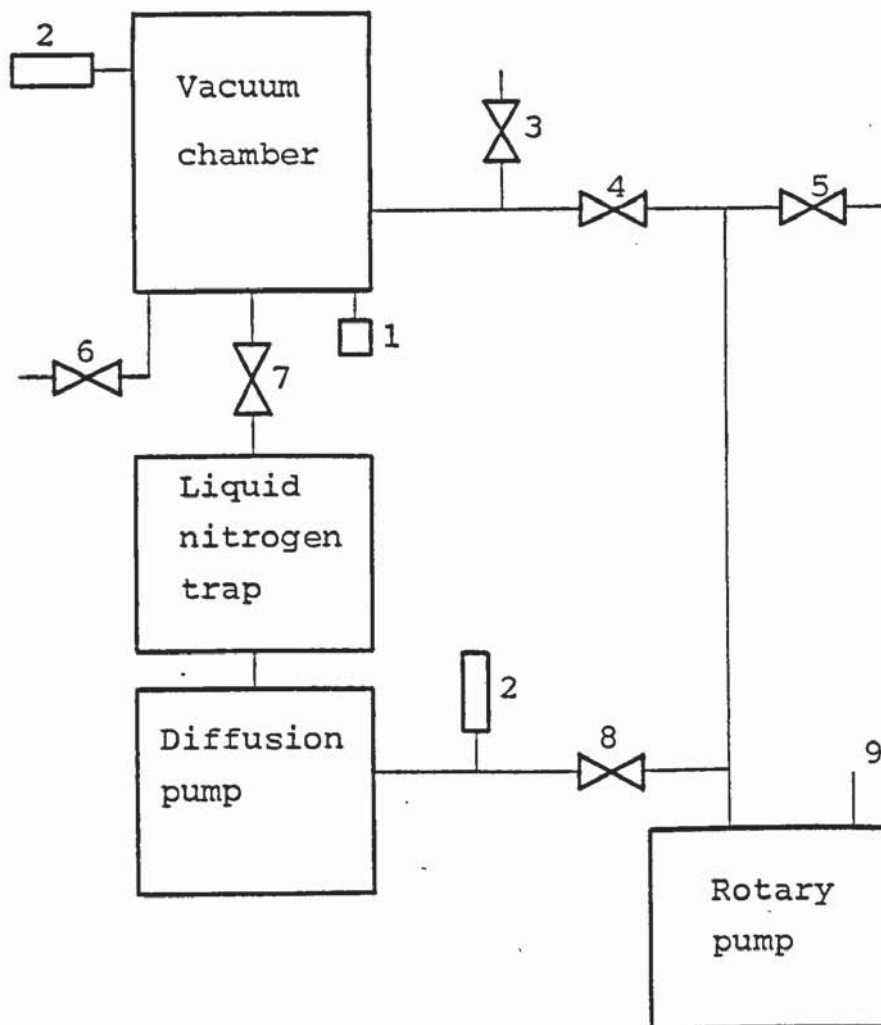


Fig.7.26(b): The vacuum line of the ion plater.

- 1: Penning gauge head,
- 2: Pirani gauge head,
- 3: vent valve,
- 4: roughing valve,
- 5: rotary pump air admittance valve,
- 6: gas inlet valve,
- 7: high vacuum valve,
- 8: backing valve,
- 9: exhaust pipe.

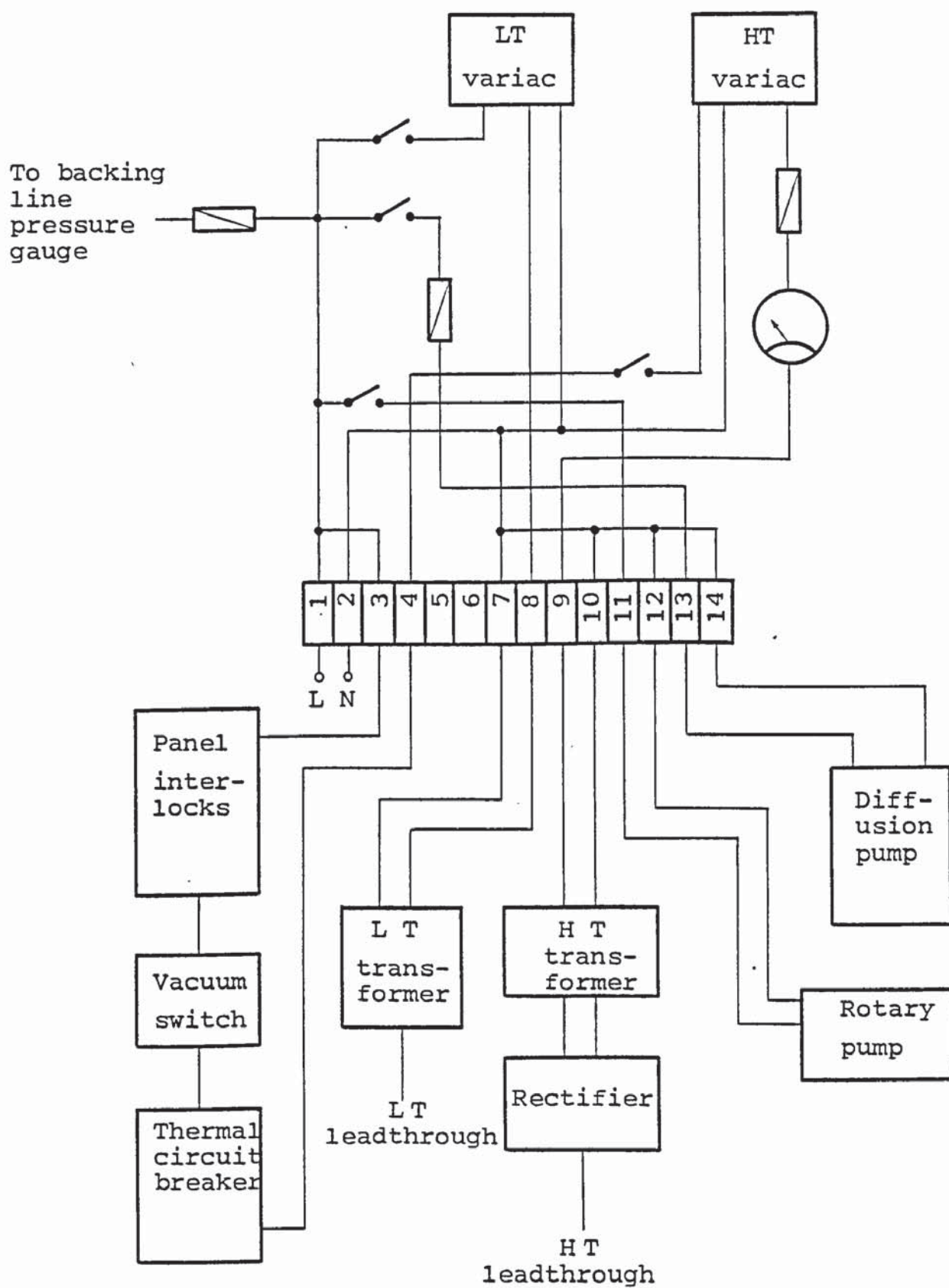


Fig.7.27: Wiring diagram of the ion plater.

A rectifier was used to obtain direct current. For close control of the low tension, a Variac variable resistance was used on the primary side of the power supply.

To provide a wider range of low tension currents, a 15 V, 120 A power supply was also used. This power supply had a three phase transformer, and was controlled from its own control panel.

7.9.3: Construction details.

First the whole "Speedivac" coating unit was stripped down and every part carefully cleaned. Then the base plate of the chamber was stripped of all coating materials by machining, and then ion plated with Chromium. The thickness of the chromium coating could not be directly measured non-destructively; however, as an indication, the coating thickness on the jig was measured at the level of the base plate. The coating was about $1.5\text{ }\mu\text{m}$ thick which indicated a thickness of more than $1.5\text{ }\mu\text{m}$ on the base plate.

The cylindrical body of the chamber was made of a $1/10$ " thick stainless steel sheet and welded at each end to the inside of a flange cut from $1/2$ " thick stainless steel plate. The water jacket was made of $1/16$ " thick stainless steel sheet and welded to the outside face of the flanges. Two short $3/8$ " OD stainless steel tubes were welded to the water jacket as inlet and drain ports. To ensure adequate circulation of water inside the jacket, ports were

located circumferentially to the chamber, so that the water path would be a helix from the top to the bottom of the jacket, with $n+0.5$ turns round the chamber (where n is an integer representing complete turns).

A 4" stainless steel tube connection, based on BS 1864, was mounted in the middle of the chamber to provide the base for a viewing port into the chamber. This connection piece had an "O" ring which was used to make a seal with a circle of 10 mm thick glass. A large hexagon nut was used to keep the glass in place.

A domed lid was made for the chamber out of 1/16" thick stainless steel sheet. The lid was welded to the inside of a flange similar to those of the chamber.

Two "O" rings were used to make vacuum seals between the lid, the chamber, and the base plate. These "O" rings were accommodated in grooves machined into the ends of the chamber flanges. Fig.7.28 shows a cross section of the chamber and its lid.

The lid incorporated a Pirani gauge head (via a short stainless steel connection piece) and a high tension lead-through. To protect the gauge head from evaporated and sputtered materials, a 3 cm diameter stainless steel disk was used to cover the opening of the connection from the inside of the chamber. This disk was mounted on the lid by means of 3 small bolts in such a way that there was a

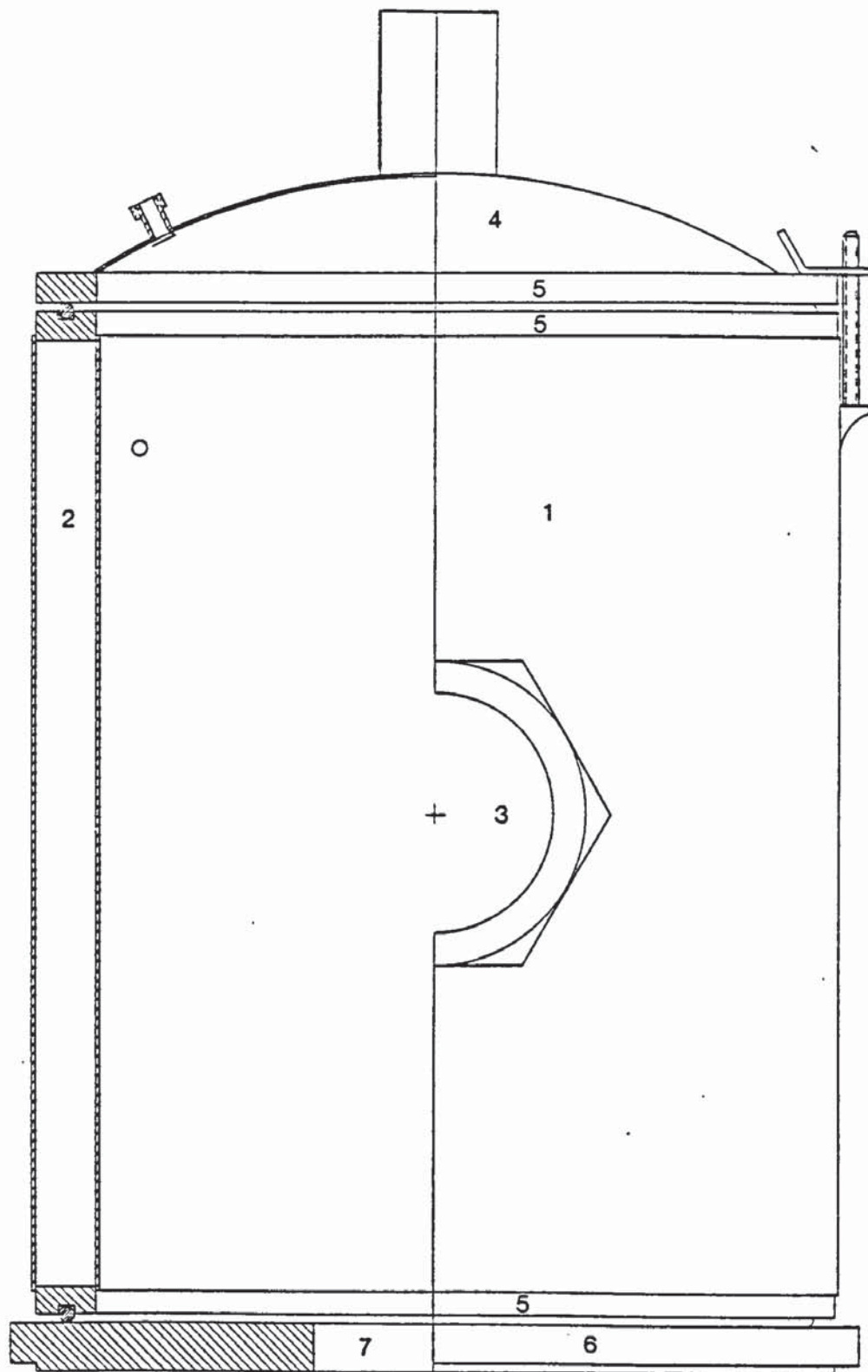


Fig.7.28: Chamber of the ion plater. Scale 1:4

- 1: body of the chamber,
- 2: water jacket,
- 3: view port,
- 4: lid,
- 5: stainless steel flange,
- 6: base plate,
- 7: high vacuum port.

gap of about 4 mm between them (see Fig.7.28).

An Edwards high tension leadthrough type 7D was used which was capable of operating at up to 150°C and carrying an electric current of up to 15 amperes at 5000 V DC. The outside surface of the lid was polished around the leadthrough entrance port to provide a smooth surface for the "O" ring sealing. Due to the domed shape of the lid, as the leadthrough was tightened in position, the "O" ring tended to squeeze out. To prevent this, a stainless steel ring was slid onto the main body of the leadthrough. The lid was too thin to allow the leadthrough to be tightened directly onto it. Therefore a 1 cm long tube was placed round the leadthrough, between the lid and the nut. Two holes were drilled into the tube in order to prevent air being trapped in the confined space within the tube.

In order to protect the ceramic insulators of the leadthrough, a stainless steel sleeve was made to cover the insulators, leaving a gap of about 3 mm from the lid. This ensured pump down of the space confined within the sleeve, while protecting the insulators from evaporated and sputtered material. This sleeve was secured to the leadthrough by a nut. The whole leadthrough assembly is shown in Fig.7.29.

To protect the operator, the high tension leadthrough was confined within a 5 cm diameter, 8 cm long stainless steel tube which was welded onto the outside of the lid. The

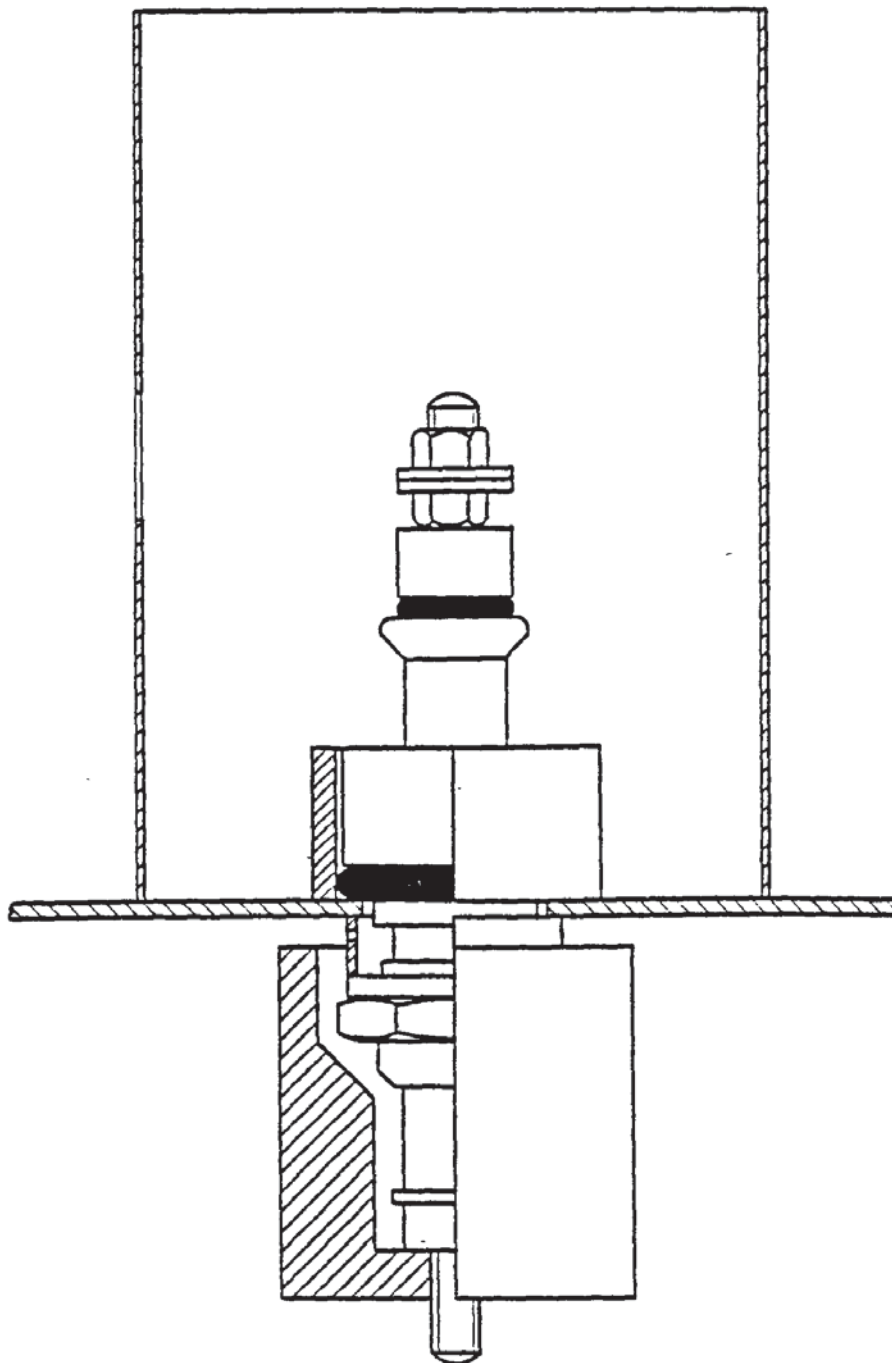


Fig.7.29: The assembly of the high tension
leadthrough. Scale 2:1


end of this tube was closed with a small stainless steel lid, secured by 4 small bolts. A hole in the tube wall provided the required access for the high tension cable.

An earth wire was used to join the earth connection of the rectifier to the lid and the chamber, to provide the anode for the glow discharge. This earth cable was carried inside a metal reinforced, flexible plastic tube together with the high tension cable. To ensure that there would be no flashover between the high tension cable and the earth wire, the latter was additionally enclosed in a small bore plastic tube. The reinforced tube was used to protect the high tension cable and the earth wire against accidental damage. This tube was fixed to the body of the cabinet at the rectifier end, and to the high tension leadthrough housing, via a support plate, at the other end. The base plate of the chamber was also earthed by means of a high current cable, connected to the low tension power supply.

The "Speedivac" low tension leadthroughs were used without any change. However, a leak developed when the 120 A power supply was used at full power. The high current caused the copper core of the leadthrough to warm up and extend. This elongation together with the weight of the boat clamps, forced the bottom plug of the leadthrough to become loose and caused the leak. The cure was to permanently seal the bottom plug and the glass tube with Araldite epoxide. To protect the glass insulator from sputtered and evaporated

material, a metal shield was constructed and used. A cross-section of the low tension leadthrough is shown in Fig.7.30.

A cold water supply was used for cooling the diffusion pump at all times of operation, and to cool the vacuum chamber during discharge cleaning and evaporation processes. A valve was used to cut off cold water from the chamber; then a hot water supply could be used to help degassing of the chamber prior to any coating or discharge cleaning.

For ease of mounting the specimen, loading the coating materials, and cleaning of the chamber, it was useful to be able to lift the lid and the chamber off the base plate separately. For this purpose a winch system was employed. The winch could carry a maximum load of 240 Kg and was bolted to the side of the main cabinet of the ion plater. A  shape post was made of right angle Dexion, with a "U" cross section. This post was also bolted to the side of the cabinet. A pre-strained nylon rope capable of carrying a maximum load of 100 Kg was used to lift the chamber. The total weight of the chamber was calculated to be about 24 Kg, including the water in the water jacket. The safety of the winch system was assessed by lifting a load of about 40 Kg, which proved to be satisfactory.

Three 2" long 1" wide strips were cut of 1/10" thick stainless steel plate, and bent to 120° at 2/5 of their

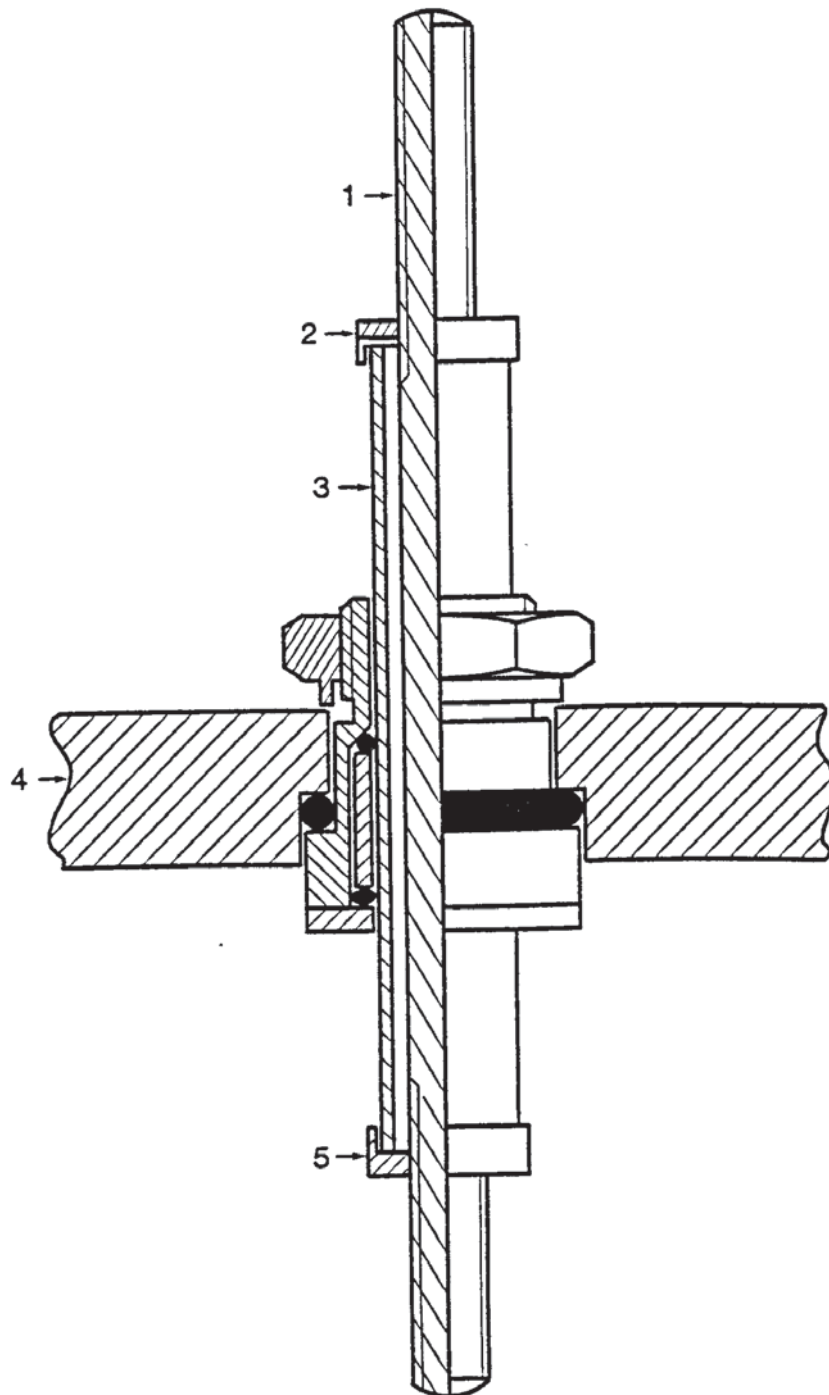


Fig.7.30: The low tension leadthrough assembly

Scale 1:1

1: Copper rod, threaded at both ends

2: top plug

3: glass tube

4: base plate

5: bottom plug

length. $\frac{1}{4}$ " holes were drilled at the middle of each part of every strip. These strips were welded to the lid flange at equal distances from each other and part of them stood out to act as small ledges. Three 1.5" long, $\frac{3}{16}$ " stainless steel bolts were welded to the water jacket so that when the lid was placed on the chamber, bolts would pass through the holes; and the lid could be held in place by 3 wing-nuts. The other holes of the strips were used to hook the lid by the rope. Fig.7.31 shows the winch system.

A high purity argon gas bottle was connected to the gas inlet valve by a $\frac{1}{4}$ " OD copper tube. Because needle valves usually do not provide complete closure of the gas flow, an ordinary gas valve was used at the high pressure side of the needle valve as a shut off valve. Provided that the bottle side of this valve remained at high pressure, contamination of the argon gas by air could not take place. A small platform equipped with a wheel was attached to the main frame of the ion plater to carry the gas bottle and maintain mobility of the unit. The gas bottle was secured in position by being chained to the main cabinet of the unit.

Fig.7.32 shows a side view of the ion plater. In this photograph the vacuum chamber, water supplies, and the gas bottle can be seen. Fig.7.31 shows the front view of the ion plater, the control panel, and valve locations.

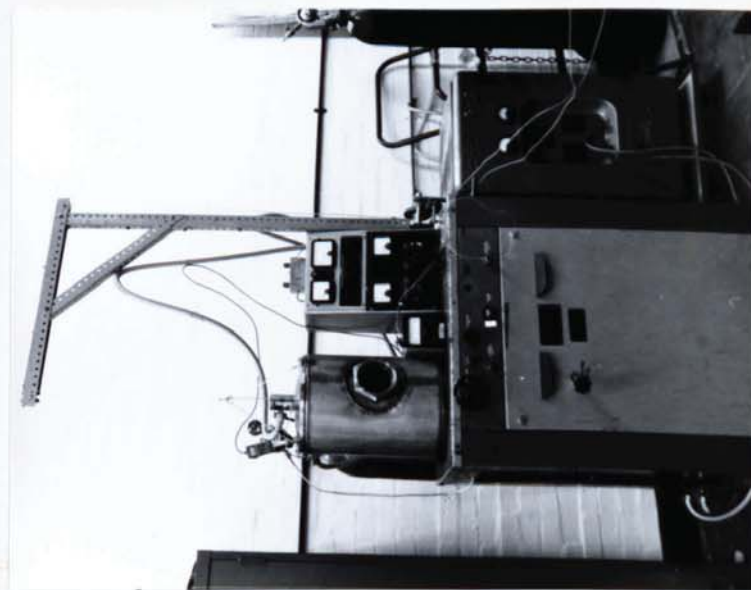


Fig.7.31: The winch system and the front view of the ion plater.

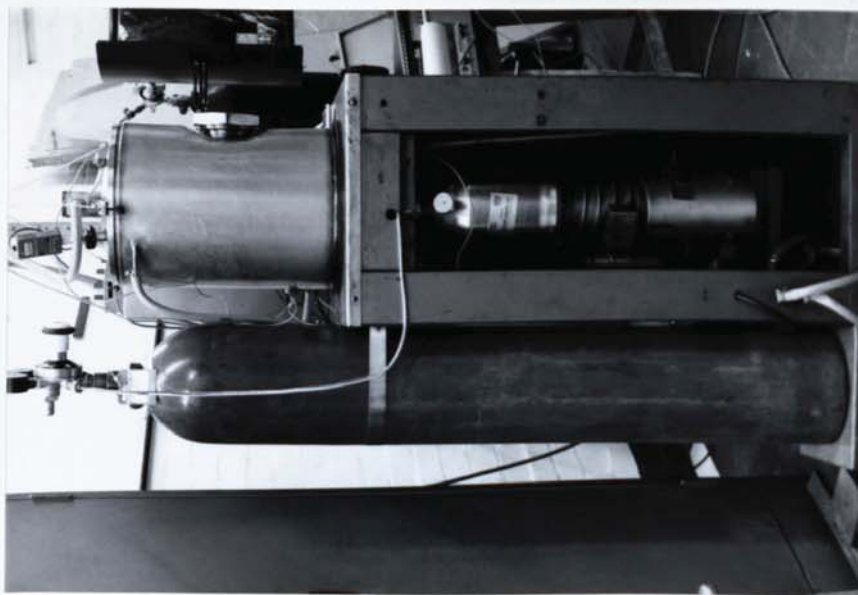


Fig.7.32: Side view of the ion plater.

7.9.4: Further requirements of the ion plater.

This ion plater, as it stands (September 1982), can be satisfactorily used for ion plating of small articles. The main limitation is the power supply. The present high tension power supply can only provide 50 mA at 3000 V. As a current density of 1 mA/cm^2 is desirable, a stronger power supply is required for larger specimens or specimens with complicated geometries which demand higher currents. This power supply should preferably provide up to 300 mA at 3000 V. Use of such a power supply would require modification of the high tension leadthrough.

To obtain higher evaporation rates, a more powerful low tension power supply is needed. At present a 300 A, 15 V power supply is available which would enable the operator to use bigger evaporation boats. Use of this power supply would necessitate employment of water cooled low tension leadthroughs.

The recommended operational procedure for this ion plater is given in Appendix B.

RESULTS AND DISCUSSION.

8.1: Sputtering results obtained using jig number 1.

Results obtained from 24 specimens tested at 20 and 30 mTorr pressure; 3, 4 and 5KV applied voltages and sputtering durations of 15, 30, 45 and 60 minutes are shown in Table 8.1. As this table indicates, there is a large variation in the sputtering rate under all conditions of operation. The only obvious and expected relationship found, is that by increasing either the voltage or the pressure, vigour of sputtering increases (see Fig.8.1). Statistical analysis of the results, presented in Table 8.2, indicates that the most suitable sputtering rates, regardless of duration, are obtained at 30 mTorr pressure and 4KV applied voltage. Visual assessment of specimens also indicates that these conditions produce more uniform etching. Fig.8.2 shows sputter etched specimens at 20 mTorr pressure and 5KV applied voltage. It is clear that, the etching is non-uniform and relatively time independent. Fig.8.3 shows 30 minutes sputter etched specimens at 20 mTorr pressure, and Fig.8.4 shows 30 minutes sputter etched specimens at 30 mTorr pressure. Comparison of these two photographs confirms the results presented in Table 8.2, i.e. 30 mTorr working pressure gives more consistent etching.

Scanning electron microscopy was used to examine the

(text cont. P.204)

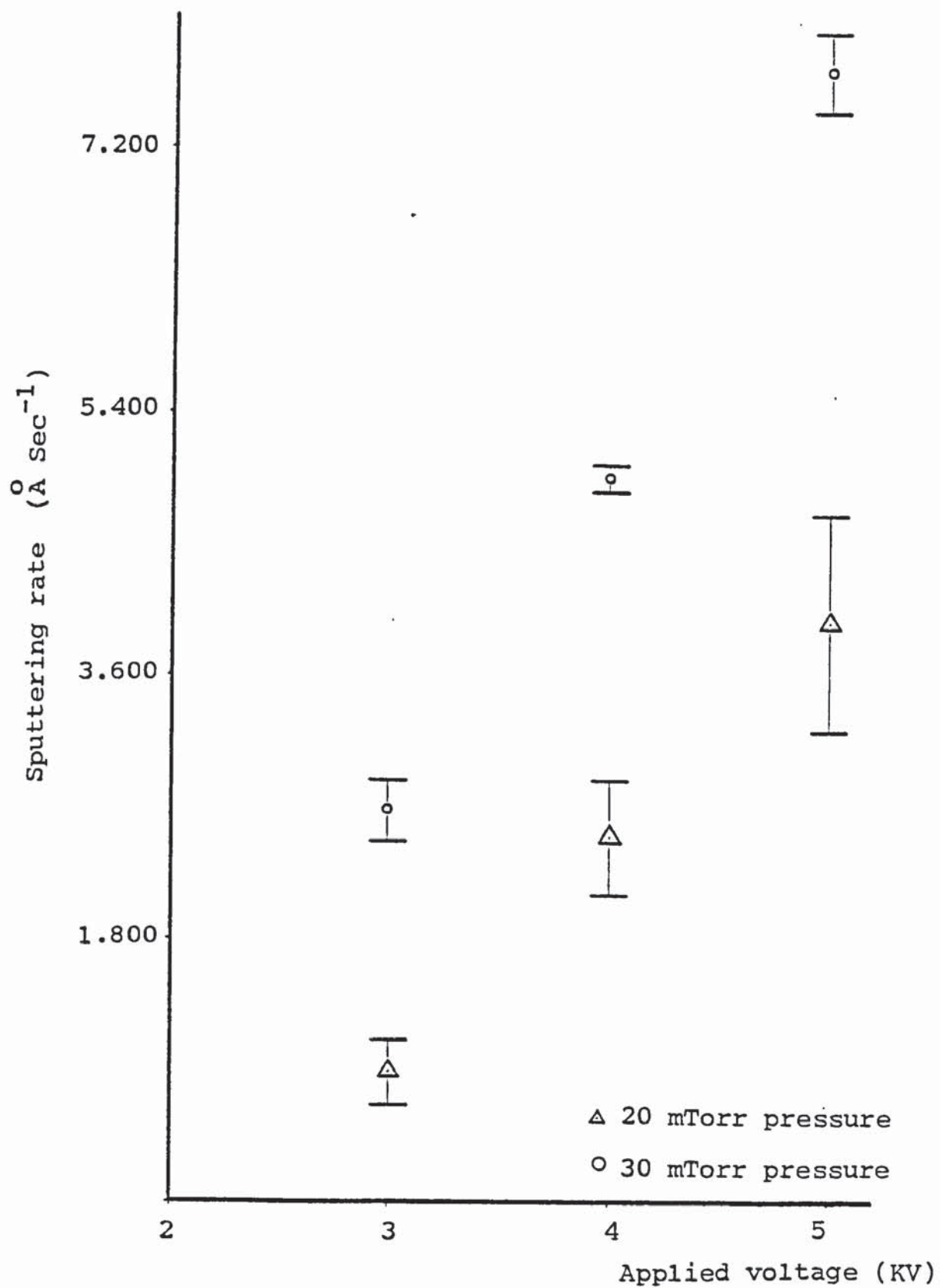


Fig.8.1: Influence of applied voltage and pressure on sputtering rate.

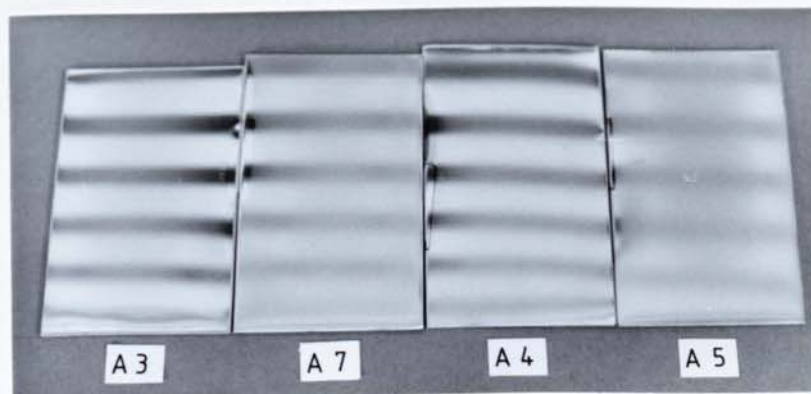


Fig.8.2: Sputter etched specimens at 20 mTorr pressure and 5 KV applied voltage.

Sputtering durations:	A3	15 min
	A7	30 min
	A4	46 min
	A5	61 min

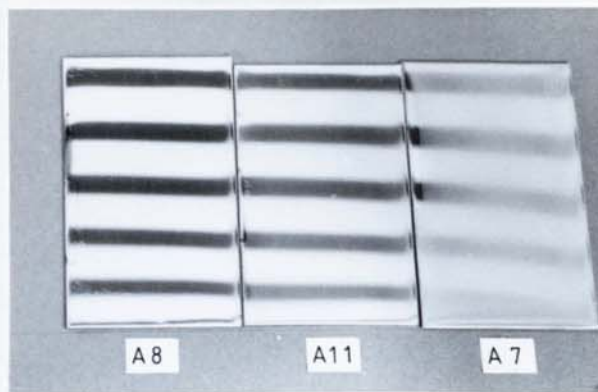


Fig.8.3: 30 minutes sputter etched specimens
at 20 mTorr pressure.

Applied voltage:	A8	3 KV
	A11	4 KV
	A7	5 KV



Fig.8.4: 30 minutes sputter etched specimens
at 30 mTorr pressure.

Applied voltage:	A26	3 KV
	A21	4 KV
	A17	5 KV

Specimen number	Original weight (g)	Weight loss (mg)	Working pressure (mTorr)	High voltage (KV)	Sputtering duration (min)	Total energy input (j)	Removed thickness	
							total (μm)	per second (\AA)
A10	39.8519	5.2	20	3	15	32476	0.065	0.72
A08	39.6639	11	20	3	30	53491	0.139	0.77
A09	39.5817	25.9	20	3	45	82935	0.327	1.21
A06	39.4137	23.7	20	3	60	98586	0.301	0.83
A14	39.5639	17.9	20	4	15	59118	0.226	2.51
A11	39.6450	30.5	20	4	30	122046	0.385	2.14
A13	39.9864	49.1	20	4	45	191484	0.614	2.27
A12	39.5088	94.5	20	4	66	336798	1.196	3.02
A03	39.3566	30	20	5	15	103912	0.381	4.23
A07	39.6354	63	20	5	30	199597	0.795	4.41
A04	39.8986	62.2	20	5	46	247114	0.779	2.82
A05	39.2337	123.4	20	5	61	396375	1.573	4.30
A27	39.8140	17.4	30	3	15	71077	0.218	2.43
A26	39.2472	39.7	30	3	30	150768	0.506	2.81
A24	39.3273	65.1	30	3	47	223821	0.828	2.93
A28	39.7464	74.4	30	3	60	255726	0.936	2.60
A22	39.7380	34.7	30	4	15	147276	0.437	4.85
A21	39.8346	74.6	30	4	32	296904	0.936	4.88
A19	39.8789	108.7	30	4	45	426642	1.363	5.05
A20	39.8571	144.9	30	4	62	608742	1.818	4.89
A18	39.5923	57	30	5	15	249630	0.720	8.00
A17	38.8224	112.9	30	5	30	482587	1.417	7.87
A15	39.4958	160.3	30	5	45	701512	2.029	7.52
A16	39.2101	210.3	30	5	60	942240	2.682	7.45

Table 8.1: Results obtained from 24 specimens, using
jig number 1.

Pressure (mTorr)	Applied voltage (KV)	Average sputtering rate ($\text{\AA}/\text{s}$)	Standard deviation ($\text{\AA}/\text{s}$)	Coefficient of variation (%)
20	3	0.88	0.22	25
20	4	2.48	0.39	15.7
20	5	3.94	0.75	19
30	3	2.69	0.22	8.2
30	4	4.92	0.09	1.8
30	5	7.71	0.27	3.5

Table 8.2: Statistical analysis of the vigour of the sputtering (based on the results presented in Table 8.1)

surface of the stainless steel after sputter etching. Figs.8.5 and 8.6 are photomicrographs showing the surface of specimen A16, which was etched at 30 mTorr pressure and 5KV applied voltage for 60 minutes. Two types of segregates may be identified on this specimen: a small amount of segregates at the grain boundaries and pillar type segregates within some grains. The pillar type structures, which are shown in Fig.8.6, are similar to the pillar structures observed by Witcomb⁽²⁰²⁾, and therefore may be fibrous MnS (this could be confirmed by X-ray micro-analysis). An important feature of this specimen is its relatively smooth etching. The orientation dependence of sputtering on this specimen can be identified by different etching of the twin bands present in some grains

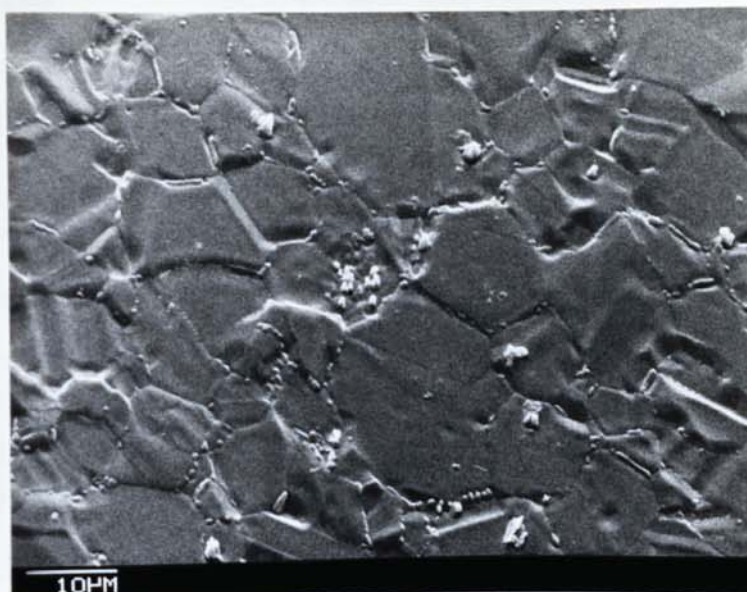


Fig.8.5: Sputter etched surface of specimen A16 showing two types of segregates
Average depth of erosion: $2.7 \mu\text{m}$



Fig.8.6: Pillar type segregates on sputter etched surface of specimen A16.

(see Fig.8.5). According to Table 8.1, an average of $2.7\text{ }\mu\text{m}$ is removed from the surface of this specimen and, as is evident from the photomicrographs, no part of the original surface is left on the specimen.

Figs. 8.7 and 8.8 show the surface of specimen A22 which was sputter etched at 30 mTorr pressure and 4KV applied voltage. This specimen also shows two types of segregates, segregates at the grain boundaries and segregates within grains. As these inclusions are much more numerous than the pillar type structures observed on specimen A16, and as they have a different shape and distribution, it is considered that they are not MnS inclusions. This view is supported by referring to the composition of the steel used, and the fact that its sulphur content was not enough to produce so much MnS. Although no elemental microanalysis was done on this specimen, the similarities between these protrusions and those observed by Witcomb⁽²⁰²⁾ suggest they may have similar compositions, i.e. they are manganese silicate inclusions with Mn and Si component composition ranging between Mn_3Si and Mn_5Si_3 .

According to Witcombe some of these second phase particles appear at grain boundaries, but the majority of them are intergranular and are not associated with any obvious nucleation sites in the fcc austenitic matrix. But in specimen A22, as shown in Figs. 8.7 and 8.8, the distribution of the second phase particles is non-uniform and differs from one to another, which is an indication of orientation dependence of the segregation. According to



Fig.8.7: Sputter etched surface of specimen
A22. Average depth of erosion: $0.44 \mu\text{m}$

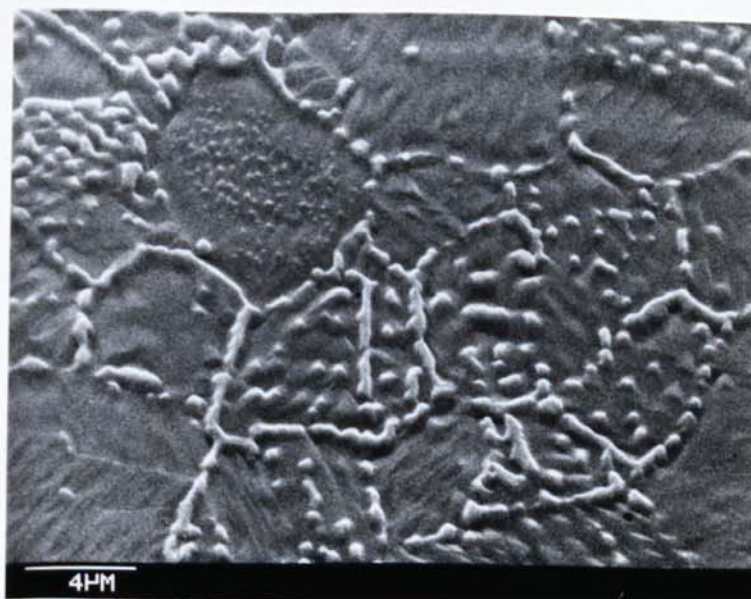


Fig.8.8: Magnesium silicate inclusion on
sputter etched surface of specimen
A22.

Table 8.1, an average of $0.44\text{ }\mu\text{m}$ was removed from the surface of this specimen, and as is evident from the photomicrographs, the original surface layers of the specimen are completely removed.

Sputter etching of specimens A21 and A17 has also caused complete removal of the original surface layers (see Figs.8.9 and 8.10), except where there was a deep indentation on the specimen, i e. A21.

Fig.8.11 shows the surface of specimen A26 which was sputter etched at 30 mTorr pressure and 3KV applied voltage for 30 minutes. An important feature of this specimen is the presence of a part of the original surface. Another important feature is the absence of any smoothly etched grain, and this is despite the fact that on average a thickness of about $0.5\text{ }\mu\text{m}$ was removed from the surface, which is more than was removed from specimen A22 (see Table 8.1). Here the important difference is between their sputtering rates, which was basically caused by the lower voltage applied to specimen A26. Therefore, it might be considered that the applied voltage has a great effect on the removal of the original surface layers, through the sputtering rate.

Figs.8.12 and 8.13 are photomicrographs showing the surface of specimen A03, which was sputter etched at 20 mTorr pressure and 5KV applied voltage for 15 minutes. As is evident from these photomicrographs, the important

(text cont. P. 212)

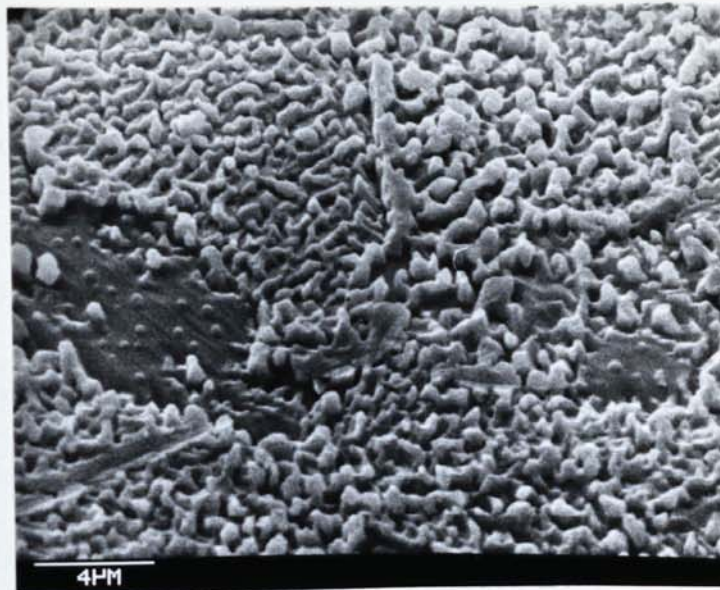


Fig.8.9: Surface of specimen A21, sputter etched at 30 mTorr pressure and 4 KV applied voltage for 30 minutes. Average depth of erosion: 0.94 μm

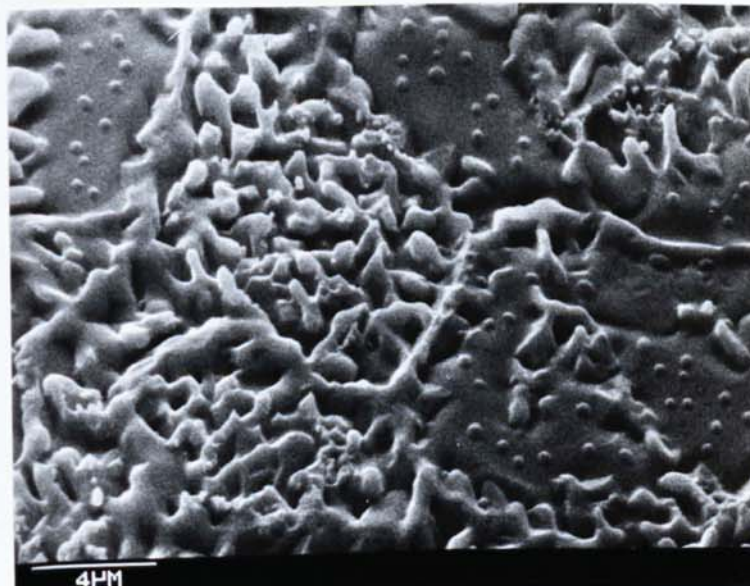


Fig.8.10: Surface of specimen A17, sputter etched at 30 mTorr pressure and 5 KV applied voltage for 30 minutes. Average depth of erosion: 1.4



Fig.8.11: Surface of specimen A26 sputter etched at 30 mTorr pressure and 3 KV applied voltage for 30 minutes. Average depth of erosion: 0.5 μm

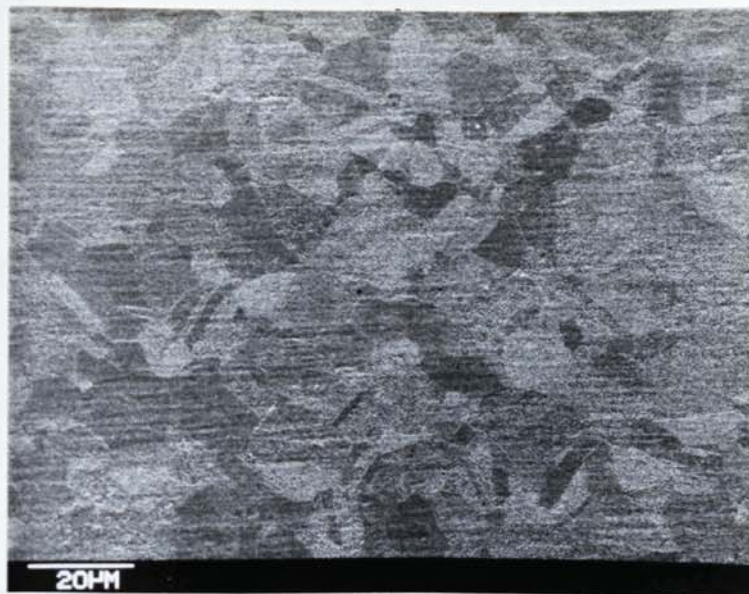


Fig.8.12: Surface of specimen A03 sputter etched at 20 mTorr pressure and 5 KV applied voltage for 15 minutes. Average depth of erosion: 0.4 μm

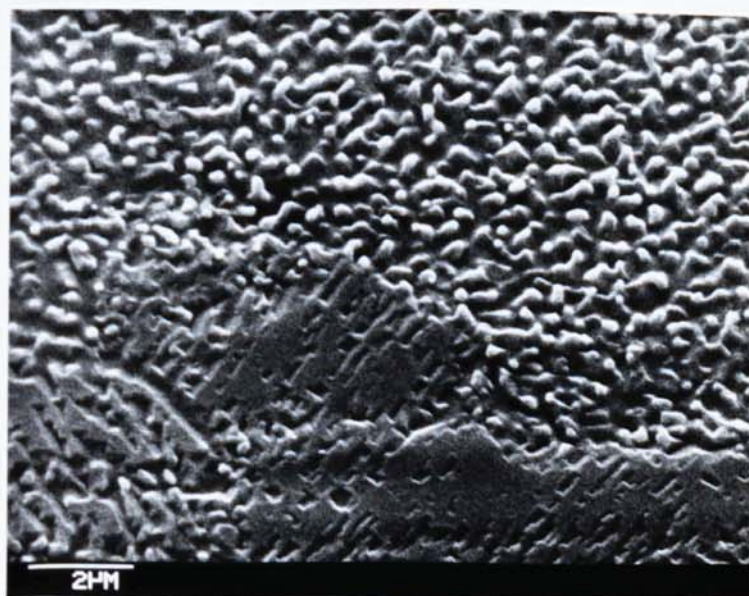


Fig.8.13: Sputter etched surface of specimen A03 showing residues of the original surface.

features of this specimen are the presence of some of the original surface and the absence of smoothly etched grains, despite the similarity of sputtering rate and average removed thickness to those of specimen A22. Here, unlike specimen A26, the applied voltage is high, and from the average values of the sputtering rate and removed material, complete removal of the original surfaces might have been expected. But the presence of parts of the original surface indicates that, although a higher applied voltage results in a higher sputtering rate, ion bombardment dose is also an important factor. This suggests that, for the removal of the original surface layers under conditions of glow discharge in a relatively short period of time, a high flux of bombarding particles with relatively high energies is required.

8.2: The edge effects.

All specimens held in jig number 1 suffered from an edge effect. This effect, which can be described as uneven etching of the specimen, was caused by the non-uniform distribution of the electrostatic field on the specimen. This affects the distribution of the ion current density near the edges.

Wehner^(257,258) has suggested that the edge effect is caused by the focusing of the bombarding ions on the near edge regions, and also the difference in angle of incidence, between the edge and the flat parts of the

specimen. According to Wehner, the field lines on the ion sheath become curved near sharp edges. As bombarding particles cannot follow the curved field lines very well, they become focused on a region somewhat away from the edge.

Fig.8.14 shows photomicrographs taken from the corner of specimen A19 which had the same appearance as specimen A21 in Fig.8.4. This specimen was selected because it was reasonably uniformly etched, and was expected to have a minimal difference in microstructure, between the edge and the central area. Part (a) of Fig.8.14 shows an area about 0.5 cm away from the corner of the specimen, towards the middle. Part (c) of the Fig. shows an area about 1.5 cm away from the corner, and part (b) shows an area between the two. Part (a), which represents the edge area, shows general etching, since different grains may be identified. The etching on this region is light, as the etch pits are small, and they have not grown enough to cut through the small ripples. Part (c) shows the central area of the specimen, which is more heavily etched than the edge region. On this area, etch pits are deeper, and have cut through most of the small surface ripples. Part (b) shows the intermediate region which is more heavily etched than the other two regions. In this region almost all ripples are cut through by the growing etch pits. The difference in etching between these three regions might have been caused by the difference in the ion current density, and angle of incidence, in line with

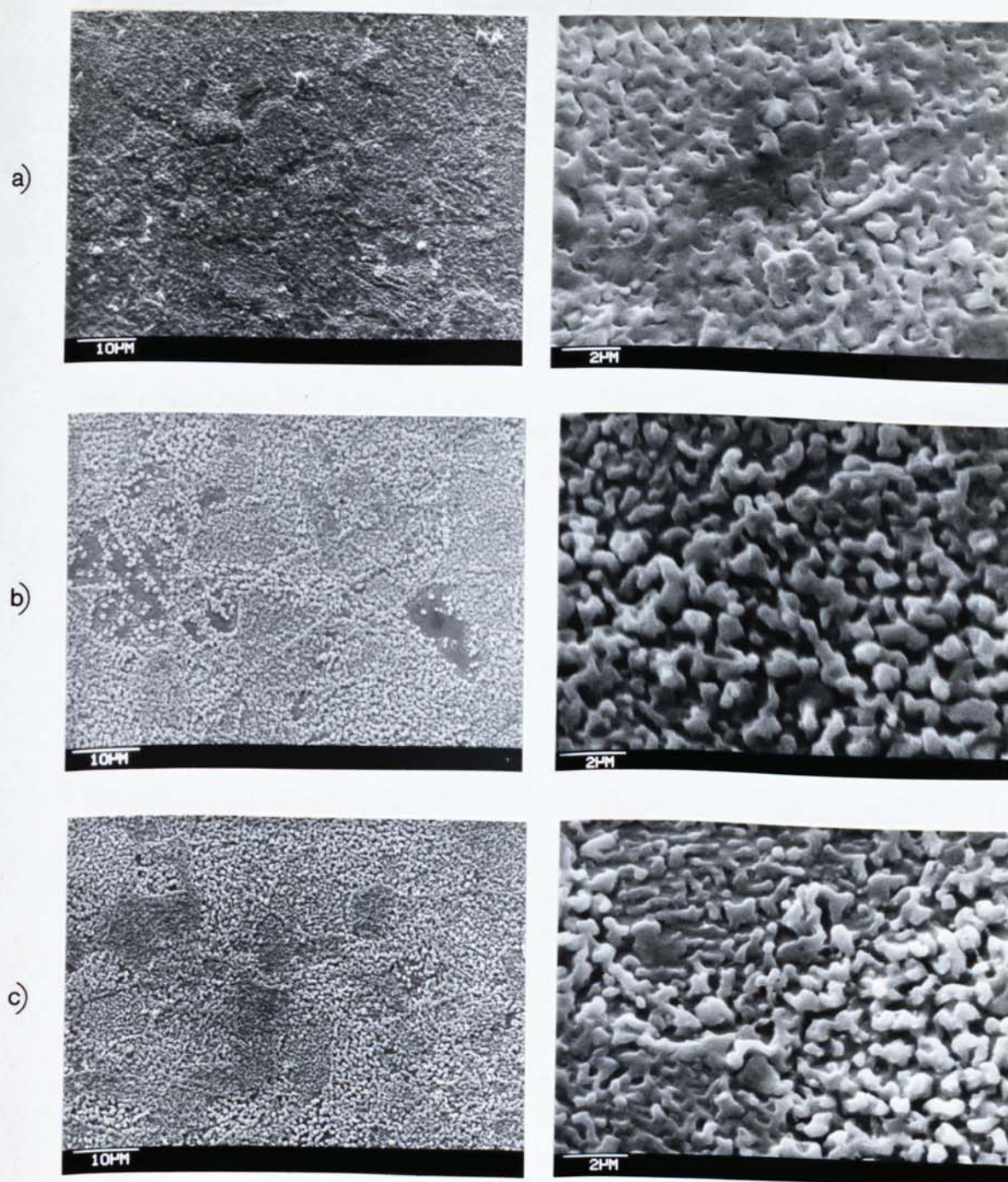


Fig.8.14: Microstructure of the edge of specimen A19

(a): 0.5cm from the corner (edge area)

(b): 1 cm from the corner (intermediate)

(c): 1.5cm from the corner (central area)

Wehner's proposed explanation. Due to the lack of sufficient information, a more accurate account of the mechanisms involved in the formation of the edge effect cannot be given.

The edge effect is most undesirable as it could become more pronounced during subsequent coating. This is due to the fact that, the difference in etching and higher local temperatures around the edge regions affect the microstructure and appearance of the coating.

8.3: Effect of background pressure.

Background pressure was expected to affect the sputtering rate. In order to investigate this factor, nine specimens were ion bombarded at 30 mTorr argon pressure and 5KV applied voltage for 60 minutes. The results of these tests are presented in Tables 8.3 and 8.4. As these tables indicate, background pressure has a pronounced effect on the sputtering rate. The main residual vapours and gases in the vacuum chamber were water vapour which resulted from outgassing of the chamber walls and oxygen and nitrogen from small leaks in the system. The other important residual vapour in the system was oil (as was indicated by an Anavac II mass spectrometer), possibly from the rotary pump⁽²⁵⁹⁾. As long as the amount of the latter vapour can be assumed to be independent of the background pressure, the aforementioned gases and vapours could be responsible for the inconsistency of sputtering rate by producing oxides and nitrides which have lower sputtering yields than the bare metal.

Specimen number	Original weight (g)	Weight loss (mg)	Background pressure (Torr)	Removed material	
				total (μm)	per second (\AA)
A31	39.6300	96.2	$\sim 10^{-5}$	1.214	3.37
A32	39.7313	117.5	$\sim 10^{-5}$	1.479	4.11
A33	39.6283	182.7	$\sim 10^{-5}$	2.305	6.40
A37	39.2827	162.2	$\sim 10^{-5}$	2.064	5.73
A34	39.2796	219.1	$\ll 10^{-5}$	2.789	7.75
A35	39.4872	223.0	$\ll 10^{-5}$	2.824	7.84
A36	38.6162	228.3	$\ll 10^{-5}$	2.956	8.21
A38	39.8374	227.0	$\ll 10^{-5}$	2.849	7.91
A39	39.0143	222.1	$\ll 10^{-5}$	2.846	7.91

Table 8.3: Effect of background pressure on specimens sputter etched at 30 mTorr working pressure and 5KV applied voltage for 60 minutes.

Background pressure (Torr)	Sputtering rate ($\text{\AA}/\text{s}$)		Coefficient of variation (%)
	Average	Standard deviation	
$\sim 10^{-5}$	4.90	1.40	28.7
$\ll 10^{-5}$	7.92	0.17	2.1

Table 8.4: Statistical analysis of the results presented in Table 8.3.

8.4: Results obtained using jig number 2.

Twenty eight specimens were sputter etched under conditions of 30 mTorr pressure, 4KV applied voltage and less than 10^{-5} Torr background pressure. The results of these tests and their statistical analysis are presented in Tables 8.5 and 8.6 respectively. As Table 8.6 and Fig.8.15 show, the sputtering rate gradually increases as the sputtering duration increases. This rise in sputtering rate might have been caused by the removal of the original surface and exposure of more bare metal to the bombarding flux, as the sputtering duration extends. Wehner⁽²⁵⁷⁾ has discussed the influence of the original oxide film, and has observed that by removal of the original surface, the sputtering rate might even drastically increase. On the other hand, if the bombarding flux contains some reactive particles, they might react with the surface and produce new surface contaminants on the specimen. As explained in the last section, background pressure has a pronounced effect on the sputtering rate. In this set of experiments, although the background pressure was kept below 10^{-5} Torr, it does not mean that the system was completely clean. Therefore, another cause for the increase in sputtering rate might be the continuous consumption of water vapour, oxygen and nitrogen by highly reactive sputtered atoms, such as chromium. This gettering effect of chromium causes the working environment to become progressively "cleaner", which in turn reduces the probability of formation of low sputtering yield materials on the specimen. As Tables 8.5 and 8.6 indicate, the use of jig number 2 under similar conditions has reduced the sputtering rate; i e. a grand average of 1.09 \AA/s compared

Specimen number	Original weight (g)	Weight loss (mg)	Time (min)	Removed thickness	
				total (μm)	per second (\AA)
A52	39.3808	6.5	15	0.082	0.92
A66	39.9166	7.2	15	0.090	1.00
A67	40.0078	8.4	15	0.105	1.17
A68	39.9900	6.9	15	0.086	0.96
A69	39.7862	8.0	15	0.100	1.12
A70	39.4488	7.7	15	0.098	1.08
A71	39.9829	7.7	15	0.096	1.07
A54	39.8900	16.3	30	0.204	1.13
A55	39.8347	14.9	30	0.187	1.04
A56	39.7160	15.0	30	0.189	1.05
A57	39.9088	15.7	30	0.197	1.09
A58	39.7952	15.3	30	0.192	1.07
A59	39.7798	14.9	30	0.187	1.04
A51	39.6069	16.6	32	0.209	1.09
A53	38.7749	21.9	45	0.282	1.05
A60	39.3500	23.2	45	0.295	1.09
A62	40.0511	24.0	45	0.300	1.11
A63	40.0097	26.3	45	0.329	1.22
A65	39.9730	22.0	45	0.275	1.02
A64	39.0790	24.6	47	0.315	1.12
A61	39.6184	25.0	48	0.315	1.09
A50	39.3373	36.0	60	0.458	1.27
A72	39.0103	31.3	60	0.401	1.11
A73	39.6156	27.0	60	0.341	0.95
A74	39.6195	32.9	60	0.415	1.15
A75	39.7890	36.4	60	0.457	1.27
A76	39.7356	31.4	60	0.395	1.10
A77	39.6776	32.1	60	0.404	1.12

Table 8.5: Results obtained using jig number 2.

Specimens sputter etched at 4KV

applied voltage and 30 mTorr working
pressure.

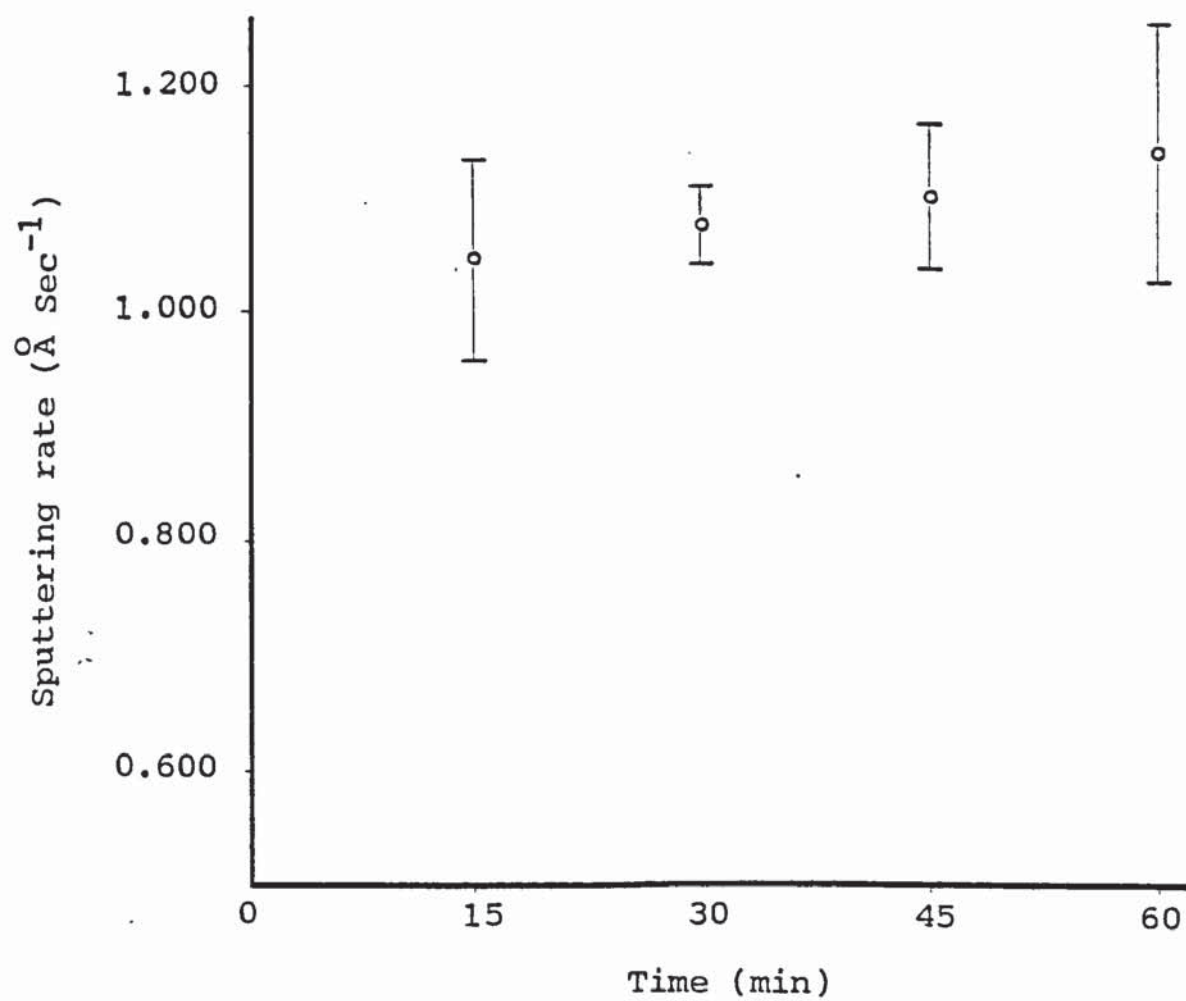


Fig.8.15: Variation of sputtering rate by sputtering time.

Time (min)	Average sputtering rate (Å/s)	Standard deviation (Å/s)	Coefficient of variation (%)
15	1.045	0.089	8.5
30	1.074	0.035	3.3
45	1.099	0.063	5.7
60	1.139	0.112	9.8

Table 8.6: Statistical analysis of the results presented in Table 8.5

with $4.92 \frac{\text{Å}}{\text{s}}$ for jig number 1. Influential parameters in determining the sputtering rate are the dose and energy of bombarding particles, and the sputtering yield of the material. As Figs. 8.16 and 8.17 show, the complete surfaces of the specimens have been subjected to a uniform bombardment; thus it can be concluded that there has been no geometrical effect protecting any part of the specimens.

Referring to the design of jig number 1, no geometrical factor can be found which could intensify the ionization efficiency of the discharge. Therefore, at similar pressures and applied voltages, changes in sputtering yield might be responsible for lower sputtering rates when jig number 2 was used. The sputtering yield greatly varies with changes in the angle of incidence; it is low at normal incidence, then increases to a maximum at an incidence angle of about 70° to the surface normal, and then sharply reduces to zero at near grasing angles (see Fig.8.18(c)). Specimens held in jig number 1 have been subjected to ion bombardment from all directions. The probability distribution of directions leads to a probability distribution of sputtering yields. The means of these two distributions indicate the mean direction

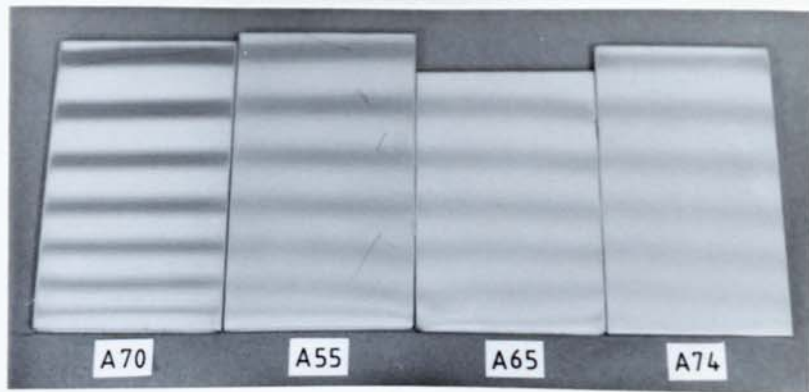


Fig.8.16: Changes in brightness of sputter etched specimens at 30 mTorr pressure and 4 KV applied voltage, fixed in jig number 2.

Sputtering durations:	A70	15 minutes
	A55	30 minutes
	A65	45 minutes
	A74	60 minutes

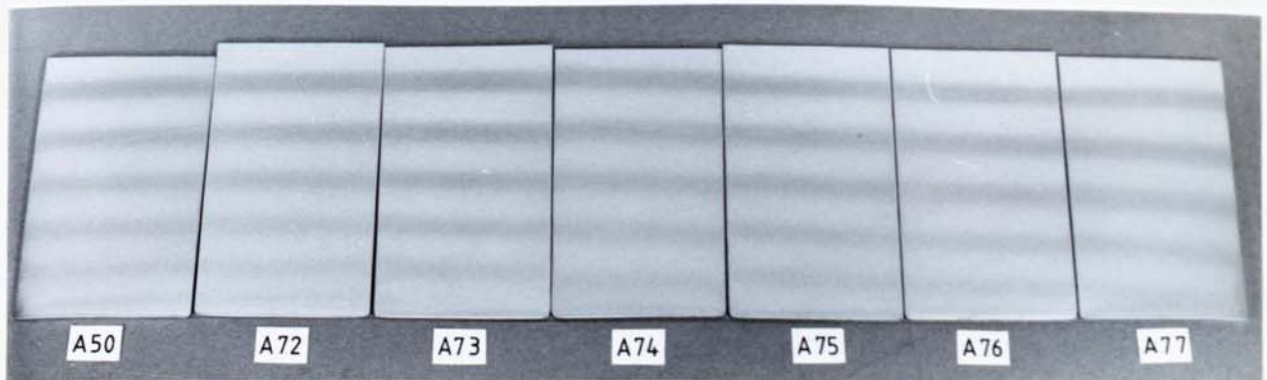


Fig.8.17: Brightness uniformity of specimens sputter etched at 30 mTorr pressure and 4 KV applied voltage for 60 minutes, held in jig number 2.

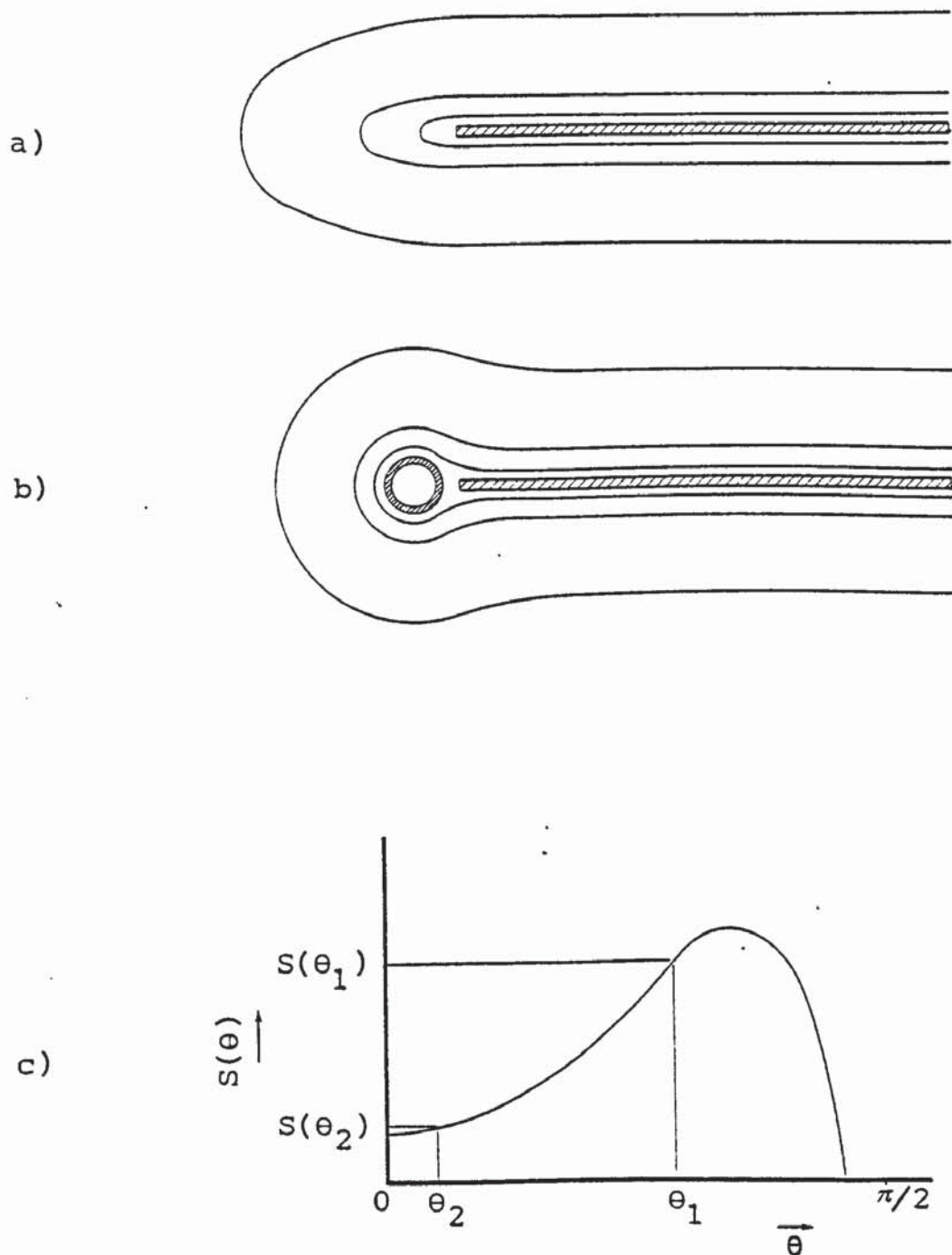


Fig.8.18:

- a) Cross section of a specimen fixed in jig number 1, and its field force lines.
- b) Cross section of a specimen fixed in jig number 2, and its field force lines.
- c) Plot of sputtering yield v angle of incidence.
 θ_1 : mean angle of incidence using jig number 1,
 θ_2 : mean angle of incidence using jig number 2.

of the bombarding particles and the corresponding sputtering yield of the specimen, respectively.

As Fig.8.18(b) shows, the presence of the loop round the specimen held in jig number 2 changes the field lines and would prevent incidence of ions at large angles to the normal of the specimen surface. This not only would reduce the total number of the striking ions, but also the distribution of the angles of incidence would become quite different from the previous case, as the majority of ions would strike the surface at angles close to normal. Therefore the mean angle of incidence would be close to the surface normal and, thus, the corresponding mean sputtering yield of the specimen would be far less than the previous case (see Fig.8.18(c)).

Fig.8.16 shows the change in brightness of specimens due to an increase in ion bombardment duration. Although, according to Table 8.6, specimens sputtered for 60 minutes have the highest coefficient of variation, Fig.8.17 shows that even these specimens have a very close degree of brightness and are uniformly etched.

These results prove the suitability of jig number 2 for obtaining reproducible results and uniform etching of specimens.

Due to low sputtering rates, specimens held by jig number 2 are suitable for investigating the development of protrusions.

Figs. 8.19, 8.22 and 8.24 are photomicrographs showing that by increasing the ion bombardment duration from 15 to 30 and 60 minutes the etched area of specimens

does not change.

Figs. 8.19 to 8.21 are photomicrographs showing the surface of specimen A67 which was sputter etched at 30 mTorr pressure and 4KV applied voltage for 15 minutes, and, according to Table 8.5, an average of $0.105\ \mu\text{m}$ was removed from its surface. As these photomicrographs show, three types of grain can be recognised. Firstly, there are the majority of grains, which are heavily etched. Surface topography of these grains resembles a finely rippled surface. From photomicrograph 8.21 those ripples seem to be parts of the original surface area filling the gaps between ion bombardment induced etch pits. Secondly, there are slightly etched grains, such as the one shown at the bottom left hand corner of photomicrograph 8.21. The important feature of this grain is the presence of a large number of ion bombardment induced etch pits positioned along large ripples on the surface. These large ripples, as can be seen in photomicrograph 8.19, are caused by rolling and indicate the rolling direction of specimens.

The top of these ripples are enriched in Ni by up to 1.2% and depleted in Cr by up to 0.5%, while the bottom of the ripples observe an opposite change in composition⁽²⁶⁰⁾. Thus, these regions are expected to have different sputtering yields. Regarding the fact that the etch pits seem to correspond to the bottom of those ripples, it might be concluded that enrichment in Cr and depletion in

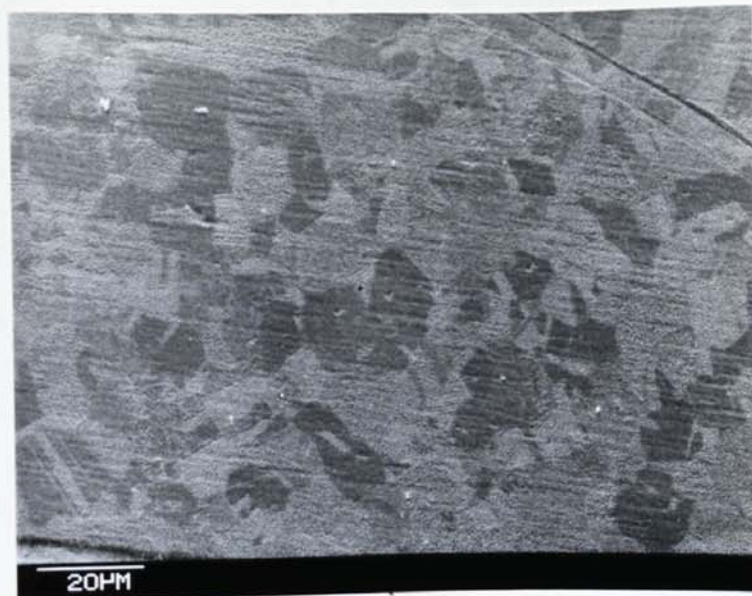


Fig.8.19: Surface of specimen A67 sputter etched at 30 mTorr pressure and 4 KV applied voltage for 15 minutes. Average depth of erosion: $0.1 \mu\text{m}$

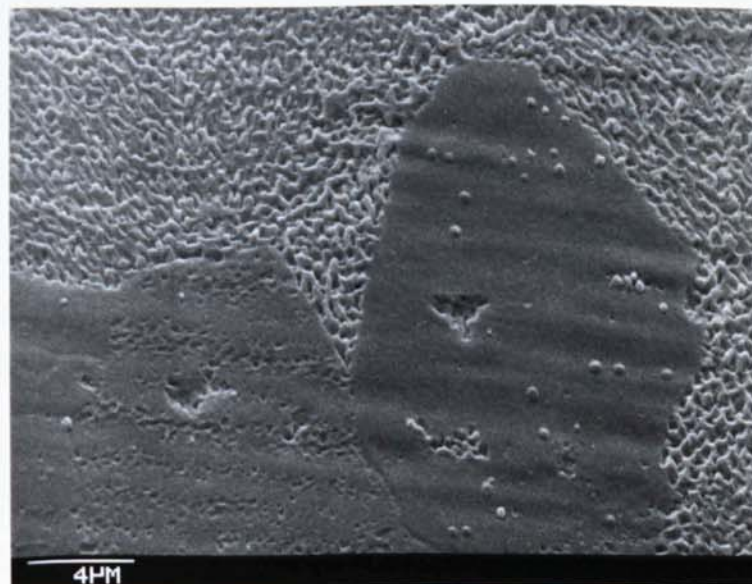


Fig.8.20: Large ripples on specimen A67 indicating the rolling direction.

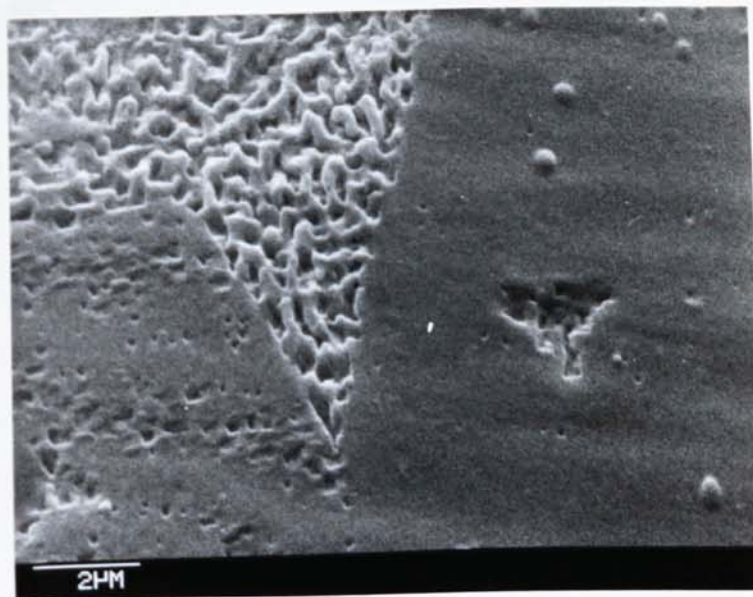


Fig.8.21: Surface of specimen A67 showing three differently etched grains, and the effect of large ripples on the location of the etch pits.

Ni has increased the susceptibility of the surface to ion bombardment induced damage.

Lastly, there are grains with little sign of etching, such as the one shown on the right hand side of photomicrograph 8.21. This grain has three important features; a few small protrusions, a few small etch pits, and a relatively large etched area. Considering that the average removed thickness of this specimen was only $0.105\text{ }\mu\text{m}$, it can safely be said that those small protrusions are not caused by ion bombardment, but are impurity particles standing proud of the surface. The small etch pits do not correspond to any particular location and, rather, seem to be randomly scattered on the surface. These etch pits might correspond to point defects in the surface layers. The relatively large etched area on this grain does not indicate any particular location. Therefore it may have been originally caused by mechanical damage received during handling of the specimen, and the subsequent ion bombardment has introduced some degree of etching into it.

Etching of the boundary between the two latter grains and the presence of some etch pits on this boundary are noticeable. Photomicrographs 8.22 and 8.23 show specimen A55 which was sputter etched at 30 mTorr pressure and 4KV applied voltage for 30 minutes. Referring to Table 8.5, an average thickness of $0.187\text{ }\mu\text{m}$ was removed from the surface of this specimen. Photomicrograph 8.23 shows the same 3 types of grain on this specimen as the previous

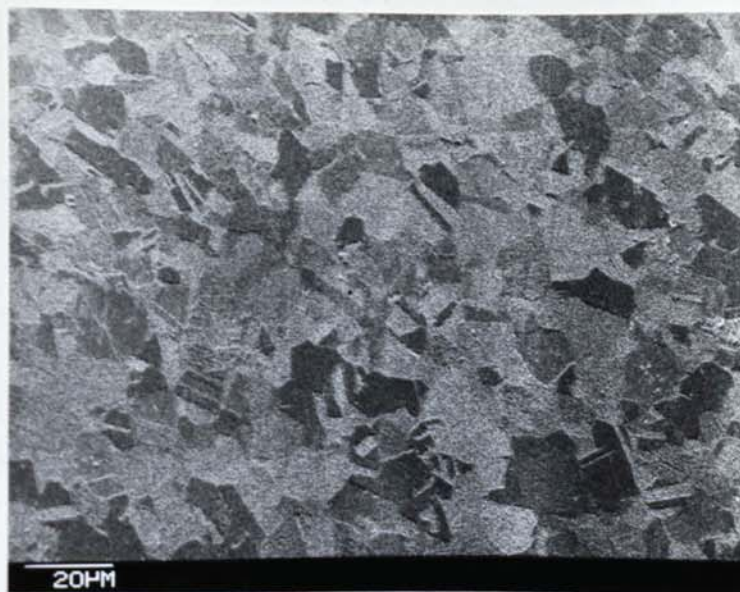


Fig.8.22: Surfaces of specimen A55, sputter etched at 30 mTorr pressure and 4 KV applied voltage for 30 minutes.
Average depth of erosion: 0.19 μm

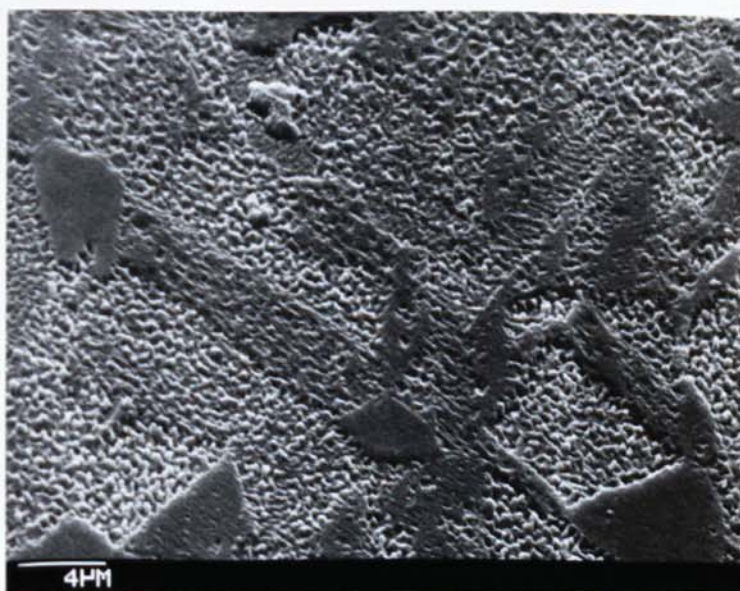


Fig.8.23: Surface of specimen A55, indicating the orientation dependence of sputtering, and the depth of etching.

one, with the difference that the etching has become deeper. This micrograph also indicates that by increasing the duration of ion bombardment, etch pits grow in size and cut through the fine ripples as shown in Fig.8.21. This would lead to the appearance of separate and free standing protrusions. Growth of the etch pits depends on orientation and the surface binding energy of the grain. This dependency is well demonstrated in photomicrograph 8.23 by the twin band and the nearly unetched grains. Another important feature of this photomicrograph is the disappearance of grain boundaries. But as can be seen, they are replaced by etch pits.

Figs. 8.24 to 8.26 show specimen A50 which was sputter etched at 30 mTorr pressure and 4KV applied voltage for 60 minutes; and, as Table 8.5 indicates, an average thickness of $0.458\text{ }\mu\text{m}$ was removed from its surface. As these micrographs indicate, all grains are to some degree etched and the surface of the specimen has become quite uneven. The difference in degree of etching between grains has become more pronounced, and the grain boundary etch pits have grown larger.

Although the three above-mentioned specimens were sputter etched under the same conditions, they cannot be regarded as a time series simply because they are three different specimens. However, from the common features of these specimens general conclusions about the surface texturing of ion bombarded stainless steel can be drawn. As

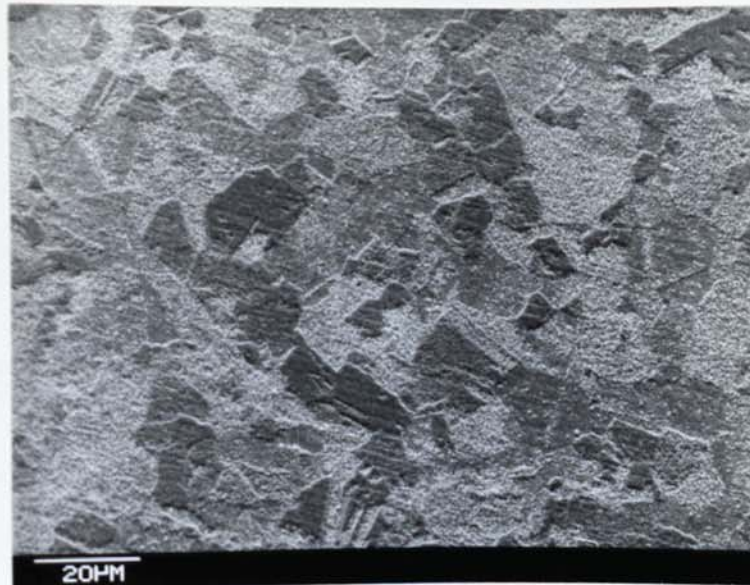


Fig.8.24: Surface of specimen A50, sputter etched at 30 mTorr pressure and 4 KV applied voltage for 60 minutes.
Average depth of erosion: 0.46 μm

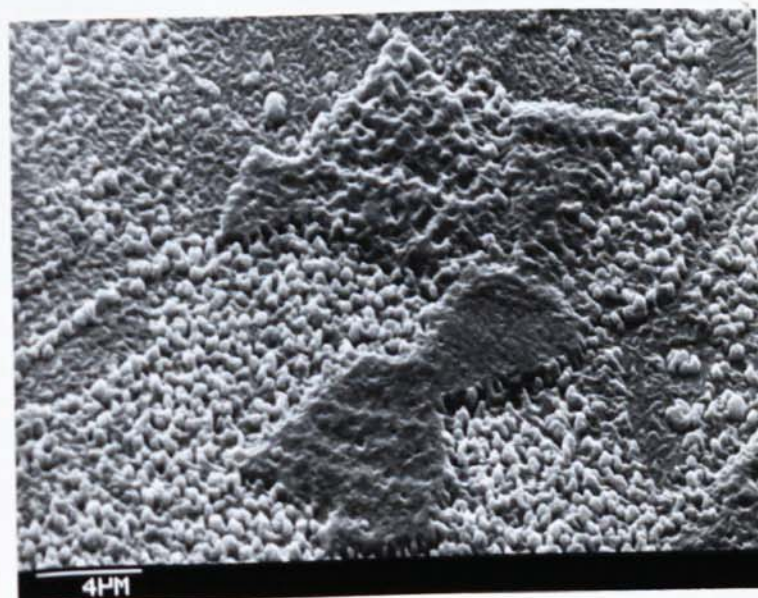


Fig.8.25: Surface of specimen A50
(see the text)

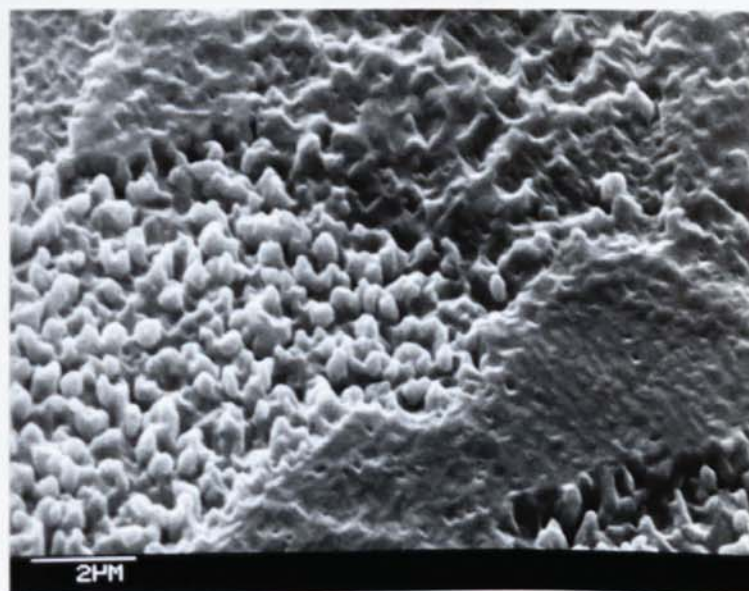


Fig.8.26: Sputter etched surface of specimen A50, showing the magnitude of surface roughness and the growth of etch pits on sides of unetched grains.

photomicrographs 8.19, 8.22 and 8.24 show, with an increase in the bombardment duration, the heavily etched area of specimens does not change significantly. But as photomicrographs 8.20, 8.23 and 8.25 indicate, the depth of etching increases as the irradiation duration becomes longer. Under the influence of ion bombardment, etch pits appear at point defects and where dislocations intersect the surface. As etch pits grow in number and size, they join together and leave protrusions standing proud of the surface. The shape and the size of these protrusions seem to depend on the orientation of individual grains.

Although these results are in agreement with the conclusion reached by Whitton et al⁽²⁶¹⁾, that impurities do not seem to be necessary for the initiation of the protrusions, they disagree with Kelly and Auciello⁽²⁶²⁾, and Stewart and Thompson⁽¹⁶⁰⁾. These authors have claimed a 1:1 correlation between pre-existing structures and the protrusions formed on the surface. This conclusion is correct in the cases of specimens like A16 and A22 (see photomicrographs 8.5 to 8.8), but not in the cases of specimens like A67, A55 and A50 (see photomicrographs 8.20, 8.23 and 8.25). Here the difference in sputtering rate might be the controlling factor.

Whitton et al have also claimed that there is a tendency for protrusions to form along grain boundaries of polycrystalline materials, while Kelly and Auciello believe that it would be the case only on extremely rough

surfaces. Based on the present results, neither of these claims can be substantiated (see photomicrographs 8.20, 8.23 and 8.25), as neither do the grain boundaries appear to be sources of protrusions nor does an increase in surface roughness generate any taller protrusions along the boundaries.

5: Solar absorptivity and thermal emissivity measurements. Fig.8.27 shows the visible range spectral reflectivity of the "mirror polished" stainless steel specimen prior to and after the ion bombardment. From this figure it is evident that the etched specimen has higher absorptivity, from 525 nm onwards, compared to the unetched specimen. The same kind of improvement in absorptivity was observed on the bright annealed surface, which is shown in Fig.8.28. As is evident from this figure, a much higher improvement in absorptivity of the bright annealed specimen was achieved compared to the "mirror polished" one. The extracted data from these two figures for the calculation of the absorptivity of specimens, is given in Tables 8.7 and 8.8. Both Weighted Ordinates and Selected Ordinates methods are used to discover if there is any significant difference between the two.

The infrared specular spectral reflectivities of the four surfaces are shown in Fig.8.29, in the 2.5 to 50 μm waveband. The extracted values, up to wavelengths of 40 μm , for the emissivity measurements are given in Table 8.9.

(text cont. P.239)

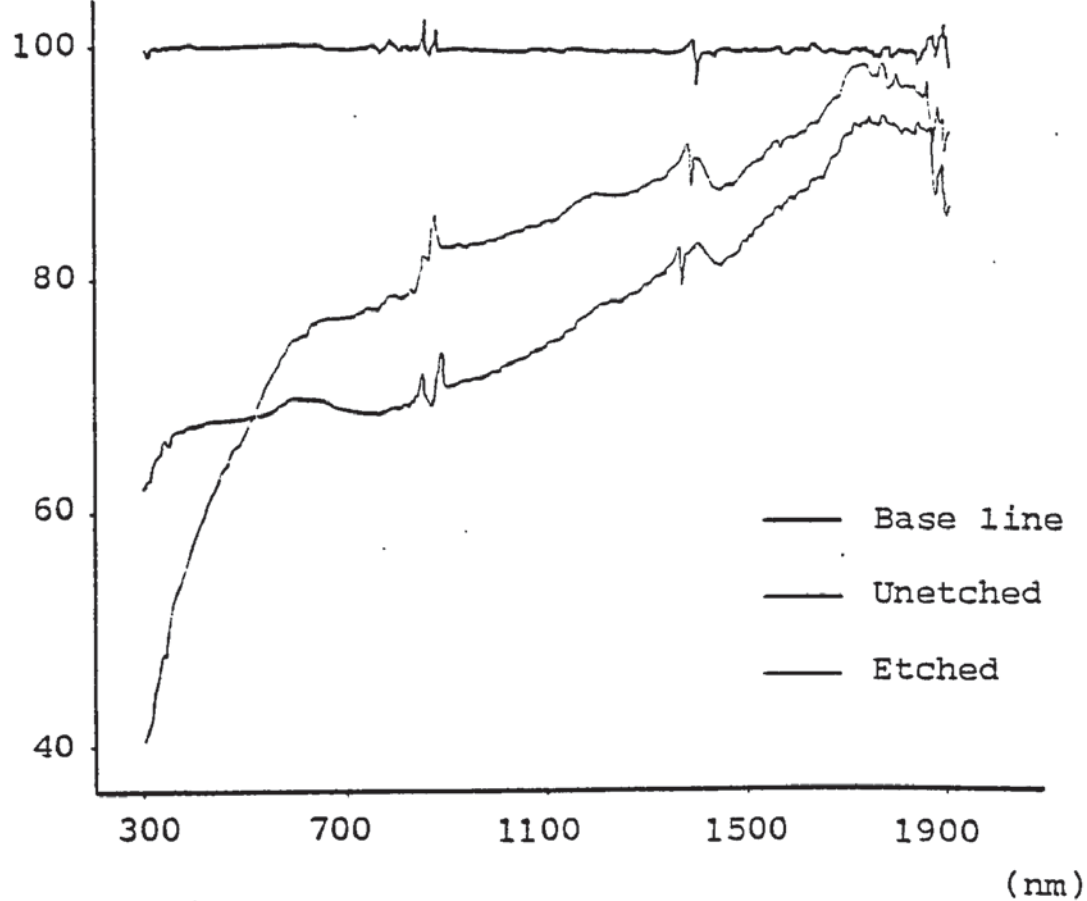


Fig.8.27: Variable range reflectivity of the "Mirror polished" specimen

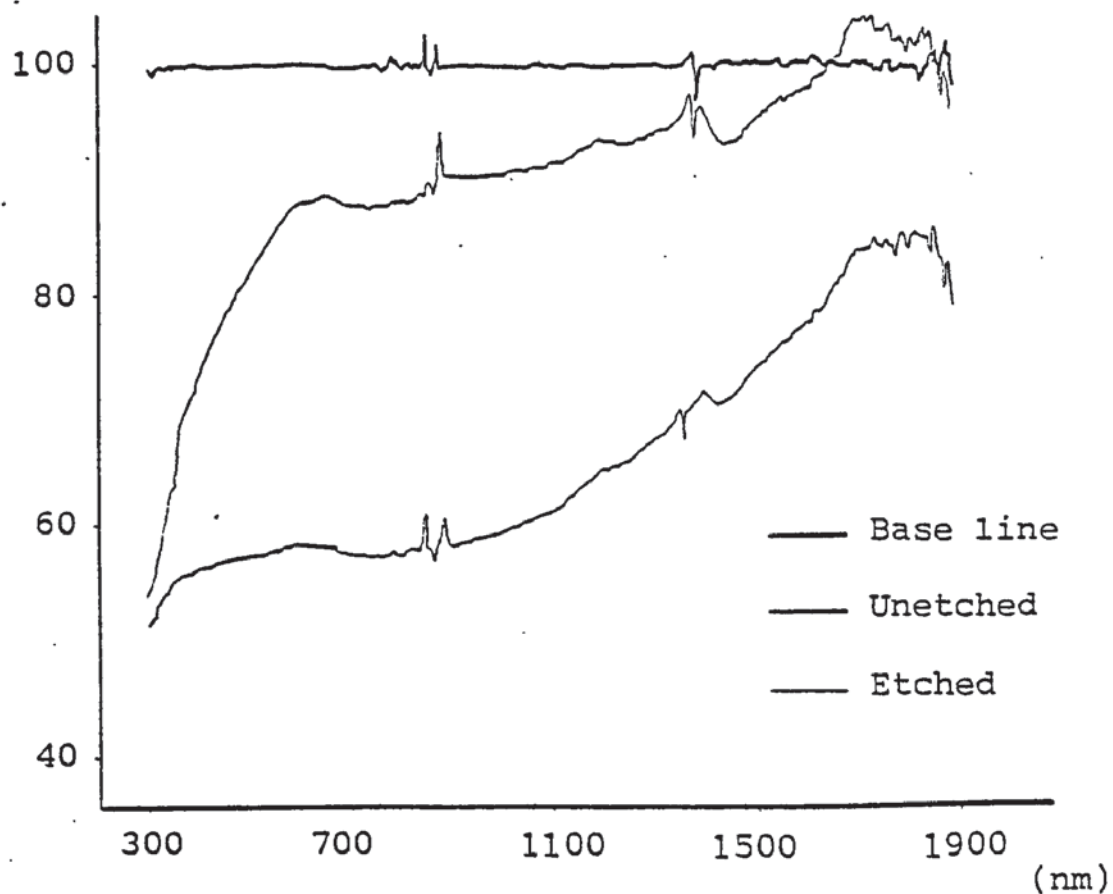


Fig.8.28: Visible range reflectivity of the Bright annealed specimen

λ (nm)	ρ_{λ} BaSO ₄	G_{λ} (%)	ρ_{λ} of Bright Annealed		ρ_{λ} of Mirror Polished	
			Unetched	Etched	Unetched	Etched
350	0.982	1.27	0.630	0.547	0.470	0.659
400	0.986	3.18	0.725	0.558	0.552	0.670
450	0.991	6.79	0.781	0.565	0.618	0.675
500	0.992	8.20	0.815	0.569	0.655	0.676
550	0.992	8.03	0.850	0.574	0.699	0.680
600	0.992	7.88	0.880	0.580	0.738	0.690
650	0.992	7.92	0.885	0.578	0.757	0.690
700	0.992	7.48	0.878	0.570	0.763	0.683
750	0.992	5.58	0.875	0.570	0.768	0.680
800	0.992	5.79	0.880	0.570	0.780	0.685
850	0.991	5.66	0.884	0.574	0.785	0.694
900	0.989	5.24	0.900	0.578	0.823	0.701
950	0.987	3.29	0.899	0.585	0.825	0.707
1000	0.983	4.25	0.902	0.590	0.830	0.715
1050	0.982	3.72	0.905	0.600	0.835	0.725
1100	0.982	1.70	0.913	0.607	0.842	0.735
1150	0.977	1.46	0.920	0.624	0.855	0.750
1200	0.973	2.52	0.932	0.642	0.867	0.768
1250	0.970	2.21	0.929	0.651	0.867	0.775
1300	0.966	1.78	0.935	0.668	0.873	0.789
1350	0.948	0.12	0.944	0.685	0.884	0.804
1400	0.895	0.00	0.961	0.710	0.900	0.827
1450	0.869	0.16	0.927	0.706	0.875	0.807
1500	0.896	1.06	0.944	0.730	0.885	0.827
1550	0.916	1.49	0.963	0.747	0.908	0.847
1600	0.920	1.36	0.972	0.767	0.920	0.863
1650	0.917	1.17	0.985	0.787	0.931	0.883
1700	0.913	0.89	1.022	0.830	0.953	0.916
1750	0.903	0.54	1.030	0.840	0.982	0.936
1800	0.892	0.01	1.016	0.852	0.962	0.930
1850	0.825	0.00	1.020	0.846	0.957	0.930

Table 8.7: ρ_{λ} measurements of the Bright Annealed and the "Mirror Polished" specimens before and after sputter etching, based on Weighted Ordinates method.

λ (nm)	ρ_{λ} BaSO ₄	ρ_{λ} of the Bright Annealed		ρ_{λ} of the "Mirror Polished"	
		Unetched	Etched	Unetched	Etched
390	0.986	0.710	0.555	0.538	0.668
444	0.991	0.723	0.564	0.604	0.675
481	0.992	0.806	0.573	0.643	0.676
510	0.992	0.824	0.570	0.660	0.678
543	0.992	0.845	0.573	0.692	0.680
574	0.992	0.865	0.579	0.716	0.687
606	0.992	0.879	0.584	0.732	0.690
639	0.992	0.881	0.584	0.748	0.690
669	0.992	0.881	0.583	0.760	0.690
705	0.992	0.876	0.577	0.752	0.683
745	0.992	0.873	0.574	0.767	0.680
786	0.992	0.878	0.578	0.777	0.680
831	0.991	0.881	0.573	0.780	0.864
877	0.990	0.896	0.576	0.816	0.687
959	0.986	0.901	0.583	0.824	0.709
1026	0.982	0.904	0.595	0.832	0.720
1105	0.982	0.912	0.612	0.842	0.736
1228	0.971	0.931	0.647	0.869	0.773
1497	0.895	0.944	0.723	0.885	0.826
1722	0.908	1.034	0.847	0.980	0.928

Table 8.8: ρ_{λ} measurements of the Bright Annealed and the "Mirror Polished" specimens before and after sputter etching, based on Selected Ordinates method.

2.5

MICRONS

4.0

5.0

6.0

8.0

10.0

12.5

15.0

17.5

20.0

25.0

30.0

35.0

40.0

45.0

50.0

55.0

60.0

65.0

70.0

75.0

80.0

85.0

90.0

95.0

100.0

105.0

110.0

115.0

120.0

125.0

130.0

135.0

140.0

145.0

150.0

155.0

160.0

165.0

170.0

175.0

180.0

185.0

190.0

195.0

200.0

205.0

210.0

215.0

220.0

225.0

230.0

235.0

240.0

245.0

250.0

255.0

260.0

265.0

270.0

275.0

280.0

285.0

290.0

295.0

300.0

305.0

310.0

315.0

320.0

325.0

330.0

335.0

340.0

345.0

350.0

355.0

360.0

365.0

370.0

375.0

380.0

385.0

390.0

395.0

400.0

405.0

410.0

415.0

420.0

425.0

430.0

435.0

440.0

445.0

450.0

455.0

460.0

465.0

470.0

475.0

480.0

485.0

490.0

495.0

500.0

505.0

510.0

515.0

520.0

525.0

530.0

535.0

540.0

545.0

550.0

555.0

560.0

565.0

570.0

575.0

580.0

585.0

590.0

595.0

600.0

605.0

610.0

615.0

620.0

625.0

630.0

635.0

640.0

645.0

650.0

655.0

660.0

665.0

670.0

675.0

680.0

685.0

690.0

695.0

700.0

705.0

710.0

715.0

720.0

725.0

730.0

735.0

740.0

745.0

750.0

755.0

760.0

765.0

770.0

775.0

780.0

785.0

790.0

795.0

800.0

805.0

810.0

815.0

820.0

825.0

830.0

835.0

840.0

845.0

850.0

855.0

860.0

865.0

870.0

875.0

880.0

885.0

890.0

895.0

900.0

905.0

910.0

915.0

920.0

925.0

930.0

935.0

940.0

945.0

950.0

955.0

960.0

965.0

970.0

975.0

980.0

985.0

990.0

995.0

1000.0

1005.0

1010.0

1015.0

1020.0

1025.0

1030.0

1035.0

1040.0

1045.0

1050.0

1055.0

1060.0

1065.0

1070.0

1075.0

1080.0

1085.0

1090.0

1095.0

1100.0

1105.0

1110.0

1115.0

1120.0

1125.0

1130.0

1135.0

1140.0

1145.0

1150.0

1155.0

1160.0

1165.0

1170.0

1175.0

1180.0

1185.0

1190.0

1195.0

1200.0

1205.0

1210.0

1215.0

1220.0

1225.0

1230.0

1235.0

1240.0

1245.0

1250.0

1255.0

1260.0

1265.0

1270.0

1275.0

1280.0

1285.0

1290.0

1295.0

1300.0

1305.0

1310.0

1315.0

1320.0

1325.0

1330.0

1335.0

1340.0

1345.0

1350.0

1355.0

1360.0

1365.0

1370.0

1375.0

1380.0

1385.0

1390.0

1395.0

1400.0

1405.0

1410.0

1415.0

1420.0

1425.0

1430.0

1435.0

1440.0

1445.0

1450.0

1455.0

1460.0

1465.0

1470.0

1475.0

1480.0

1485.0

1490.0

1495.0

1500.0

1505.0

1510.0

1515.0

1520.0

1525.0

1530.0

1535.0

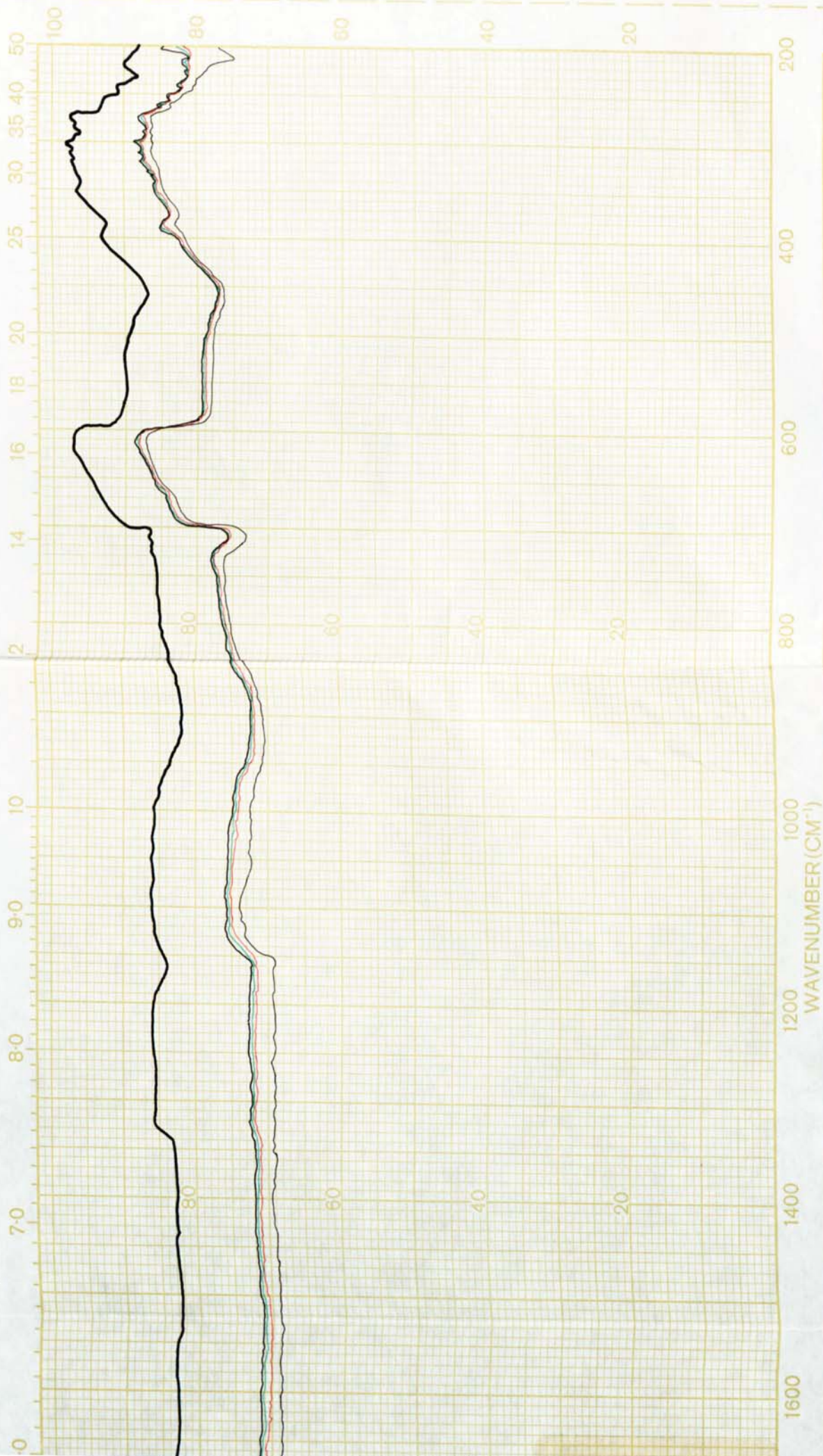
1540.0

1545.0

1550.0

1555.0

459 K



SLIT PROGRAM

SCAN TIME

MULTIPLIER

TIME CONSTANT

T A SB

ORDINATE EXP

ABSCISSA EXP

TIME DRIVE

cm/min

OPERATOR

DATE

REF No.

PERKIN-ELMER

CHART No. 5100-4367

MADE IN WEST GERMANY

λ (cm^{-1})	ρ_λ BaSO ₄	ρ_λ of the Bright Annealed				ρ_λ of the "Mirror Polished"			
		Unetched		Etched		Unetched		Etched	
		relative	absolute	relative	absolute	relative	absolute	relative	absolute
4000	0.765	0.590	0.771	0.500	0.654	0.580	0.758	0.555	0.725
3800	0.770	0.605	0.786	0.515	0.669	0.590	0.766	0.560	0.727
3600	0.780	0.620	0.795	0.540	0.692	0.610	0.782	0.580	0.744
3400	0.790	0.640	0.810	0.560	0.709	0.625	0.791	0.605	0.766
3200	0.805	0.655	0.814	0.585	0.727	0.645	0.801	0.620	0.770
3000	0.835	0.675	0.801	0.610	0.730	0.660	0.790	0.645	0.772
2800	0.835	0.675	0.801	0.610	0.730	0.660	0.790	0.645	0.772
2600	0.835	0.680	0.814	0.620	0.742	0.665	0.796	0.650	0.778
2400	0.840	0.695	0.827	0.650	0.774	0.685	0.816	0.675	0.804
2200	0.820	0.685	0.836	0.645	0.787	0.680	0.829	0.670	0.817
2000	0.790	0.675	0.854	0.635	0.804	0.665	0.842	0.655	0.829
1800	0.835	0.715	0.856	0.680	0.814	0.705	0.844	0.700	0.838
1600	0.830	0.715	0.861	0.690	0.831	0.710	0.856	0.705	0.849
1400	0.830	0.720	0.867	0.695	0.837	0.720	0.867	0.710	0.856
1200	0.855	0.725	0.848	0.690	0.807	0.720	0.842	0.715	0.836
1000	0.855	0.750	0.877	0.720	0.842	0.740	0.866	0.740	0.865
800	0.850	0.765	0.900	0.755	0.888	0.764	0.899	0.765	0.900
600	0.970	0.880	0.907	0.830	0.856	0.860	0.887	0.850	0.876
400	0.930	0.820	0.882	0.805	0.866	0.810	0.871	0.810	0.871
Total reflectivity		0.837			0.777		0.826		0.810

Table 8.9: Results of infrared specular spectral reflectivity measurements of the Bright Annealed and the "Mirror Polished" specimens before and after sputter etching.

The calculated absorptivities and emissivities of the four surfaces are given in Table 8.10, while Table 8.11 shows α/ϵ values of the surfaces. As far as improvement in the performance of a selective surface is concerned, changes in α/ϵ may be used as an indication.

		Bright Annealed		"Mirror Polished"	
		Unetched	Etched	Unetched	Etched
Solar absorptivity	Weighted Ordinates	0.142	0.412	0.252	0.301
	Selected Ordinates	0.146	0.411	0.256	0.304
specular emissivity		0.163	0.223	0.174	0.190

Table 8.10: Measured solar absorptivity of the Bright Annealed and the "Mirror Polished" specimens in the range of 300-2300 nm waveband, and the corresponding infrared specular emissivity.

		Bright Annealed		"Mirror Polished"	
		Unetched	Etched	Unetched	Etched
α/ϵ	Weighted Ordinates	0.871	1.847	1.448	1.584
	Selected Ordinates	0.896	1.843	1.471	1.600
$\frac{\alpha/\epsilon \text{ etched}}{\alpha/\epsilon \text{ unetched}}$	Weighted Ordinates	2.121		1.094	
	Selective Ordinates	2.057		1.088	

Table 8.11: Performance of the Bright Annealed and the "Mirror Polished" specimens before and after sputter etching, as selective surfaces.

Table 8.11 also shows the changes of α/ϵ ratio due to ion etching. From this table it is clear that a twofold improvement in the performance of a bright annealed 304 stainless steel plate might be achieved by ion etching, while the same process does not significantly improve the performance of a similar, but "mirror polished" specimen. This difference can only be caused by the mechanical work put into the steel by the polishing.

An important feature of Figs. 8.27 and 8.28 is that the unetched bright annealed specimen has a higher reflectivity than the unetched "mirror polished" one. This was due to the fact that the latter surface was used as received, and no further polishing was applied. Visual inspection has shown that the "polished" surface was highly scratched in the rolling direction, and looked rather like a very faint "satin" finish. Such scratches could not have been caused by mis-handling, as the protective plastic cover of the surface was not damaged.

Another important feature of Figs. 8.27 and 8.28 is the split in absorption peaks at about 900 and 1175 nm wavelengths for etched specimens compared to the unetched ones. This indicates a surface composition change which might be explained by preferential removal of elements by sputtering.

The difference in absorptivity improvements due to ion etching is another feature of the two figures, and might be explained by the dependency of the sputtering yield on

the surface energy of the irradiated surface.

6: Cooling curve thermal emittance measurements.

Results of the emittance measurements based on the cooling curves of twelve specimens sputter etched under 20 and 30 mTorr argon pressure, and 3 and 4KV applied voltages are presented in Table 8.13. Measured temperatures of the specimens together with their calculated radiative cooling curves are shown in Table 8.12 and Figs.8.30 to 8.32

Columns 7 and 8 of Table 8.13 show the time periods and temperature ranges over which the emittance was calculated.

Referring to Table 8.10, page 239, emissivity of a bright annealed stainless steel specimen increases from 0.163 to 0.223 after a heavy ion bombardment. Therefore it might be expected that the emissivity must increase where etching duration increased, probably to a maximum. But according to Table 8.13 this trend was not observed. This might have been due to inaccuracies in temperature measurements, or heat losses other than radiation. On the subject of heat losses, as jig number two was used, the whole jig was subjected to the glow discharge. Heating of the jig and specimen is a function of their surface area, mass, specific heat and their heat losses. Because the jig and specimen were made of the same material, they had the same specific heat. As the jig was not water cooled, and it had a relatively long arm between the

(text cont. P.251)

Specimen Time(s)	Temperature (°C)											
	D03	D02	D04	D01	D08	D07	D06	D05	D12	D10	D11	D09
90			281									
105			275			253		257				
120			270			248		252				
135	280		264			242		248				
150	271		259			238		244				
165	263		255			233		240			223	
180	257		250	249		229		236		221	220	
195	251		246	244		226		232		218	217	
210	245		242	239		222		228		215	214	
225	240		238	235	201	219		224		213	211	
240	235		234	231	199	216		221	199	210	208	204
255	231		230	227	198	212		217	296	207	205	200
270	227		227	224	196	209		214	194	204	203	198
285	223	205	224	220	195	206		210	192	201	200	196
300	219	202	221	217	193	204		207	190	198	197	193
315	215	199	218	214	190	201		205	188	195	195	191
330	212	197	216	211	188	199		202	186	193	192	189
345	209	194	213	208	186	196		199	184	190	189	187
360	207	192	211	205	184	194		196	182	187	186	186
375	204	190	209	202	182	192		194	180	184	183	185
390	201	188	205	200	180	190	192	191	178	182	180	184
405	199	186	202	197	178	187	188	189	175	180	178	183
420	196	183	199	195	177	185	185	186	173	178	175	181
435	194	181	196	193	175	183	183	184	172	176	173	178
450	192	179	194	191	173	181	181	182	170	173	171	176
465	189	178	192	188	171	179	178	180	168	171	169	174
480	187	176	190	186	169	177	176	178	166	169	168	172
495	185	175	189	184	168	175	174	176	164	167	166	170
510	182	173	187	182	166	172	172	174	162	165	164	168
525	181	171	186	181	165	171	170	172	161	162	162	166
540	179	170	184	179	163	169	168	171	160	160	161	164
555	177	169	182	177	161	167	166	169	158	158	160	164
570	175	167	181	175	159	165	165	167	156	156	158	162
585	173	165	179	174	158	163	163	165	154	154	156	160
600	171	164	178	172	157	162	162	164	153	153	154	158

Table 8.12 (continued)

Specimen Time(s)	Temperature (°C)											
	D03	D02	D04	D01	D08	D07	D06	D05	D12	D10	D11	D09
615	169	163	176	170	155	160	160	162	151	143	153	157
630	167	161	174	169	153	159	158	160	149	141	151	155
645	166	160	173	167	151	157	157	159	147	139	150	153
660	164	158	171	166	149	155	155	157	146	138	149	152
675	162	157	170	164		153	154	156	144	137	147	150
690	160	156	168	163		152	152	154	143	136	146	149
705	159	154	167	161		151	151	153	141	135	145	147
720	157	153	166	160		149	149	151	140	134	144	146
735	155	152	164	159		148	148	150	138	133	142	144
750	154	151	163	157		147	146	148	137	132	141	143
765	152	150	161	156		145	145	147	136	131	139	142
780	151	148	160	155		144	144	146	134	130	138	140
795	149	147	159	154		142	142	145	133	129	137	139
810	148	146	158	152		141	141	144	132	128	136	138
825	146	145	156	151		139	140	142	130	127	135	137
840	145	144	155	150		138	139	141	129		134	136
855	143	143	154	149		137	137	140	127		133	134
870	142	142	153	147		135	136	139	125		132	133
885	141	140	152	146		134	135	138	124		131	132
900	139	139	150	145		132	134	137	123		130	131
915	138	138				131	133	136	121		130	129
930	137	137				130	132	135	119			128
945	136	136				129	130	134	118			127
960	134	135				128	129	133	117			126
975	133	134					128		117			125
990	132	134					127		116			124
1005	131	133							115			123
1020	130	132							114			122
1035	129	131										121
1050	128	130										120
1065												119
1080												118
1095												117

Table 8.12: Measured temperatures for calculation of emittance.

Specimen number	Time/pressure/ applied voltage (min/mTorr/KV)	Original weight (g)	Weight loss (mg)	Removed thickness		t_1/t_2 (min)	T_1/T_2 (°C)	ϵ
				total (μm)	per second ($\text{\AA}/\text{s}$)			
D03	15/30/4	40.6015	9.9	0.122	1.35	7.30/17.30	189/128	0.16
D02	30/30/4	40.5800	32.6	0.402	2.23	7.30/17.30	178/130	0.12
D04	52/30/4	39.5396	45.4	0.574	1.84	5/15	218/150	0.13
D01	60/30/4	40.0560	47.6	0.594	1.65	5/15	214/145	0.14
D08	15/30/3	40.5769	4.7	0.058	0.64	3.30/11	201/149	0.13
D07	30/30/3	41.0112	10.0	0.122	0.68	6/16	192/128	0.15
D06	45/30/3	40.8134	16.9	0.207	0.77	6.30/16.30	188/127	0.15
D05	60/30/3	40.7560	26.1	0.320	0.89	6/16	194/133	0.15
D12	15/20/4	40.8471	11.3	0.138	1.54	7/17	172/114	0.15
D10	30/20/4	40.8416	23.1	0.283	1.57	3.45/13.45	210/127	0.15
D11	45/20/4	40.8374	36.9	0.452	1.67	5.15/15.15	192/130	0.15
D09	61/20/4	40.8707	50.7	0.620	1.69	8.15/18.15	168/117	0.15

Table 8.13: Calculated thermal emittances based on cooling curves.

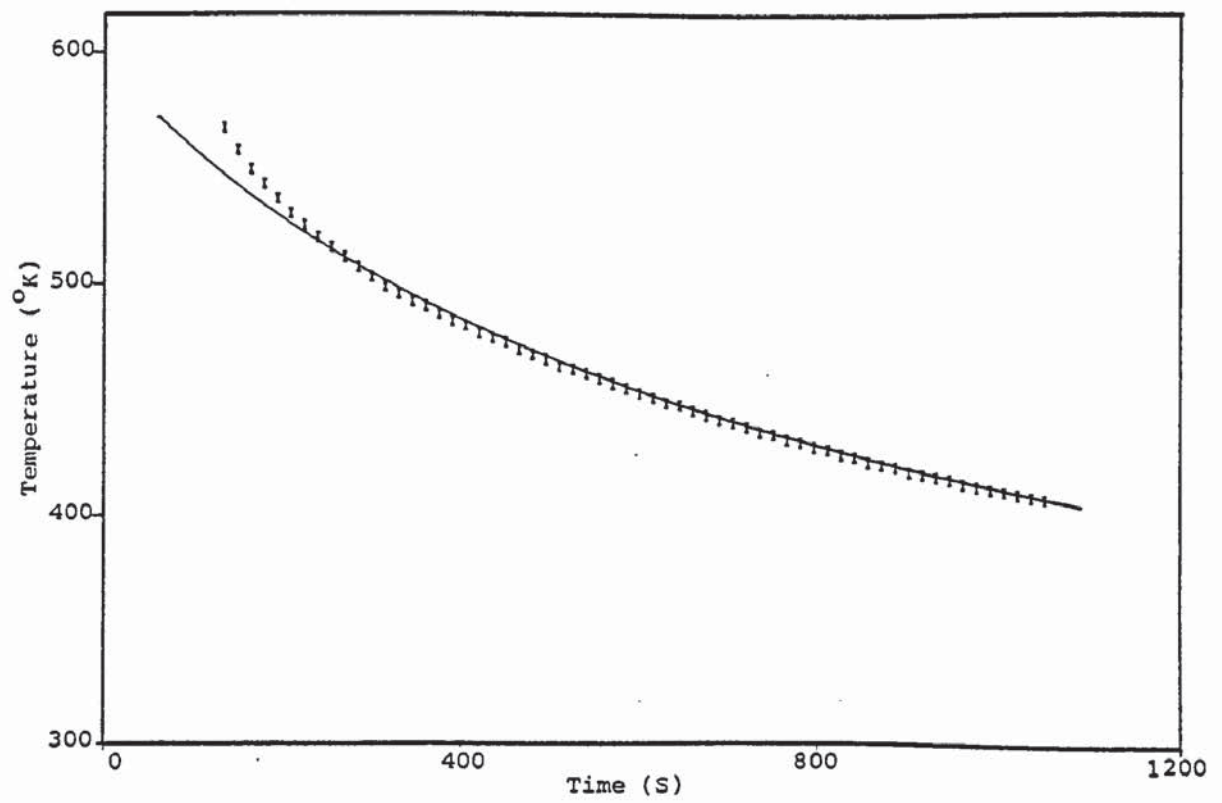


Fig.8.30a: Measured temperatures and the calculated cooling curve of specimen D03

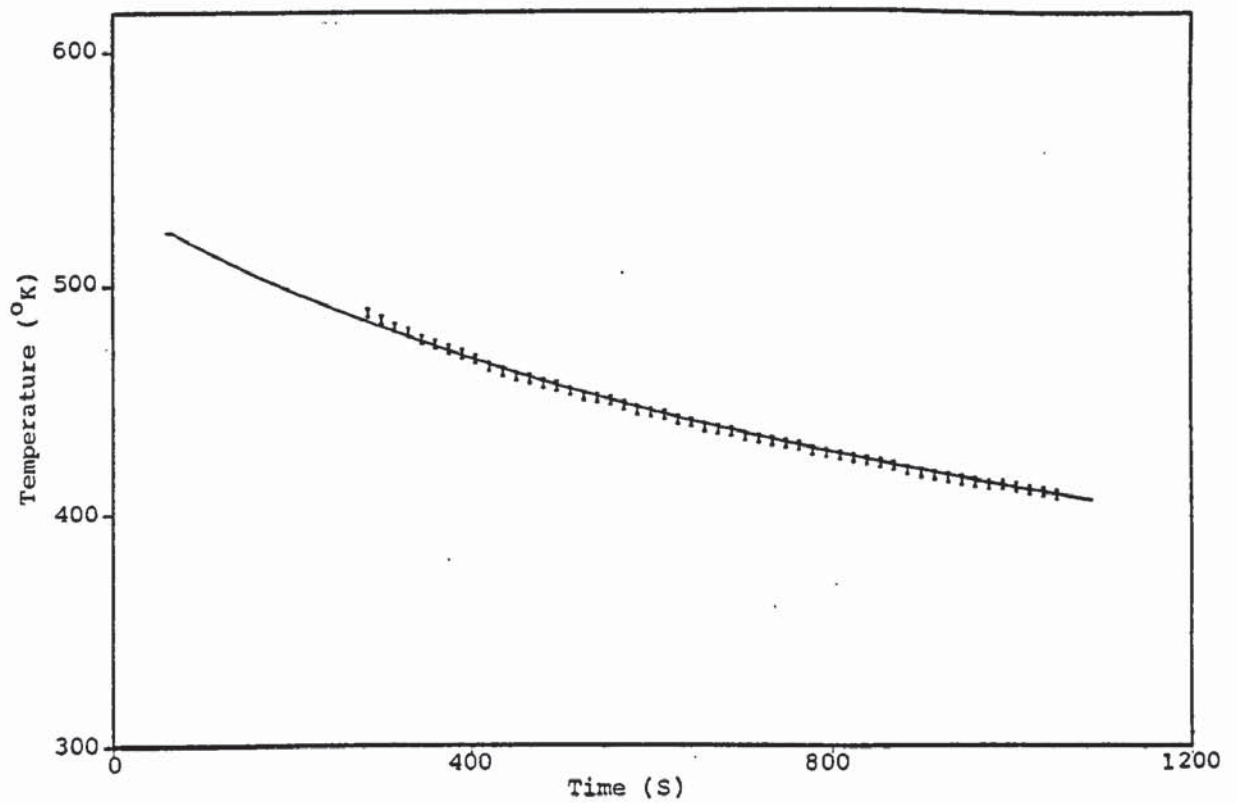


Fig.8.30b: Measured temperatures and the calculated cooling curve of specimen D02

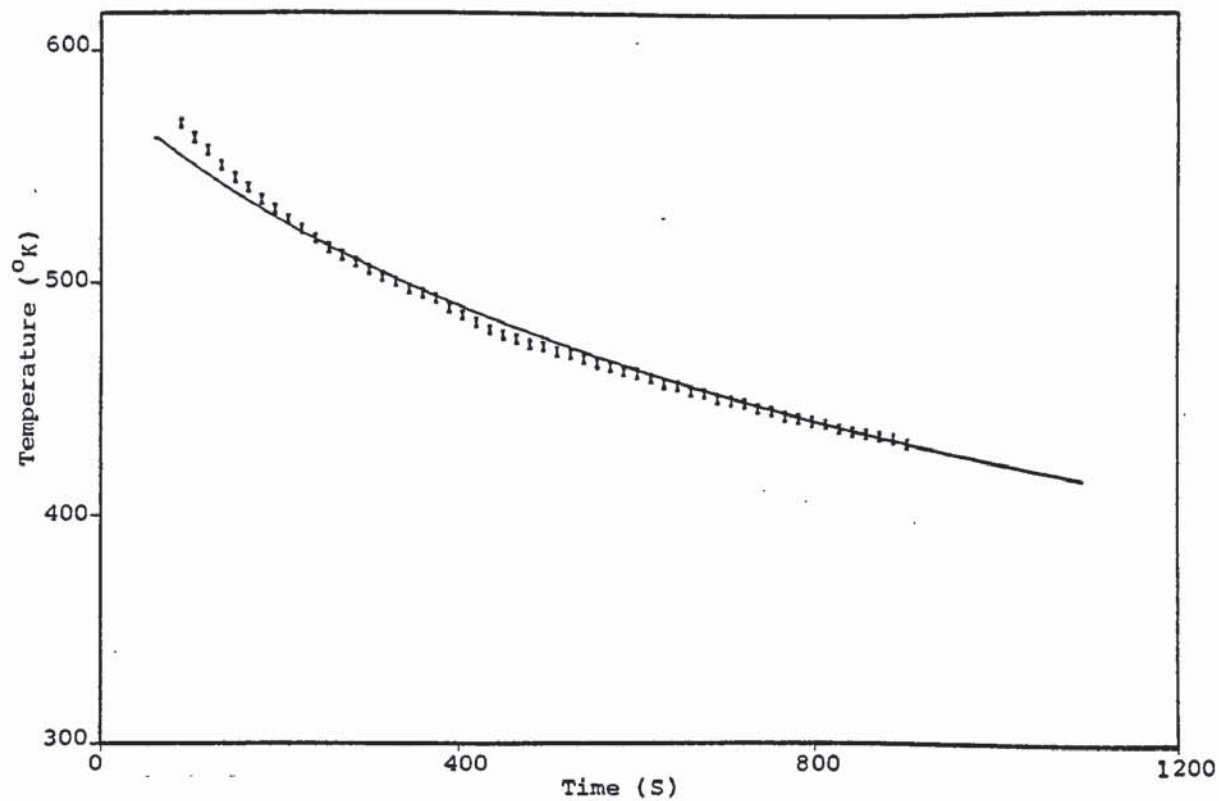


Fig.8.30c: Measured temperatures and the calculated cooling curve of specimen D04

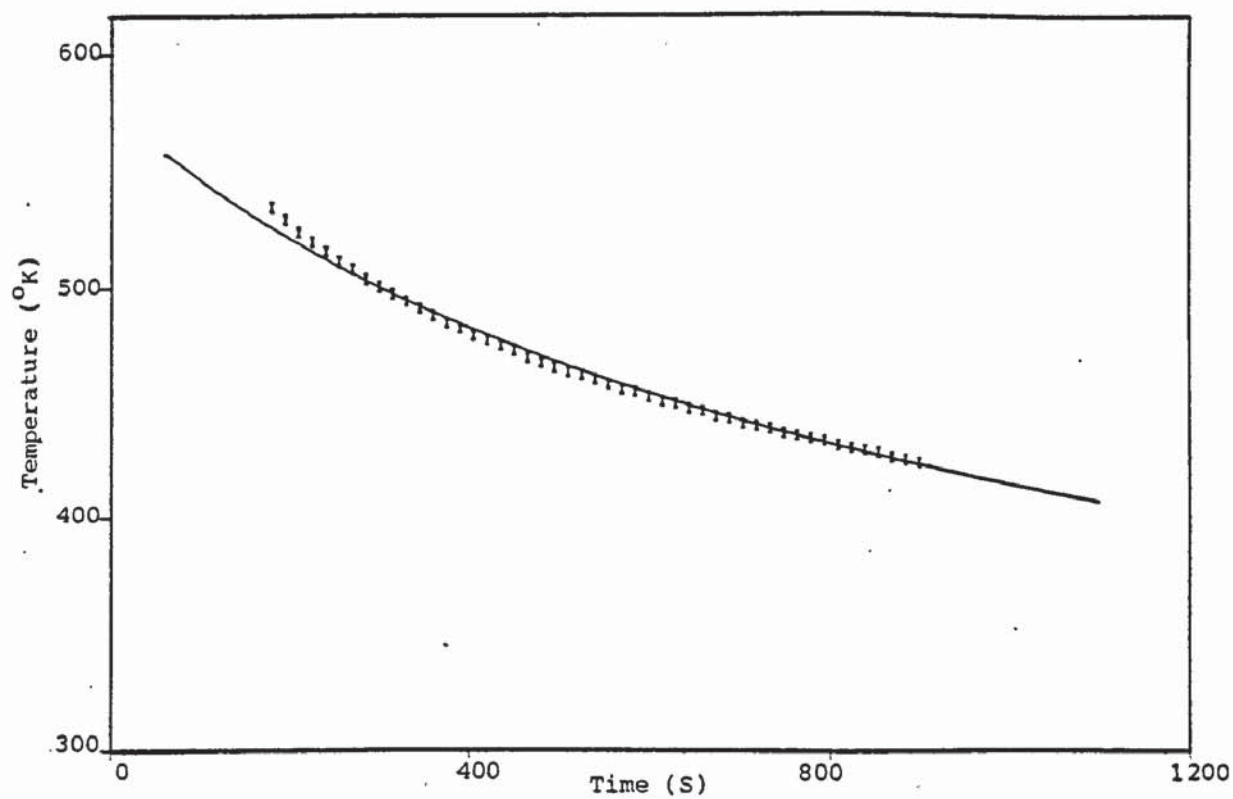


Fig.8.30d: Measured temperatures and the calculated cooling curve of specimen D01

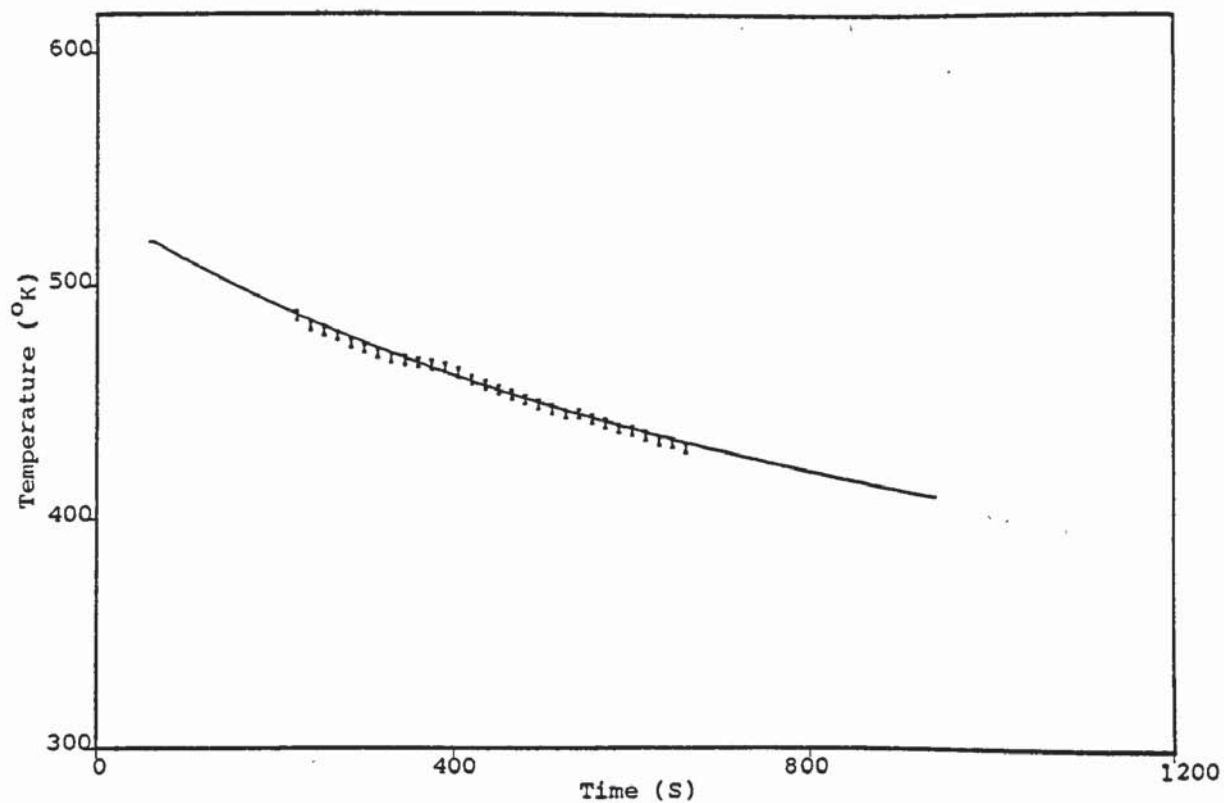


Fig.8.31a: Measured temperatures and the calculated cooling curve of specimen D08

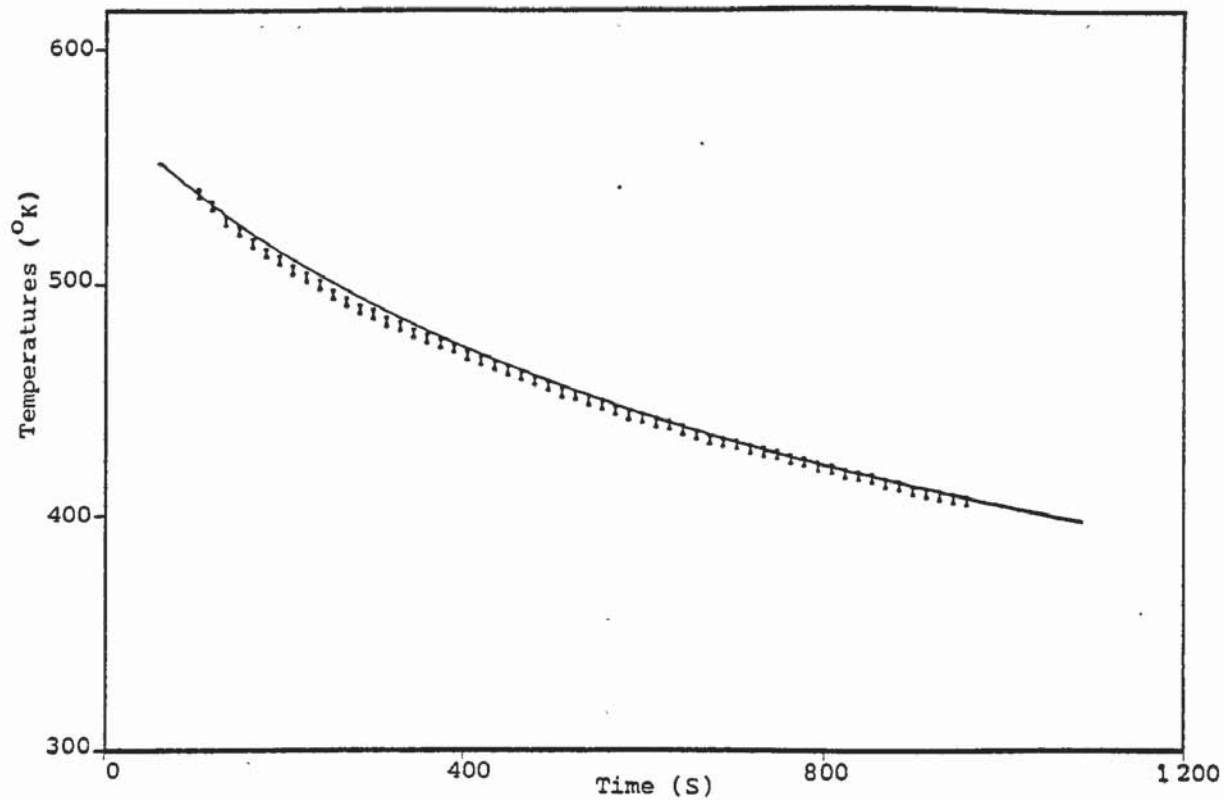


Fig.8.31b: Measured temperatures and the calculated cooling curves of specimen D07

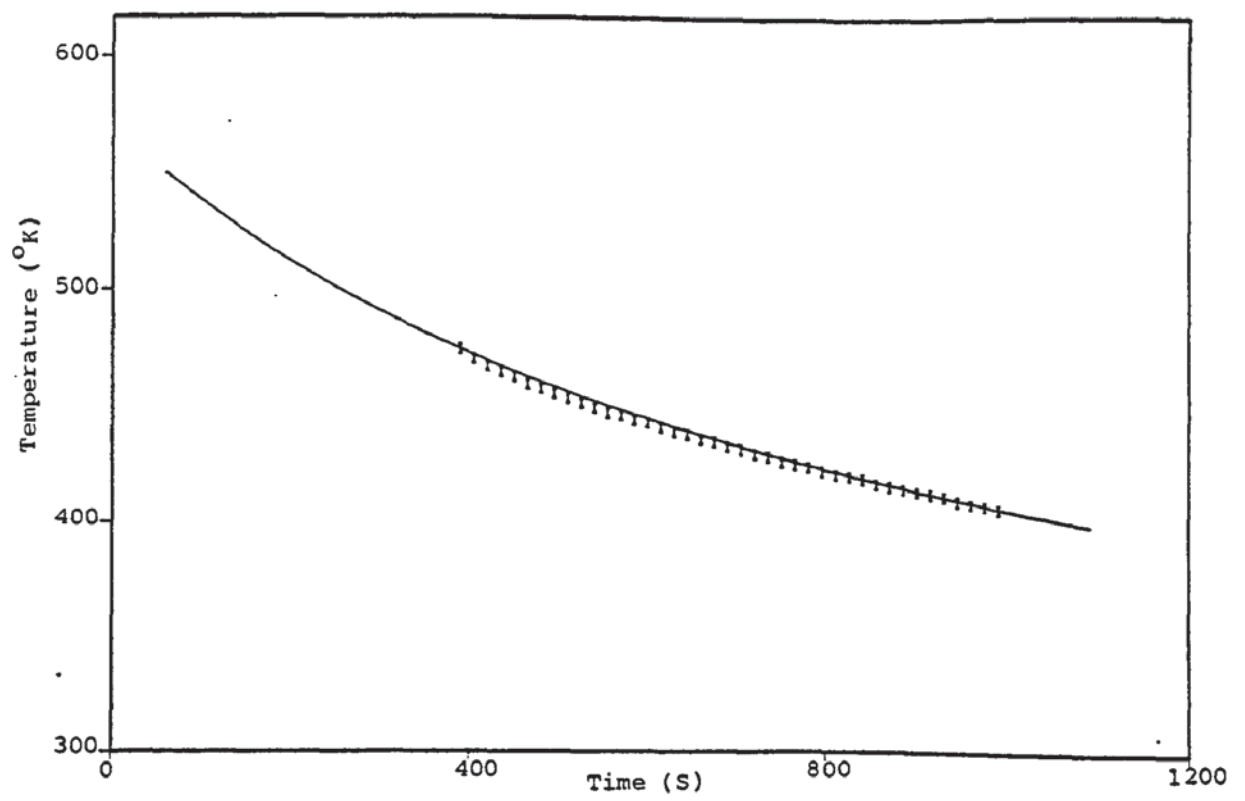


Fig. 8.31c: Measured temperatures and the calculated cooling curve of specimen D06

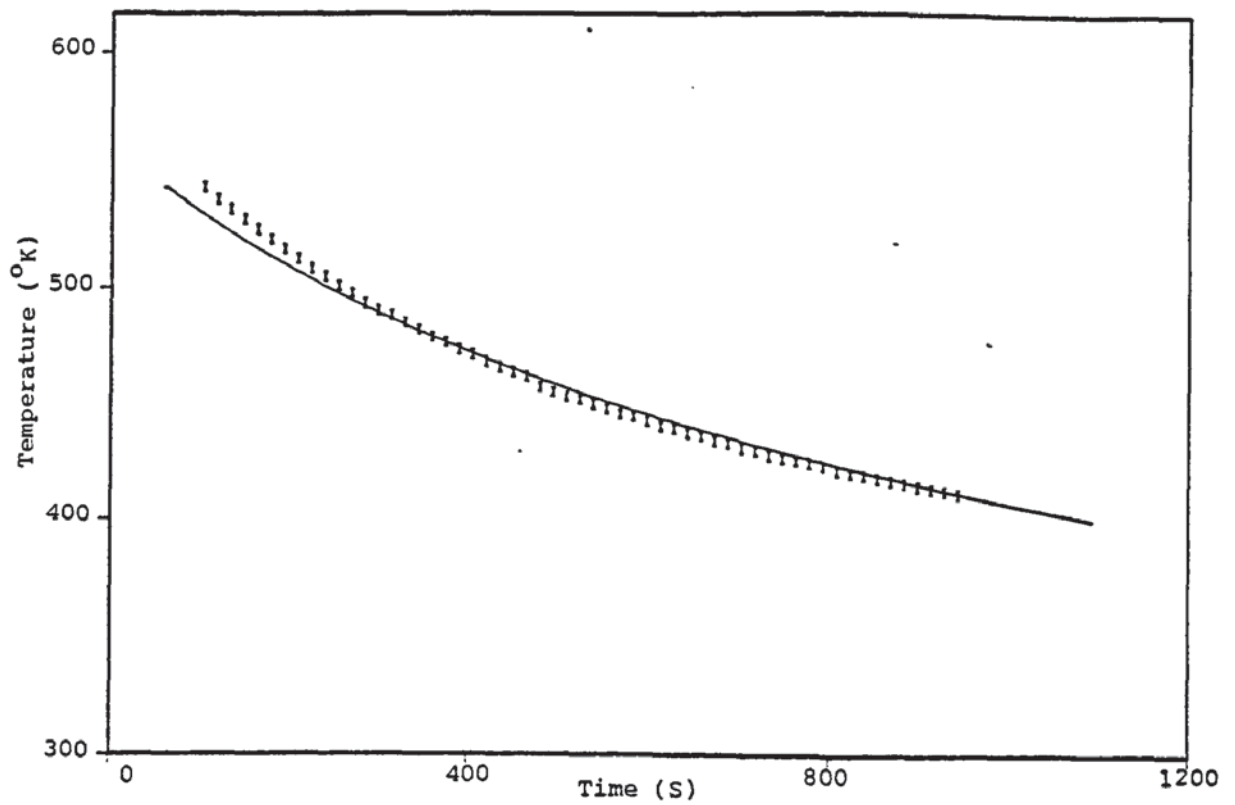


Fig. 8.31d: Measured temperatures and the calculated cooling curve of specimen D05

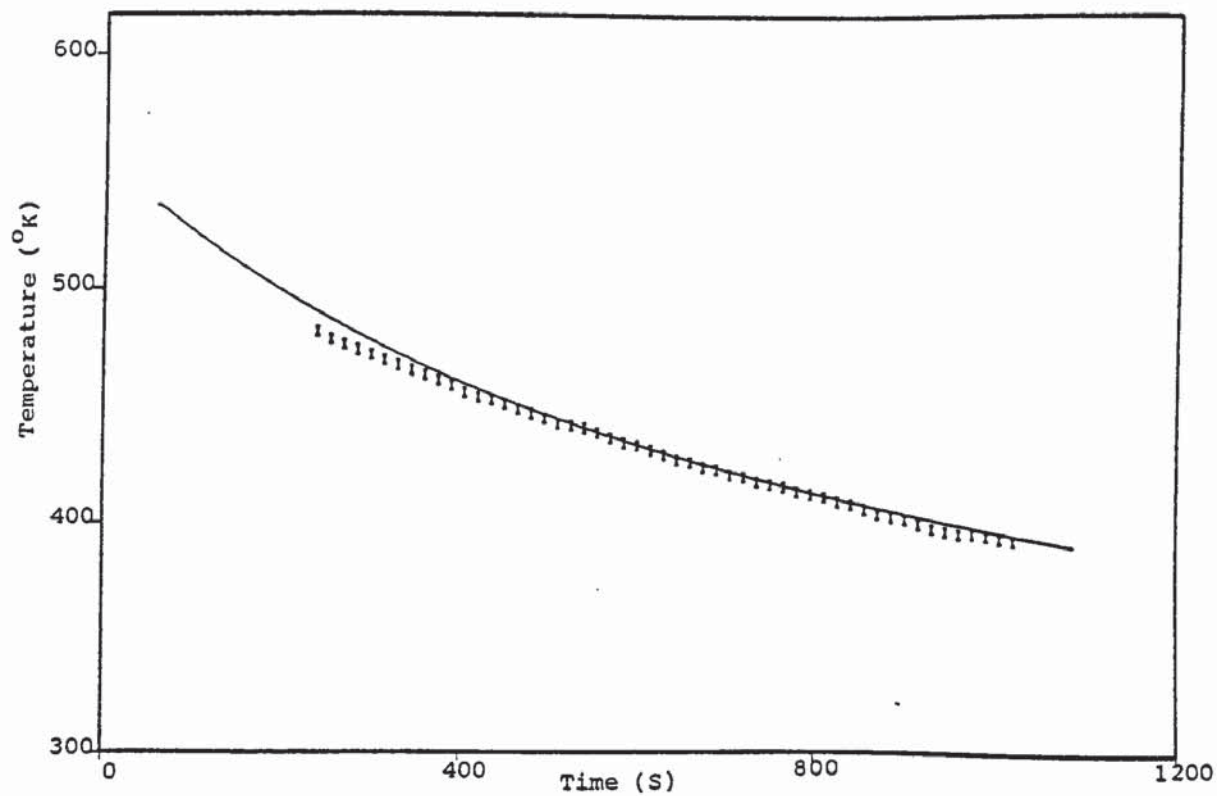


Fig.8.32a: Measured temperatures and the calculated cooling curve of specimen D12

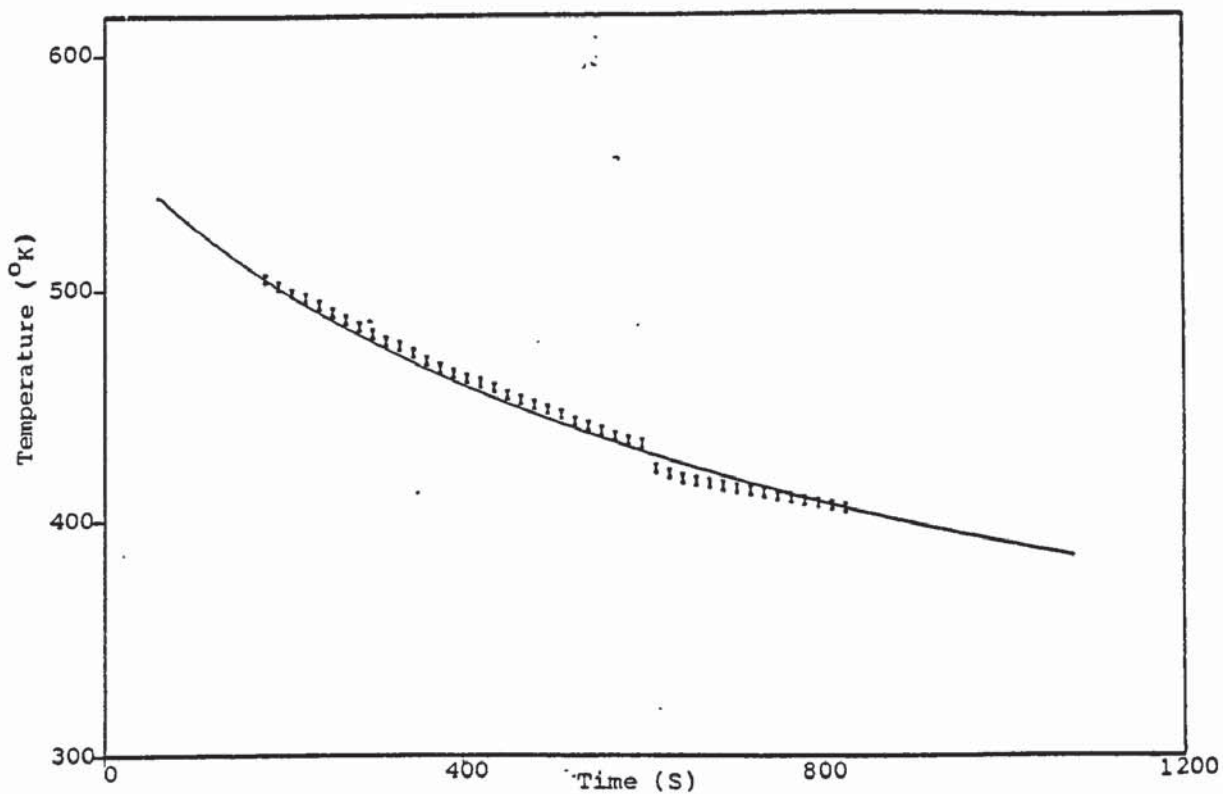


Fig.8.32b: Measured temperatures and the calculated cooling curve of specimen D10

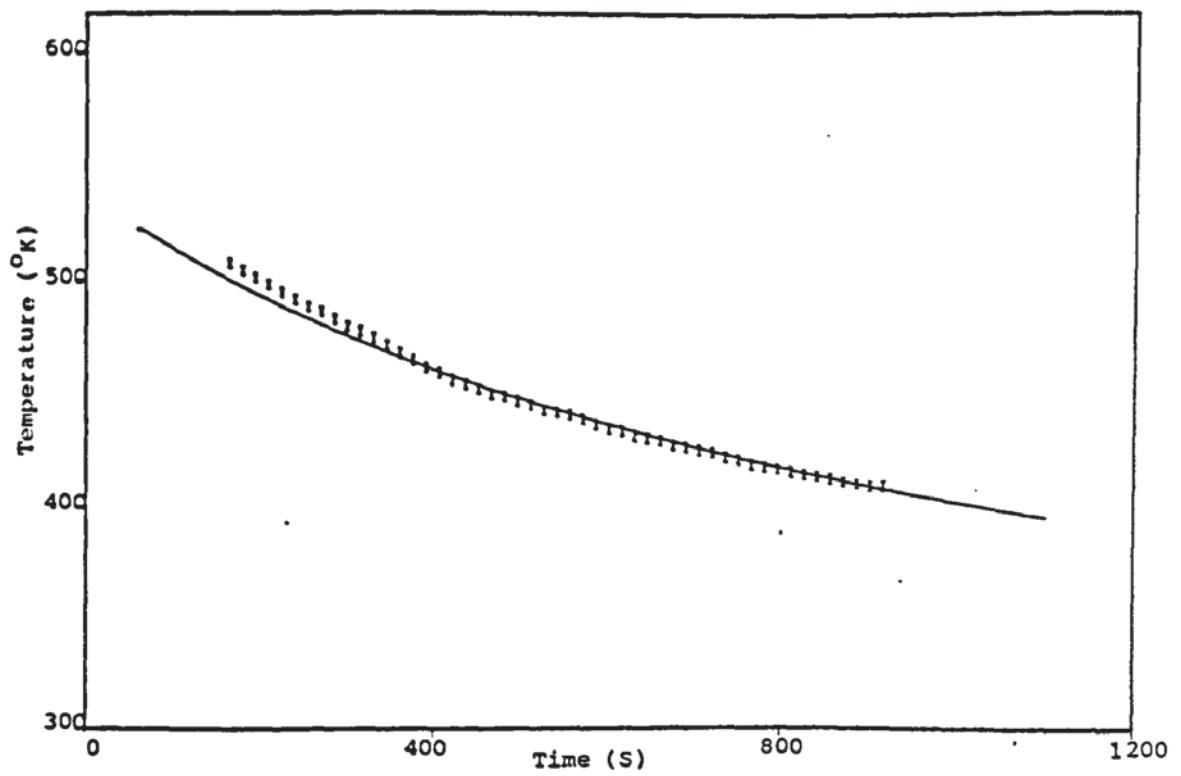


Fig.8.32c: Measured temperatures and the calculated cooling curve of specimen D11

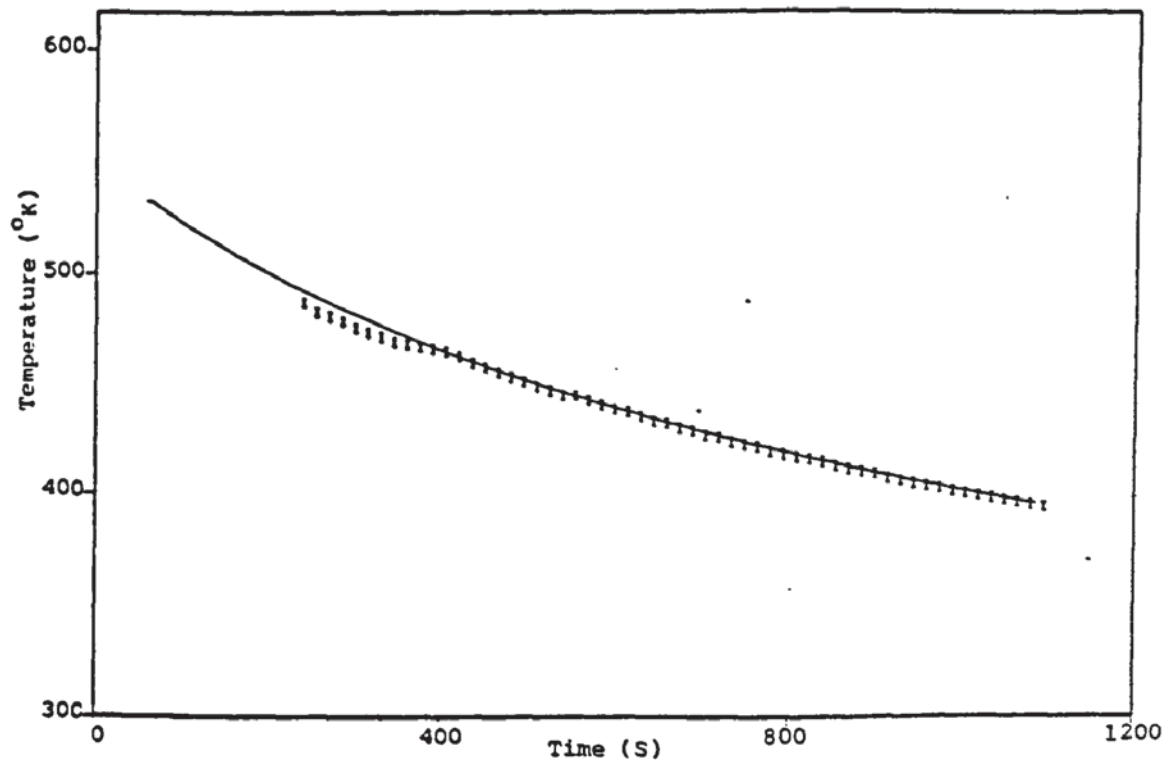


Fig.8.32d: Measured temperatures and calculated cooling curve of specimen D09

leadthrough and the loop (see design of jig number 2, Appendix A, page 274), and also because the contact area between the specimen and the jig was very small, the conduction heat losses were greatly reduced. Another important factor in heating the jig and specimen, and therefore their final temperature difference, is their surface area to mass ratios. The surface area to volume ratio of specimen was $100/5 = 20$, and the unit length of the jig's stainless steel tube had a ratio of $1.178/0.061 = 19.3$. This means that with the same mass, the loop had received a smaller discharge current and accordingly its temperature rose slightly less. But as the difference between the two ratios was very small (3.5%), it can be assumed that the final temperature difference was small and therefore the effect of jig temperature on the cooling of the specimen can be ignored. This analysis may lead to the conclusion that a more accurate method of temperature measurement is required. The temperature measurements were done with the mobile thermocouple. This mobile thermocouple technique had the disadvantage that the thermocouple could not be seen visually during operation in the Electrotech ion plater. Thus its position had to be checked prior to the closure of the chamber by counting the number of turns required to bring the thermocouple from the horizontal position into contact with the specimen (see design of the thermocouple holder in Appendix A, page 277). Therefore the contact area between the hot junction of the thermocouple and the specimen could have varied, either through uncertainty of the point of contact,

or due to the flexibility of the thermocouple, or by thermal expansion and contraction of the specimen and the thermocouple.

An alternative method was to spot weld the thermocouple wires onto the specimens. This meant that the thermocouple indicator and compensation leads had to be at floating potential and at the specimen applied voltage when it was subjected to glow discharge. This technique was rejected by the university officers on grounds of safety. Another alternative was the use of a pyrometer. This technique also encounters numerous difficulties, including the viewing of the specimen.

8.7: Deposition of copper.

Two sets of experiments were carried out to find conditions for reproducible deposition rates. In the first set of experiments 10KV was chosen as the acceleration voltage with 0.7 A as the beam current. The melt level was kept at position A as shown in Fig.8.33, which gave a 33.5 cm source to specimen distance. Results of eight tests carried out under these conditions are presented in Table 8.14. The coefficient of variation of these results was:

$$0.0416 / 0.0812 = 0.5127$$

This value indicates that the reproducibility was unacceptably low.

The reason behind fluctuations in evaporation rates at any

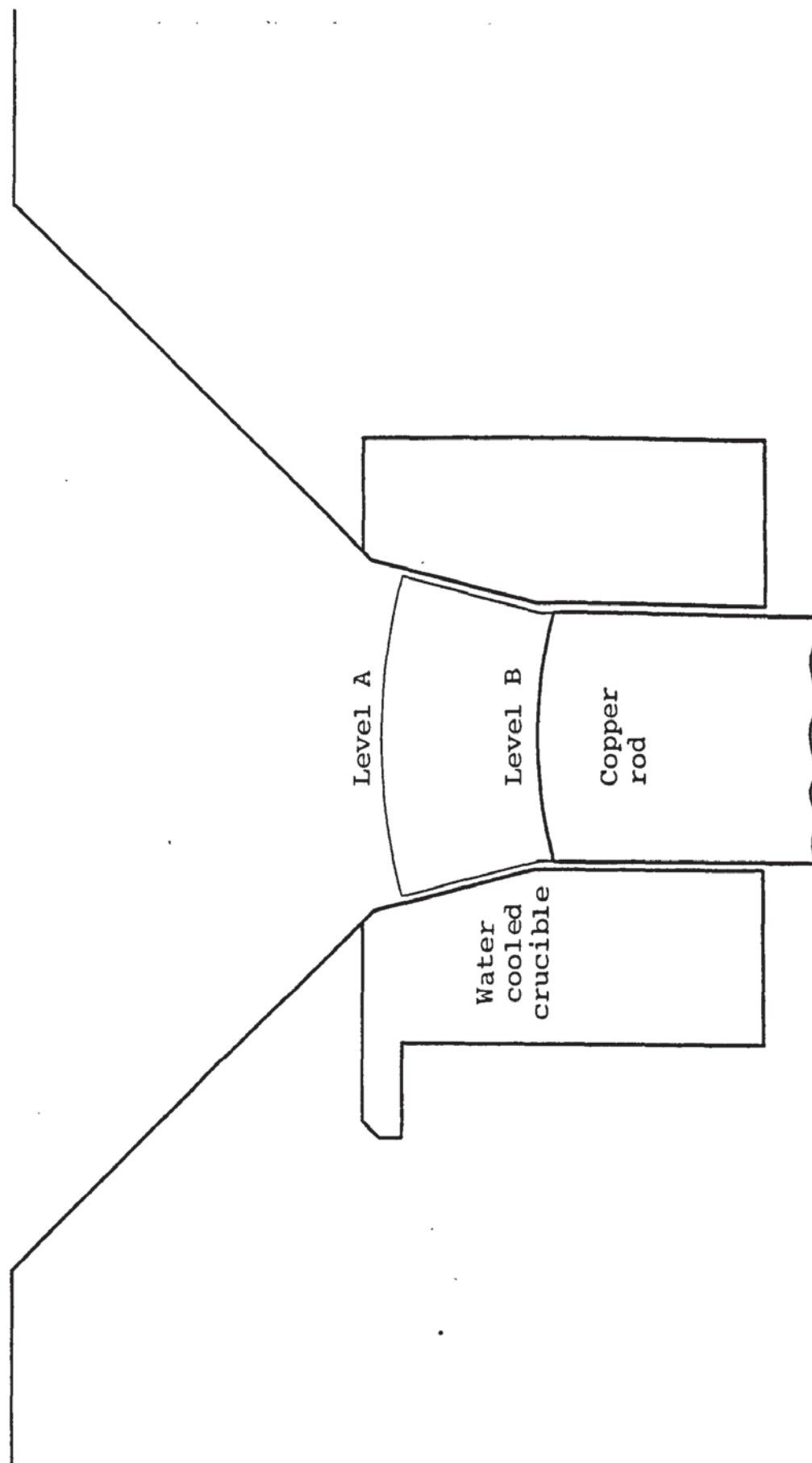


Fig.8.33: Two positions of the melt level in the water cooled crucible.

Specimen number	Specimen area (cm ²)	Deposited weight (mg)	Deposition rate (mg/min/cm ²)
C01	49.75	35.0	0.1407
C02	49.75	28.9	0.1162
C03	49.75	21.6	0.0868
C04	49.75	24.0	0.0965
C05	49.75	22.5	0.0904
C06	49.50	17.3	0.0699
C07	49.35	10.0	0.0405
C08	49.87	2.2	0.0088

Table 8.14: Deposition rates of copper on stainless steel.

Source to specimen distance = 33.5 cm

Power input : 7 KW

Deposition duration : 5 minutes.

given power input level is fluctuation in heat transfer at metal/crucible interface. The amount of this heat loss depends on the temperature difference between the molten pool and the crucible, and the contact area between the two. As the evaporant ideally does not wet the crucible, the thermal conductivity between the two participants fluctuates continuously. This is due to the intense thermal agitation produced by the very sharp temperature gradient between the molten pool and the crucible. Ideally the rod diameter must be such that, taking into account thermal expansion, it maintains a small clearance gap with the

crucible at a temperature near the melting point. This ensures ease of rod rotation, which is essential for maintaining a uniform pool, and minimizing the heat loss fluctuations.

Keeping the melt level at position A of Fig.8.33 causes the following problems:

- a)- the contact area between rod and crucible is large, which results in high heat losses;
- b)- evaporation from this position leaves a recess at the middle of the top area of the rod, which makes it difficult to find the correct source to specimen distance;
- c)- to keep the distance constant, it becomes necessary to raise the rod. But then, due to reduced contact area, the rate of heat loss drops drastically and the pool becomes larger, which softens the near edge area of the top of the rod. This causes a run down of metal back to the crucible and the re-establishing of the contact area. This new area changes the heat loss characteristics of the system once more, and increases its inconsistency.

To overcome these problems, the second set of experiments was carried out with the melt level at position B of the Fig.8.33, which gave a source to specimen distance of 35.6 cm. In this set of experiments four levels of beam current were tried, viz. 0.6, 0.7, 0.8 and 0.9 A, at 10KV acceleration voltage. Eight tests were done at each beam current, with their results presented in Table 8.15 and Fig.8.34. Table 8.16 shows the statistical analysis of the results.

Specimen number	Power input (KW)	Specimen area (cm ²)	Deposit weight (mg)	Deposition rate (mg/min/cm ²)
C10	6	49.75	102.9	0.4137
C11	6	49.75	34.1	0.1371
C12	6	49.75	102.6	0.4125
C13	6	49.75	49.1	0.1974
C31	6	49.75	48.7	0.1958
C32	6	49.75	95.8	0.3851
C33	6	49.75	25.0	0.1005
C34	6	49.75	114.1	0.4587
C25	7	51.25	172.5	0.6732
C26	7	51.25	175.0	0.6829
C27	7	51.25	208.3	0.8129
C28	7	51.25	165.5	0.6458
C29	7	51.25	145.5	0.5678
C35	7	50.63	142.4	0.5625
C36	7	51.00	175.2	0.6871
C37	7	51.25	199.8	0.7797
C20	8	51.25	168.0	0.6556
C21	8	51.25	226.2	0.8827
C22	8	51.00	169.7	0.6655
C23	8	51.25	243.5	0.9502
C24	8	50.63	166.0	0.6557
C38	8	51.25	160.2	0.6252
C39	8	51.25	180.8	0.7056
C40	8	51.25	246.0	0.9600
C15	9	50.00	278.0	1.1120
C16	9	51.25	329.9	1.2874
C17	9	51.00	272.7	1.0694
C18	9	51.25	305.2	1.1910
C19	9	50.75	282.0	1.1113
C41	9	51.25	266.6	1.0404
C42	9	51.25	301.4	1.1762
C43	9	51.25	319.4	1.2464

Table 8.15: Deposition rates of copper for a source to specimen distance of 35.6 cm (melt at level B)
Deposition duration : 5 minutes.

Power input (KW)	Deposition rate (mg /min / cm ²)			
	Standard deviation	Mean	Coefficient of variation	Limits of mean at 95% confidence
6	0.1437	0.2876	49.9 %	0.1201
7	0.0887	0.6765	13.1 %	0.0742
8	0.1429	0.7626	18.7 %	0.1195
9	0.0861	1.154	7.4 %	0.072

Table 8.16: Statistical analysis of the results
presented in Table 8.15.

Attention must be drawn to the fact that, in all of the experiments, only one side of the specimens was coated, except for the experiments carried at 9KW power input. Cross-section examination of these specimens showed that the coating thickness on the back side of the specimens was about a quarter that of the front side. For this reason, although Tables 8.15 and 8.16 show the overall deposition rates, in Fig.8.34 the coating of the back surfaces is taken into account by dividing the deposition rates by 1.25.

As the rod diameter was 37 mm and the internal diameter of the cylindrical part of the crucible was 39.6 mm, the clearance gap should have been 1.95 mm, taking $17 \times 10^{-6} / ^\circ\text{K}$ as the linear expansivity of copper. However, there was mis-alignment in manufacturing and assembly of the water cooled crucible and the rod feed mechanisms. This led to asymmetry of the feed hole and the necessity of using a

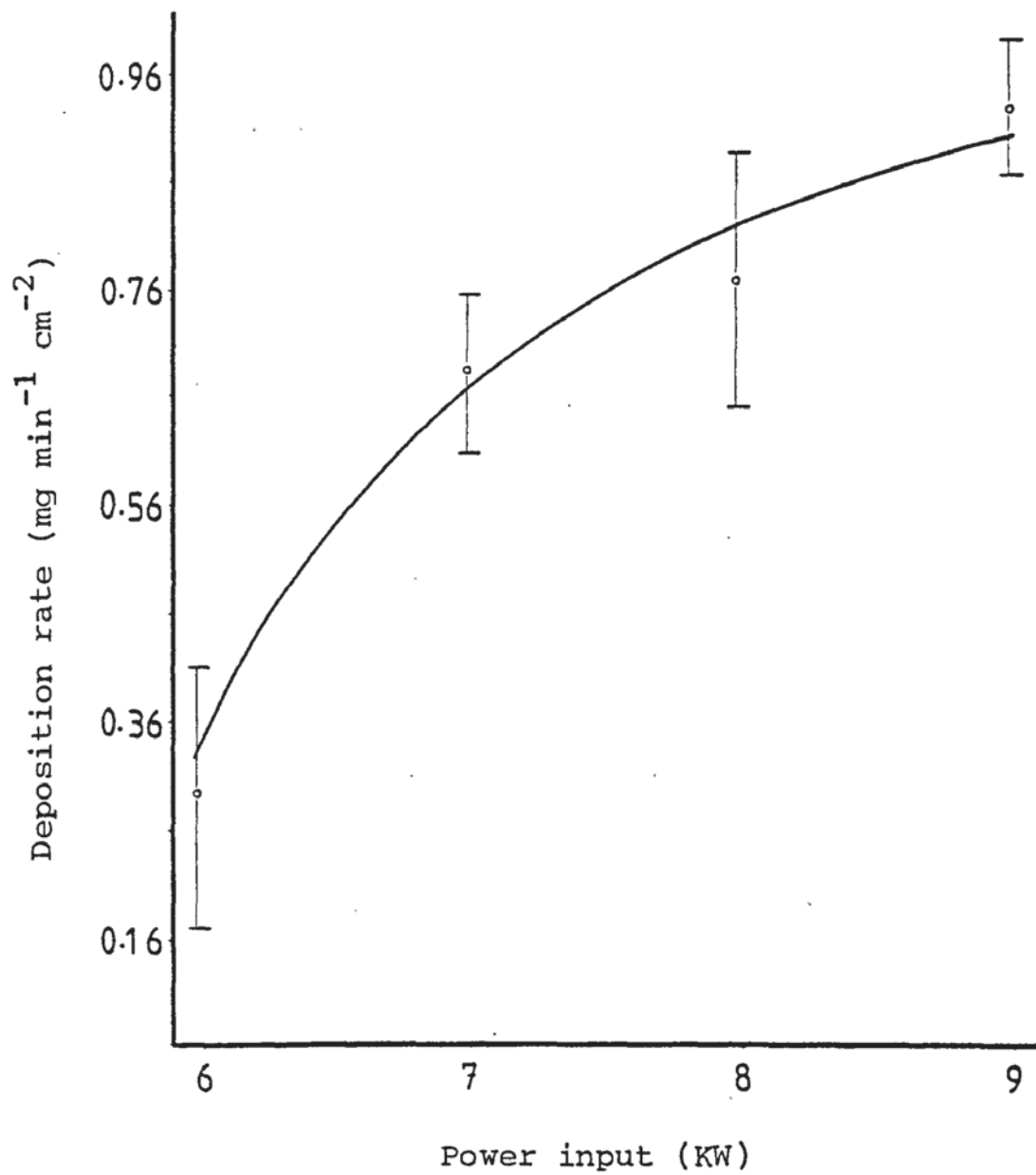


Fig.8.34: Plot of deposition rate versus power input
(melt at level B).

smaller rod diameter than the ideal size. The asymmetry also caused a slight tilt of the rod, which in turn produced an asymmetric clearance gap. The final result of this chain of asymmetries, in the second set of experiments, was a run of molten metal down one side of the rod. This not only caused interruption of the rod rotation at near melting point temperatures, but also caused inconsistency in the contact area between rod and crucible.

As is demonstrated in Fig.8.34, initially by increasing the power input, the deposition rate increases but at higher powers the curve tends to flatten. This is caused by the vapour cloud just above the pool.

The case will now be considered where evaporation has started at a high vacuum and low power inputs. As the power is gradually increased, evaporation proceeds as follows: At low power inputs the evaporation rate is small and therefore the vapour does not produce a viscous cloud above the source. Until a viscous cloud is formed molecular flow of the evaporated material pervades the region just above the source. In this region the vapour pressure is low, and movement of vapour particles is virtually independent of other particles. As the power input increases, the evaporation rate increases and eventually a viscous vapour cloud will be formed just above the source. This cloud has two effects; first its pressure reduces the evaporation rate at any constant

temperature, which means a higher power input is required to maintain the evaporation rate. As the power input is further increased, the vapour cloud becomes more viscous and a point will be reached at which the rate of evaporation is equal to the rate of viscous flow of the vapour away from the source region. At this point the evaporation rate has its maximum possible value. Secondly, the vapour cloud increases collisions between the electron beam and vapour particles, which reduces the number of electrons striking the surface of the melt. The magnitude of this effect depends on the viscosity of the vapour cloud and the path of the electron beam through it. Therefore there is an optimum power input which gives the maximum rate of evaporation for a fixed set of conditions. Beyond this value the evaporation rate might even decrease⁽²⁵⁶⁾.

Up to the formation of the vapour cloud, the molten pool can be considered as the actual evaporation source for calculations of spatial distribution of the evaporated materials. But as the viscous cloud is formed, evaporation should be considered to be from the cloud rather than the molten pool. At this stage the source to specimen distance is no longer the molten pool to specimen distance, but should be taken to be the distance between the specimen and the centre of the cloud. Depending on how large the vapour cloud is, specimens may be found to be surrounded by the cloud. This causes vapour deposition on surfaces out of line of sight of the crucible. Copper deposition on the back surfaces of the specimens coated at 9KW power

input was caused by this effect and is an indication of how large the vapour cloud can be. A complete review of this subject is given by R.J.Hill⁽²⁵⁶⁾.

Further experiments have shown that the maximum possible power input, for copper and with baffle valve to the upper chamber partially open, is 9.5KW. This value was obtained based on 10KV acceleration voltage and 0.95 A beam current.

CONCLUSIONS.

The following summarises the conclusions that can be drawn from the work.

1. The background pressure has a pronounced effect on the sputtering rate of stainless steel and on the reproducibility of the results. The chamber should be pumped to a pressure $\ll 10^{-5}$ Torr prior to ion bombardment.
2. The combination of 30 mTorr argon pressure and 4 KV applied voltage provides the best conditions for good reproducibility of sputtering rates.
3. The design of the electron beam gun assembly needs to be improved as detailed in Fig.7.25. To prevent damage (and possible consequent contamination) from arcing.
4. A fault in the trip switch circuit of the arc protection unit as supplied by the manufacturer requires investigation and remedial action.
5. Uneven etching of specimens, especially at edges can be overcome by using curved sections close to the sharp edges, as was shown by the improved design of jig number 2.
6. The edge effects are caused by the non-uniform distribution of the electrostatic field. Altering the jig design to that of jig number 2 changed the field lines and limited the angles of incidence to close to normal. This produced a uniform etching, and reduced the sputtering rate by $\frac{3}{4}$.

7. Protrusions developed on stainless steel specimens held in jig number 2 do not appear to have originated from inclusions or grain boundaries. They appear to have formed between neighbouring etch pits as part of the process of pit growth.
8. Sputter etching of specimens is affected by local composition variations in the steel and by the mechanical work applied to the surface prior to ion bombardment.
9. Sputter etching improves the performance of stainless steel as a solar selective surface. This is caused by an improvement in solar absorptivity, despite increased thermal emissivity of the surface.
10. A mobile thermocouple can be used to measure the emittance of specimens over small temperature ranges. But great care must be exercised to obtain reliable temperature measurements.
11. To obtain a reproducible rate of evaporation, the melt level should be kept just below the top of the cylindrical part of the rod fed crucible.
12. The feed rod diameter was found to be critical for the maintenance of a uniform rate of evaporation. The rod should be made to a diameter that after expansion at near melting point temperature leaves a small clearance gap with the crucible.

CHAPTER TEN:

FURTHER WORK.

The following suggestions for further work are proposed:-

1. An electron beam gun assembly should be built to the new design as detailed on p.181, and then assessed over a range of different operating conditions.
2. After each ion plating process the jig becomes coated as well as the specimen. This coating may act as seeding material during sputter etching of the next specimen. This should be investigated and particular attention given to edge effects.
3. Information must be obtained on the effect of contaminants such as oxygen and nitrogen on the edge effects. Also the pressure and potential ranges within which jig number 2 minimizes edge effects should be determined.
4. The mobile thermocouple technique needs to be developed and assessed, probably by accurate and reliable measurements of specimen properties which have known temperature-property relationships.
5. The results of the cooling curve emittance measurements should be checked against an infrared spectrophotometer to test the accuracy of the technique.

APPENDIX

A

1: Design and construction of jig number 1.

Jig number 1 was designed to minimize the current carried by the jig and therefore to enable the operator to measure the specimen current density accurately. To achieve this target it was required to shield most parts of the jig. Figure A1 shows different components of the jig assembly. Items 1 and 2 form the jaws of a vice which hold the specimen. Because these parts would be subjected to glow discharge, to avoid seeding of specimens by sputter deposition from the jig, they had to be constructed from the same material as specimens, i e. stainless steel. In order to connect the specimen holder to the high tension leadthrough, a copper rod was used (item number 3). To minimize back sputtering from the chamber walls onto the specimen, it was desirable to keep a reasonable distance between the two. This was achieved by having the copper rod, 180 mm long. This rod had a screw fit onto the high tension leadthrough and could be connected to item 2 via a $\frac{1}{4}$ " BSF nut at the other end.

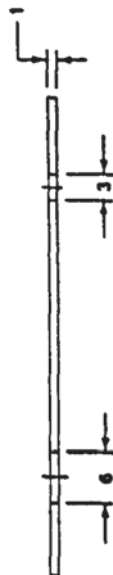
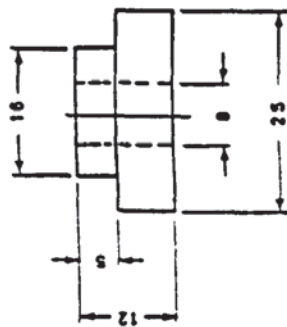
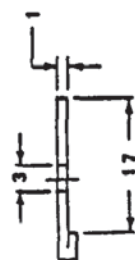
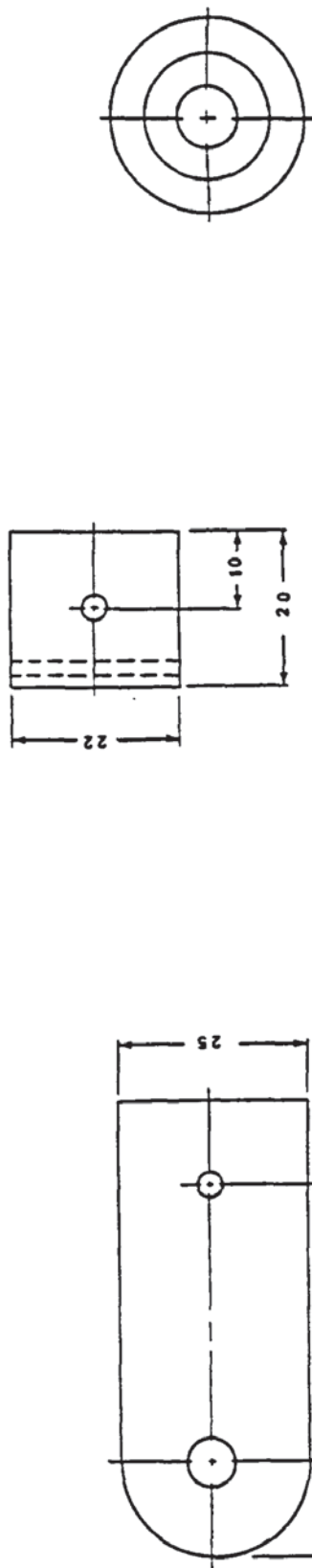
Items number 4 and 5 together, provided a cylindrical enclosure which enclosed the junction of the specimen holder and the copper rod. A slot was machined into item number 4 to provide the exit port for item number 2. This slot maintained a gap smaller than the thickness of the dark space layer between the two parts, preventing occurrence of a glow discharge in that region.

In order to shield the copper rod, a 190 mm long stainless

steel tube (item number 6) was used. This tube had two holes drilled into it to help pumping down of the space contained inside it, and was threaded at one end to screw-fit into item number 7. Item number 4 could slide on the other end of the tube, and could be adjusted and fixed by means of a 6 BA bolt to maintain a uniform gap between the slot and the specimen holder. Item number 7 was positioned onto the body of the high tension leadthrough and was fixed by means of three 8 BA bolts. This also provided the earth connection for the whole shield.

Item number 8 was made of compressed asbestos and slides onto the copper rod. Being positioned on top of the specimen holder and partly inside the stainless steel tube, it ensured electrical insulation between high tension parts (the specimen holder and the copper rod) and the earth shield.

Figure A2 shows the jig assembly. Photograph A3 shows the 3 parts of the jig assembly and their relative positions, while photograph A4 shows the jig holding a specimen.



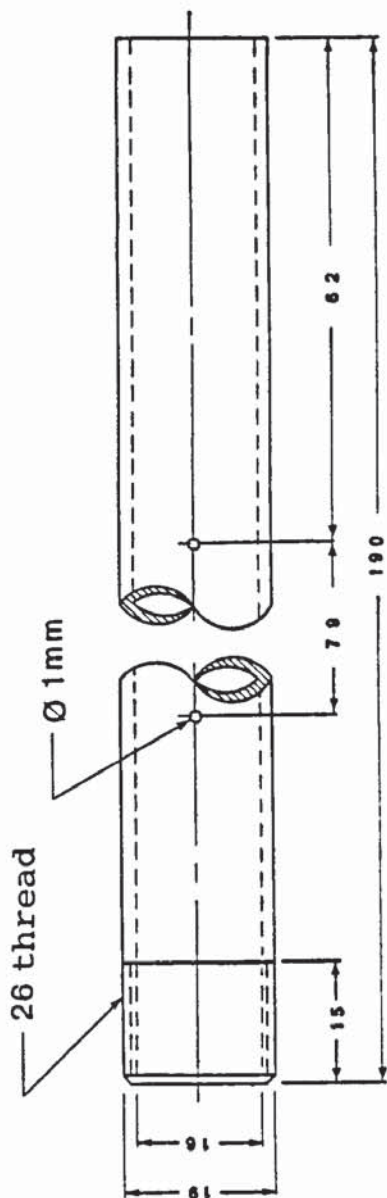
Item 2

Item 1

Item 8

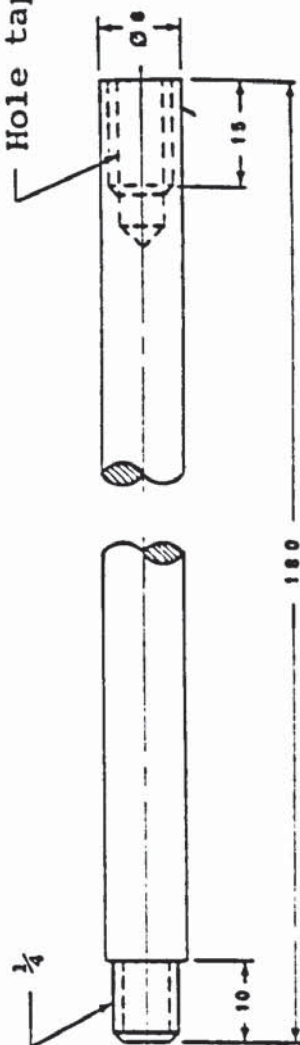
Fig.A 1: Parts of jig number 1

3, 3 EQ SP holes
to fit item 4

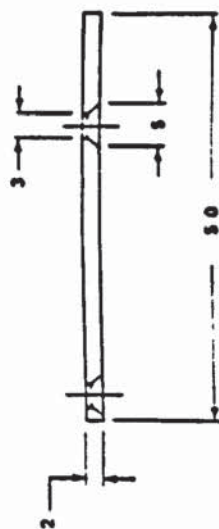


Item 6

Hole tapped $\frac{1}{4}$

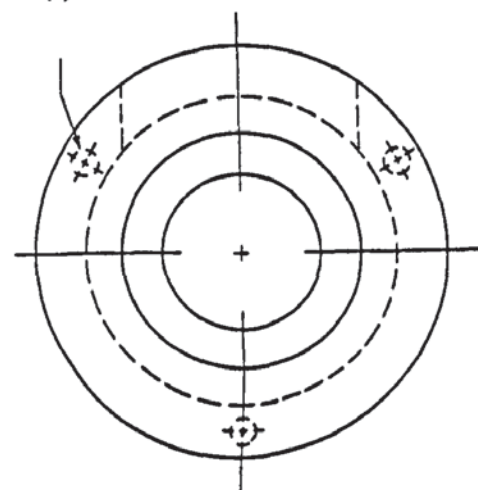
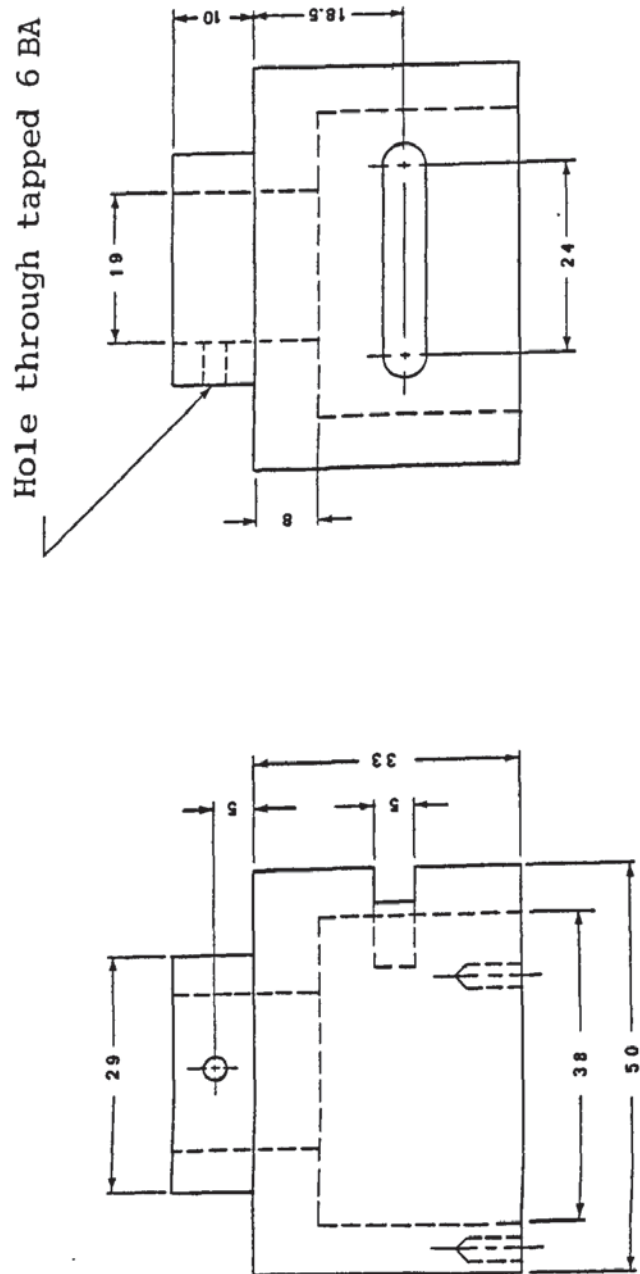


Item 3



Item 5

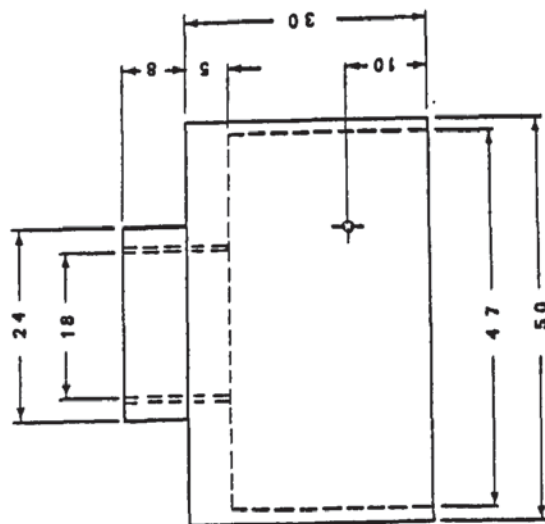
Fig.A 1: Parts of jig number 1



3 EQ SP holes. Tapped 4 BA, 4 mm deep.

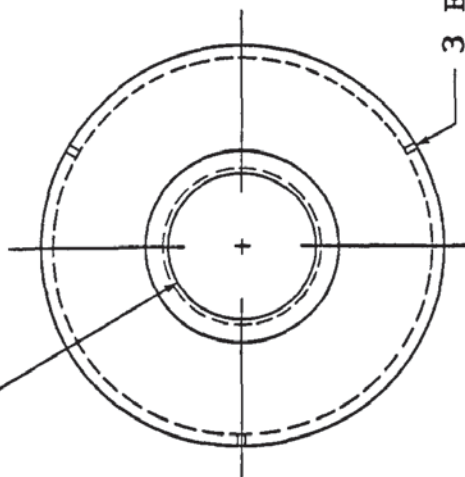
Item 4

Fig.A 1: Parts of jig number 1.



Item 7

Hole threaded to suit $\frac{3}{4}$ " OD
26 thread tube (item 6).



3 EQ SP holes
Tapped 8 BA

Fig.A 1: Parts of jig number 1.

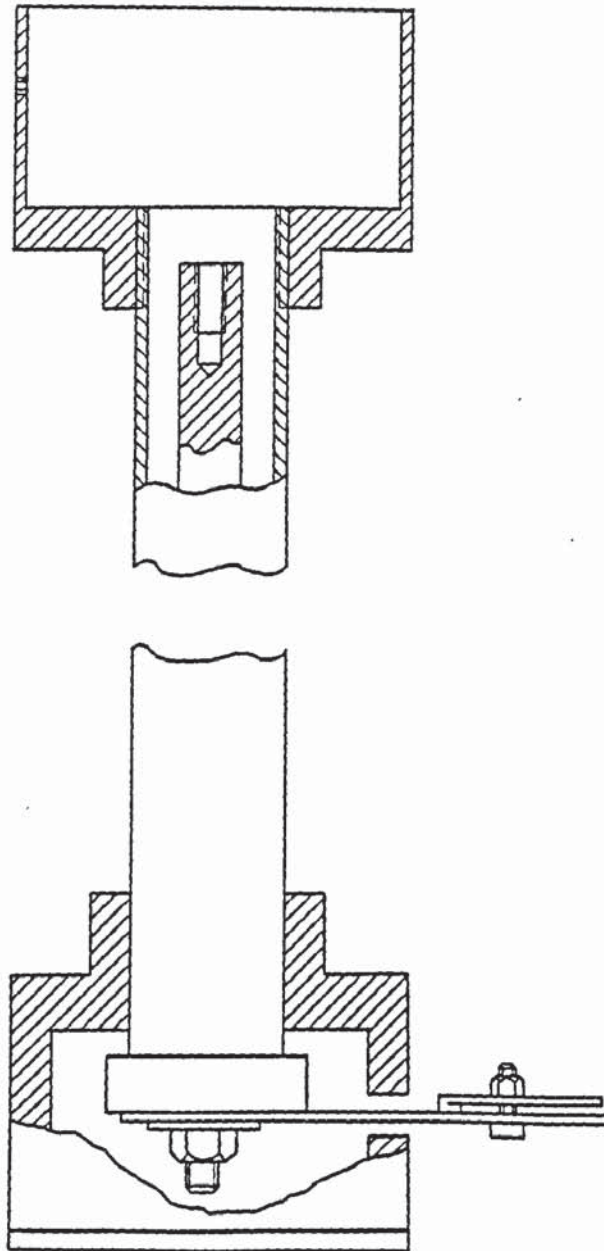


Fig.A 2: Assembly of jig number 1.



Fig.A3: Three main parts of
jig number 1.




Fig.A4: The assembled jig number
1, holding a specimen.

2: Design and construction of jig number 2.

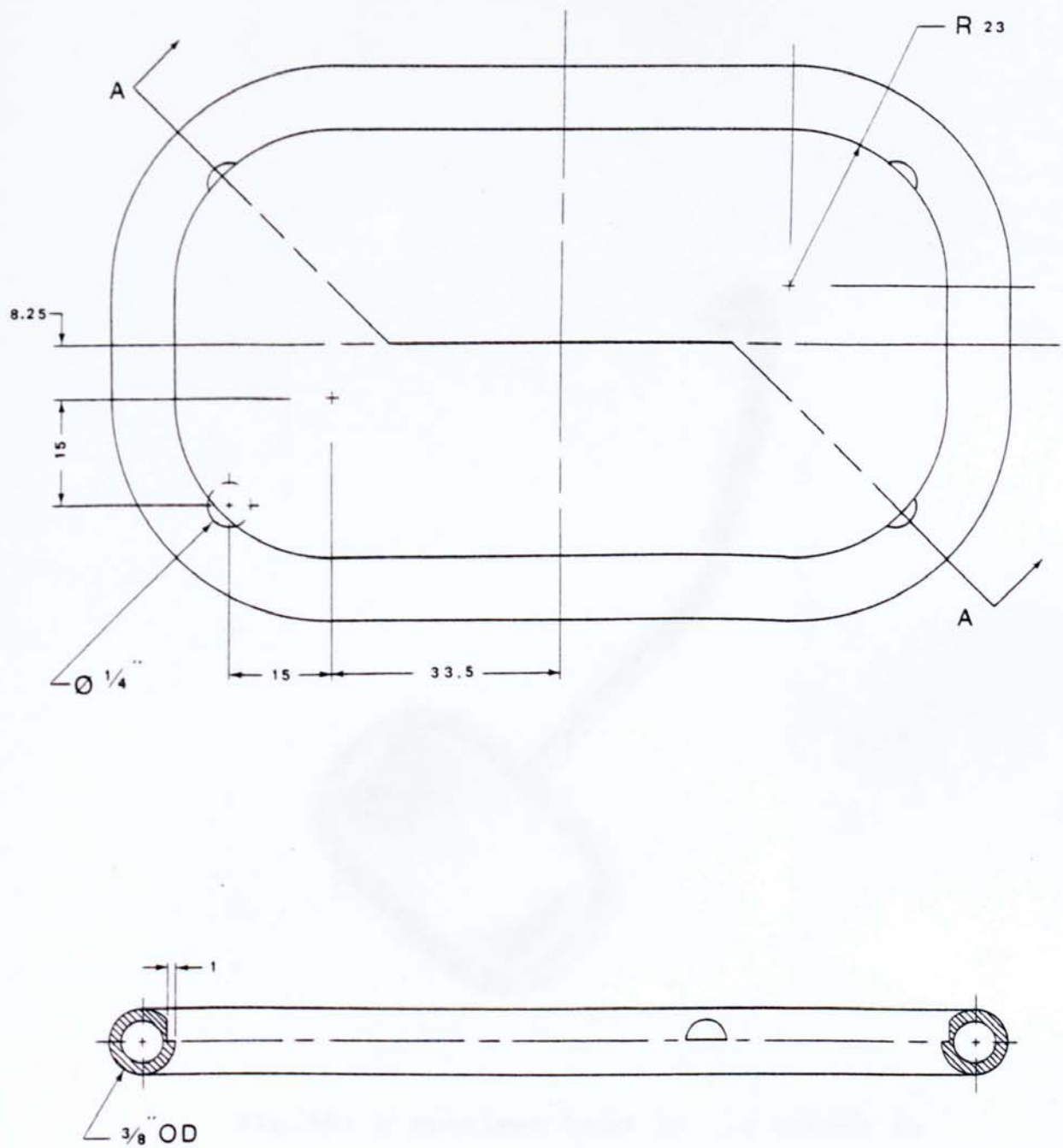
This jig was designed to exclude the edge effects which were observed in using jig number 1. As the edge effect is discussed in some detail in page 212 chapter 8, it will not be discussed here.

Practically, a large radius curved edge close to a sharp edge would modify the field lines in order to create a more uniform electrostatic field (see figure 8.18(a and b) page 222).

Jig number 2 was composed of 2 parts which were welded together, a specimen holder and a hanger, both made of a 3/8" OD 1/16" wall thickness 304 stainless steel tube.

The hanger was made to shape . The short arm of this hanger was pressed flat in the plane normal to the plane of the hanger. A 7 mm diameter hole was drilled in this arm, in order to connect it to the high tension leadthrough. The longer arm was welded to the specimen holder, so that it would be held horizontally at a distance of 28 cm above the water cooled crucible. The specimen holder was made by bending the tube to a closed loop. Four small platforms were machined into the tube wall thickness, at inner corners of the loop, so that a 10x5 cm specimen could rest on them.

Details of specimen holder are shown in Fig.A5, and photograph number A6 shows a specimen held by the jig.



AA plane

Fig.A 5: Jig number 2.



Fig.A6: A specimen held in jig number 2.

3: Design and construction of the thermocouple holder.

The thermocouple holder is shown in photographs A7 and A8. As can be seen, the thermocouple is shielded in a tube which can swing around a fixed point inside the protection box; and when the tube swings down, the thermocouple slides out.

Figure A9 shows the principal mechanism of the relative movements of the tube and the thermocouple. The length of the tube is presented by line \bar{AD} passing through the point C; and the end of the tube, point D, is fixed to point O_2 through the arm \bar{DO}_2 and can swing around O_2 on a circle. The length of the thermocouple is presented by line \bar{BC} . As point C moves on the circle O_1 , free end of the tube (point A) follows path number 1, and the thermocouple tip follows path number 2. In figure A9, part of path 2 which is on the left hand side of path 1 indicates that the thermocouple tip is out of the tube. Thus, the desired length of thermocouple out of the tube at any position can be obtained by the right choice of the lengths of the tube (\bar{AD}), the thermocouple (\bar{BC}), and the tube arm (\bar{DO}_2).

In the present work, an 8" long 3/8" OD, 304 stainless steel tube was used to carry and shield a 6.7" long thermocouple (details of the thermocouple can be found in page 127, chapter 6). This tube was slotted longitudinally to a length of 4", from the fixed end. A brass T piece was made to a size which could slide into the tube via its straight length, and had its arm extended out of the tube through

the slot. The straight length of the T piece had a longitudinal hole drilled into it, such that the thermocouple could just pass through it. The arm of the T piece could fit into a hole drilled into the face of a brass wheel, forming the point C in Fig.A9. This brass piece was threaded on its thickness and could be revolved by a worm screw from outside of the vacuum chamber via a feedthrough. This Edwards made feedthrough was claimed to be leak-proof up to a vacuum as high as 10^{-7} Torr.

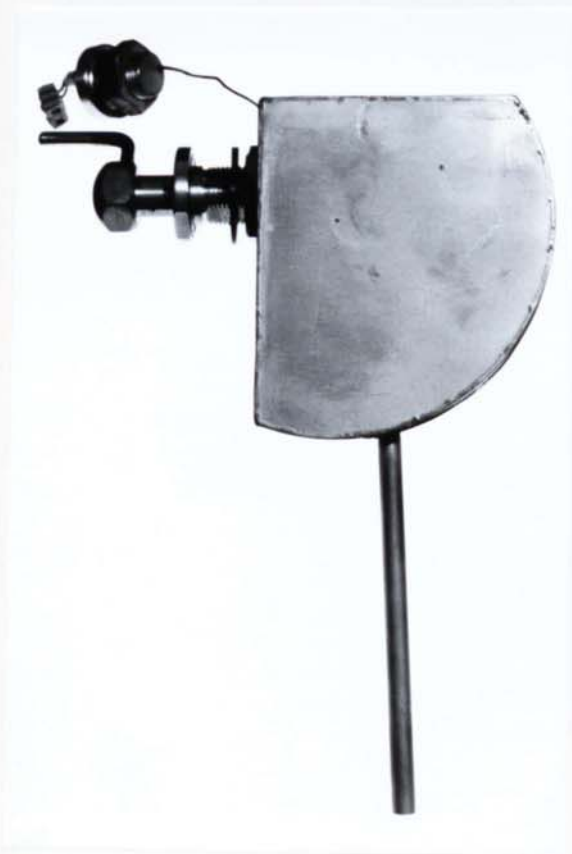
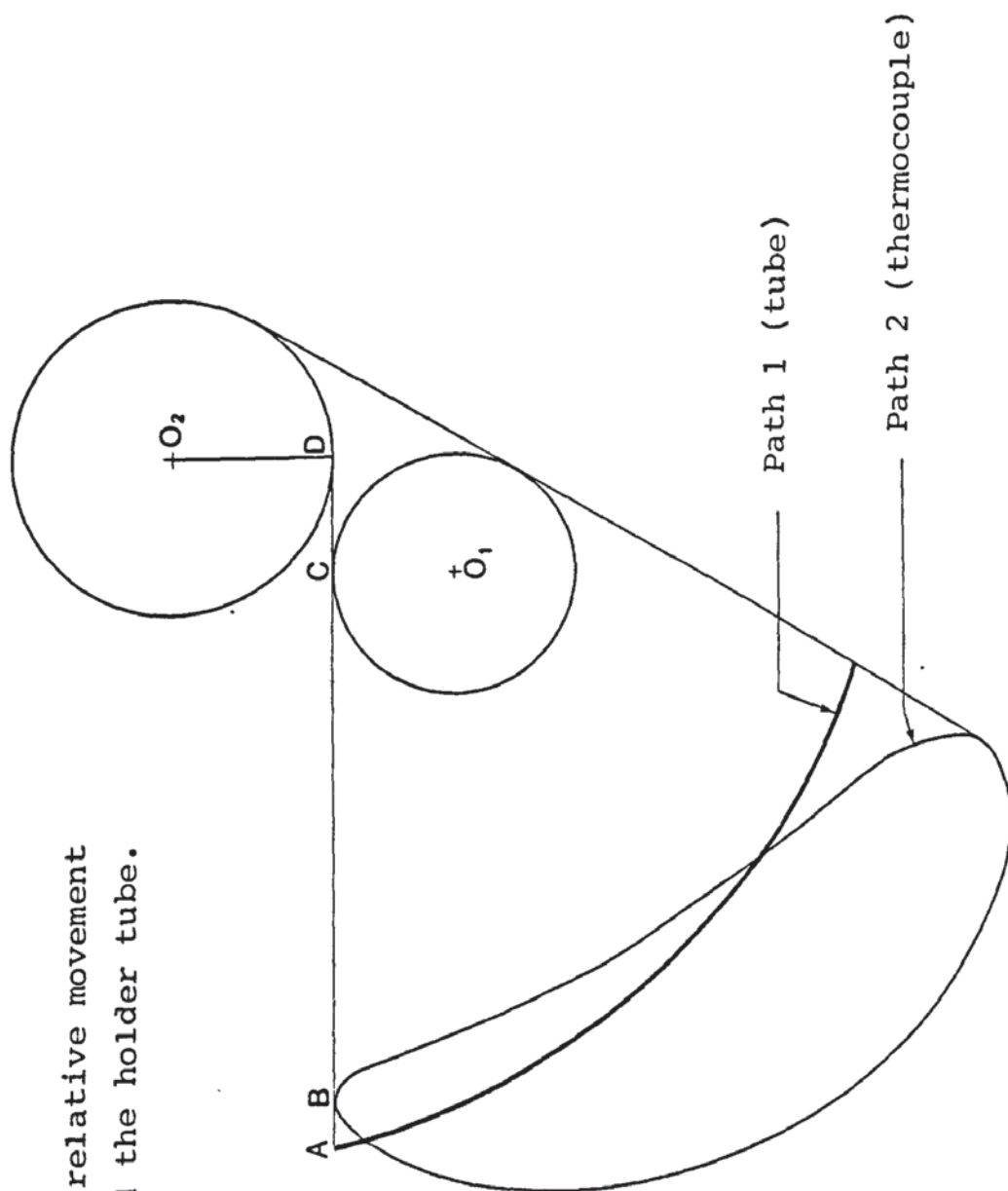


Fig.A7: The thermocouple holder.
The holder tube in horizontal
position.



Fig.A8: The operational position.
The thermocouple is out
of the holder tube.

Fig.A9: Principal mechanism of relative movement of the thermocouple and the holder tube.



APPENDIX

B

Operational procedure for the small ion plater:

1. Original switch on:

1. Switch the mains on,
2. Open the cold water tap $\frac{1}{2}$ turn,
3. Close the chamber cold water valve, if it is open,
4. Open the hot water tap,
5. Switch the rotary pump on, and then close the rotary pump air admittance valve,
6. Make sure that roughing and high vacuum valves are closed,
7. Open the backing valve,
8. Switch on the diffusion pump,
9. Switch on the Speedivac Pirani-Penning gauge panel,
10. Wait 15-20 minutes to warm up the diffusion pump,
11. Turn the Pirani knob to position S.V. and adjust the SET VOLTAGE knob to bring the pointer to the S.V. red mark on the meter and then switch to position HEAD 1.

2. To open the chamber:

1. Close the chamber's cold water valve (if it is open), and open the hot water tap and close the cold water tap $\frac{1}{4}$ turn,
2. Make sure that roughing and high vacuum valves are closed,
3. Open the chamber air admittance valve and vent the chamber,
4. Switch off the chamber Pirani gauge if it is on,

5. Winch up the lid alone (to change specimen or for maintenance purposes), or together with the chamber (to load the coating material or for maintenance purposes); and lock the winch.

3. Pump down procedures.

1. Make sure that the sealing areas are clean, the chamber is positioned correctly on the base plate, and the wing nuts connecting the lid to the chamber body are reasonably tight,
2. Close the chamber air admittance valve,
3. Close the backing valve, and open the roughing valve,
4. Switch on the chamber's Pirani gauge, and wait until the pressure drops to about 10^{-1} m bar.
5. Close the roughing valve, and open the backing valve,
6. Open the high vacuum valve very slowly, and watch that the backing line pressure does not rise beyond $100 \mu\text{m}$,
7. Switch the chamber Pirani gauge to range 2 and wait until the pressure drops below 10^{-2} m bar, and then switch it off.
8. Switch the Penning gauge to S.V. and adjust the SET VOLTAGE knob to bring the pointer to the red S.V. mark on the meter, and then turn the switch to range 1,
9. Wait until the pressure drops below .1 on range 1, and then turn the Penning gauge to range 2,
10. Turn the hot water tap off and open the chamber cold water valve, and then open the cold water tap a further $\frac{1}{4}$ turn,

11. Wait until the pressure drops to the required level.

4. Glow discharge operation.

1. Switch the Penning gauge to S.V.,
2. Close the high vacuum valve,
3. Open the main argon gas bottle valve (if it is closed) and adjust the pressure to about 4 psi,
4. Switch on the chamber Pirani gauge,
5. Open the shut off valve, and open the gas inlet needle valve one turn,
6. Open the high vacuum valve slightly, and adjust it to obtain the required pressure, and wait for 5 minutes to ensure that the pressure is steady,
7. Switch on the high tension power supply and adjust the voltage via the high tension variable Variac; and wait for the required period,
8. Turn off the voltage and switch off the high tension power supply,
9. Close the needle and the shut off valves.

5. Evaporation procedure.

1. Switch on the low tension power supply,
2. Gradually increase the current via the three (viz. coarse, medium and fine) control knobs to obtain the required current,
3. Gradually turn down the current to zero when the evaporation is completed, and then switch off the power supply.

6. Complete shut off procedure.

1. Make sure that the chamber is under vacuum,
2. Make sure that roughing, high vacuum, chamber air admittance and gas inlet valves are closed,
3. Switch off all the gauges,
4. Switch off the diffusion pump and wait for 30 minutes to cool down,
5. Close the backing valve,
6. Open the rotary pump air admittance valve, and then switch off the rotary pump,
7. Switch off the mains, and turn off the water taps.

7. Emergency shut off procedure.

1. Turn off electricity from mains,
2. Turn off water taps,
3. Attempt to close all valves if possible,

8. Proposed guide lines.

1. Have the hot water running through the chamber's water jacket when the chamber is open to air, and if possible, keep it running while the chamber is open.
2. When inserting specimen, make sure that the connection with the jig is firm and also the jig is properly connected to the *high* tension leadthrough.
3. Make sure that there is a good contact between the evaporating boat/filament and the low tension electrode,
4. Every time that a correct reading of the backing line's Pirani gauge or the Penning gauge is required, the SET VOLTAGE must be adjusted as it is explained in sections

1 and 3 of this appendix,

5. Regularly clean the view port glass, but avoid scratching it,
6. Clean inside the chamber regularly and use Methylated spirit to remove any oil or grease,
7. The sealing areas MUST NOT be scratched,
8. Use liquid nitrogen to eliminate oil back-streaming from the diffusion pump.

REFERENCES

- 1 - B. Berghaus British Patent 510,993 (1938)
- 2 - D. M. Mattox Sandia Corporation Report
SC-DR-281-63, 1963;
Electrochem. Technol. 1964, 2, 295
- 3 - D. M. Mattox Proc. 2nd Int. Conf. Ion Plating and
Allied Techniques.
C. E.P. Consultants Ltd. 1979, p 1
- 4 - D. M. Mattox "Sputter Deposition and Ion Plating
Technology" AVS- Thin Film Division
Monograph (1974);
also Sandia Laboratories Report
SLA-73-0619 (July 1973)
- 5 - D. M. Mattox Jpn. J. Appl. Phys. Suppl. 1974, 1, 443
- 6 - D. M. Mattox J. Vac. Sci. Technol. 1973, 10, 47
- 7 - D. M. Mattox "Design Considerations for Ion Plating"
Sandia Corporation Report
SC-R-65-997 (1966)
- 8 - D. M. Mattox "Bibliography of Ion Plating and
Related Ion Bombardment Effects"
Sandia Laboratories Report SAND 79-0524J
- 9 - D. G. Teer Trans. Inst. Met. Fin. 1976, 54, 159
- 10- N. A. G. Ahmed M. Sc. Dissertation Salford Univ.
U.K. 1974

- 11 - K. D. Kennedy, G. R. Schenermann & H. R. Smith
Research & Dev. 1971, 22, 40
- 12 - W. R. Stowell Thin Solid Films 1974, 22, 111
- 13 - J. G. Davy & J. J. Hanak
J. Vac. Sci. Technol. 1974, 11, 43
- 14 - P. A. Walley Proc. 1st Int Conf. Ion Plating and
Allied Techniques.
C. E. P. Consultants Ltd. 1977, p 1
- 15 - R. D. Ivanov, G. V. Spivak & G. K. Kislova
Izv. Akad. Nauk.-U.S.S.R. Ser. Fiz.
1961, 25, 1524
- 16 - J. Edgecumbe, L. G. Rosner & D. E. Anderson
J. Appl. Phys. 1964, 35, 2198
- 17 - F. M. Penning & J. H. A. Moubis
Proc. Koninkl. Ned. Akad. Wetenschap
1940, 43, 41
- 18 - K. L. Chopra "Thin Film Phenomena"
R. Krieger Publishing Co. N. Y. 1979
- 19 - W. D. Gill & E. Kay
Rev. Sci. Instrum. 1965, 36, 277
- 20 - E. Kay J. Appl. Phys. 1963, 34, 760
- 21 - L. Holland "Vacuum Deposition of Thin Films"
Chapman & Hall 1963

- 22 - R. W. Berry, P. M. Hall & M. T. Harris
"Thin Film Technology"
D. Van Nostrand Company Inc. N. Y. 1968
- 23 - L. Holland Electronic Components 1970, 11,
181 & 285 & 429 & 533
- 24 - L. S. Palatnik, G. V. Federov, & P. N. Bogatov
Phys. Met. R 1966, 21, 89
- 25 - L. Harris & B. M. Siegel
J. Appl. Phys. 1948, 19, 739
- 26 - W. R. Beam & T. Takahashi
Rev. Sci. Instrum. 1964, 35, 1623
- 27 - S. G. Ellis J. Appl. Phys. 1976, 38, 2906
- 28 - J. A. Turner, J. K. Birtwistle & G. R. Hoffman
J. Sci. Instrum. 1963, 40, 557
- 29 - E. A. Roth, E. A. Margerum & J. A. Amick
Rev. Sci. Instrum. 1962, 33, 686
- 30 - J. Van Audenhove
Rev. Sci. Instrum. 1965, 36, 383
- 31 - T. Spalvins & W. A. Brainard
N. A. S. A. Tech. Mem. X3330
N. A. S. A. Washington 1976
- 32 - J. R. Morley U. S. Patent 3,562,141 (Feb. 9. 1971)
- 33 - P. A. Walley, M. Wineberg & M. St J. Burden
J. Phys. (E) 1971, 4, 501

- 34 - D. L. Chambers, & D. C. Carmichael
Research & Dev. 1971, 22, 32
- 35 - E. D. Erikson J. Vac. Sci. Technol. 1974, 11, 366
- 36 - H. R. Harker & R. J. Hill
J. Vac. Sci. Technol. 1972, 9, 1395
- 37 - G. Hughes Proc. 1st Int. Conf. Ion Plating and
Allied Techniques
C. E. P. Consultants Ltd. 1977, p 169
- 38 - R. Culbertson, & D. M. Mattox
8th Conf. Tube Technology
I. E. E. E. Conf. Record 1966, p 101
- 39 - D. Stacey Lucas Research Centre, Birmingham, U. K.
Private communication
- 40 - N. J. Archer Proc. 3rd Conf. Ion and Plasma
Assisted Techniques
Thin Solid Films 1981, 80, 221
- 41 - J. L. Vossen Trans. Conf. Applications of Sputtering
Tuxedo N. Y. (M. R. C. Oranbug
N. Y. 1969)
- 42 - Y. Murayama J. Vac. Sci. Technol. 1975, 12, 818
- 43 - R. F. Bunshah 16th Ann. Conf. Soc. Vac. Coaters
Soc. Vac. Coaters N. J. 1973, p 5
- 44 - D. G. Teer Proc. 1st Conf. Ion Plating and
Allied Techniques
C. E. P. Consultants Ltd. 1977, p 13

- 45 - L. B. Leder Met. Fin. 1973, 72, 41
- 46 - M. El-Sherbiney
 Ph. D. Thesis Salford Univ., U.K. 1974
- 47 - B. T. Lundin N. A. S. A. Report SP-5111, 1972
- 48 - S. Aisenberg N. A. S. A. Report SP-5111, 1972 p 171
- 49 - S. Aisenberg & R. W. Chabot
 J. Vac. Sci. Technol. 1973, 10, 104
- 50 - E. D. Davis & T. A. Vaderslice
 Phys. Rev. 1963, 131, 319
- 51 - D. G. Teer In a technical report to Lucas
 Research Centre, U.K.
 Private communication with Lucas
 Research Centre.
- 52 - D. G. Teer, B. L. Delcea & A. Kirkham
 J. Adhesion 1976, 8, 171
- 53 - W. D. Westwood Prog. Surf. Sci. 1976, 7, 71
- 54 - M. Bader, F. Witteborn & T. W. Snouse
 N. A. S. A. Tech. Report TR-R105 1961
- 55 - L. I. Maissel "Physics of Thin Films" Vol. 3
 Eds. G. Hass & R. E. Thun
 Academic Press Inc. N. Y. 1966, P 61
- 56 - J. S. Colligon & M. H. Patel
 Rad. Effects 1977, 32, 193

- 57 - B. Navinšek Prog. Surf. Sci. 1976, 7, 71
- 58 - R. L. Maddox & H. L. Parker
 Solid State Technology 1978, 21 (4), 107
- 59 - G. J. Kominiak & D. M. Mattox
 Thin Solid Films 1977, 40, 141
- 60 - R. S. Nelson & D. J. Mazey
 "Ion Surface Interaction, Sputtering,
 and Related Phenomena"
 Eds. R. Behrisch, W. Heiland,
 W. Pochenrieder, P. Staib & H. Verbeek
 Max-Planck-Institute für Plasmaphysik
 Gordon & Breach Science Publishers
 1973, P 199
- 61 - D. Edwards, Jr., & E. V. Kornelsen
 Rad. Effects 1975, 26, 155
- 62 - R. J. MacDonald & D. Haneman
 J. Appl. Phys. 1966, 37, 1609
- 63 - R. J. MacDonald & D. Haneman
 J. Appl. Phys. 1966, 37, 3048
- 64 - J. J. Bellina, Jr. & H. E. Farnsworth
 J. Vac. Sci. Technol. 1972, 9, 616
- 65 - J. J. Cuomo, & R. J. Gambino
 J. Vac. Sci. Technol. 1977, 14, 152
- 66 - D. Chleck, R. Maehl, O. Cucchiara & E. Carnevale
 Int. J. Appl. Rad. & Isotopes 1963, 14, 581

- 67 - D. M. Mattox & G. J. Kominiak
J. Vac. Sci. Technol. 1971, 8, 194
- 68 - P. S. Ho, J. E. Lewis, H. S. Wildman & J. K. Howard
Surf. Sci. 1976, 57, 393
- 69 - J. S. Colligon, G. Fischer & M. H. Patel
J. Mat Sci. 1977, 12, 829
- 70 - Y. Adda, M. Beyeler & G. Brebec
Thin Solid Films 1975, 25, 107
- 71 - R. A. Johnson & N. Q. Lum
Phys. Rev. (B) 1976, 13, 4364
- 72 - D. M. Mattox "Thin Film Adhesion and Adhesion Failure -
A Perspective" Adhesion Measurement of
Thin Films, Thick Films and Bulk Coatings.
American Society for Testing and Materials
ASTM STP 640 1978, P 54
- 73 - G. J. Kominiak & J. E. Uhl
J. Vac. Sci. Technol. 1976, 13, 1193
- 74 - K. C. Stephens & I. H. Nilson
Thin Solid Films 1978, 50, 325
- 75 - G. Fischer, A. E. Hill & J. S. Colligon
Vacuum 1978, 28, 277
- 76 - D. G. Teer J. Adhesion 1977, 8, 289
- 77 - Z. L. Liau, B. Y. Tsaur & J. W. Mayer
J. Vac. Sci. Technol. 1979, 16, 121

- 78 - D. M. Mattox Thin Solid Films 1973, 18, 173
- 79 - S. Nakahara Thin Solid Films 1977, 45, 421
- 80 - C. A. Neugebauer
"Condensation, Nucleation and Growth
of Thin Films"
Handbook of Thin Film Technology
Eds. L. I. Maissel & R. Glang
McGraw-Hill Book Company N. Y. 1970, P 8
- 81 - M. A. Nicolet Thin Solid Films 1978, 52, 415
- 82 - J. L. Vossen, J. J. O'Neill, Jr. O. R. Mesker &
E. A. James J. Vac. Sci. Technol. 1977, 14, 85
- 83 - D. M. Mattox Thin Solid Films 1978, 53, 81
- 84 - Z. L. Liau & J. W. Mayer
J. Appl. Phys. 1978, 49, 5294
- 85 - L. I. Maissel, R. E. Jones & C. L. Standley
I. B. M. Research & Dev. 1970, 14, 176
- 86 - D. H. Boone, D. Lee & J. M. Schafer
Proc. 1st Int. Conf. Ion Plating and
Allied Techniques
C. E. P. Consultants Ltd. 1977, p 141
- 87 - Y. Saito, S. Yatsuya, K. Mihama & R. Uyeda
Japan. J. Appl. Phys. 1978, 17, 291

- 88 - T. Takagi, I. Yamada & A. Sasaki
Proc. 1st Int. Conf. Ion Plating and
Allied Techniques
C. E. P. Consultants Ltd. 1977, p 50
- 89 - R. D. Bland, G. J. Kominiak & D. M. Mattox
J. Vac. Sci. Technol. 1974, 11, 671
- 90 - J. L. Vossen J. Vac. Sci. Technol. 1974, 11, 875
- 91 - B. A. Movchan & A. V. Demchishan
Phys. Met. Metallogr. 1969, 28, 83
- 92 - J. A. Thornton Ann. Rev. Mat. Sci. 1977, 7, 239
- 93 - J. J. Garrido, D. Gerstenberg & R. W. Berry
Thin Solid Films 1977, 41, 87
- 94 - J. A. Thornton Thin Solid Films 1977, 40, 335
- 95 - D. S. Campbell "Mechanical Properties of Thin Films"
Eds. L. I. Maissel & R. Glang
McGraw-Hill Book Company N. Y. 1970
- 96 - D. W. Hoffman & J. A. Thornton
J. Vac. Sci. Technol. 1979, 16, 134
- 97 - D. W. Hoffman & J. A. Thornton
Thin Solid Films 1977, 40, 355
- 98 - J. A. Thornton & D. W. Hoffman
J. Vac. Sci. Technol. 1977, 14, 164
- 99 - D. W. Hoffman & J. A. Thornton
Thin Solid Films 1977, 45, 387

- 100 - J. A. Thornton, J. Tabock & D. W. Hoffman
Thin Solid Films 1979, 64, 111
- 101 - D. W. Hoffman & J. A. Thornton
J. Vac. Sci Technol. 1980, 17, 380
- 102 - D. M. Mattox "Interface Formation & the Adherence
of Deposited Thin Films"
Sandia Corporation Report
SC-R-65-852 (1965)
- 103 - D. G. Teer Tribology 1975, 8, 247
- 104 - M. El-Sherbiney & J. Halling
Wear 1977, 45, 211
- 105 - T. Narusawa, & S. Komya
J. Vac. Sci. Technol. 1974, 11, 312
- 106 - C. W. B. Martinson, I. J. Nordlander & S. E. Karlsson
Vacuum 1977, 27, 119
- 107 - B. Swaroop & I. Adler
J. Vac. Sci. Technol. 1973, 10, 503
- 108 - J. M. Walls, D. D. Hall, D. G. Teer & B. L. Delcea
Thin Solid Films 1978, 54, 303
- 109 - T. Spalvins "Characterization of Defect Growth
Structures in Ion Plated Films by
Scanning Electron Microscopy"
N. A. S. A. TM-79110 (1979)
- 110 - T. Spalvins J. Vac. Sci. Technol. 1980, 17, 315

- 123 - D. M. Mattox & R. D. Bland
J. Nucl. Mats. 1967, 21, 349
- 124 - "The Cadmium Coating of Very Strong
Steel Parts by Vacuum Evaporation"
Min. Tech. Process Spec. DTD 940 (Nov 1968)
- 125 - R. J. Smith Inst. Met. Fin.
Vac. Deposition Symp. (Oct. 1975)
- 126 - K. E. Steube & L. E. McCrary
J. Vac. Sci. Technol. 1974, 11, 362
- 127 - R. C. Krutenat
U. S. Patent 3,639,151 (1969)
- 128 - R. Pichoir Proc. 5th Int. Conf. C. V. D. 1975, p 298
- 129 - R. F. Janninck, C. R. Heiden & A. E. Guttensohn
J. Vac. Sci Technol. 1974, 11, 535
- 130 - E. L. Hollar, F. N. Rebarchik & D. M. Mattox
J. Electrochem. Soc. 1970, 117, 1461
- 131 - I. M. Reid, H. A. Macleod, E. Henderson & M. J. Carter
Proc. 2nd Int. Conf. Ion Plating and
Allied Techniques
C. E. P. Consultants Ltd. 1979, p 114
- 132 - R. S. Nowicki J. Vac. Sci. Technol. 1980, 17, 384
- 133 - L. D. Hartsough & D. R. Denison
"Aluminium-Silicon Sputter Deposition"
Perkin Elmer Ultek Devision
Tech. Report 79.01

- 134 - P. McLeod & L. D. Hartsough
J. Vac. Sci. Technol. 1977, 14, 263
- 135 - A. von Engel "Ionized Gases" 2nd Ed.
Oxford University Press (1965)
- 136 - R. Seeliger & G. Mierdel
"Handbook of Exp. Phys." 13/3
Akad. Verlag, Leipzig (1929)
- 137 - A. von Engel Phil. Mag. 1941, 32, 417
- 138 - A. Guntherschulze
Z. Phys. 1930, 59, 433
- 139 - A. Guntherschulze & H. Fricke
Z. Phys. 1933, 86, 451 & 778 & 821
- 140 - P. Sigmund Phys. Rev. 1969, 184, 383
- 141 - P. Sigmund Rev. Roum. Phys. 1972, 17, 823 & 969 &
1079
- 142 - P. Sigmund "Radiation Damage Processes in Materials"
Ed. C. H. S. Dupuy
Noordhoff The Netherlands 1975, p 3
- 143 - P. Sigmund J. Vac. Sci. Technol. 1980, 17, 396
- 144 - J. Lindhard, V. Nielsen & M. Scharff
Mat. Fys. Medd. Dansk. Vid. Selsk.
1968, 36, 1
- 145 - P. Sigmund Ann. Israel Phys. Soc. 1977, 1, 69

146 - K. B. Winterbon

"Ion Implantation Range & Energy
Deposition Distribution" Vol.2
Plenum N. Y. 1975

147 - H. H. Andersen & H. L. Bay

"Ion Surface Interaction, Sputtering
and Related Phenomena"
Eds. R. Behrisch, W. Heiland,
W. Poschenrieder, P. Stail & H. Verbeek
Max-Planck-Institute für Plasmaphysik
Gordon & Breach Science Publishers
1973, p 63

148 - P. Sigmund

"Inelastic Ion-Surface Collisions"
Ed. N. H. Tolk
Academic Press N. Y. 1977, p 121

149 - H. H. Andersen

J. Vac. Sci. Technol. 1979, 16, 770

150 - G. Betz

Surf. Sci. 1980, 92, 283

151 - N. Andersen & P. Sigmund

Mat. Fis. Medd. Dan. Vid. Selsk
1974, 39, 1 & 3 & 10

152 - P. Sigmund

J. Appl. Phys. 1979, 50, 7261

153 - R. Kelby & J. B. Sanders

Nucl. Instrum. Meth. 1976, 132, 335

154 - N. Q. Lam, P. R. Okamoto & R. A. Johnson

J. Nucl. Mater. 1978, 78, 408

- 155 - T. Ishitami & R. Schmizu
J. Appl. Phys. 1975, 6, 241
- 156 - H. H. Andersen
J. Appl. Phys. 1979, 18, 131
- 157 - W. O. Hofer & U. Littmark
Phys. Letters (A) 1979, 71, 457
- 158 - P. Sigmund & A. Gras-Marty
Nucl. Instrum. Meth. 1980, 168, 389
- 159 - Z. L. Liao, J. W. Mayer, W. L. Brown & J. M. Poate
J. Appl. Phys. 1978, 49, 5295
- 160 - A. D. G. Stewart & M. W. Thompson
J. Mat.Sci. 1969, 4, 56
- 161 - M. W. Thompson
"Defects & Radiation Damage in Metals"
Cambridge University Press 1968
- 162 - O. Almqvist & G. Bruce
Nucl. Instrum. Meth. 1961, 2, 257 & 279
- 163 - G. K. Wehner J. Appl. Phys. 1959, 30, 1762
- 164 - J. Fluit Thesis Leiden University 1962
- 165 - D. Onderdelinden
Can. J. Phys. 1976, 46, 739
- 166 - W. Gibson In reference No.160, Private communication
- 167 - J. Lindhard Matt. Fys. Medd. 1965, 34, 14

- 168 - A. Guentheschulze & W. Tollmier
Z. Physik 1942, 119, 685
- 169 - G. K. Wehner & D. J. Hajicek
J. Appl. Phys. 1971, 42, 1145
- 170 - W. R. Hudson J. Vac. Sci. Technol. 1977, 14, 286
- 171 - G. K. Wehner Proc. 5th Int. Conf. Ionization
Phenomena in Gases. Vol. 2
Ed. H. Maecker
N. Holand The Netherlands 1962, p 1141
- 172 - G. K. Wehner & D. Rosenberg
J. Appl. Phys. 1961, 32, 887
- 173 - R. S. Berg & G. J. Kominiak
J. Vac. Sci. Technol. 1976, 13, 403
- 174 - H. R. Kaufman & R. S. Robinson
J. Vac. Sci. Technol. 1979, 16, 175
- 175 - G. A. Somorjai
"Principles of Surface Chemistry"
Prentic Hall N. J. 1972, p 77
- 176 - P. Sigmund J. Mat Sci. 1973, 8, 1545
- 177 - K. B. Winterbon, P. Sigmund & J. B. Sanders
Mat. Fys. Medd. Dan. Vid. Selsk
1970, 37, 14
- 178 - I. H. Wilson & M. W. Kidd
J. Mat. Sci. 1971, 6, 1362

- 179 - G. Staudenmeier
Rad. Effects 1972, 13, 87
- 180 - W. Heiland & E. Taglauer
Rad. Effects 1973, 19, 1
- 181 - A. R. Bayly J. Mat Sci. 1972, 7, 404
- 182 - M. J. Lighthill & G. B. Whitham
Proc. Roy. Soc. (A) 1955, 229, 281
- 183 - M.J. Lighthill & G. B. Whitham
Proc. Roy. Soc. (A) 1955, 229, 317
- 184 - F. C. Frank "Growth & Perfection of Crystals"
John Wiley & Sons Inc. 1958, p 411
- 185 - F. C. Frank Z. Phys. Chem. Neue. Folge. 1972, 77, 84
- 186 - F. C. Frank & M. B. Ives
J. Appl. Phys. 1960, 31, 1996
- 187 - M. B. Ives J. Appl. Phys. 1961, 32, 1534
- 188 - D. J. Barber, F. C. Frank, M. Moss, J. W. Steed &
I. S. T. Tsong
J. Mat Sci. 1973, 8, 1030
- 189 - H. Bach J. Non-Crystalline Solids 1970, 3, 1
- 190 - C. Catana, J. S. Colligon & G. Carter
J. Mat. Sci. 1972, 7, 467
- 191 - M. B. Ives Ph. D. Thesis Bristol University,
U. K. 1959

- 192 - F. Vasiliu, I. A. Teodorescu & F. Glodeanu
J. Mat. Sci. 1975, 10, 399
- 193 - I. A. Teodorecu
Rev. Roum. Phys. 1967, 12, 305
- 194 - G. V. Spivak, I. N. Prilezhaeva & O. I. Savochkina
Dokl. Acad. U. S. S. R. 1953, 88, 511
- 195 - M. T. Robinson & A. L. Southern
J. Appl. Phys. 1968, 39, 3470
- 196 - J. M. Fluit, C. Snoeck & J. Kistmaker
Physica 1964, 30, 144
- 197 - C. E. Carlson, G. D. Magnuson, A. Comeaux &
P. Mahavedan
Phys. Rev. 1965, 138, 759
- 198 - O. Almen & G. Bruce
Nucl. Instrum. Meth. 1961, 11, 257
- 199 - T. V. Snouse & M. Bader
Trans. 2nd Int. Vac. Cong. 1962, 1, 271
- 200 - J. M. Fluit "Le Bomb. Ionique"
C. N. R. S. 1962, p 119
- 201 - R. S. Bhattacharya, D. K. Mukherjee &
S. B. Karmohapatro
Nucl. Instrum. Meth. 1972, 99, 509
- 202 - M. J. Witcomb
J. Mat. Sci. 1974, 9, 551

- 203 - G. K. Wehner J. Appl. Phys. 1958, 112, 1120
- 204 - G. Carter & J. S. Colligon
"Ion Bombardment of Solids"
Heinemann 1968
- 205 - N. Laegreid & G. K. Wehner
J. Appl. Phys. 1961, 32, 365
- 206 - I. H. Wilson & M. W. Kidd
J. Mat Sci. 1971, 6, 1362
- 207 - R. L. Cunningham & J. Ng-Yelim
J. Appl. Phys. 1969, 40, 2904
- 208 - J. A. Duffie & W. A. Beckman
"Solar Energy Thermal Processes"
John Wiley & Sons. Inc. 1974
- 209 - M. P. Thekaekara & A. J. Drummond
Nat. Phys. Sci. 1971, 229, 6
- 210 - "Solar Electromagnetic Radiation "
N. A. S. A. Report SP-8005
- 211 - F. K. Richtmyer & E. H. Kennard
"Introduction to Modern Physics" 4th Ed.
McGraw-Hill Book Company N. Y. 1947
- 212 - R. Siegel & J. R. Howell
"Thermal Radiation Heat Transfer"
McGraw-Hill Book Company N. Y. 1972

- 213 - D. K. Edwards, K. E. Nelson, R. D. Roddick &
J. T. Gier
Dept. Eng. Report 60-93
University of California Oct. 1960
- 214 - H. C. Hottel & B. B. Woertz
Trans. A. S. M. E. 1942, 14, 91
- 215 - J. T. Gier & V. R. Dunkle
Trans. Conf. on the Use of Solar Energy
University of Arizona Press 1958, p 41
- 216 - H. Tabor Bull. Res. Coun. Israel 1956, 5A (2), 119
- 217 - H. Tabor, J. Harris, H. Weinberger & B. Doron
Proc. U. N. Conf. on New Sources of
Energy 1964, 4, 618
- 218 - H. Tabor "Selective Surfaces for Solar Collectors"
Low Temperature Engineering Applications
of Solar Energy
ASHRAE N. Y. 1976
- 219 - H. C. Hottel & T. A. Unger
Solar Energy 1959, 3, 10
- 220 - P. Kokoropoulos, E. Salem & F. Daniels
Solar Energy 1959, 3, 19
- 221 - D. A. Williams, T. A. Lappin & J. A. Duffie
J. Eng. Power 1963, 85 (A), 213

222 - C. D. Martin & R. Bell

Proc. Conf. on Coatings for Aerospace
Environment

Wright Air Development Division

WADD-TR-60-TB

Dayton Ohio Nov. 1960

223 - K. G. T. Hollands

Solar Energy 1963, 7, 108

224 - H. Tabor

Trans. Conf. on the Use of the Solar
Energy. Vol. 2, Part 1, Section A

1955, p 24

225 - R. B. Gillette

Solar Energy 1960, 4, 24

226 - B. P. Kozyrev & O. E. Vershinin

Optics & Spectroscopy 1959, 6, 345

227 - J. F. Zeigler & J. M. Woodwall

Appl. Phys. Letters 1975, 26, 557

228 - D. P. Grimmer, K. C. Herr & W. J. McCreary

J. Vac. Sci. Technol. 1978, 15, 59

229 - P. M. Curmi & G. L. Harding

J. Vac. Sci. Technol. 1980, 17, 1320

230 - M. R. Lake & G. L. Harding

J. Vac. Sci. Technol. 1981, 19, 173

- 231 - D. R. McKenzie, B. Window, G. L. Harding, A. R. Collins
& D. W. Mackey
J. Vac. Sci. Technol. 1981, 19, 93
- 232 - D. R. McKenzie
J. Vac. Sci. Technol. 1981, 19, 181
- 233 - G. L. Harding
J. Vac. Sci. Technol. 1976, 13, 1070
- 234 - G. L. Harding & S. Craig
J. Vac. Sci. Technol. 1979, 16, 857
- 235 - I. T. Ritchie & B. Window
Appl. Optics 1977, 16, 1438
- 236 - S. J. Walker & D. R. McKenzie
J. Vac. Sci. Technol. 1981, 19, 700
- 237 - J. A. Thornton
J. Vac. Sci. Technol. 1974, 11, 666
- 238 - J. A. Thornton
J. Vac. Sci. Technol. 1975, 12, 830
- 239 - S. Craig & G. L. Harding
J. Vac. Sci. Technol. 1981, 19, 205
- 240 - A. I. Shaldervan & N. G. Nakhodkin
Sov. Phys. Solid State 1970, 11, 2773
- 241 - J. G. W. van de Waterbeemd & G. W. van Oosterhout
Philips Res. Rep. 1967, 22, 375

- 242 - N. G. Nakhodkin & A. I. Shaldervan
Sov. Phys. Solid State 1972, 13, 1627
- 243 - A. I. Shaldervan & N. G. Nakhodkin
Sov. Phys. Solid State 1971, 12, 1748
- 244 - T. W. Barbee Jr., W. H. Holmes, D. L. Keith,
M. K. Pyzyna & G. Ilonca
Thin Solid Films 1977, 45, 591
- 245 - H. A. Beale & W. Grossklaus
Thin Solid Films 1977, 40, 281
- 246 - A. van der Drift
Philips Res. Rep. 1976, 22, 267
- 247 - M. Neiryneck, W. Samaey & L. van Poucke
J. Vac. Sci. Technol. 1974, 11, 647
- 248 - R. F. Bunshah & R. S. Juntz
Metall. Trans. 1973, 4, 21
- 249 - P. Moon J. Franklin Institute 1940, 230, 583
- 250 - M. E. Hutchins
Solar Energy Unit, University College,
Cardiff, U. K.
Private communication
- 251 - F. Grum & G. W. Luckey
Appl. Optics 1968, 7, 2289

252 - P. J. Schneider

"Mathematical Methods"

Handbook of Heat Transfer

Eds. W. M. Rohsenow & J. P. Hartnett

McGraw-Hill Book Company N. Y. 1973,

p 1-48

253 - W. B. Fussell, J. J. Triolo & J. H. Henninger

"A Dynamic Thermal Vacuum Technique
for Measuring the Solar Absorptance
and Thermal Emittance of Spacecraft
Coatings"

N. A. S. A. Technical Note number D-1716

254 - J. R. Pierce "Theory of Design of Electronic Beams"

D. Van Nostrand Company Inc. N. Y. 1954

255 - S. Schiller, H. Foerster, P. Lenk & G. Jaesch

"High Power Electron Beam Guns for
Evaporation (Axial Systems)"

Electron and Ion Beam Science and
Technology

5th Int. Conf. Proceeding

The Electrochemical Society Inc.

N. J. 1972, pp 399-411

256 - R. J. Hill "Physical Vapour Deposition"

Airco Temscal 1975

257 - G. K. Wehner Phys. Rev. 1956, 102, 690

258 - G. K. Wehner J. Appl. Phys. 1954, 25, 270

259 - N. Mykura Department of Metallurgy and Materials
Engineering, University of Aston in
Birmingham, U. K.
Private communication.

260 - J. S. Sullivan
Department of Physics, University of
Aston in Birmingham, U. K.
Private communication.

261 - J. L. Whitton, O. Holck, G. Carter & M. J. Nobes
Nucl. Inst. Methods 1980, 170, 371

262 - R. Kelly & O. Auciello
Surf. Sci. 1980, 100, 135